Institut für Mathematik
Numerische Mathematik - Inverse Probleme

Microphysical retrieval of non-spherical aerosol particles using regularized inversion of multi-wavelength lidar data

Dissertation zur Erlangung des akademischen Grades
doctor rerum naturalium (Dr. rer. nat.)
in der Wissenschaftsdisziplin Numerische Mathematik

eingerichtet an der
Mathematisch-Naturwissenschaftliche Fakultät
der Universität Potsdam

von Stefanos Samaras

Potsdam, den 12 Dezember 2016

A mind once stretched by a new idea, never regains its original dimensions

$\sim$ *Oliver Wendell Holmes*

Abstract

Numerous reports of relatively rapid climate changes over the past century make a clear case of the impact of aerosols and clouds, identified as sources of largest uncertainty in climate projections. Earth's radiation balance is altered by aerosols depending on their size, morphology and chemical composition. Competing effects in the atmosphere can be further studied by investigating the evolution of aerosol microphysical properties, which are the focus of the present work.

The aerosol size distribution, the refractive index, and the single scattering albedo are commonly used such properties linked to aerosol type, and radiative forcing. Highly advanced lidars (light detection and ranging) have reduced aerosol monitoring and optical profiling into a routine process. Lidar data have been widely used to retrieve the size distribution through the inversion of the so-called Lorenz-Mie model (LMM). This model offers a reasonable treatment for spherically approximated particles, it no longer provides, though, a viable description for other naturally occurring arbitrarily shaped particles, such as dust particles. On the other hand, non-spherical geometries as simple as spheroids reproduce certain optical properties with enhanced accuracy. Motivated by this, we adapt the LMM to accommodate the spheroid-particle approximation introducing the notion of a two-dimensional (2D) shape-size distribution.

Inverting only a few optical data points to retrieve the shape-size distribution is classified as a non-linear ill-posed problem. A brief mathematical analysis is presented which reveals the inherent tendency towards highly oscillatory solutions, explores the available options for a generalized solution through regularization methods and quantifies the ill-posedness. The latter will improve our understanding on the main cause fomenting instability in the produced solution spaces. The new approach facilitates the exploitation of additional lidar data points from depolarization measurements, associated with particle non-sphericity. However, the generalization of LMM vastly increases the complexity of the problem. The underlying theory for the calculation of the involved optical cross sections (T-matrix theory) is computationally so costly, that would limit a retrieval analysis to an unpractical point. Moreover the discretization of the model equation by a 2D collocation method, proposed in this work, involves double integrations which are further time consuming. We overcome these difficulties by using precalculated databases and a sophisticated retrieval software (SphInX: Spheroidal Inversion eXperiments) especially developed for our purposes, capable of performing multiple-dataset inversions and producing a wide range of microphysical retrieval outputs.

Hybrid regularization in conjunction with minimization processes is used as a basis for our algorithms. Synthetic data retrievals are performed simulating various atmospheric scenarios in order to test the efficiency of different regularization methods. The gap in contemporary literature in providing full sets of uncertainties in a wide variety of numerical instances is of major concern here. For this, the most appropriate methods are identified through a thorough analysis on an overall-behavior basis regarding accuracy and stability. The general trend of the initial size distributions is captured in our numerical experiments and the reconstruction quality depends on data error level. Moreover, the need for more or less depolarization points is explored for the first time from the point of view of the microphysical retrieval. Finally, our approach is tested in various measurement cases giving further insight for future algorithm improvements.

Zusammenfassung

Zahlreiche Berichte von relativ schnellen Klimaveränderungen im vergangenen Jahrhundert liefern überzeugende Argumente über die Auswirkungen von Aerosolen und Wolken auf Wetter und Klima. Aerosole und Wolken wurden als Quellen größter Unsicherheit in Klimaprognosen identifiziert. Die Strahlungsbilanz der Erde wird verändert durch die Partikelgröße, ihre Morphologie und ihre chemische Zusammensetzung. Konkurrierende Effekte in der Atmosphäre können durch die Bestimmung von mikrophysikalischen Partikeleigenschaften weiter untersucht werden, was der Fokus der vorliegenden Arbeit ist.

Die Aerosolgrößenverteilung, der Brechungsindex der Partikeln und die Einzel-Streu-Albedo sind solche häufig verwendeten Parameter, die mit dem Aerosoltyp und dem Strahlungsantrieb verbunden sind. Hoch entwickelte Lidare (Light Detection and Ranging) haben die Aerosolüberwachung und die optische Profilierung zu einem Routineprozess gemacht. Lidar-Daten wurden verwendet um die Größenverteilung zu bestimmen, was durch die Inversion des sogenannten Lorenz-Mie-Modells (LMM) gelingt. Dieses Modell bietet eine angemessene Behandlung für sphärisch angenäherte Partikeln, es stellt aber keine brauchbare Beschreibung für andere natürlich auftretende beliebig geformte Partikeln -wie z.B. Staubpartikeln- bereit. Andererseits stellt die Einbeziehung einer nicht kugelförmigen Geometrie -wie z.B. einfache Sphäroide- bestimmte optische Eigenschaften mit verbesserter Genauigkeit dar. Angesichts dieser Tatsache erweitern wir das LMM durch die Approximation von Sphäroid-Partikeln. Dazu ist es notwendig den Begriff einer zweidimensionalen Größenverteilung einzuführen.

Die Inversion einer sehr geringen Anzahl optischer Datenpunkte zur Bestimmung der Form der Größenverteilung ist als ein nichtlineares schlecht gestelltes Problem bekannt. Eine kurze mathematische Analyse wird vorgestellt, die die inhärente Tendenz zu stark oszillierenden Lösungen zeigt. Weiterhin werden Optionen für eine verallgemeinerte Lösung durch Regularisierungsmethoden untersucht und der Grad der Schlechtgestelltheit quantifiziert. Letzteres wird unser Verständnis für die Hauptursache der Instabilität bei den berechneten Lösungsräumen verbessern. Der neue Ansatz ermöglicht es uns, zusätzliche Lidar-Datenpunkte aus Depolarisationsmessungen zu nutzen, die sich aus der Nichtsphärizität der Partikeln assoziieren. Die Verallgemeinerung des LMMs erhöht erheblich die Komplexität des Problems. Die zugrundeliegende Theorie für die Berechnung der beteiligten optischen Querschnitte (T-Matrix-Ansatz) ist rechnerisch so aufwendig, dass eine Neuberechnung dieser nicht sinnvoll erscheint. Darüber hinaus wird ein zweidimensionales Kollokationsverfahren für die Diskretisierung der Modellgleichung vorgeschlagen. Dieses Verfahren beinhaltet Doppelintegrationen, die wiederum zeitaufwendig sind. Wir überwinden diese Schwierigkeiten durch Verwendung vorgerechneter Datenbanken sowie einer hochentwickelten Retrieval-Software (SphInX: Spheroidal Inversion eXperiments). Diese Software wurde speziell für unseren Zweck entwickelt und ist in der Lage mehrere Datensatzinversionen gleichzeitig durchzuführen und eine große Auswahl von mikrophysikalischen Retrieval-Ausgaben bereitzustellen.

Eine hybride Regularisierung in Verbindung mit einem Minimierungsverfahren wird als Grundlage für unsere Algorithmen verwendet. Synthetische Daten-Inversionen werden mit verschiedenen atmosphärischen Szenarien durchgeführt, um die Effizienz verschiedener Regularisierungsmethoden zu untersuchen. Die Lücke in der gegenwärtigen wissenschaftlichen Literatur gewisse Unsicherheiten durch breitgefächerte numerische Fälle bereitzustellen, ist ein Hauptanliegen dieser Arbeit. Motiviert davon werden die am besten geeigneten Verfahren einer gründlichen Analyse in Bezug auf ihr Gesamtverhalten, d.h. Genauigkeit und Stabilität, unterzogen. Der allgemeine Trend der Anfangsgrößenverteilung wird in unseren numerischen Experimenten erfasst. Zusätzlich hängt die Rekonstruktionsqualität vom Datenfehler ab. Darüber hinaus wird die Anzahl der notwendigen Depolarisationspunkte zum ersten Mal aus der Sicht des mikrophysikalischen Parameter-Retrievals erforscht. Abschließend verwenden wir unsere Software für verschiedene Messfälle, was weitere Einblicke für künftige Verbesserungen des Algorithmus gibt.

The present work is dedicated to my beloved parents Stamatis and Maria

Contents

List of Figures

List of Tables

Introduction

Climate research has become nowadays more favorable than ever, largely due to the rise of powerful machines which have the capacity to watch closely the atmospheric processes. The ongoing global temperature increase is known to be only one aspect of the change of the climate patterns, now supported by compelling evidence. The imminent risks on agriculture, human health and safety and the long-term preservation of our planet in relatively stable conditions are the predominant reasons of keeping this field at the acme of interest. Keeping in mind that some of the effects to come are inevitable e.g. principal greenhouse gases CO_2, CH_4, N_2O, CFCs may reside in the atmosphere for hundreds of years (see [41] for a comprehensive list of the atmospheric lifetime of various gases) our greatest concern is the limit of predictability and the extent of such effects on climate.

The Intergovernmental Panel on Climate Change (IPCC) reports are an attempt to communicate the available information about climate change based on published sources led by experts all over the world. Their latest efforts (see [64], working group one) included for the first time policy relevant background based on sophisticated climate models which will help decision-makers develop adaptation strategies in possible future climate projections in a global and regional level, see [63]. The 4th and 5th assessment reports, see [62, 64] not only highlight the anthropogenic influence driven by greenhouse emissions, mostly attributed to energy production, but also developed high confidence that aerosol-radiation- and aerosol-cloud interactions still carry the largest uncertainty to the total radiative forcing estimate. The latter have set off a substantial portion of global mean forcing from well-mixed greenhouse gases, see Fig. 1.

As a result, a deeper understanding of the link between climate processes and the aerosol direct and indirect effect, requires focus on aerosol profiling and especially on the temporal and spatial variability of aerosol microphysical properties, for which instruments have only recently started to fill in the observational gap. The derivation of the microphysical properties will exclusively be the focus of the present thesis. Widely known such properties are the aerosol size distribution, the complex refractive index, the mean particle radius (effective radius), the volume concentration and the single scattering albedo, the combined knowledge of which could provide information for particle size, scattering, and absorption and by extension shape and chemical composition. These properties, in turn, link to human health, Earth's radiation budget (upwelling and downwelling radiance) [76], and precipitation when aerosols act as cloud condensation nuclei of water vapor [93].

The structural and chemical complexity of aerosols is too high to analyze which is why the aerosol size distribution is of central interest among the microphysical properties for a probabilistic approach. Alterations in chemical composition of aerosols directly affect their number and size and cloud microphysics as well. In addition, the accurate knowledge of the size distribution is often a prerequisite for other important parameters like the aerosol effective radius or the number concentration. However, there are only a few real-time measurements of the size distribution to date but they are often limited in size-ranges, e.g. measurements with Aerosol Mass Spectrometers [68], and they are costly as well when they refer to instruments attached to an aircraft (e.g. [6]). A common practice is to derive instead of measuring the size distribution through some knowledge on scattering and absorption phenomena, i.e. the aerosol optical properties, involving the target aerosols. Indeed, today's technology allows for a variety of instruments to measure these properties practicing remote sensing. As R. Colwell, a pioneer in photogrammetry, put it, the latter is "...the art, science, and technology of obtaining reliable information about physical objects and the environment, through the process of recording, measuring and interpreting imagery and digital representations of energy patterns derived from non-contact sensor systems" (requoted from [21]).

One of the most popular examples of passive remote sensing is the sun-sky radiometer (or sun photometer) operated by NASA's AErosol RObotic NETwork (AERONET). AERONET provides a long-
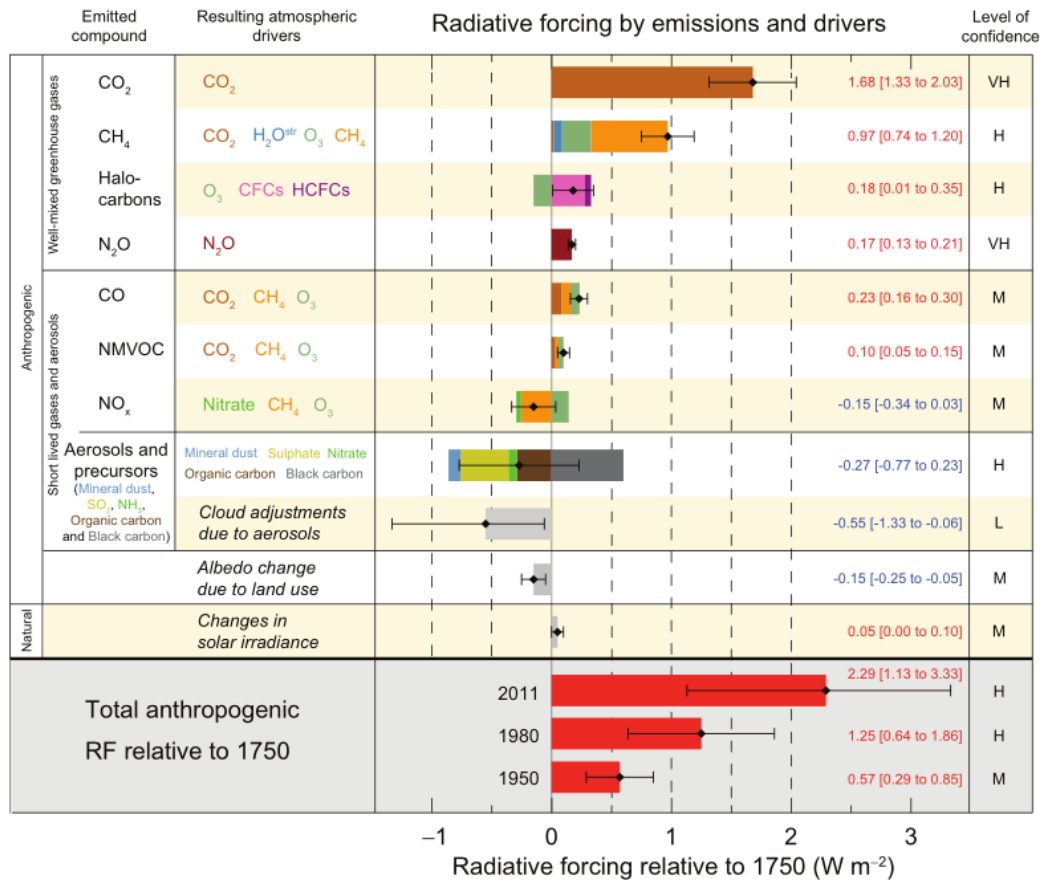
Figure 1: Working Group I Contribution to the IPCC 5th assessment report, 2013: The Physical Science Basis, Figure SPM.5. Role of the greenhouse gases in total radiative forcing estimate in 2011 relative to 1750 and aggregated uncertainties for the main drivers of climate change. Black diamonds indicate the best estimates of the net radiative forcing with corresponding uncertainty intervals on the right of the figure, and the confidence level in the net forcing (VH: very high, H: high, M: medium, L: low, VL: very low). Figure credit: [65]

term, continuous database of aerosol optical and microphysical properties extracted by sun photometer measurements and inversions worldwide. The operational protocol of AERONET consists of sky radiances inversions together with measurements of aerosol optical depth to produce the aerosol size distribution and various microphysical and forcing parameters. Sun photometers are impressive fully automated energy-autonomous devices, providing measurements characteristic of the entire atmospheric column but on the other hand lack information regarding the vertical distribution of aerosols. A detailed description of the inversion advancement and the retrieval products of AERONET can be found in [33, 34, 35, 36, 136]. Other examples of passive sensors can be found in microwave radiometers, imaging radiometers, spectrometers and sounders.

Laser invention in 1960 [95] has literally brought to light the concept of remote sensing already used with radars. Optical radars known as lidars (light detection and ranging), see [153], are an evolving technology leading the branch of active atmospheric remote sensing. Although it was not after 1962 that a ruby laser was involved in atmospheric observation [40] that their potential was revealed, the idea of light-based study of the atmosphere dates back to World war II with search-light beams (e.g. [69]) for military purposes, and later on we have the first studies involving cloud heights [1]. Lidars do not depend on a clear sky like sun photometers, since they emit their own radiation probing the target of interest and collecting the returning light from the scattering scene they trigger. They now allow for continuous routine vertical profiling of atmospheric constituents with high spatial and temporal resolution enhancing our observational capacity. The advancement of a lidar system reflects its ability to analyze

spectrally the atmospheric response to the emitted pulsed laser beam; the elastic scattered light, the pure rotational Raman spectra and the rotational-vibrational Raman spectra of atmospheric molecules (N_2, O_2). Elastic-Raman multi-wavelength (355, 532, 1064 nm) polarization lidars offer a variety of intensive and extensive aerosol properties, among which are the particle extinction and backscatter, lidar ratio, water vapor mixing ratio, temperature and particle depolarization ratio.

At this point we need to mention the great efforts of European Aerosol Research Lidar Network (EARLINET), now part of the ACTRIS project (Aerosols, Clouds, and Trace gases Research Infrastructure network), to provide a comprehensive, and statistically significant database for the horizontal, vertical, and temporal distribution of aerosols on a continental scale, see [118] for the recent state of the network. Since its foundation in 2000 it has been a milestone for aerosol research carrying the most extensive ground-based data collection for the aerosol vertical profiling over Europe with increasingly higher quality assurance standards and instrumental optimization.

Lidar products cover knowledge on the atmospheric state as well as aerosol typing. The extinction and backscatter coefficients are relatively straightforward to obtain through a relation between the power of the backscattered light (converted to electrical signal) and lidar geometrical characteristics, called the lidar equation. In this work, we will use these parameters as inputs for the retrieval of the size distribution. The latter is related to the optical parameters through an integral operator which actually contains most of what we care about, namely shape, size and composition of the particles, in the form of the so-called kernel functions. For one we have to solve an inverse problem, which mathematically suffers from non-uniqueness of solutions (if any) and great instability even in the presence of low rounding, modelling or measurement errors, producing dubious results. As seen from the standing point of the forward problem, the noise-related loss of control is a result of the smoothing phenomenon of the operator acting to the size distribution and therefore, conversely, the very process of inversion could magnify potential noisy components. This defect has been effectively dealt using regularization to suppress the noise spikes for particles which resemble spheres e.g. very small particles, fresh smoke (biomass burning) or stratospheric sulphate (volcanic eruptions). Algorithms have been employing textbook techniques e.g. the Truncated SVD [14, 17], and Tikhonov regularization, [86, 107, 145], but also iterative methods, [16, 113] and continue to evolve since late 90's mainly by using various physical and mathematical rules to confine the solution space. Simulated retrievals have reached a good level of theoretical maturity, so that real lidar data are now efficiently inverted and analyzed, e.g. [2, 104, 113, 117, 131, 150]. Artificial data as opposed to real-life data include no risk of mishandling some of the initial parameters (e.g. the size range) as physical entities. Dealing with real-life data, on the other hand, requires their predetermination. Numerical experiments show that poor selection of these parameters directly affects the solution space quality and compromises the retrieval regardless of the robustness of the regularization algorithm. As demonstrated in [131], sensitivity tests have to be taken over as preliminary retrievals in order to set the ground for a meaningful solution.

Spheres are nonetheless no longer a viable representation for the non-spherical case such as mineral dust. This aerosol type is important since its forcing is underlined for its global significance and its impact on the alteration of cloudoptical properties by the Saharan Mineral Dust Experiment (SAMUM), see [4]. In addition, particle shape is known to have substantial effects for the scattering in sideward and backward direction [100]. Since there is no prescription-formula to cover every possible shape, one needs to presuppose in some manner the shape and reduce the problem to finding out what are the characteristics of the particular geometrical symmetry which was chosen. T-matrix theory [100, 152] is among the very few powerful techniques for solving the electromagnetic scattering problem for a given shape but its computational complexity keeps research for the non-spherical aerosols still in its early years of development. Indeed, the computations of the kernel functions even for one of the simplest non-spherical approximation, i.e. spheroids, require extensive stability tests which would hold back the microphysical inversion significantly. This is the reason why, all microphysical codes based on this theory to date, operate with precalculated look-up tables and it also the case for this work as we will see later on.

There are only two basic works to our knowledge which use the spheroid-particle approximation for the microphysical retrieval problem, namely [35, 143]. The algorithms used are based on a model of randomly oriented spheroids where aerosols are modeled as a mixture of spherical and non-spherical components, but ultimately for simplicity shape and size are assumed to be independent. In this work we also adopt the spheroid-particle approximation with a simultaneous generalization of the size distribution to a shape-size distribution in two dimensions first proposed by [18, 112], where the entanglement of shape

and size is yet to be found. After investigating how the 2D-generalization affects our problem in terms of complexity (e.g. discretization, shape-size distribution reconstruction) we proceed to build a database to be able to conduct massive synthetic retrievals. In a first stage, the performed simulations pertain to a large atmospheric diversity (size, shape, refractive index) using most of the regularization techniques in literature, in the search for the most suitable one. This will allow us to familiarize deeply with the retrieval outcomes and unveil the robustness but also crucial limitations of our approach. Moreover, we will be able to differentiate between dissimilar needs that each method covers. A missing piece from today's literature is a systematic way for a first level evaluation of an algorithm, to which this work contributes employing different error-related uncertainties. These quantities will be the key feature not only for our (method) comparisons but also for analyzing statistically the effect of different physical factors in the inversion.

The ideal lidar setup is one of the most important topics which concerned researchers since the early years of the microphysical retrievals and forged today's lidar engineering. The minimum requirement at least for the spherical case is now established to be a set of 3 backscatter coefficients (β) at 355, 532 and 1064 nm and 2 extinction coefficients (α) at 355 and 532 nm ("$3\beta + 2\alpha$"). The current consensus strongly points to the use of depolarization profiles to account for particle non-sphericity, but it is still unknown what is the ideal combination of α and β for data inversion either quantitatively or qualitatively. This work provides an answer for the first time for what is theoretically possible by comparing the microphysical outputs of several lidar setups in terms of the aforementioned uncertainties.

The applicability of our algorithm is tested with measurement cases carried out in different lidar sites and covering real-life physical phenomena. Finally, our conclusions are summarized and followed by a discussion about what can be achieved in the future.

This dissertation is structured as follows:

- In Chapter 1 we present an up-to-date mathematical view of inverse ill-posed problems, and introduce the general framework within which the computations will take place.

- Chapter 2 exposes the physical setting of our problem in the context of electromagnetic theory and summarizes all the important physical entities for this work.

- In Chapter 3 we introduce the generalized physical model and show technical details and computational aspects about the microphysical retrieval problem.

- Chapter 4 constitutes the core of this work and is occupied with extensive numerical tests on our methods and algorithms with simulations, through which we elaborate on the different topics discussed in the previous paragraphs.

- In Chapter 5 we apply our approach to measurement data from different lidar stations.

- Finally, we conclude this work with a full synopsis of the main results followed by a discussion on limitations of the developed software and potential advancements for the future.

Table 1: List of abbreviations.

Name	Abbreviation
Appendix	App.
Chapter	Ch.
Definition	Def.
Example	Ex.
Figure	Fig.
Section	Sec.
Theorem	Th.

Chapter 1

Mathematical apparatus

Foreword

There is not enough room to expand on every mathematical aspect we came about during this work. Here we borrow some basic definitions and results from the field of inverse ill-posed problems where the need for the regularization technique arises. We present, an operator decomposition (Singular Value Decomposition - SVD) of great theoretical interest which has fundamental role for the study of the degree of ill-posedness of a certain case scenario and gives an insightful demonstration of the noise effect. SVD analysis can further result in a regularization method (Truncated SVD) through a noise-filter procedure introducing the notion of parameter choice rules (PCRs). We will use this opportunity to define intuitively another filter method, Tikhonov, and an iterative method (Padé iteration) from the family of the generalized Runge-Kutta iterative methods. Several popular PCRs are shown here emphasizing their importance in parallel with the underlying regularizer; if regularization is the driving wheel to reach a meaningful solution space, PCRs are the brakes. Finally we define the B-spline functions which hold an eminent position in our work, both for the discretization and the solution reconstruction. We note that most of the theoretical background is given in the context of Hilbert spaces, although in some cases they can be generalized to Banach spaces. We follow this line, since later in our work we will have to use orthogonality and projection spaces which require a Hilbert space configuration. For more details in the theory of inverse problems see e.g. [10, 57, 123].

1.1 Inverse problems & ill-posedness

In the physical world, distinguishing the link between forward and inverse problems, usually implies a form of cause and causality. What makes a problem be in "forward mode" is that it usually refers to a collection of data (from a sort of measurement) for which the causal agent is sought and where the conversion mechanism between them is assumed to be known. The inversion process is intuitively not a "spontaneous" act. We need to set a bar above which a problem qualifies to be solved (inverted), and at the same time try to see to what extent it meets a physical problem. For this we recall the definition of well-posedness by J. Hadamard, see [52] which applies to any problem.

In what follows, $\mathscr{L}(V, G)$ denotes the set of linear bounded operators between the normed spaces V and G with the inner products $\langle \cdot, \cdot \rangle_V$ and $\langle \cdot, \cdot \rangle_G$ respectively, and $\mathscr{K}(V, G) = \{T \in \mathscr{L}(V, G) | T \text{ is compact}\}$. Note, that we often omit the space-subscripts in the inner products for brevity when there is no risk of confusion.

Definition 1.1.1 (Well-posedness by Hadamard)**.** Let $T : V \to G$ be a linear operator between Hilbert spaces. We consider the model linear equation $Tv = g$, where v is the unknown function. If all the following statements hold true:

1. There is a solution $v \in V$ of the Eq. $Tv = g$ for every $g \in G$,

2. The solution is unique.

3. The solution is stable in the sense that a perturbed right hand side should cause a distortion of the solution of equal strength,

then the problem (T, V, G) is called *well-posed*, otherwise is called *ill-posed*.

The bijectivity of T (1, 2), will assure the existence of the inverse of T, T^{-1} and the stability requirement (3) translates into a form of continuity. The following result shows when an inverse operator inherits the stability property from the forward operator.

Theorem 1.1 (Banach's inverse mapping theorem). *If $T : V \to G$ is a bijective bounded linear operator then T^{-1} exists and is also bounded, i.e. T is an isomorphism.*

We note that boundedness in linear operators between normed spaces is equivalent to continuity and does not necessarily imply the usual boundedness in the sense of a function. It turns out that we need one-to-one correspondence to assure the desired noise control in the solution, but this demand is not everyday-life in applications. In principle we may be able to rule out an injective T (2) by subtracting the nullspace of T from V, thus restricting to $V \smallsetminus \ker T$. The so-called *annihilators*, i.e. the elements of $\ker T$ can often be detected numerically, despite the discretization errors which might hinder the process. However, the surjective part of the requirement cannot be bypassed. For instance, what we get as input from a measurement is a noisy version of g, g^ϵ, for which there might not exist v^ϵ such that $Tv^\epsilon = g^\epsilon$, or $g^\epsilon \notin \text{im}(T)$.

We will see shortly how the first two requirements (1, 2) are treated by the theory and focus later on the main struggle in an application associated with an ill-posed problem, which is the restoration of continuity (3). As already hinted, the spaces where the problem is defined make all the difference regarding its solvability and stability. Let us demonstrate this through a well-known ill-posed problem.

Example 1.1.1 (The problem of the first derivative). The first derivative of a function g with $g(0) = 0$, can be defined as follows

$$(Tv)(r) = \int_0^r v(x)\, dx = g(r), \tag{1.1.1}$$

where $r \geq 0$. For every continuously differentiable function $g \in C_*^1[0,1]$ there is a unique solution of 1.1.1. Using the standard norms of the spaces C and C^1 and the definition of the operator norm, it is straightforward to show that $\|T^{-1}\| \leq 1$ and thus the triple $(T, C[0,1], C_*^1[0,1])$ is a well-posed problem.

Choose now $V = G = L^2[0,1]$, endowed with the usual (L^2) inner product. Clearly, every function in the range of T is continuous, hence $C[0,1] \supseteq \text{im}(T) \nsubseteq L^2[0,1]$. Picking a perturbed right hand side $g^\epsilon(x) = \epsilon \sin(\epsilon^{-2}x)$, we can see that $\|g^\epsilon\|_{L^2[0,1]}$ stays small for a small $\epsilon > 0$. However, a solution $v^\epsilon(x) = \epsilon^{-1} \cos(\epsilon^{-2}x)$ has very large L^2-norm.

Compact linear operators are the extension of matrices in Hilbert places, in which one is able to generalize the spectral theorems. A special compact linear operator which models precisely our problem and many other applications, arises from the so-called *Fredholm equation* defined below.

Definition 1.1.2. A Fredholm integral equation of the first kind has the following general form

$$Tv = \int_a^b K(\lambda, r)v(r)dr = g(\lambda), \tag{1.1.2}$$

where, $K(\lambda, r)$ is called *kernel function*.

Choosing $[a, b] = [0, 1]$ and

$$K(\lambda, r) = \begin{cases} 1, & if \ \ 0 \leq \lambda \leq r \leq 1 \\ 0, & if \ \ 0 \leq r < \lambda < 1 \end{cases} \tag{1.1.3}$$

leads back to the Ex. 1.1.1, i.e. the problem of the first derivative belongs to this class of integral operator equations (also in the class of Volterra integral equations).

The following theorem states the underlying reason for the ill-posedness of these integral equations.

Lemma 1.2 (Riemann-Lebesgue Lemma). *Consider the function sequence $v_n(r) = \sin(2n\pi r)$. Then for a Riemann-integrable function $K(s, t)$ it holds*

$$\lim_{n \to \infty} \int_0^1 K(\lambda, r)v_n(r)dr \to 0. \tag{1.1.4}$$
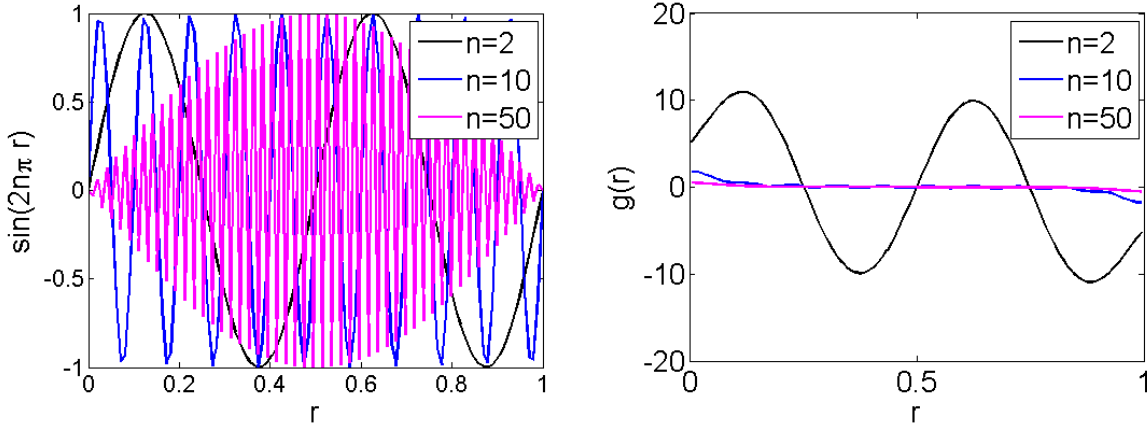
Figure 1.1: Illustration of the Riemann-Lebesgue lemma 1.2 for the gravity surveying problem. Left: Plots of the function $v(r) = \sin(2n\pi r)$, for $n = 2, 10$ and 50. Right: Plots of the right hand side by running the forward model. This example is also shown in [57].

This result summarizes the smoothing phenomenon imposed by the Fredholm operator to any solution candidate. Let us demonstrate this rather discouraging property through an example from geophysics which belongs to the important family of deconvolution problems.

Example 1.1.2 (The gravity surveying problem)**.** We look at the forward problem in 1.1.2 with $[a,b] = [0,1]$ and $K(\lambda, r) = 16/(1 + 16(\lambda - r)^2)^{-3/2}$, where $0 \leq \lambda \leq 1$ and $0 \leq r \leq 1$, and $v(r) = \sin(2n\pi r)$. Fig. 1.1 left shows 3 instances of $v(r)$ for $n = 2, 10$ and 50 and the right hand sides by running the forward model each time. The oscillations are drastically suppressed, eliminating any sign of what the source function was like. We are going to look more into this, by analyzing the general operator with a special decomposition of fundamental theoretical interest.

Theorem 1.3 (Singular Value Decomposition - SVD)**.** *Let $T \in \mathscr{K}(V, G)$ and let T^* be the adjoint of T. There exist sequences $f_j \in V$, $h_j \in G$, and $\mu_j \in \mathbb{R}$ with $0 < \mu_{j+1} \leq \mu_j$ and $j \in \mathbb{N}$ such that the following statements hold:*

i. $\lim_{j \to \infty} \mu_j = 0$.

ii. The sequences $\{h_j\}_{j \in \mathbb{N}}$ and $\{f_j\}_{j \in \mathbb{N}}$ form a complete orthonormal system of the spaces $\overline{\text{im}(T)}$ and $\overline{\text{ker}(T)^{\perp}}$ respectively.

iii. $Tf_j = \mu_j h_j$ *and* $T^* h_j = \mu_j f_j$ *for all* $j \in \mathbb{N}$.

iv. $Tv = \sum_{j=1}^{\infty} \mu_j \langle v, f_j \rangle_V h_j$, *and* $T^* v = \sum_{j=1}^{\infty} \mu_j \langle v, h_j \rangle_G f_j$ *for all* $v \in V$.

The triple $(\mu_j, f_j, h_j)_{j \in \mathbb{N}}$ is called the singular system of the compact operator T. In particular, the sequences $\{f_j\}_{j \in \mathbb{N}}$ and $\{h_j\}_{j \in \mathbb{N}}$ are called the left and right singular functions respectively and the sequences $\{\mu_j\}_{j \in \mathbb{N}}$ are called the singular values of T.

At this point it is interesting to see what happens if we assure the bijectivity of T. The following result comes out of Th. 1.1 for Hilbert spaces and Th. 1.3.

Proposition 1.4. *Let $T \in \mathscr{K}(V, G)$ be a bijective operator and (μ_j, f_j, h_j) its singular system. Then there exists a unique solution of $Tv = g$ given by:*

$$v(r) = \sum_{j=1}^{\infty} \frac{\langle g, h_j \rangle_G}{\mu_j} f_j(r). \tag{1.1.5}$$

Remark. 1. In the general case, if solutions exist they will be of the form

$$v(r) = \sum_{j=1}^{\infty} \frac{\langle g, h_j \rangle_G}{\mu_j} f_j(r) + q, \tag{1.1.6}$$

where $q \in \ker(T)$. Consider an element $g \in \text{im}(T)$ and use the expression 1.1.6 to obtain

$$g = Tv = \sum_{j=1}^{\infty} \mu_j^{-1} \langle g, h_j \rangle_G T f_j = \sum_{j=1}^{\infty} \langle g, h_j \rangle_G h_j = \mathscr{P}_{\mathscr{H}} g, \tag{1.1.7}$$

where $\mathscr{P}$ is a projection operator onto the space $\mathscr{H} = \overline{\text{im}(T)}$. Indeed, the terms $\langle g, h_j \rangle$ are the expansion coefficients of the projection of $g \in \text{im}(T)$ through the h_j basis functions. The convergence of $\sum_{j=1}^{\infty} \langle g, h_j \rangle_G h_j$ to $g \in \text{im}(T)$ is assured if $\text{im}(T)$ is closed, see 1.3, ii. This is an important observation which we will use later on to characterize the ill-posedness.

2. Consider a perturbed right hand side g^{ϵ} such that $\|g - g^{\epsilon}\| < \epsilon$, in particular set $g^{\epsilon} = g + ch_k$ with $0 < c < \epsilon$. Then, using the orthonormality of the singular functions f_j, h_j (ii) and the fact that the singular values decay to zero (i), we have

$$\|v - v^{\epsilon}\| = \frac{c}{\mu_k} \to \infty, \quad \text{for} \quad k \to \infty, \tag{1.1.8}$$

i.e. the solution blows up. This demonstrates the inherent instability of the inversion process and hints that even a tiny perturbation ϵ could cause oscillations of the solution in huge amplitudes.

These remarks are inviting the next result, which sets ground for the least requirement for the existence of a solution, namely that it should own a controllable (finite) norm.

Theorem 1.5 (Picard condition). *Let $T : V \to G$ a compact operator and $(\mu_j, f_j, h_j)_{j \in \mathbb{N}}$ its singular system. An element $g \in \overline{\text{im}(T)}$ is an element of $\text{im}(T)$ exactly then, when*

$$\sum_{j=1}^{\infty} \left(\frac{|\langle g, h_j \rangle|}{\mu_j} \right)^2 < \infty. \tag{1.1.9}$$

This lemma exposes the decisive role of the convergence rate of the singular values; there only exists a solution if the terms $|\langle g, h_j \rangle|$ decay faster in competition to the singular values. This brings us to a characterization of the ill-posedness through the singular values.

Definition 1.1.3 (Degree of ill-posedness). Let $\mathscr{M}$ be a positive real number. Then the problem (T,V,G)

1. is mildly ill-posed if μ_j has a polynomial behaviour, i.e. $\mu_j = \mathscr{O}(j^{-\mathscr{M}})$.

2. is severely ill-posed if μ_j has an exponential behaviour, i.e. $\mu_j = \mathscr{O}(e^{-\mathscr{M}j})$.

Example 1.1.3. According to Def. 1.1.3 we can see how difficult it is to solve a specific ill-posed, and thus and how sensitive it is to possible errors.

1. Recall the problem of the first derivative from Ex. 1.1.1. Observing that the adjoint operator of T is expressed by $T^*v = \int_t^1 v(r) \, dr$ we can easily solve the eigenvalue problem of T^*T using iii, and deduce that the singular system is

$$\mu_j = 1/((j - 1/2)\pi), \quad f_j = \sqrt{2}\cos\left((j - 1/2)\pi r\right), \quad h_j = \sqrt{2}\sin\left((j - 1/2)\pi r\right). \tag{1.1.10}$$

Hence it is a mildly ill-posed problem.

2. Let $V = G = L^2([0, \pi])$ and consider the heat transfer problem with Dirichlet boundary conditions

$$\frac{\partial v}{\partial t} = \frac{\partial^2 v}{\partial x^2}, \quad t > 0, \tag{1.1.11}$$

$$v(0, t) = v(\pi, t) = 0. \tag{1.1.12}$$

Suppose that $u(x) = v(x, 1)$ is measurable and known and we seek to find the initial ($t = 0$) temperature $g(x) = v(x, 0)$. The kernel function of the operator $T : u \mapsto g$ is not explicitly given but it can be found by the general solution of 1.1.11 (separation of variables) to be $K(x, y) = \sum_{j=1}^{\infty} \frac{2}{\pi} e^{-j^2} \sin(ix) \sin(iy)$. Noticing that T is self-adjoint and using iii, it is a mere observation that the singular system is

$$\mu_j = e^{-j^2}, \quad f_j = h_j = \sqrt{\frac{2}{\pi}} \sin(jx), \tag{1.1.13}$$

and therefore the problem is severely ill-posed.

Fig. 1.2 shows plots of the singular values μ_j (blue triangles) and the SVD-terms $\langle g, h_j \rangle$ (green squares) for the two examples discussed above. On the left panel (Ex. 1.1.3, 1.) we see the SVD-terms decay faster than the singular values for $j > 4$ in a gradual step. The right panel (Ex. 1.1.3, 2.) shows a totally different situation: the singular values have predominantly rapid convergence and become essentially zero for $j > 25$ (machine's lowest value). We should note that introducing any error in our examples could even result in (faster) divergence after a certain value of j, even if the problem has a moderate ill-posedness. Searching for a threshold, above which the additional terms in the sum in Eq. 1.4 don't do any good to the solution, is very important for practical purpose. This will be the topic of a posterior section as soon as we introduce the discrete analog of SVD. More details on SVD regarding its computation can be found e.g. in [53] and its mathematical formulation in [88].
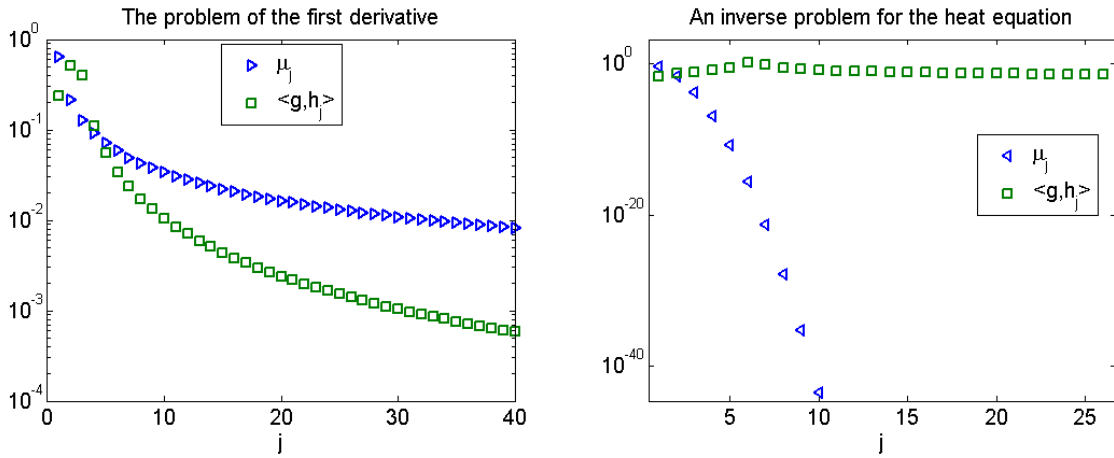
Figure 1.2: Illustration of the Picard condition (see 1.1.9) for the problem of the first derivative (left) and an inverse problem for the heat equation (right). In each panel, both the singular values μ_j (blue triangles) and the SVD-terms $\langle g, h_j \rangle$ (green squares) are shown. The y-axis is shown in logarithmic scale.

The ambiguity in the solution space is apparently undesired. It is possible to search for a unique solution by replacing the problem with

$$T^*Tv = T^*g \iff T^*(Tv - g) = 0 \iff Tv - g \in \ker(T^*) = \mathrm{im}(T)^\perp, \tag{1.1.14}$$

which turns out to be equivalent to a least-squares problem. We will see now how this last observation marries with the theory presented earlier.

Theorem 1.6. *Let $g \in G$ and $T \in \mathscr{L}(V, G)$ such that $Tv = g$ and let $\mathscr{P}_{\mathscr{H}} \in \mathscr{L}(G)$ be a projection operator from G onto the subset $\mathscr{H} \subset G$. The following are equivalent:*

1. v satisfies the equation $Tv = \mathscr{P}_{\overline{\mathrm{im}(T)}}g$

2. v solves the normal equation $T^*Tv = T^*g$.

3. v minimizes the norm of the residual function, i.e. $\|Tv - g\|_G = \inf_{f \in V} \{\|Tf - g\| | f \in V\}$.

Lemma 1.7. *For $g \in \mathrm{im}(T) \oplus \mathrm{im}(T)^\perp$, the set of the solutions of the normal equation $T^*Tv = T^*g$ is non-empty, closed and convex. Moreover, there is a unique solution $v^\dagger$ of minimal norm.*

This property of the normal equation along with continuity of the norm, allows the existence of a unique solution of minimal norm and strikes out uniqueness from Hadamard's requirements. We shall define this as a solution of $Tv = g$ in generalized terms.

Definition 1.1.4 (Moore-Penrose Inverse)**.** The operator $T^\dagger : \mathscr{D}(T^\dagger) \to V$, with the domain $\mathscr{D}(T^\dagger) := \mathrm{im}(T) \oplus \mathrm{im}(T)^\perp$, which assigns uniquely an element $v^\dagger$ of minimal norm to any $g \in \mathscr{D}(T^\dagger)$ is called *Moore-Penrose inverse* or *generalized inverse* of $T \in \mathscr{L}(V, G)$. The element $v^\dagger = T^\dagger g$ is called *minimum-norm solution* of $Tv = g$.

We are now able to answer by what means and under which circumstances we can invert the equation $Tv = g$.

Theorem 1.8. *Let $T \in \mathscr{L}(V, G)$, then its generalized inverse $T^\dagger$ has the following properties:*

1. *$v^\dagger = T^\dagger g$ is the unique solution of the normal equation $T^*Tv = T^*g$ in $\ker(T)^\perp$, for every $g \in \mathscr{D}(T^\dagger)$.*

2. *$T^\dagger$ is linear.*

3. *$\operatorname{im}(T^\dagger) = \ker(T)^\perp$.*

4. *$T^\dagger$ is continuous if and only if $\operatorname{im}(T)$ is closed. Then $T^\dagger$ is defined in the whole G.*

5. *If T is compact, then it is continuous if $\operatorname{im}(T)$ is finite.*

As shown, $\operatorname{im}(T) = \overline{\operatorname{im}(T)}$ is indeed the key to assure the well-posedness of our problem. In fact, (4) allows for another characterization of ill-posedness through the closedness of the range $\operatorname{im}(T)$. Moreover, 5 tells us that we can find a smooth solution by making a finitedimensional projection of the problem, which is actually what discretization does (see Sec. 1.4). A modern theoretical definition of ill-posedness follows directly from 4.

Definition 1.1.5 (Ill-posedness by Nashed). The problem (T, V, G) is called ill-posed if $\operatorname{im}(T)$ is not closed. Otherwise is called well-posed.

1.2 Regularization with spectral filters

Evidently, the ill-posedness resides within the very inversion process. Regularization comes as a natural antidote to suppress possible blow-ups of the solution. The decay rate of the singular values reflect the difficulty of achieving stability and will be our guide and first source of intuition when defining "filters" to dismantle the noise factor. First, let us define regularization through a family of operators approximating the desired (generalized) inverse, see e.g. [11, 88].

Definition 1.2.1 (Regularization scheme). The family of linear bounded operators $\{R_\zeta\}_{\zeta>0}$ from G into V is called a *regularization scheme* or a *regularizer* for T if we have the following pointwise convergenge

$$\lim_{\zeta \to 0} R_\zeta Tv = v, \quad \text{for all } v \in V. \tag{1.2.1}$$

Let there be given noisy data with g^δ, $\delta > 0$, with $\|g^\delta - g\| < \delta$ and let $\{R_\zeta\}_{\zeta>0}$ be a regularization scheme, where $\zeta = \zeta(\delta, g^\delta) > 0$. If for all $g \in \operatorname{im}(T)$ and all $g^\delta \in G$ with $\|g^\delta - g\| < \delta$ we have

$$\lim_{\delta \to 0} R_\zeta g^\delta = T^\dagger g, \tag{1.2.2}$$

then the pair (R_ζ, ζ) is called a *regularization method* for $Tv = g$. Furthermore, ζ is called *a-priori parameter choice rule* (PCR) if it only depends on δ, otherwise is called *a-posteriori parameter choice rule*.

Note that the regularization scheme cannot "repair" a discontinuous operator T by itself by finding a close continuous approximate. Indeed, Banach-Steinhaus theorem (or uniform boundedness principle, see any book in functional analysis, e.g. [127]) prevents $R_\zeta T$ from norm-converging to the identity for an unbounded operator T. On the other hand, the convergence rate of any regularization method (R, ζ) can be arbitrarily slow. The following result demonstrates this.

Theorem 1.9. *Let $T \in \mathscr{L}(V, G)$, and let there be a regularization method (R_ζ, ζ) for $Tv = g$ with $R_\zeta 0 = 0$ for all $\zeta > 0$, and a function $\rho : [0, \infty) \to [0, \infty)$ with $\lim_{\delta \to 0} \rho(\delta) = 0$ such that*

$$sup\{\|R_{\zeta(\delta, g^\delta)} g^\delta - T^\dagger g\|_V : g \in \operatorname{im}(T), \|g\| \leq 1, g^\delta \in G, \|g^\delta - g\|_G \leq \delta\} \leq \rho(\delta), \tag{1.2.3}$$

then $T^\dagger$ is continuous.

As it seems, the fate of the convergence rate is auspicious only as long as we assure the closedness of the range of T. Additional conditions on the generalized solution $v^\dagger$ may offer further results on convergence rates, see [123].

Regularity and data fit are competing quantities, meaning that one cannot achieve simultaneously the best of both. We can easily observe this by splitting the so-called *total reconstruction error* E into the regularity term $I = \|R_\zeta\|$ and the *approximation error* $J = \|R_\zeta Tv - v\|$

$$E = \|v^{(\zeta,\delta)} - v\| \le \|R_\zeta g^\delta - R_\zeta g\| + \|R_\zeta Tv - v\| \le \delta\|R_\zeta\| + \|R_\zeta Tv - v\|, \tag{1.2.4}$$

where $v^{(\zeta,\delta)} = R_\zeta g^\delta$, v is assumed to be the exact (unique) solution of $Tv = g$ and g^δ are perturbed data with $\|g^\delta - g\| \le \delta$. A value of ζ close to zero would result in an infinite regularity and leave the solution uncontrollable, therefore ζ cannot be too small. Too large ζ would shade some of the solution information resulting in a poor approximation. Hence this parameter has to be optimal preventing an explosive solution and preserving most of data integrity which is exactly the aim of a parameter choice rule.

In case of having a unique solution $v^\dagger = T^\dagger g = (T^*T)^{-1}T^*g$, we can see that the troubling part, regarding stability, is T^*T. Moreover, recalling the singular system of T, $(\mu_j, f_j, h_j)_{j \in \mathbb{N}}$ and using Eq. 1.1.5, we have $T^\dagger = \sum_{j=1}^\infty \mu_j^{-1}\langle \cdot, h_j\rangle f_j(r)$ and therefore our filters need to target the singular values. This motivates the candidate filter function $b(\zeta, \mu)$ for the regularization scheme

$$R_\zeta g^\delta = \sum_{j=1}^\infty b(\zeta, \mu_j)\mu_j^{-1}\langle g^\delta, h_j\rangle f_j(r). \tag{1.2.5}$$

Getting to know this function is obviously a critical step since it describes the depth of the regularization with respect to the parameter selection. An immediate question is what the properties are of such a function in order to result in a regularization method.

Theorem 1.10 (Regularizing filters). *Let T be an injective compact operator with singular system $(\mu_j, f_j, h_j)_{j \in \mathbb{N}}$. If the function $b : (0, \infty] \times (0, \|T\|) \to \mathbb{R}$, satisfies the following conditions:*

1. *$b(\zeta, \mu)$ is bounded for all $\zeta > 0, \mu \in (0, \|T\|)$ and $\lim_{\zeta \to 0} b(\zeta, \mu) = 1$ for all $\mu \in (0, \|T\|)$,*

2. *for all $\zeta > 0$ there exists a positive constant $d(\zeta)$ such that for all $\mu \in (0, \|T\|)$ holds either of the following relations,*

   (i) *$|b(\zeta, \mu)| \le d(\zeta)\mu$*
   (ii) *$|b(\zeta, \mu)| \le d(\zeta)\mu^2$*

then R_ζ is a regularization scheme defined as in 1.2.5 and $v^{(\delta,\zeta)} = R_\zeta g^\delta$. Moreover, we have $\|R_\zeta\| \le \tau$ and the reconstruction error estimate

$$\|v^{(\delta,\zeta)} - v\|^2 \le \|v\|^2 \sup_{\mu \in (0,\|T\|)} |b(\zeta,\mu) - 1|^2 + \delta^2\tau^2, \tag{1.2.6}$$

where $\tau = d(\zeta)$ in case of (i) or $\tau = \sqrt{Cd(\zeta)}$ in case of (ii) with C denoting a bound on q. The function $b(\zeta, \mu)$ is then called a regularizing filter.

A proof can be found e.g. in [88]. The properties 1 and 2 are designed to keep $\|R_\zeta\|$ contained and take care of the convergence of 1.2.1. The quantity $\sup_{\mu \in (0,\|T\|)} |b(\zeta, \mu) - 1|^2$ in 1.2.6 can usually take an explicit form independent of $\|T\|$. As examples for the filter function we will subsequently introduce all the methods we are going to use in this thesis.

1.2.1 Truncated SVD

Singular values close to zero are the ones who are responsible for a wild enlargement of possible error-related high frequencies; the steeper the decay rate the higher the degree of ill-posedness. Knowing this alone, it would not take much of our intuition to suggest keeping only the most significant singular values and dismiss the rest. A threshold $\zeta > 0$ will be the cut-off (regularization) parameter below which no

singular value makes it to the previously infinite sum in 1.1.5. We summarize this discussion to the introduction of the reqularizing filter b of what we call the *Truncated SVD* (TSVD):

$$b(\zeta, \mu) = \begin{cases} 1, & \mu \geq \zeta \\ 0, & \text{otherwise} \end{cases} \tag{1.2.7}$$

Setting the auxiliary $\alpha = \mu/\zeta$ we obtain $|b(\alpha)| \leq \alpha \Rightarrow d(\zeta) = 1/\zeta$ and $|1 - b(\zeta, \mu)| \leq \frac{\zeta}{\mu}$ for all (ζ, μ).

As shown, SVD is of great theoretical interest but there is a discrete analog of SVD, see [140], which is of practical interest too. After all, everything finally reduces to matrices so that data can be handled by a computer for every practical purpose.

Theorem 1.11 (Discrete SVD). *For any matrix $M \in \mathbb{R}^{m \times n}$ there exist orthogonal matrices $U \in \mathbb{R}^{m \times m}$ and $V \in \mathbb{R}^{n \times n}$ and a matrix $\Sigma = \text{diag}(\sigma_1, \sigma_2, \ldots, \sigma_r) \in \mathbb{R}^{m \times n}$ where $r = \min\{m, n\}$ and $\sigma_1 \geq \sigma_2 \geq \cdots \geq \sigma_p > \sigma_{p+1} = \cdots = \sigma_r = 0$, so that M is decomposed to*

$$M = U\Sigma V^T = \sum_{i=1}^{p} \sigma_i v_i \nu_i^T, \tag{1.2.8}$$

where v_i, ν_i are the orthonormal columns of U and V and they are called left and right singular vectors of M respectively. The σ_i-s are called singular values of M and the triple (σ_i, v_i, ν_i) is called singular system of M.

It can be shown that using the Galerkin discretization method, the discrete singular triple (σ_i, u_i, v_i) can be arbitrarily close to (μ_j, f_j, h_j) (notation from Th. 1.3), see [57], and therefore we can study the ill-posedness much easier. We should mention that all the properties of the discrete SVD are identical to the ones in Th. 1.3 including the Picard condition 1.1.9 with just a change in notation $M \leftrightarrow T$ and $(\sigma_i, v_i, \nu_i) \leftrightarrow (\mu_j, f_j, h_j)$ and a little less care about the range of M; recall that from 5, in an application M is the projected version of T in a finitedimensional space.

Perturbation theory, not only based on the right hand side but also on the matrix, gives many insightful results regarding stability and the limits of TSVD. Of particular interest is that a TSVD regularized solution v_k keeping only k SVD terms of 1.2.8 (or removing the last $n - k$) is reliable to the degree that the difference $\sigma_k - \sigma_{k+1}$ is well-determined, see [54].

Since the original grasp of the discrete SVD by both E. Beltrami [13] and C. Jordan in 1873-1874, and the efficient implementation of G. Golub in 1965 [46], TSVD became a wide-spread technique. Among the numerous applications of TSVD perhaps data compression and pattern recognition are the most recognizable.

Note that for brevity, the terms "SVD" and "TSVD" might refer from now on to the discrete case too depending on the context.

1.2.2 Tikhonov regularization

TSVD is a straightforward regularization tool which aims to identify and cut the most vulnerable part of the solution. However, doing so it loses all the solution information associated with the disposed part. Furthermore, in cases where there is a lot of noise, the "ripping" nature of TSVD may result an oversmoothed solution. Therefore it might be more prudent, instead of cutting some part, to give it a shift by a parameter ζ^2 ($\zeta > 0$) to counteract its spectral weakness. This correcting procedure enabling the search of an optimal balance (ζ) of the good against the troubling solution content is attributed to A. N. Tikhonov [139]. The concept of Tikhonov regularization is described by the filter function b:

$$b(\zeta, \mu) = \frac{\mu^2}{\mu^2 + \zeta^2}. \tag{1.2.9}$$

Using the inequality $\mu^2 + \zeta^2 \geq 2\mu\zeta$ it is easily verifiable that $d(\zeta) = \frac{1}{2\zeta}$ and $|1 - b(\zeta, \mu)| \leq \frac{\zeta}{\mu}$ for all ζ, μ. For large μ_j relative to ζ the filter 1.2.9 is close to 1, giving a pass to the SVD terms in 1.1.5, while for $\mu \ll \zeta$ we have $b(\zeta, \mu) = \frac{\mu^2}{\zeta^2} + O(\frac{\mu^4}{\zeta^4})$ which neutralizes the huge terms $\langle g, h_j \rangle / \mu_j$ (with tiny μ_j) and satisfies the Picard condition 1.1.9.

We introduced Tikhonov's method from the point of view of the singular values following a possible flaw of the behavior of SVD. There are, nevertheless, a few ways of defining this method basically

through a minimization procedure. The idea of dampening the effect of small singular values just in the degree that it does not mess the solution content is again actually a matter of seeking a balance between regularity and approximation, see 1.2.4. As previously shown, inverting T^*T is problematic for an unbounded T, therefore by the same logic we can perturb it by λI, with a small $\lambda > 0$ to overcome this deficiency. It turns outs that choosing $\lambda = \zeta^2$ is equivalent to the use of the filter 1.2.9.

Theorem 1.12 (Tikhonov regularization). *Let $T : V \to G$ be a linear operator between Hilbert spaces and let $Q : \mathscr{D}_Q \to W$ be a closed linear operator with $\mathscr{D}_Q$ a dense subset of V and W be a Hilbert space. Moreover, let there be noisy data g^δ, $\|g^\delta - g\| < \delta$ with $g \in \mathscr{D}(T^\dagger)$ and $\delta > 0$. Then, the following statements are equivalent:*

1. *$v^{(\delta,\zeta)} = \inf\limits_{v \in \mathscr{D}_Q} \{\|Tv - g^\delta\|_G + \zeta^2 \|Qv\|_W\}$.*

2. *$v^{(\delta,\zeta)}$ is the regularized solution of $T^*Tv = T^*g$ with regularization scheme $R_\zeta = (T^*T + \zeta^2 Q^*Q)^{-1}T^*$. Moreover, for $Q = I_V$ the filter function is given by 1.2.9.*

The operator Q is often called the *smoothness constraint* emphasizing that the term $\|Qx\|$ quantifies the regularity, e.g. Q can be a differential operator. In case $Q = I_V$, which we will use in this work, the regularity is only the magnitude (norm) of the solution forced to stay small.

1.2.3 Iterative operators as regularizers

Showalter's method

Previously, we established the fact that in order to find a unique solution (probably unstable) for $Tv = g$ we need to turn to the minimization of $\|Tv - g\|$. Here we follow a version of the steepest descent principle in which we achieve a monotonically decreasing functional $F(v) = \|Tv - g\|^2$ by setting

$$\dot{v}(t) = -T^*Tv(t) + T^*g, \quad t > 0, \tag{1.2.10}$$

where we assume the initialization $v(0) = v_0$. This is a method first published by D. W. Showalter, see [134, 135]. In case T is a bounded linear operator and $g \in \mathscr{D}(T^\dagger)$, using basic theory on systems of ordinary differential equations, we can have an explicit (unique) solution for 1.2.10 $v(t)$ which is expected to fulfil asymptotically the normal equation 2, i.e. $\lim_{t \to \infty} v(t) = T^\dagger g$, where

$$T^\dagger = \lim_{t \to \infty} (I - e^{-tT^*T})(T^*T)^{-1}T^*. \tag{1.2.11}$$

Setting $t = 1/\zeta$ with $0 < \zeta \leq 1$, the function

$$b(\zeta,\mu) = 1 - e^{-\frac{\mu^2}{\zeta}}, \tag{1.2.12}$$

satisfies 1 trivially and 2 (ii) with $d(\zeta) = \frac{1}{\zeta}$ using the inequality $1 - e^{-x} \leq x$, for all $x > 0$. Hence, according to Th. 1.10, $b(\zeta,\mu)$ qualifies for a regularizing filter. Moreover $1 - b(\zeta,\mu) \leq 1 - \frac{\mu^2}{\zeta}$.

While it is fair to say that our intuition is built upon SVD, we should note that its calculation is costly for large scale problems. In this context, iterative methods can be advantageous as regularization methods producing a sequence of regularized solutions with increasingly better solution characteristics (according to a PCR) without altering the initial operator. However, our problem does not need to handle lots of data (in fact the opposite) and in our case iterative methods are, in fact, the most time consuming.

We are interested to solve Eq. 1.2.10 iteratively. For this, we introduce the general iterative scheme

$$v_\zeta = v_{\zeta-1} + s\mathscr{J}^{-1}(T^*g - T^*Tv_{\zeta-1}) = (I - s\mathscr{J}^{-1}T^*T)v_{\zeta-1} + s\mathscr{J}^{-1}T^*g, \quad i = 1, 2, \ldots, \tag{1.2.13}$$

with a starting value $v_0 = sT^*g$. s is the relaxation parameter and $\mathscr{J}^{-1}$ is a preconditioner used to accelerate the convergence rate, see e.g. [28].

The special case of 1.2.13 with $\mathscr{J} = I$, which actually predated Showalter's method, was defined in 1951 by L. Landweber [90] and meets convergence for $0 < s < 2/\|T\|^2$. A few iterations of 1.2.13 and the identity $\left[1 - (1-\lambda)^{n+1}\right]/\lambda = \sum_{k=0}^{n}(1-\lambda)^k$ are only needed to derive the Landweber filter

$$b(\zeta, \mu) = 1 - (1 - s\mu^2)^{\lfloor \frac{1}{\zeta} \rfloor}, \tag{1.2.14}$$

for $0 < \zeta \leq 1$. The latter is bounded with $0 \leq b(\zeta, \mu) \leq 1$ for $\mu \in (0, \|T\|]$, choosing $s < \frac{1}{\|T\|^2}$. Since $\|T\|^2 \geq \mu_1 \geq \mu > 0$, we have $-s\mu^2 > -1$, hence according to Bernoulli's inequality $(1 - s\mu^2)^{\lfloor \frac{1}{\zeta} \rfloor} \geq 1 - \lfloor \frac{1}{\zeta} \rfloor s\mu^2$, we obtain $b(\zeta, \mu) \leq s\lfloor \frac{1}{\zeta} \rfloor \mu^2$. Moreover, $\lim_{\zeta \to 0} b(\zeta, \mu) = 1$ for all $\mu \in (0, \|T\|]$ hence, according to Th. 1.10, $b(\zeta, \mu)$ is indeed a regularizing filter.

Nevertheless Landweber's iteration is proved to have a slow pace towards convergence, which is why it is a less preferable choice for an application. Padé-type methods were found suitable for expediting the convergence behavior, see [15, 81]. Following the work done in [80, 123], we are going to define them through the well-known Runge-Kutta methods, which will subsequently brake loose to a generalized scheme.

Generalized Runge-Kutta regularizers

Runge-Kutta (RK) methods are born, when solving numerically an ordinary differential equation (ODE), by allowing the polynomial collocation coefficients to unhook from quadrature rules (e.g. the trapezoidal rule) and take on arbitrary values, fulfiling nonetheless the so-called *consistency requirements* for a desired accuracy. Let the following be an initial value problem

$$\dot{v} = H(v, t), \quad t > 0 \tag{1.2.15}$$
$$v(t_0) = v_0.$$

Choosing a step size $0 < h = t_j - t_{j-1}$, $j = 1, 2, \ldots, N$. We seek an approximation $v_j = v(t_j)$, given by the formula:

$$v_j = v_{j-1} + h \sum_{n=1}^{k} z_n r_n, \tag{1.2.16}$$

where

$$r_i = H\left(t + c_i h, v + h \sum_{s=1}^{k} m_{is} r_s\right), \quad \text{for} \quad i = 1, 2, \ldots, k, \tag{1.2.17}$$

is the i−th stage of the (generally implicit) Runge-Kutta method. Considering m_{ij}, c_j, z_j as the matrix elements of $M^{k \times k}$, $\mathbf{c}^{k \times 1}$, and $\mathbf{z}^{k \times 1}$ respectively, the formalism is lightened by the mnemonic device

$$\begin{array}{c|c} \mathbf{c} & M \\ \hline & \mathbf{z^T} \end{array}$$

called the *Butcher's tableau*, developed in 1960 by J. C. Butcher [24]. There are further relations between m_{ij}, c_j, z_j by imposing the local truncation error of the approximated solution of 1.2.15 to be of certain order, which is then said to be the order of the Runge-Kutta method; they can virtually be found at any book of numerical analysis about ODEs, see e.g. [25, 26, 89].

Since, in our case $H(v) = -T^*Tv + T^*g$, see Eq. 1.2.10 we will now appeal to the class of time invariant (autonomous) linear ODEs, in which case there are well-known results about stability. Consider the autonomous ODE system, $\dot{v}(t) = \lambda v(t) + \phi$ and combine it with Eq. 1.2.16 and 1.2.17 to derive

$$\mathbf{r} = (I - h\lambda M)^{-1}(\lambda v_{i-1} + \phi)\mathbb{1}, \tag{1.2.18}$$
$$v_j = S(h\lambda)v_{j-1} + hW(h\lambda)\phi, \tag{1.2.19}$$

where $S(x) = 1 + x\mathbf{z^T}(I - xM)^{-1}\mathbb{1}$, known as the stability function, $W(x) = \left[S(x) - 1\right]/x$ and $\mathbb{1} = [1, \ldots, 1]^T \in \mathbb{R}^k$. Then it can be verified by induction that

$$v_n = S^n v_0 - (1 - S^n)\lambda^{-1}\phi, \quad n = 1, 2, \ldots \tag{1.2.20}$$

Setting $\lambda = -T^*T$ and $\phi = T^*g$, i.e. $S = S(-hT^*T)$, to Eq. 1.2.20 it can be shown, that for an injective compact linear operator T with singular system $(\mu_j, f_j, h_j)_{j \in \mathbb{N}}$ and $|S| < 1$

$$v^\dagger = \lim_{n \to \infty} v_n = \lim_{n \to \infty} \sum_{j=1}^{\infty} (1 - S^n)\mu_j^{-1}\langle g, h_j \rangle f_j(r), \qquad (1.2.21)$$

where $v^\dagger$ is the minimum-norm solution (Moore-Penrose), see [80, 123]. This is as far as we can get with the implied filter function $(1 - S^{\lfloor \frac{1}{\zeta} \rfloor}, 0 < \zeta \leq 1)$ in Eq. 1.2.21 with no more assumptions about the stability function. The requirements of Th. 1.10 can be met as follows.

Theorem 1.13 (Generalized Runge-Kutta iteration). *Let $0 < \omega < \frac{\tilde{x}}{\|T\|}$ with $\tilde{x} \in \mathbb{R}^+ \cup \{\infty\}$. If there is a function $S(x)$ fulfilling the following properties:*

(i) *$|S(x)| < 1$ for $x \in (-\tilde{x}, 0)$,*

(ii) *there is a constant $\xi > 0$ such that $S(x) \geq 1 + \xi x$, for all $x \in (-\tilde{x}, 0)$,*

then the function $b(\zeta, \mu) = 1 - S(-\omega\mu)^{\lfloor \frac{1}{\zeta} \rfloor}$ with $\mu \in (0, \|T\|]$ defining the scheme

$$R_\zeta g = \sum_{j=1}^{\infty} (1 - S^{\lfloor \frac{1}{\zeta} \rfloor})\mu_j^{-1}\langle g, h_j \rangle f_j(r), \qquad (1.2.22)$$

is a regularizing filter. If $S = p/q$, where p and q be real coprime polynomials with $p(0) = q(0) = 1$, the iterative scheme defined through $b(\zeta, \mu)$ is called generalized Runge-Kutta iteration, and ω is called the relaxation parameter.

Proof. For all $\mu \in (0, \|T\|]$ and $0 < \omega < \frac{\tilde{x}}{\|T\|}$, it holds $\omega\mu < \tilde{x}$, hence $|S(-\omega\mu)| < 1$, so that

$$\lim_{\zeta \to 0} b(\zeta, \mu) = \lim_{n \to \infty} 1 - S^n = 1. \qquad (1.2.23)$$

We have $S(-\omega\mu) \geq 1 - \xi\omega\mu \geq 1 - \xi\omega\|T\|$ and $1 - S(-\omega\mu) \leq \xi\omega\mu$. We examine the sign of S. $S(-\omega\mu) \geq 0$ holds for $\omega < \frac{1}{\xi\|T\|}$ for all $\mu \in (0, \|T\|]$ and $b(\zeta, \mu)$ is bounded with $0 < b(\zeta, \mu) < 1$. In this case, applying Bernoulli's inequality, $t^\kappa \geq 1 + \kappa(t - 1)$ for $t > 0$ and $\kappa > 1$, we obtain

$$1 - S^{\lfloor \frac{1}{\zeta} \rfloor} \leq \lfloor \frac{1}{\zeta} \rfloor (1 - S) \leq \lfloor \frac{1}{\zeta} \rfloor \xi\omega\mu.$$

Assume now there exists $\omega \in (0, \frac{\tilde{x}}{\|T\|})$ such that $S(-\omega\mu) < 0$ for all $\mu \in (0, \|T\|]$. We have

$$|1 - S^{\lfloor \frac{1}{\zeta} \rfloor}| \leq 1 + |S|^{\lfloor \frac{1}{\zeta} \rfloor} \leq 2,$$

therefore $b(\zeta, \mu)$ is bounded. If $\zeta > 1/2$, then $\lfloor \frac{1}{\zeta} \rfloor = 1$ which leads to the trivial $|1 - S^{\lfloor \frac{1}{\zeta} \rfloor}| \leq \lfloor \frac{1}{\zeta} \rfloor (1 - S)$. If $\zeta \leq 1/2$ then $\lfloor \frac{1}{\zeta} \rfloor \geq 2$ and $\lfloor \frac{1}{\zeta} \rfloor (1 - S) \geq 2$.

Therefore for all $\zeta \in (0, 1]$ and all $\mu \in (0, \|T\|]$ we have $1 - S^{\lfloor \frac{1}{\zeta} \rfloor} \leq \lfloor \frac{1}{\zeta} \rfloor (1 - S) \leq \lfloor \frac{1}{\zeta} \rfloor \xi\omega\mu = d(\zeta)\mu$, with $d(\zeta) = \xi\omega\lfloor \frac{1}{\zeta} \rfloor$. The requirements 1 and 2 of Th. 1.10 are satisfied, hence $b(\zeta, \mu)$ is a regularizing filter.

Stiff ODEs cannot be encountered by explicit RK methods, which is the main reason of the rise of the implicit RK methods, for which $S(x)$ is a rational function. This motivates the study of polynomial quotients of variable degrees, known as Padé approximants, to approximate the exponential function, which is what the stability function does by definition. In this sense the rational function $S(x)$ may disassociate from the Runge-Kutta method and instead follow the requirements of Th. 1.13 which will ensure the regularizing effect of the method.

Definition 1.2.2 (Padé approximants). Consider the power series $f(x) = \sum_{i=1}^{\infty} a_i x^i$ and the polynomials $p(x)$ and $q(x)$ with $\deg p = n$ and $\deg q = m$. The rational function $S(x) = \frac{p(x)}{q(x)}$ is called *Padé approximant* of $f(x)$ of order (m, n) if

$$f(x) - S(x) = \mathcal{O}(x^{m+n+1}). \qquad (1.2.24)$$

11

The normalization $q(0) = 1$ is a usual additional constraint to overcome the undetermined system of equations for the coefficients of p and q yielding from 1.2.24. Although the relation 1.2.24 was known back in 1776 by J. L. Lagrange it was not after the thesis of H. Padé (inventor of the *Padé table*) in 1892 [116] that they were thoroughly studied, see more historical remarks in [72]. It can be shown [80] that a Padé approximant of the exponential function can define a generalized Runge-Kutta method, which can theoretically achieve arbitrarily high convergence rates [82] depending on the degrees of the polynomials in the rational function.

Theorem 1.14 (Padé iterations)**.** *Let* $(m, n) \in \mathbb{N}^2 \setminus \{(0, 0)\}$. *The iteration scheme defined by the stability function* $S_{m,n} = p_{m,n}/q_{m,n}$ *as a Padé approximant of* $f(x) = e^x$ *is a generalized Runge-Kutta iteration. It is called the* (m, n)-*Padé iteration. Moreover, if* ω *is the relaxation parameter then we have the following convergence behavior:*

1. *If* $m \geq n$, *the* (m, n)-*Padé iteration converges for all* $\omega \in \mathbb{R}^+$.

2. *If* $m < n$, *there exists a constant* $\bar{\omega} \in \mathbb{R}^+$ *such that the* (m, n)-*Padé iteration converges for all* $\omega < \bar{\omega}$ *and diverges otherwise.*

3. *If* $m \leq n$, *there exists unique optimal relaxation parameter.*

4. *If* $m > n$, *there exists no optimal relaxation parameter, i.e. the convergence rate becomes higher with growing* ω.

1.3 Parameter choice rules

Regularization describes the way to reverse the noise effect and restore the "natural" regularity of the solution, but does not prescribe the depth of its act inherently. The use of parameter choice rules is not an optional addition but necessary in order to make a regularization method successful, or in other words, to minimize regularization errors in some sense.

We saw a glimpse of the latter through the relation 1.2.4, where a balance was sought between the filtered noise $I = \delta \|R_\zeta\|$ and the deviation of the expected value of the solution from the exact solution $J = \|R_\zeta g^\delta - R_\zeta g\|$; this summarizes the aim of a PCR. The SVD coefficients $\langle g, h_j \rangle$ (Eq. 1.1.5) keep decreasing in general (see Fig. 1.2) till they reach a point associated with the error level, at which they level off. [57] shows that using the Picard condition on the exact data (g), one can mark this transition point which leads to the desired balance between the two errors (I, J). However, this methodology is often a dead end if we aim to select the parameter a-priori, since the actual decay rates are unpredictable and highly depend on the error level.

In this section, we present the most widely used PCRs in bibliography, highlighting their assets and drawbacks. A practical exploration of all the presented PCRs will be done later on through their application to our problem in combination with a regularization method.

Before the PCR exposé we give a result of particular importance, known as the Bakushinskiǐ's veto [8], highlighting the need of supplemental information in an application, e.g. the error level.

Theorem 1.15 (Bakushinskiǐ's veto)**.** *A purely data driven regularization method, in deterministic context, is convergent if and only if the generalized inverse* $T^\dagger$ *is continuous.*

The extention of Bakushinskiǐ's veto for a statistical inverse problem, where the classic uniform convergence is out of question is disproved by [12], since the noise may be unbounded. Note that despite the validity of Th. 1.15, purely data-driven PCRs such as the L-curve and Generalized Cross Validation keep appearing very successful in the bibliography.

Hereupon a few known practical results will be shown about the most widely used PCRs. For this, the following sections assume a regularization method (R_ζ, ζ) imposed to the discretized problem (see Sec. 1.4) $Tv = g$ and a perturbed right hand side $\|g^\delta - g\| = \delta$, for $\delta > 0$, where $T^{m \times n}, v^{n \times 1}$ and $g^{m \times 1}$ are real matrices with dimensions in accordance with the given projection space, and $\| \cdot \|$ is the Euclidean norm (2-norm). Moreover, we denote with $b(\zeta, \sigma_i), i = 1, 2, \ldots, m$ the discrete filter functions for a regularizer with regularization parameter ζ and the singular values σ_j of the discrete SVD.

1.3.1 The discrepancy principle

Among all the parameter choice rules, the discrepancy principle is the most facile both conceptually and computationally. It is based on the "reasonable" demand that the data should be approximated with a same-order accuracy as the actual data (e.g. measurement-) error. The obvious dependence on distorted-data information (g^δ) classifies this technique as an a-posteriori PCR. This technique is formalized as follows.

Definition 1.3.1 (Morozov's discrepancy principle). Let $v^{(\zeta,\delta)}$ be the regularized solution of $Tv = g$ produced by the regularization method $(R_{\zeta(\delta,g^\delta)}, \zeta)$ and let $c > 1$ be a constant. The regularization parameter $\zeta^* \leq \zeta$ is determined such that

$$\|Tv^{(\zeta^*,\delta)} - g^\delta\| \leq c\delta < \|Tv^{(\zeta,\delta)} - g^\delta\|. \tag{1.3.1}$$

The constant c is often called *safety factor* and allows a somewhat safer approach preventing possible oversmoothing. This constraint means that the data are allowed to be approximated with the data error (δ) as a maximum possible accuracy.

The applicability of discrepancy principle (DP) is obviously limited when the knowledge on exact measurement errors is absent. Moreover, estimation tolerance of the error level should be low enough since the resulting solution is quite sensitive to its selection. It is demonstrated in [128] through a simulation with a severely ill-posed test problem from [57] that even a small deviation (5-10%) of the data discrepancy alters or destroys the reconstructed result. We should note though that in the off-chance that we do know the error level, this method demonstrates a very good solution behavior as we will witness later through its application in our problem.

1.3.2 The L-curve method

Despite the unique ease of the discrepancy principle, the insufficient knowledge on the error level often strikes it out as an option. This is the basic motivation behind the development of PCRs solely based on the available data. The idea of the L-curve method lies within the plot of the regularity term against the residual error, first suggested by [91].

This way of displaying data appears to be quite informative regarding the regularization parameter (ζ), i.e. the level of smoothness imposed to the solution, especially when the plot is shown in double-logarithmic scale. Ideally, when plotting the residual error on x-axis and the regularity term (see Th. 1.12) on y-axis, an L-shaped curve is formed, see Fig. 1.3 where two separate territories are distinguished. Moving along the vertical part of the "L" from top to bottom, i.e. following a diminishing regularity term, the regularization parameter becomes larger producing increasingly smoother solutions. On the other hand moving along the horizontal part of the "L" from right to left, the residual error is contained, which means that the regularity "loses" over the fit, hence the regularization parameter decreases. This leads us to consider finding the optimal parameter ζ^* at the corner of the L-curve. An appropriate magnitude for locating the corner is the curvature function which needs to be maximized. This procedure is summarized as follows.

Definition 1.3.2 (L-curve criterion). Let $(\tilde{J}, \tilde{I}) = \left(\log\|Tv^{(\zeta,\delta)} - g^\delta\|, \log\|Qv^{(\zeta,\delta)}\|\right)$ be the points constituting the L-curve. The regularization parameter is determined by maximizing its curvature function $\omega(\zeta)$

$$\omega(\zeta) = \frac{\tilde{J}'\tilde{I}'' - \tilde{J}''\tilde{I}'}{[(\tilde{J}')^2 + (\tilde{I}')^2]^{3/2}}.$$

For our purposes, we will use the L-curve criterion, combined either with the Tikhonov method with $Q = I_m$ or with the Padé iteration. P. C. Hansen [56] showed that for the Tikhonov method with $Q = I_m$, and an error-free right hand side, the function $I(\tilde{J})$ is indeed decreasing and concave.

L-curve method ends elegantly the bargain between the competing error terms but there are some liabilities to oversee. First, ignoring for a moment Th. 1.15, this methodology's supporting arguments are based entirely on heuristics. Second, the resulting graph for a noisy right hand side (g^δ) is not always either "L-shaped" (missing the vertical or horizontal part, or having "local" corners, or being arbitrary shaped), or a curve in cases where the regularization parameter is discrete (e.g. the cut-off level of TSVD), so that the inversion is incurred by interpolation. All the latter scenarios might result
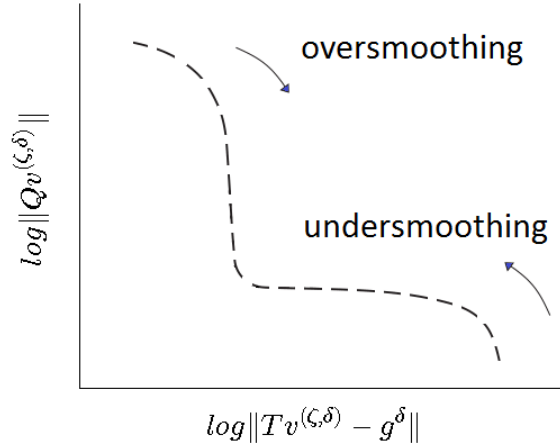
Figure 1.3: Illustration of the L-curve method. Moving along the direction pointed by the arrows leads to an overestimation or underestimation of the regularization parameter. The optimal value is expected to be found at the corner of the L-curve.

in occasional failure of the method. We note that in this work, for the combination Padé iteration - L-curve, with the number of iterations being the regularization parameter, we "fill in" the gaps of the discrete L-curve with cubic spline interpolation.

L-curve method was mainly popularized by P. C. Hansen [55], but since then there are other variations of the method, for instance [92] finds the corner point through a minimization of the product of the abcissas and ordinates of the L-curve while [122] uses 1.3.2 in an L-shaped curve formed (proved for the error-free case) by the points $(\zeta^2, \|v^{\zeta,\delta}\|^2)$.

1.3.3 Generalized cross validation

Cross validation [137] is a well-known learning algorithm from the research area of statistics, which offers another way out to the purely-data-driven regularization enterprize. A missing point from the previous PCRs is that it is not taken into account how good a prediction would be with data that the procedure hasn't been "trained" to deal with. The first step of this approach includes splitting the data in sets of "trainer" and "trainee". Then the model equation (see Def. 1.1.1) "learns" by being inverted for the data in the trainer set and subsequently it uses the collected knowledge $v_-^{(\zeta,\delta)}$ ("-" expresses the missing data) to reproduce the data from the trainee set with forward calculations ($R_\zeta v_-^{(\zeta,\delta)}$). Finally, the mean error from the predictions is used to evaluate the prediction.

Different ways to split the aforementioned sets introduce variations on the definition of the cross validation (CV) method. In this work we will use the "leave-one-out" partition, which removes only one point every time from the data, trains the rest and goes back to predict the missing one. This is repeated for every data point and the regularization parameter is chosen so that the mean prediction error is minimized.

We will restrict now to the combination of CV with Tikhonov method (TCV), which is the one we will use later on in our application (Ch. 4). In addition, an advancement of TCV is used, which is independent of the particular ordering of the data (in the right hand side) called *Generalized Cross Validation* (GCV), see [47, 147]. As computationally costly as it seems to perform the inversion-prediction pattern for every point, it can be shown (for the Tikhonov method) that it all comes down to the minimization of a simple function, [47, 57, 147].

Definition 1.3.3 (Generalized Cross Validation method)**.** Let the Tikhonov regularizing filter $b(\zeta, \sigma) = \frac{\sigma^2}{\sigma^2 + \zeta^2}$ and the associated regularization scheme R_ζ shown in 2 with $Q = I_m$. The regularization parameter is determined by minimizing the so-called *GCV function* $\omega(\zeta)$

$$\omega(\zeta) = \frac{\|Tv^{(\zeta,\delta)} - g^\delta\|^2}{\left(m - \sum_{i=1}^n b(\zeta, \sigma_i)\right)^2}. \tag{1.3.2}$$

14

GCV has also an expected shape-type with a horizontal and a skew part, and the regularization parameter is ideally found near the transition of the one part to the other. If not, it produces overfitted solutions in which case the point is shifted to the flat part of the GCV curve. More details on GCV theory and the latter downside can be found in [147].

The arguments in favor of this data-driven method are, as in the case of L-curve method, heuristic rather than compelling; a good prediction of the at-the-time unknown data points is an intuitive and desirable asset, but not a guarantee of the optimality of the regularization parameter.

With all our regularization tools on board, the question is now which is the most suitable combination of a regularization method with a parameter choice rule to solve our microphysical retrieval problem. The answer enables even a bigger dilemma since one has to define first by what means will a method be more suitable against another. Indeed early experiments with synthetic data revealed ample variations in the behavior of the solution. Not only that, but the "solution", as defined in 1.1.1 is different than the final regularization products we actually want to investigate, on which we expand in Ch. 3. Only to complicate things more, the final (microphysical) parameters do not have the same sensitivity in the error level, nor do the regularization methods have the capacity to filter different parameters with same efficiency. Finally there is one more catch. The regularization theory, the way it was unfolded, is not directly applicable to our problem in the sense that a more advanced algorithm has to be developed to counteract measurement uncertainties, and physical and technical limitations which lead to ambiguity in the solution space. This issue is resolved by using *hybrid algorithms* which exploit simultaneously several mathematical constraints. These algorithms will be revisited in detail in Ch. 3.

1.4 Discretization

As every other equation in real-life applications, so does the underlying integral equation of our problem need to be discretized in order to have a practical use. Although discretizing a problem can be seen as a regularization with no explicit parameter as the regularization parameter, see [37], here we regard it as a seperate step before the inversion. Projecting the problem to a finite space which we can subsequently handle computationally is the first decisive step towards its solution. Such a space must reflect properties of the real (solution) space, which we, at best, know little about. For this, it is useful to introduce a special type of base functions (B-spline functions) which will carry out this task throughout this work.

1.4.1 B-spline functions

B-spline functions probably remain the most malleable tool regarding the local control of the curve (control points), although somewhat complicated e.g. compared to its fraternal predecessor the Bézier (or Bernstein) functions. The conceptual and practical upgrade of the latter to the B-spline functions lies on the consideration of a special knot set, designed to offer this flexibility.

Definition 1.4.1 (B-spline curve). Let $\mathscr{R}$ be a set of $t+1$ non-decreasing numbers, $r_0 \leq r_1 \leq r_2 \leq \ldots \leq r_t$, called the *knot set* which is augmented to $r_{-d} = \ldots = r_{-1} = r_0 \leq r_1 \leq r_2 \leq \ldots \leq r_t \leq r_{t+1} = \ldots = r_n$, where $n = t + d + 1$ is called the *number of basis functions*. Then the $j-$th B-spline of degree d is defined by the De Boor-Cox recursion, [29]:

$$S_{j,0}(r) = \begin{cases} 1, & \text{if } r_j \leq r < r_{r+1} \\ 0, & \text{otherwise.} \end{cases} \tag{1.4.1}$$

$$S_{j,d+1}(r) = \omega_{j,d+1}(r)S_{j,d}(r) + \left(1 - \omega_{j+1,d+1}(r)\right)S_{j+1,d}(r), \ d \geq 1 \tag{1.4.2}$$

where

$$\omega_{j,d}(r) = \begin{cases} \frac{r-r_j}{r_{j+d}-r_j}, & \text{if } r_{j+d} \neq r_j \\ 0, & \text{otherwise.} \end{cases} \tag{1.4.3}$$

Moreover, the curve defined by

$$v(r) = \sum_{j=1}^{n} p_j S_{j,d}(r) \tag{1.4.4}$$

is called a *B-spline curve* and $(p_j)_{j=1}^{n}$ its *control points*.

A B-spline curve is a piecewise polynomial function which can be used to represent a function of one variable in the projected space. A natural generalization of the B-spline curve in two dimensions by products of b-spline curves is the following.

Definition 1.4.2 (B-spline surface). Consider the B-spline curve schemes

$$u(r) = \sum_{j=1}^{n} p_j S_{j,d}(r) \quad \text{with knot set} \quad (r_j)_{j=1}^{n+d+1}, \quad \text{and}$$

$$w(a) = \sum_{k=1}^{l} q_k S_{k,h}(a) \quad \text{with knot set} \quad (a_k)_{k=1}^{l+h+1}$$

The tensor product

$$v(r, a) = u \otimes w = \sum_{j=1}^{n} \sum_{k=1}^{l} p_j q_k S_{j,d}(r) S_{k,h}(a) \quad \text{with knot set} \quad (r_j)_{j=1}^{n+d+1} \times (a_k)_{k=1}^{l+h+1}, \tag{1.4.5}$$

is called a *B-spline surface*.

Note that the elements $p_j q_k$ (matrix of control points) can be allowed to take arbitrary values leading to a more general B-spline surface formula.

The apparent additional complexity of B-splines versus the usual spline functions is counterbalanced by the computational relief due to their local support (at a given point $r \in [r_j, r_{j+1})$, only d+1 numbers are non-zero) and the efficient representation of a yet unknown solution, shown later, as the crucial step of the collocation method, see 1.4.3. The identity of a spline (spline number and degree), is in the core of the present thesis since the algorithms we adopted, partly owe (the projected dimension is still under debate) their robustness in this and at the same time provide the means to analyze the variability of the solution space. Note that from now on whenever we refer to "spline points" for a B-spline curve, the knot set $\mathscr{R}$ (before the augmentation) is implied.

Let us now introduce two important special cases of projection methods, the collocation method and Galerkin method, which we will use throughout this work. There is a rich bibliographic material for these methods, see e.g. [7, 38, 87].

1.4.2 Collocation methods

As we will see in our application (microphysical retrieval problem), the measurement data g^δ (lidar inputs, see Introduction) are known in certain points, rather than continuously. Projection methods by collocation exploit this very feature most appropriately.

Definition 1.4.3 (Collocation methods). Let $G = C(W)$, where $W \subset \mathbb{R}$ compact subset and let $T : V \to G$ be an injective bounded linear operator, with V and G Hilbert spaces and $Tv = g$, with $v \in V$ and a given $g \in G$. Let the subspace sequences $V_n \subset V$, and $G_m \subset G$ satisfy $\dim V_n = n$ and $\dim G_m = m$. Choose m points $\tilde{\lambda} = \{\lambda_1, \lambda_2, \ldots, \lambda_m\} \in W$ such that G_m is unisolvent with respect to $\tilde{\lambda}$, i.e. any function from G_m that vanishes in $\tilde{\lambda}$ vanishes identically. Then the collocation method applied to the equation $Tv = g$, gives an approximation of the solution (v), $v_n \in V_n$, satisfying

$$(Tv_n)(\lambda_i) = g(\lambda_i), \quad i = 1, 2, \ldots, m. \tag{1.4.6}$$

Let us see how this definition affects the formalization of our actual model equation, i.e. the Fredholm integral model, see Eq. 1.1.2. Consider $V_n = \text{span}(\mathscr{B})$, where $\mathscr{B} = \{\psi_1, \psi_2, \ldots, \psi_n\}$ are B-spline functions. Every solution approximation can now be expressed with respect to the basis $\mathscr{B}$,

$$v_n(r) = \sum_{j=1}^{n} p_j \psi_j(r), \tag{1.4.7}$$

where $(p_j)_{j=1}^n$ are the expansion coefficients. Using the abbreviated notation $g_i = g(\lambda_i)$, and $K_{ij} = K(\lambda_i, r_j)$, the model equation 1.1.2 casts to the linear system

$$\sum_{j=1}^{n} \left(\int_a^b K_{ij} \psi_j dr \right) p_j = g_i, \quad i = 1, \ldots, m. \tag{1.4.8}$$

Choosing a quadrature rule for the calculation of the integrals in Eq. 1.4.8 concludes the transformation of the model equation to a discrete (matrix-vector) problem. Obviously, the last step enables quadrature errors which will be considered negligible for our further analysis. After solving the system 1.4.8 for the coefficients p_j (regularization), one has to go back to the expansion 1.4.7 to finally obtain v_n.

Consider now the following generalization of Eq. 1.1.2

$$Tv(r, a) = \int_a^b \int_c^d K(\lambda, r, a) v(r, a) dr da = g(\lambda), \quad \text{with} \quad (r, a) \in [a, b] \times [c, d]. \tag{1.4.9}$$

The unknown function v acquires an additional dimension (a) but the right hand side (input data) remains a function of a single variable, which is why we shall call Eq. 1.4.9 the *quasi-two-dimensional case* (quasi-2D case). Assume now an expansion of the form 1.4.5 with basis functions $\{\psi_j(r)\}_{j=1}^n$ and $\{\chi_k(a)\}_{k=1}^l$ and set $K_{ijk} = K(\lambda_i, r_j, a_k)$ for brevity. Applying formally the collocation steps to Eq. 1.4.9 for each available data point $\{g_i\}_{i=1}^m$, we have the scheme

$$\sum_{j=1}^{n} \sum_{k=1}^{l} \left(\int_a^b \int_c^d K_{ijk} \psi_j \chi_k dr da \right) p_j q_k \stackrel{?}{=} g_i, \quad i = 1, \ldots, m. \tag{1.4.10}$$

The parenthesized term is now an element of a two-dimensional matrix (3rd order tensor) with i rows, j columns and k layers, which makes the equation ambiguous. How to deal with such a scheme most efficiently is a subject of current research on multilinear analysis, with its solvability being under question in the first place. In order to overcome this difficulty we follow a concept from image processing (see [79]) where the indices (i, j) are "compressed" to one index h with the bijective index reordering $\mathscr{F} : \mathbb{N}^2 \to \mathbb{N}$

$$(j, k) \mapsto (k - 1)n + j. \tag{1.4.11}$$

Now the collocation process forms a matrix again with dimensions $m \times ln$ and v_n is assumed to have a (compatible to the matrix dimension) B-spline expansion $v_{nl} = \sum_{h=1}^{ln} z_h \phi_h$, hence the problem is reduced to the one-dimensional case 1.4.8. In contrast to the one-dimensional case, after inverting the discrete equation, the resulting approximation v_h has to be "decompressed" again to obtain a (quasi-)2D solution

$$v_{nl} = \sum_{h=1}^{nl} z_{\mathscr{F}^{-1}(h)} \phi_{\mathscr{F}^{-1}(h)}. \tag{1.4.12}$$

1.4.3 Galerkin methods

Another important discretization method, attributed to B. Galerkin [43] encounters the continuous operator problem through the so-called *weak formulation*.

Definition 1.4.4 (Galerkin method). Let $T : V \to G$ be an injective bounded linear operator, between the Hilbert spaces V and G and $Tv = g$, with $v \in V$ and a given $g \in G$. Let the subspace sequences $V_n \subset V$, and $G_m \subset G$ satisfy $\dim V_n = n$ and $\dim G_m = m$. Then the Galerkin method applied to the equation $Tv = g$, gives an approximation of the solution (v), $v_n \in V_n$, satisfying the (Galerkin) orthogonality requirement

$$\langle Tv_n - g, f \rangle = 0, \quad f \in G_n. \tag{1.4.13}$$

Consider now $V_n = \text{span}\{\psi_1, \psi_2, \ldots, \psi_n\}$, and $G_m = \text{span}\{\xi_1, \xi_2, \ldots, \xi_m\}$. Then we have the expansions $v_n(r) = \sum_{j=1}^n p_j \psi_j(r)$ and $g(\lambda) = \sum_{i=1}^m \eta_i \xi_i(\lambda)$ and Eq. 1.4.13 becomes

$$\sum_{j=1}^{n} \langle T\psi_j, \xi_i \rangle p_j = \langle g, \xi_i \rangle, \quad i = 1, 2, \ldots, m. \tag{1.4.14}$$

The resulting $m \times n$ linear system can have a more explicit form if we specify the spaces V and G. For $V = L^2[a,b]$ and $G = L^2[c,d]$ and switching to the Fredholm equation 1.1.2, the matrix elements will be $t_{ij} = \int_a^b \int_c^d K(\lambda,r)\psi_j(r)\xi_i(\lambda)\,d\lambda\,dr$ and the right hand side $c_i = \int_c^d g(\lambda)\xi_i(\lambda)d\lambda$.

A clear downside of the Galerkin method versus the collocation method is the computational load especially for our case where double integrals are involved. Moreover, several numerical experiments showed the Galerkin discretized equation is more likely to produce unstable solutions (huge condition numbers of the Galerkin matrix). One more reason that this method is unattractive in our case is that the input data have to be known continuously, which led us to use collocation throughout this work. As discussed earlier, the Galerkin method can be exploited in order to "transfer" efficiently the ill-posedness (see Th. 1.11) from the continuous to the discrete problem for the one-dimensional case (1.1.2). Regarding the ill-posedness of the generalized model 1.4.9, the quadruple integrals involved, when using Galerkin method, are prohibitive for our analysis. Instead, possible instabilities will be investigated by looking directly at the discretized problem and keeping track of the condition numbers and simple non-linear fits of the singular values.

Chapter 2

Physical apparatus

Foreword

We expose here some basic physical concepts, assumptions and results, from electromagnetism (EM) and atmospheric physics upon which this work is based. We would need several chapters to describe the high mathematical level behind these theories, but instead we will only touch it superficially, since the focus here is mainly the physical motivation. Related literature should bridge the gaps of the occasional leaps in theory. We start with describing the basic EM phenomena occuring in a general framework so that we present important measurable quantities regarding the polarization state of the light. The real goal is to highlight the scattering process by objects fulfilling single scattering criteria. This is a benchmark from which all important scattering quantities pop out, with most important for the present work being the optical cross sections linking to the kernel functions of our model equation. T-matrix theory sets the ground for the practical calculation of the kernel functions. Finally, a short complementary background from atmospheric physics is given for aerosol forcing and the optical properties measured by the laser remote sensing (lidar) technique.

2.1 Electromagnetic field description of time-harmonic fields with plane-wave solutions

Back in 1865, J. C. Maxwell demonstrated that unifying laws govern electricity, magnetism and light. Perhaps the capstone among many important discoveries of his profound work, is the existence of electromagnetic waves. The flawlessly elegant Maxwell's equations state the fundamentals of electromagnetism and cover concisely all physical optics phenomena. Although much of the inherited physical insight comes from the classical microscopic Maxwell's equations, here we need to approach the problem from a macroscopical standpoint, see e.g. [48, 66]:

$$\nabla \cdot \mathbf{D} = \rho \qquad (2.1.1)$$

$$\nabla \times \mathbf{E} = -\frac{\partial \mathbf{B}}{\partial t} \quad \text{(Faraday's law)} \qquad (2.1.2)$$

$$\nabla \cdot \mathbf{B} = 0 \qquad (2.1.3)$$

$$\nabla \times \mathbf{H} - \frac{\partial \mathbf{D}}{\partial t} = \mathbf{J}. \qquad (2.1.4)$$

All equations are expressed in SI units and every quantity is assumed to be both time- (t) and spatially ($\mathbf{r}$) dependent. $\mathbf{E}$ and $\mathbf{B}$ are the fundamental vector quantities, denoting the electric field and magnetic induction field respectively, while $\mathbf{D}$ is the electric displacement, $\mathbf{H}$ is the magnetic field, ρ is the (macroscopic) charge density and $\mathbf{J}$ is the (macroscopic) current density.

The generality of Maxwell's equations needs to be confined in order to solve for a specific physical problem. Unfolding the equations 2.1.1-2.1.4 to scalar equations, we have 8 equations (the $\times$-product equations hide 3 scalar equations each) with 12 unknowns (one for every spatial dimension). The unique

determination of the electromagnetic (EM) fields requires the so-called *constitutive relations* to further connect $\mathbf{J}, \mathbf{D}$ with $\mathbf{E}$ and $\mathbf{B}$ with $\mathbf{H}$:

$$\mathbf{D} = \epsilon\mathbf{E}, \quad \mathbf{J} = \sigma\mathbf{E} \quad \text{(Ohm's law)}, \quad \text{and} \quad \mathbf{B} = \mu\mathbf{H}, \tag{2.1.5}$$

where ϵ is the electric permittivity and μ is the magnetic permeability, both of which are tensors of order 2 and reduce to scalars in the case of linear isotropic media, and σ is the conductivity. Maxwell's equations in integral form involve closed surfaces and paths that might encompass a boundary separating two different media; their validity strongly depends on a continuous variation of their properties locally. The link between the two sides of the boundary lies within the boundary conditions. Drawing either a Gaussian pillbox or an Amperian loop to exceed slightly the surface boundary in both sides and shrinking their dimensions, the integral analogs of Eq. 2.1.1-2.1.4 lead to:

$$\hat{\mathbf{n}} \cdot (\mathbf{B_2} - \mathbf{B_1}) = 0, \quad \text{or} \quad \mathbf{B_2^{\perp}} - \mathbf{B_1^{\perp}} = \mathbf{0} \tag{2.1.6}$$

$$\hat{\mathbf{n}} \times (\mathbf{E_2} - \mathbf{E_1}) = 0, \quad \text{or} \quad \mathbf{E_2^{\|}} - \mathbf{E_1^{\|}} = 0 \tag{2.1.7}$$

$$\hat{\mathbf{n}} \cdot (\mathbf{D_2} - \mathbf{D_1}) = \kappa, \quad \text{or} \quad \mathbf{D_2^{\perp}} - \mathbf{D_1^{\perp}} = \kappa, \tag{2.1.8}$$

$$\hat{\mathbf{n}} \times (\mathbf{H_2} - \mathbf{H_1}) = \mathbf{K}, \quad \text{or} \quad \mathbf{H_2^{\|}} - \mathbf{H_1^{\|}} = \mathbf{K} \times \hat{\mathbf{n}} \tag{2.1.9}$$

where $\hat{\mathbf{n}}$ is the unit vector to the surface, directed from medium 1 into medium 2, κ is the surface charge density and $\mathbf{K}$ is the surface current density. These equations express either continuity of the normal/tangential EM components (2.1.6, 2.1.7) or a discontinuity jump (2.1.7, 2.1.9). Finally, in the case of finite conductivity (not perfect conductors), $\mathbf{H}$ has a continuous tangential component while entering medium 2, similar to Eq. 2.1.7.

Combining Maxwell's equations, one can easily derive the well-known EM wave equation, describing the wave propagation in a homogeneous isotropic sourceless medium

$$\nabla^2 T - \mu\epsilon\frac{\partial T}{\partial t} = 0, \tag{2.1.10}$$

where $T = \mathbf{E}, \mathbf{H}$, ϵ is electric permittivity and μ the magnetic permeability of the medium. Eq. 2.1.10 accepts as a general solution the linear superposition of waves of the form $f(\mathbf{k} \cdot \mathbf{r} - \omega t)$, where $\mathbf{r}$ is the position (radius) vector, $\mathbf{k}$ is the wave vector, and ω is the angular frequency. Perhaps the most common solutions are monochromatic plane waves, whose wavefronts are infinite parallel planes, $\mathbf{k} \cdot \mathbf{r} - \omega t = const$ for any given time. Assume now time-harmonic (sinusoidal) fields of the form $\mathbf{A}(\mathbf{r}, t) = \mathbf{A_0} \exp(\mathrm{i}\mathbf{k} \cdot \mathbf{r} - \mathrm{i}\omega t)$ where $\mathbf{A_0}$ is a constant complex vector, for an homogeneous, isotropic and sourceless medium. Then Maxwell's equations become

$$\mathbf{k} \cdot \mathbf{E_0} = 0, \quad \mathbf{k} \cdot \mathbf{H_0} = 0, \tag{2.1.11}$$

$$\mathbf{k} \times \mathbf{E_0} = \omega\mu\mathbf{H_0}, \quad \mathbf{k} \times \mathbf{H_0} = -\omega\epsilon\mathbf{E_0}. \tag{2.1.12}$$

Combining these equations and assuming homogeneous plane waves, i.e. $\mathfrak{Re}(\mathbf{k}) /\!/ \mathfrak{Im}(\mathbf{k})$, $\mathbf{k} = k\hat{\mathbf{n}}$ with $k \in \mathbb{C}$, gives rise to two characteristic quantities of the medium,

$$m = \frac{ck}{\omega} = c\sqrt{\epsilon\mu}, \quad v = \frac{c}{\mathfrak{Re}(m)}, \tag{2.1.13}$$

where c is the speed of light for free space, m is called the *refractive index* (ϵ and μ are not restricted to be real-valued) and v is called the *phase velocity* of the wave.

$$\mathbf{E}(\mathbf{r}, t) = \mathbf{E_0} \exp\left(-\frac{\omega}{c}\mathfrak{Im}(m)\hat{\mathbf{n}} \cdot \mathbf{r}\right) \exp\left(\mathrm{i}\frac{\omega}{c}\mathfrak{Re}(m)\hat{\mathbf{n}} \cdot \mathbf{r} - \mathrm{i}\omega t\right). \tag{2.1.14}$$

It is evident that a non-zero imaginary part results in an exponential decrease of the amplitude of the travelling wave, serving as an indicator of the absorption level of the medium.

2.2 Polarization states

Polarization is an intrinsic property of the electric field of a plane wave. G. G. Stokes in 1852, came up with a set of 4 values (S_0, S_1, S_2, S_3), known as the Stokes parameters (or Stokes vector), to describe any

polarization state of light waves either emitted, in a single direction (polarized light) in random -not all light waves with the same- directions (unpolarized light) or a combination of the previous cases (partially polarized light) in terms of its total intensity I (see [45]). The latter is a measurable quantity for optical detectors, built almost a century later (!):

$$I\left(\tilde{\theta}, \tilde{\phi}\right) = \frac{1}{2}\left[S_0 + S_1 \cos\left(2\tilde{\theta}\right) + S_2 \cos\left(\tilde{\phi}\right)\sin\left(2\tilde{\theta}\right) + S_3 \sin\left(\tilde{\phi}\right)\sin\left(2\tilde{\theta}\right)\right],\qquad(2.2.1)$$

where $\tilde{\theta}$ and $\tilde{\phi}$ are polar and azimuth laboratory angles related to the so-called *polarizer* (**E**-component filter) and *retarder* (**E**-phase control), respectively.

Most measurements with optical detectors can not bear the fast oscillating nature of the field vector, e.g. for a wavelength $\lambda = 1064\,\text{nm}$, the period of a monochromatic light beam is $T \sim 3\,\text{fs}$, therefore instead of instantaneous values, time-averaging quantities are used,

$$\langle E_i(t)E_j(t)\rangle = \lim_{T\to\infty}\frac{1}{T}\int_0^T E_i(t)E_j(t)\,dt,\qquad(2.2.2)$$

where $\langle\cdot,\cdot\rangle$ is denotes here exceptionally the time average. Consider incident monochromatic plane waves $\mathbf{E} = \mathbf{E_0}\exp(ik\hat{\mathbf{n}}\cdot\mathbf{r} - i\omega t)$ in a non-absorbing homogeneous medium travelling in the direction of the unit vector $\hat{\mathbf{n}} = \hat{\theta}\times\hat{\phi}$, where $\hat{\theta}$ resides in the plane defined by $\hat{\mathbf{n}}$ and z-axis, and $\hat{\phi}$ is perpendicular to this plane. Then, the time-averaged Stokes parameters are defined in spherical coordinates with the help of the electric field components E_θ, E_ϕ

$$S_0 = \langle E_\theta E_\theta^* + E_\phi E_\phi^*\rangle,\qquad(2.2.3)$$
$$S_1 = \langle E_\theta E_\theta^* - E_\phi E_\phi^*\rangle,\qquad(2.2.4)$$
$$S_2 = 2\langle\mathfrak{Re}(E_\theta E_\phi^*)\rangle,\qquad(2.2.5)$$
$$S_3 = -2\langle\mathfrak{Im}(E_\theta E_\phi^*)\rangle.\qquad(2.2.6)$$

Combining Eq. 2.2.3-2.2.6 we are a few algebraic operations away from the insightful formula

$$a_\phi^2 E_\theta^2 + (-2\cos\delta a_\theta a_\phi)E_\theta E_\phi + a_\theta^2 E_\phi^2 + a_\theta^2 a_\phi^2\sin^2\delta = 0,\qquad(2.2.7)$$

where δ is the phase difference between the θ- and ϕ-components of the complex amplitude $\mathbf{E_0}$, and $a_\phi = |E_{0\phi}|$ and $a_\theta = |E_{0\theta}|$. The conic section in Eq. 2.2.7 is a tilted (at a derivable inclination angle) ellipse, which is swept by the endpoint of the electric field vector. Elliptic polarization describes the general form of polarized light, but it can degenerate to two other interesting cases, (i) the linear polarization, for $\delta = 0$ or $\delta = \pi$ and (ii) the circular polarization for $\delta = \pm\frac{\pi}{2}$.

The elliptical helix created by the endpoint of the electric vector is uniquely defined by the length of its major and minor axis, the inclination angle and the orientation (clockwise or counter-clockwise) is another explanation of the sufficiency of four parameters for a polarization state. The Stokes vector might vary depending on the basis vectors, e.g. the one induced by the linear or circular polarization and transform to any other through a similarity transformation. Finally, for partially polarized light it can be shown that Stokes parameters depend on each other in the following sense

$$S_1^2 + S_2^2 + S_3^2 \leq S_0^2,\qquad(2.2.8)$$

where equality holds for the polarized light. Considering relative intensities (or a total intensity of $S_0 = 1$), a solid sphere of unit radius can be drawn, called *Poincaré sphere* (see Eq. 2.2.8), which includes all possible polarization states (S_1, S_2, S_3), see [155]. Fig. 2.1 illustrates several special cases in the surface of Poincaré sphere, using the phase difference δ and the angle $\psi = \arctan\left(\frac{E_{0\phi}}{E_{0\theta}}\right)$, with $0 < \psi < \frac{\pi}{2}$. Each point stands for a different polarization state. E.g. the two poles $(0, 0, 1)$ and $(0, 0, -1)$ correspond to a left-handed circular (LHC) or right-handed circular- (RHC) polarization respectively, while $(1, 0, 0)$ and $(-1, 0, 0)$ correspond to a horizontal or a vertical linear polarization respectively. Non-equatorial points designate elliptical polarization.

The averaged Stokes parameters deal successfully with quasi-monochromatic light where the amplitude of the electric field vector and the phase difference are allowed to change relatively slow with respect to the detection time. Moreover, if the phases of a number of plane waves develop temporally in a completely random fashion (incoherence), the "interference" intensities have a zero (time-) average and we
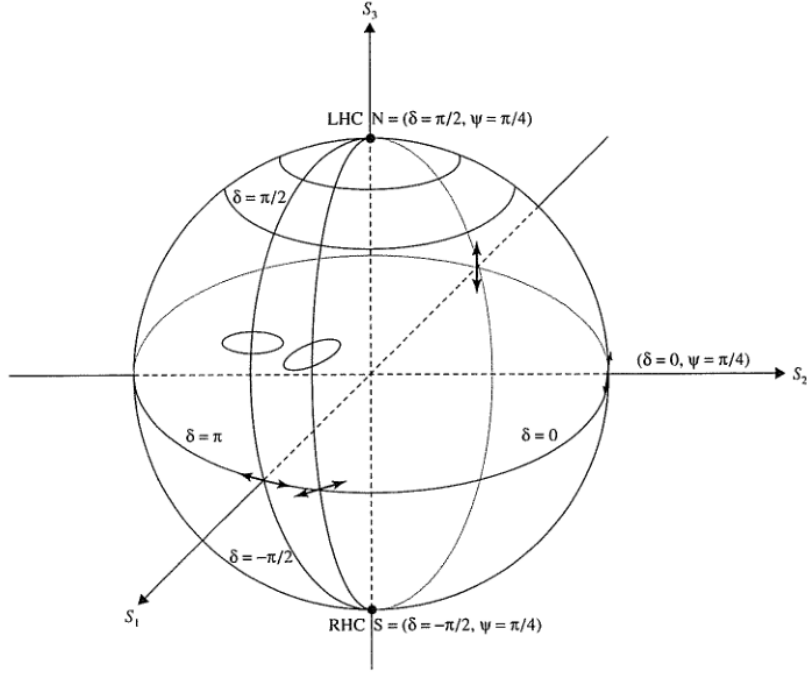
Figure 2.1: Illustration of Poincaré sphere. Figure credit: [155].

can just add up the total intensities of every single wave, and this extends to the rest components of the Stokes vector. We take a step farther to realize that this convenience is also a weakness as it turns out that no (usual) optical device can make out different light beams having the same Stokes parameters.

Stokes parameters own spectral radiance units, which is essentially energy flow passing over a differential area element confined to a differential solid angle and normalized by the wavelength of the monochromatic plane wave. Energy transfer is an equally important aspect of electrodynamics. Intuitively, in the absence of electric current, the rate of loss of the energy stored within the EM wave in a volume must be attributed of EM energy flowing out through the surface of that volume. Accounting for a continuous distribution of charge and current, the total work done per unit volume by an electromagnetic field is $\mathbf{J} \cdot \mathbf{E}$. A suitable manipulation of Maxwell's equations along with some vector calculus operations yield

$$\frac{\partial U}{\partial t} + \nabla \cdot \mathbf{S} = -\mathbf{J} \cdot \mathbf{E}, \tag{2.2.9}$$

In the first term in the left hand side, $U = \frac{1}{2}(\mathbf{E} \cdot \mathbf{D}^* + \mathbf{B} \cdot \mathbf{H}^*)$ is the total energy density of the field and $\mathbf{S} = \mathbf{E} \times \mathbf{H}^*$ is the term, known as the Poynting vector, which balances the energy conservation shown in the expression 2.2.9, representing the energy flux. For a plane wave propagating in a homogeneous medium the time-averaged Poynting vector is

$$\langle \mathbf{S}(\mathbf{r}) \rangle = \frac{1}{2} \, \mathfrak{Re}(\mathbf{E} \times \mathbf{H}^*) = \frac{1}{2} \, \mathfrak{Re} \left(\sqrt{\frac{\epsilon}{\mu}} \right) |\mathbf{E_0}|^2 \mathrm{e}^{-\alpha \hat{\mathbf{n}} \cdot \mathbf{r}} \hat{\mathbf{n}} \tag{2.2.10}$$

where $\alpha = \frac{2\omega \, \mathfrak{Im}(m)}{c}$ is called the *absorption coefficient*. Eq. 2.2.10 demonstrates the energy outflow along the direction of propagation.

2.3 Interaction of a finite particle with light

Light starts really getting interesting via its interaction with matter. Our rich visual perception is based on the huge variability of possible outcomes due to three basic processes taking place, i.e. emission, absorption and scattering of light. The nature of the obstacle (size, geometry, chemistry) standing in its way has a key role. Scattering, being the redistribution of incoming light, can be thought as a process of
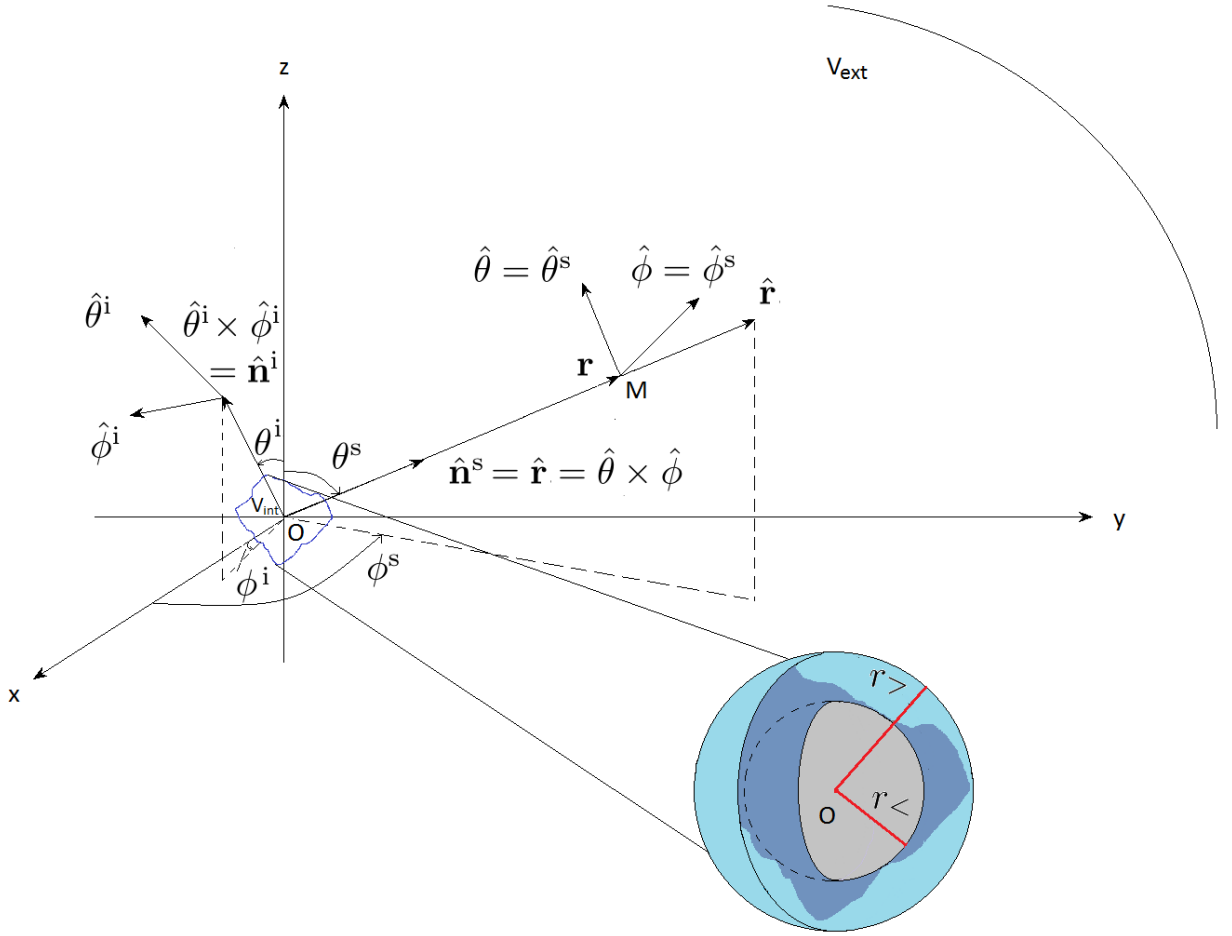
Figure 2.2: Auxiliary diagram for the incident and scattering fields where the origin (O) of the coordinate system coincides with the geometrical center of the scatterer. "M" is the scattering observation point. The bottom right part of the graph depicts a magnification of the scatterer placed in (O), to which we drew an external sphere of smallest radius $r_>$ and an internal sphere of largest radius $r_<$ for the analysis of the T-matrix method in Sec. 2.5.

absorption and re-emission of radiative energy with or without negligible energy conversion, all of which happening due to the collision of photons with the atoms of the material. Therefore, observing the scattered light could ideally (neglecting further interactions, e.g. multiple scattering) serve as particle identification which is directly in the heart of remote sensing. In the following section we are going to briefly show some results from scattering theory with the ulterior motive the relation between the scattered and the incident field (T-matrix). In the meantime we will show how to calculate two important scattering quantities regarding atmospheric attenuation and scattering in the backward direction, which will allow us, later on, introduce the lidar equation as the link between the lidar systems and these observable quantities. The marvelous contemporary work of [98] on scattering by small particles, is strongly followed here.

2.4 Scattering

We would like to initially examine scattering in a general framework. Consider a single small finite scattering object (still bulky enough so that Maxwell's equations 2.1.1 apply) or a fixed aggregate with an isotropic, linear and (generally) inhomogeneous material enclosed by the volume V_{int}, while the rest of the space denoted by V_{ext} (everything but V_{int}) in an infinite, homogeneous, isotropic medium and let the subscripts 1 and 2 designate the regions associated with V_{ext} and V_{int} respectively. Both the medium

and the object are considered non-magnetic $\mu_2(\mathbf{r}) = \mu_1 = \mu_0$, where μ_0 is the free-space permeability. Moreover, spherical coordinates are used (r, θ, ϕ), with $\theta \in [0, \pi]$ being the polar angle and $\phi \in [0, 2\pi)$ the azimuthal angle and the field components are expressed in terms of the unit vector basis $\hat{\mathbf{n}}, \hat{\theta}, \hat{\phi}$, where $\hat{\mathbf{n}}$ points to the direction of propagation of the incident or the scattering wave, $\hat{\theta}$ lies in the plane defined by $\hat{\mathbf{n}}$ and z-axis and $\hat{\phi}$ is perpendicular to this plane, see Fig. 2.2. Maxwell's equations, for the total field $\mathbf{E}$ in the whole region $r \in V_{ext} \cup V_{int}$ can take the condense form

$$\nabla \times \nabla \times \mathbf{E}(\mathbf{r}) - k_1^2 \mathbf{E}(\mathbf{r}) = \mathbf{j}(\mathbf{r}), \qquad r \in V, \tag{2.4.1}$$

with the inhomogeneous term $\mathbf{j}(\mathbf{r})$ defined by,

$$\mathbf{j}(\mathbf{r}) = \begin{cases} 0, & \mathbf{r} \in V_{\text{ext}} \\ (k_2^2(\mathbf{r}) - k_1^2)\mathbf{E}(\mathbf{r}), & \mathbf{r} \in V_{\text{int}}, \end{cases} \tag{2.4.2}$$

where k_1 and $k_2(\mathbf{r})$ are the wave numbers of the exterior and interior regions respectively. This formalism is actually convenient when searching for a solution despite the self-referential part of Eq. 2.4.1 (second branch of $\mathbf{j}(\mathbf{r})$). Indeed, the solution of 2.4.1 is split into a general solution of the associated homogeneous problem which refers to the incident (superscript "i") field $\mathbf{E}^{\text{i}}$ (in the absence of the scatterer) and a particular solution of 2.4.1 which can be attributed to the scattered (superscript "s") field $\mathbf{E}^{\text{s}}$. It should further vanish in large distances far from the scatterer for it to be a physically consistent.

In general, in order to solve for $\mathbf{E}^{\text{s}}$ one has to employ tensor calculus (dyadics) along with the free space dyadic Green's function to end up with the scalar inhomogeneous Helmholtz equation, see e.g. [66, 125], leading finally to an expression depending on the internal field of the scatterer (unknown). Here we are interested in solutions in the so-called *far-field zone*, i.e. $k_1 r \gg 1$ and $r \gg r'$ for any $\mathbf{r}' \in V^{\text{i}}$, which allows us to consider outgoing transverse (zero radial component $\hat{\mathbf{r}}$) spherical waves asymptotically as solutions for the $\mathbf{E}^{\text{s}}$,

$$\mathbf{E}^{\text{s}}(\mathbf{r}) = \frac{e^{ik_1 r}}{r} \mathscr{E}(\hat{\mathbf{r}}), \quad \hat{\mathbf{r}} \cdot \mathscr{E}(\hat{\mathbf{r}}) = \mathbf{0}, \tag{2.4.3}$$

where $\mathscr{E}(\hat{\mathbf{r}})$ is the amplitude of the spherical wave. Assume additionally an incident plane electromagnetic wave $\mathbf{E}^{\text{i}}(\mathbf{r}) = \mathbf{E}_0^{\text{i}} e^{ik_1 \hat{\mathbf{n}}^{\text{i}} \cdot \mathbf{r}}$, with $\mathbf{E}_0^{\text{i}} = E_{0\theta}^i \hat{\theta}^{\text{i}} + E_{0\phi}^i \hat{\phi}^{\text{i}}$ and let the origin of the radius vectors O coincide with the geometrical center of the scatterer, see Fig. 2.2. Then it can be shown that incident and scattering field components depend on each other linearly. This can be expressed by a 2x2 matrix, called the *amplitude scattering matrix* $\mathbf{S}$:

$$\begin{bmatrix} \mathbf{E}_{\theta(\text{L})}^{\text{s}}(r\hat{\mathbf{n}}^{\text{s}}) \\ \mathbf{E}_{\phi(\text{L})}^{\text{s}}(r\hat{\mathbf{n}}^{\text{s}}) \end{bmatrix} = \frac{e^{ik_1 r}}{r} \mathbf{S}^{(\text{L})}(\hat{\mathbf{n}}^{\text{s}}, \hat{\mathbf{n}}^{\text{i}}; e) \begin{bmatrix} \mathbf{E}_{0\theta(\text{L})}^{\text{i}} \\ \mathbf{E}_{0\phi(\text{L})}^{\text{i}} \end{bmatrix}, \tag{2.4.4}$$

where $\mathbf{E}_\theta^{\text{i}}, \mathbf{E}_{0\phi}^{\text{i}}$ and $\mathbf{E}_\theta^{\text{s}}, \mathbf{E}_{0\phi}^{\text{s}}$ are the θ- and ϕ-components of the incident and scattered field respectively and $e = (\alpha, \beta, \gamma)$ is the Euler rotation-angle triple of the particle reference frame (P) with respect to the common laboratory reference frame (L) in case they are not aligned. It is a common trick in electromagnetism to work on (P) in order to exploit possible particle symmetries and avoid further mathematical acrobatics.

The amplitude scattering matrix is a good theoretical tool carrying efficiently all the scattering information in the far-field zone we need, but in practice, even if we know the scatterer's internal and external structure, we will still stumble upon the experimental complete determination (both phase and amplitude) of the incident and scattered electric fields. On the other hand, energy-flux-related quantities are easily measurable and this is where the Stokes parameters come in handy. The relation between the Stokes vector $\mathbf{B}$ and scattering amplitude matrix is

$$\mathbf{B}^{\text{s}}(r\hat{\mathbf{n}}^{\text{s}}) = \frac{1}{r^2} \mathbf{Z} \mathbf{B}^{\text{i}}, \quad \text{with} \quad \mathbf{Z} = \mathbf{D}(\mathbf{S} \otimes_{\mathbb{R}} \mathbf{S}^*) \mathbf{D}^{-1}, \tag{2.4.5}$$

where $\mathbf{S} = \mathbf{S}(\hat{\mathbf{n}}^{\text{s}}, \hat{\mathbf{n}}^{\text{i}})$ and the standard basis of $\mathbb{R}^2 \otimes \mathbb{R}^2$ is implied and $\mathbf{Z} = \mathbf{Z}(\hat{\mathbf{n}}^{\text{s}}, \hat{\mathbf{n}}^{\text{i}})$ is called the *Stokes phase matrix* while the matrix $\mathbf{D}$ is defined by

$$\mathbf{D} = \begin{pmatrix} 1 & 0 & 0 & 1 \\ 1 & 0 & 0 & -1 \\ 0 & -1 & -1 & 0 \\ 0 & -i & i & 0 \end{pmatrix}. \tag{2.4.6}$$

The phase matrix for a single scatterer with fixed orientation is generally a full matrix (16 non-zero elements) comprised by only 7 independent values, as an expanded version of the quadratic formula 2.4.5 would reveal. Later on we will see a reduced form of this matrix in the special but practically interesting case of randomly oriented particles. Optical characteristics such as the scattering cross sections can be expressed through the scattering phase matrix as well. We are going to postpone their appearance until the presentation of the T-matrix method, which is the way these quantities are calculated in our application.

2.5 Extended boundary condition method

In the pursuit of a good understanding of scattering phenomena one has to employ theoretical as much as experimental techniques to quantify scattering and absorption. The cost of measurement equipment and the lack of direct microphysical characterization makes exact methods still quite favorable in spite of the questionable range of applicability that they might actually have for a real application. Attempts for analytical solutions of the wave equation 2.4.1 under the "separation of variables" prescription , see [101], can handle a few cases e.g. spherical scatterers [97], infinite elliptical cylinders [78], but may become an onerous computational burden for more complex shapes. In this section we will introduce the extended boundary condition method, firstly developed by P. C. Waterman [152], and flourished particularly in our days owing to its efficiency and systematic use in non-spherical-scatterer endeavors.

Once again, consider an incident plane wave scattered by an arbitrary-shaped object, and draw two fictitious concentric spheres, one of smallest radius $r_>$ circumscribing the scatterer and another of largest radius $r_<$ inscribed in the scatterer, whose geometrical center coincides with the origin of the laboratory coordinate system. See Fig. 2.2 for a depiction of such a scenery. The incident and scattered field can be expanded in spherical wave functions $\mathrm{Rg}\mathbf{M}, \mathbf{M}, \mathrm{Rg}\mathbf{N}$ and $\mathbf{N}$, see App. A Eq. A.0.1-A.0.4

$$\mathbf{E}^i(\mathbf{r}) = \sum_{n=1}^{\infty} \sum_{m=-n}^{n} [a_{mn}\mathrm{Rg}\mathbf{M}_{mn}(k_1\mathbf{r}) + b_{mn}\mathrm{Rg}\mathbf{N}_{mn}(k_1\mathbf{r})] \tag{2.5.1}$$

$$\mathbf{E}^s(\mathbf{r}) = \sum_{n=1}^{\infty} \sum_{m=-n}^{n} [p_{mn}\mathbf{M}_{mn}(k_1\mathbf{r}) + q_{mn}\mathbf{N}_{mn}(k_1\mathbf{r})], \quad r > r_> \tag{2.5.2}$$

where the expansion coefficients a_{mn} and b_{mn} are explicitly related to $\mathbf{E_0^i}$ and to basis functions (Legendre polynomials or Wigner d-functions), see App. A, Eq. A.0.8-A.0.12. The linearity of Maxwell's equation allows a matrix-vector representation between the expansion coefficients of the incident and the scattered field through the transition matrix, or T-matrix, $\mathbf{T}$. This is succinctly expressed by

$$\begin{bmatrix} \mathbf{p} \\ \mathbf{q} \end{bmatrix} = \mathbf{T} \begin{bmatrix} \mathbf{a} \\ \mathbf{b} \end{bmatrix}. \tag{2.5.3}$$

In case the particle orientation differs from the laboratory reference frame, the transformation into (L) is quite straightforward by employing the Euler angles (α, β, γ)

$$T_{mnm'n'}^{kl\,(L)}(\alpha, \beta, \gamma) = \sum_{m_1=-n}^{n} \sum_{m_2=-n'}^{n'} D_{mm_1}^{n}(\alpha, \beta, \gamma) T_{m_1nm_2n'}^{kl\,(P)} D_{m_2m'}^{n'}(-\gamma, -\beta, -\alpha), \quad k, l = 1, 2 \tag{2.5.4}$$

with $D_{bc}^s(\alpha, \beta, \gamma) = \mathrm{e}^{-iba}d_{bc}^s(\beta)\mathrm{e}^{-ib\gamma}$, where d_{bc}^s are the Wigner d-functions, see App. A Eq. A.0.4.

This is the T-matrix method in a nutshell, but as neat as its formalization might seem, there is an infinite system of equations to solve, whose matrix ($\mathbf{T}$) coefficients are still unknown and, of course, depend on physical (e.g. size, refractive index) and chemical characteristics of the scatterer (e.g. internal fields).

A way out for the calculation of T-matrix is given by the extended boundary condition (EBC) method or Null-field method, see [152], which is summarized as follows. Assuming an homogeneous, isotropic, sourceless and non-absorbing medium ($\mu = \mu_0$) and using Green's identity we obtain

$$\mathbf{E}^s(\mathbf{r}') = \int_S \mathrm{d}S \left\{ i\omega\mu_0 [\hat{\mathbf{n}} \times \mathbf{H}_+(\mathbf{r})] \cdot \overset{\leftrightarrow}{G}(\mathbf{r}, \mathbf{r}') + [\hat{\mathbf{n}} \times \mathbf{E}_+(\mathbf{r})] \cdot \left[\nabla \times \overset{\leftrightarrow}{G}(\mathbf{r}, \mathbf{r}') \right] \right\}, \quad \mathbf{r}' \in \mathbf{V}_{\mathrm{ext}}, \tag{2.5.5}$$

where $\overset{\leftrightarrow}{G}(\mathbf{r}, \mathbf{r}')$ is the dyadic Green's function for free space, and the "-" and "+" subscripts will stand for the fields in the interior domain and exterior domain respectively. The key-assumption is that this formula holds true for the interior region V_{int} too, where the total field is manufactured to be zero. The latter is achieved using the surface equivalence theorem (see [132], Huygens's principle), by replacing the scatterer with appropriate electric and magnetic current densities in its surface, which fulfil the boundary conditions and result in the radiation produced by the actual sources. Since $\mathbf{E} = \mathbf{E}^{\text{i}} + \mathbf{E}^{\text{s}}$, the EBC is to force the assignment $\mathbf{E}^{\text{i}}(\mathbf{r}') = -\mathbf{E}^{\text{s}}(\mathbf{r}')$ for $\mathbf{r}' \in \mathbf{V}_{\text{int}}$. The plan is now, knowing the incident field, to calculate the $\mathbf{E}_+$ and $\mathbf{H}_+$ using the EBC condition, and use them to find the scattered field.

Denoting the surface current densities $\mathbf{K}^{E\pm}(\mathbf{r}) = \hat{\mathbf{n}} \times \mathbf{E}_{\pm}(\mathbf{r})$ and $\mathbf{K}^{H\pm}(\mathbf{r}) = \hat{\mathbf{n}} \times \mathbf{H}_{\pm}(\mathbf{r})$, we obtain $\mathbf{K}^{E-} = \mathbf{K}^{E+}$ and $\mathbf{K}^{H-} = \mathbf{K}^{H+}$, due to the boundary conditions, for every surface point ($r \in S$). Expressing the free space dyadic Green's function in terms of vector spherical wave functions, see App. A, Eq. A.0.13, the expansion coefficients of $\mathbf{E}^{\text{i}}(\mathbf{r}')$ for $r' < r_<$ and $\mathbf{E}^{\text{s}}(\mathbf{r}')$ for $r' > r_>$, see Eq. 2.5.1, 2.5.2, are

$$a_{mn} = k_1(-1)^m \int_S \mathrm{d}S \left\{ \omega\mu_0 \mathbf{K}^{H+}(\mathbf{r}) \cdot \mathbf{M}_{-mn}(k_1 r, \theta, \phi) - ik_1 \mathbf{K}^{E+}(\mathbf{r}) \cdot \mathbf{N}_{-mn}(k_1 r, \theta, \phi) \right\}, \tag{2.5.6}$$

$$b_{mn} = k_1(-1)^m \int_S \mathrm{d}S \left\{ \omega\mu_0 \mathbf{K}^{H+}(\mathbf{r}) \cdot \mathbf{N}_{-mn}(k_1 r, \theta, \phi) - ik_1 \mathbf{K}^{E+}(\mathbf{r}) \cdot \mathbf{M}_{-mn}(k_1 r, \theta, \phi) \right\}, \tag{2.5.7}$$

$$p_{mn} = k_1(-1)^m \int_S \mathrm{d}S \left\{ \omega\mu_0 \mathbf{K}^{H+}(\mathbf{r}) \cdot \mathrm{Rg}\mathbf{M}_{-mn}(k_1 r, \theta, \phi) - ik_1 \mathbf{K}^{E+}(\mathbf{r}) \cdot \mathrm{Rg}\mathbf{N}_{-mn}(k_1 r, \theta, \phi) \right\}, \tag{2.5.8}$$

$$q_{mn} = k_1(-1)^m \int_S \mathrm{d}S \left\{ \omega\mu_0 \mathbf{K}^{H+}(\mathbf{r}) \cdot \mathrm{Rg}\mathbf{N}_{-mn}(k_1 r, \theta, \phi) - ik_1 \mathbf{K}^{E+}(\mathbf{r}) \cdot \mathrm{Rg}\mathbf{M}_{-mn}(k_1 r, \theta, \phi) \right\}, \tag{2.5.9}$$

The interior fields are further assumed to be able to be expanded in the regular spherical wave functions $\mathrm{Rg}\mathbf{M}$ and $\mathrm{Rg}\mathbf{N}$

$$\mathbf{E}(\mathbf{r}) = \sum_{n'=1}^{\infty} \sum_{m'=-n'}^{n'} \left[c_{m'n'} \mathrm{Rg}\mathbf{M}_{m'n'}(k_2\mathbf{r}) + d_{m'n'} \mathrm{Rg}\mathbf{N}_{m'n'}(k_2\mathbf{r}) \right], \quad r \in V_{\text{int}} \tag{2.5.10}$$

The combination of the EBC condition (see also 2.5.5), Eq. 2.5.6-2.5.9, the boundary condition requirements, Eq. 2.5.10, and (the simplification of) 2.1.4, results in the T-matrix-alike linear relations,

$$\begin{bmatrix} \mathbf{a} \\ \mathbf{b} \end{bmatrix} = \mathbf{Q} \begin{bmatrix} \mathbf{c} \\ \mathbf{d} \end{bmatrix}, \quad \begin{bmatrix} \mathbf{p} \\ \mathbf{q} \end{bmatrix} = -\mathbf{RgQ} \begin{bmatrix} \mathbf{c} \\ \mathbf{d} \end{bmatrix}, \tag{2.5.11}$$

Eq. 2.5.11 and 2.5.3 combined lead to the simple relation $\mathbf{T} = -(\mathrm{Rg}\mathbf{Q})\mathbf{Q}^{-1}$, referring to the particle reference frame (see also Eq. 2.5.4). The matrix elements of $\mathbf{Q}$ and $\mathrm{Rg}\mathbf{Q}$ are given by

$$Q^{11}_{mnm'n'} = -ik_1k_2 J^{21}_{mnm'n'} - ik_1^2 J^{12}_{mnm'n'}, \tag{2.5.12}$$

$$Q^{12}_{mnm'n'} = -ik_1k_2 J^{11}_{mnm'n'} - ik_1^2 J^{22}_{mnm'n'}, \tag{2.5.13}$$

$$Q^{21}_{mnm'n'} = -ik_1k_2 J^{22}_{mnm'n'} - ik_1^2 J^{11}_{mnm'n'}, \tag{2.5.14}$$

$$Q^{22}_{mnm'n'} = -ik_1k_2 J^{12}_{mnm'n'} - ik_1^2 J^{21}_{mnm'n'}, \tag{2.5.15}$$

where

$$\begin{bmatrix} J^{11}_{mnm'n'} \\ J^{12}_{mnm'n'} \\ J^{21}_{mnm'n'} \\ J^{22}_{mnm'n'} \end{bmatrix} (-1)^m \int_S \mathrm{d}S\hat{\mathbf{n}} \cdot \begin{bmatrix} \mathrm{Rg}\mathbf{M}_{m'n'}(k_2 r, \theta, \phi) \times \mathbf{M}_{-m'n'}(k_1 r, \theta, \phi) \\ \mathrm{Rg}\mathbf{M}_{m'n'}(k_2 r, \theta, \phi) \times \mathbf{N}_{-m'n'}(k_1 r, \theta, \phi), \\ \mathrm{Rg}\mathbf{N}_{m'n'}(k_2 r, \theta, \phi) \times \mathbf{M}_{-m'n'}(k_1 r, \theta, \phi), \\ \mathrm{Rg}\mathbf{N}_{m'n'}(k_2 r, \theta, \phi) \times \mathbf{N}_{-m'n'}(k_1 r, \theta, \phi), \end{bmatrix} \tag{2.5.16}$$

and

$$\mathrm{Rg}Q^{11}_{mnm'n'} = -ik_1k_2\mathrm{Rg}J^{21}_{mnm'n'} - ik_1^2\mathrm{Rg}J^{12}_{mnm'n'}, \tag{2.5.17}$$

$$\mathrm{Rg}Q^{12}_{mnm'n'} = -ik_1k_2\mathrm{Rg}J^{11}_{mnm'n'} - ik_1^2\mathrm{Rg}J^{22}_{mnm'n'}, \tag{2.5.18}$$

$$\mathrm{Rg}Q^{21}_{mnm'n'} = -ik_1k_2\mathrm{Rg}J^{22}_{mnm'n'} - ik_1^2\mathrm{Rg}J^{11}_{mnm'n'}, \tag{2.5.19}$$

$$\mathrm{Rg}Q^{22}_{mnm'n'} = -ik_1k_2\mathrm{Rg}J^{12}_{mnm'n'} - ik_1^2\mathrm{Rg}J^{21}_{mnm'n'}, \tag{2.5.20}$$

where

$$
\begin{bmatrix}
\mathrm{Rg}J^{11}_{mnm'n'} \\
\mathrm{Rg}J^{12}_{mnm'n'} \\
\mathrm{Rg}J^{21}_{mnm'n'} \\
\mathrm{Rg}J^{22}_{mnm'n'}
\end{bmatrix}
= (-1)^m \int_S \mathrm{d}S\hat{\mathbf{n}} \cdot
\begin{bmatrix}
\mathrm{Rg}\mathbf{M}_{m'n'}(k_2 r, \theta, \phi) \times \mathrm{Rg}\mathbf{M}_{-m'n'}(k_1 r, \theta, \phi) \\
\mathrm{Rg}\mathbf{M}_{m'n'}(k_2 r, \theta, \phi) \times \mathrm{Rg}\mathbf{N}_{-m'n'}(k_1 r, \theta, \phi) \\
\mathrm{Rg}\mathbf{N}_{m'n'}(k_2 r, \theta, \phi) \times \mathrm{Rg}\mathbf{M}_{-m'n'}(k_1 r, \theta, \phi) \\
\mathrm{Rg}\mathbf{N}_{m'n'}(k_2 r, \theta, \phi) \times \mathrm{Rg}\mathbf{N}_{-m'n'}(k_1 r, \theta, \phi)
\end{bmatrix}.
\tag{2.5.21}
$$

It is clear that the benefit of using T-matrix method (EBC) is its independence of incidence and scattering directions, which means that its elements need only a single calculation for any direction- or incident polarization candidate. Another noteworthy property of T-matrix is the scale invariance, which transfers the dependency on "sheer" values of particle typical dimension and refractive index to relative values. For instance, a usual treatment of arbitrary shapes is to consider surface- or volume equivalent spheres of radius κ. In this case, T-matrix elements depend on the parameter $x = 2\pi\kappa/\lambda$, called the *size parameter*, where λ is the wavelength of the incident wave, and the relative refractive index $m = k_1/k_2 = m_1/m_2$, where m_1, m_2 are the refractive indices of the exterior and interior particle regions respectively, see an example in Sec. 2.6. Finally, symmetry relations result in simplified versions of the T-matrix. We are going to see a demonstration of this efficiency through the case of randomly oriented particles with a plane of symmetry in the following section.

2.6 Optical cross sections for randomly oriented objects

Eq. 2.1.14 and 2.2.10 trigger the interest on the quantification of absorption and scattering. A way to achieve this is through the optical cross sections which measure the effective area, tantamount to the probability of an event to take place. Moreover, cross sections multiplied by the intensity of incident light yield the corresponding power loss. The quantity associated with the total power loss is called *extinction cross section* C_{ext}, and is defined as the sum of the scattering cross section C_{sca} and the absorption cross section C_{abs}. For many applications (in our case too), there is high interest in the percentage which favors scattered light as opposed to absorbed light (or the converse), which stimulates the definition of a parameter, important for radiative transfer, called the *single scattering albedo*

$$
\varsigma = \frac{C_{\mathrm{sca}}}{C_{\mathrm{ext}}}.
\tag{2.6.1}
$$

Denoting by A the geometrical cross section of the particle (as "seen" from the detector), we also define the dimensionless so-called *particle efficiencies*

$$
Q_{\mathrm{sca}} = \frac{C_{\mathrm{sca}}}{A}, \quad Q_{\mathrm{abs}} = \frac{C_{\mathrm{abs}}}{A}, \quad \text{and} \quad Q_{\mathrm{ext}} = \frac{C_{\mathrm{ext}}}{A}.
\tag{2.6.2}
$$

The generally arbitrary direction of the scattered radiation is behind the rationale of measuring the distributed light over a solid angle Ω expressed by a quantity called the *differential cross section* denoted by $\mathrm{d}C_{\mathrm{sca}}/\mathrm{d}\Omega$.

A measure of the fraction of incident light being scattered in a specific direction is given by the *phase function* $p(\Theta)$ (also an input parameter for radiative transfer equation), normalized over the entire spherical surface

$$
p(\Theta) = \frac{4\pi}{C_{\mathrm{sca}}} \frac{\mathrm{d}C_{\mathrm{sca}}}{\mathrm{d}\Omega}, \quad \frac{1}{4\pi} \int_{S=4\pi} p(\Theta)d\Omega = 1
\tag{2.6.3}
$$

where $\Theta = \angle(\hat{\mathbf{r}}, \hat{\mathbf{n}}^{\mathrm{i}})$, $\Theta \in [0, \pi]$ is the scattering angle with $\cos\Theta = \cos\theta^{\mathrm{s}}\cos\theta^{\mathrm{i}} + \sin\theta^{\mathrm{s}}\sin\theta^{\mathrm{i}}\cos(\phi^{\mathrm{s}} - \phi^{\mathrm{i}})$. The average of the latter defines a direction index called the *asymmetry parameter*

$$
g = \langle\cos\Theta\rangle = \frac{1}{4\pi} \int_{S=4\pi} p(\Theta)\cos\Theta d\Omega.
\tag{2.6.4}
$$

When g is close to -1, or 1, scattering in $\Theta < \pi/2$ (backward) or $\Theta > \pi/2$ (forward) is strongly favored respectively, while a zero g infers isotropic scattering.

In a little more realistic scenario than scattering by a single small object, we can treat a finite (small) number ν of randomly oriented particles as a whole with minor effects in what is shown up to now. For

this we have to assume the volume element enclosing the particles is sufficiently sparse so that we can pretend that there are no interaction terms between the partial scattered electric fields from each particle and so that the average interparticle space is larger than the wavelength of the incident light and the mean particle size (avoid quantum interference). It is also vital that the randomness in particle position is such that it provides negligible phase correlation of the observed scattered waves.

In this sense, we only need to solve the same problem for each particle separately (employing the same far-field assumptions for each), ignoring momentarily the other ones. Subsequently, considering the particles as one entity, the same way it is depicted in Fig. 2.2, and denoting with the subscript ν the quantities associated with the ν-th particle, the total amplitude scattering matrix is $\mathbf{S} = \sum_{\nu} e^{ik_1 \mathbf{r}_\nu (\hat{\mathbf{n}}^i - \hat{\mathbf{r}})} \mathbf{S}_\nu$. By appealing to the aforementioned argument of the sufficient particle randomness, it can be shown that the total cross section is a sum of the individual cross sections from each particle

$$C_{\mathrm{j}} = \sum_{\nu} (C_{\mathrm{j}})_{\nu} = \nu \langle C_{\mathrm{j}} \rangle, \tag{2.6.5}$$

where $\langle \cdot \rangle$ denotes the average cross section per particle and j={sca, abs, ext}. In this case, the geometrical cross section in Eq. 2.6.2 makes now sense as the average area per particle $\langle A \rangle$.

The averaging introduced in the relation 2.6.5 is an essential feature. Indeed, atmospheric particles differ in all possible ways (size, morphology, orientation, etc.), and therefore in practice it makes sense to calculate averages over representative particle ensembles. Especially, randomly oriented particles with a plane of symmetry or with equal amount of mirror-symmetric counterparts are of particular interest in applications. A suitable, but otherwise cumbersome (regarding the previous sections' analysis), reference frame configuration for this purpose is to ovelap the incidence direction with $z-$axis and work on the plane defined by the incident and scattered waves (xz half-plane, $x \geq 0$) in which case, only the scattering angle Θ matters. H. Van de Hulst showed in [142] that in this setting, and taking orientation averages of particles with a plane of symmetry, the scattering matrix

$$\mathbf{F}(\Theta) = \mathbf{Z}(\theta^{\mathrm{s}} = \Theta, \phi^{\mathrm{s}} = 0, \theta^{\mathrm{i}} = 0; \theta^{\mathrm{i}} = 0, \phi^{\mathrm{i}} = 0) \tag{2.6.6}$$

has a simple block-diagonal form with an upper-symmetric- and lower antisymmetric 2×2 block, i.e. only six independent elements. The matrix element $F_{11}(\Theta)$ is equal to the phase function 2.6.3 and therefore it can be used to compute C_{sca}.

In lidar applications the term "backscatter cross section" is (improperly) reserved for the differential cross section in the exact backward direction, $\Theta = \pi$. We will keep this convention and denote the latter quantity with C_{bsca}. It is obvious that $C_{\mathrm{bsca}} = F_{11}(\pi) C_{\mathrm{sca}} / (4\pi)$.

The cross sections can be expressed in terms of the incident field amplitude $\mathbf{E}_0^{\mathrm{i}}$ and the scattered field amplitude $\mathscr{E}$ (see Sec. 2.4 and Eq. 2.4.3) using the energy conservation law, but the averaged cross sections turn out to be independent of the incident polarization and propagation direction, see [20, 98]. Here we will focus on formulas for practical computations with the T-matrix method, which are exceptionally efficient in the case of randomly oriented particles. Using the notation from Sec. 2.5, the cross sections per particle for randomly oriented particles with a plane of symmetry can be calculated by

$$\langle C_{ext} \rangle = -\frac{2\pi}{k_1^2} \, \mathfrak{Re} \sum_{n=1}^{\infty} \sum_{m=-n}^{n} \left(T_{mnmn}^{11} + T_{mnmn}^{22} \right), \tag{2.6.7}$$

$$\langle C_{sca} \rangle = \frac{2\pi}{k_1^2} \sum_{n=1}^{\infty} \sum_{m=-n}^{n} \sum_{n'=1}^{\infty} \sum_{m'=-n'}^{n'} \sum_{k=1}^{2} \sum_{l=1}^{2} \left| T_{mnm'n'}^{kl} \right|^2 \tag{2.6.8}$$

These formulas stay intact for any choice of the reference frame since the orientation isotropy enables this invariance. Physical knowledge of the particle (shape, size, refractive index) is sufficient for the average cross section calculations. T-matrix theory is thoroughly studied and there is an abundance of interesting formulas translating useful quantities (e.g. the scattering matrix) into T-matrix language, see [98].

In the special and simplest case of homogeneous spherical scatterers, developed much earlier by L. Lorenz and G. Mie (Lorenz-Mie theory,[97]) independently, T-matrix theory reduces to the exact same

formulas derived by C. F. Bohren and D. R. Huffman, [20]

$$C_{\text{ext}} = \frac{2\pi}{k^2} \sum_{n=1}^{\infty} (2n+1) \, \mathfrak{Re}(a_n + b_n), \tag{2.6.9}$$

$$C_{\text{sca}} = \frac{2\pi}{k^2} \sum_{n=1}^{\infty} (2n+1) \left(|a_n|^2 + |b_n|^2 \right), \tag{2.6.10}$$

$$C_{\text{bsca}} = \frac{\pi}{k^2} \left| \sum_{n=1}^{\infty} (2n+1)(-1)^n (a_n - b_n) \right|^2, \tag{2.6.11}$$

with

$$a_n = \frac{m\psi_n(mx)\psi_n'(x) - \psi_n(x)\psi_n'(mx)}{m\psi_n(mx)\xi_n'(x) - \xi_n(x)\psi_n'(mx)}, \tag{2.6.12}$$

$$b_n = \frac{\psi_n(mx)\psi_n'(x) - m\psi_n(x)\psi_n'(mx)}{\psi_n(mx)\xi_n'(x) - m\xi_n(x)\psi_n'(mx)}, \tag{2.6.13}$$

where $m = m_1/m_2$ is the relative refractive index, $x = 2\pi\kappa/\lambda$ is the size parameter, κ is the radius of the sphere, $\psi_n(t) = t j_n(t)$, and $\xi_n(t) = t h_n^{(1)}(t)$ with j_n denoting the Bessel functions of the first kind and $h_n^{(1)}$ the Hankel functions of the first kind.

In this special case of randomly oriented spherical particles, it is proved that the phase function is simplified to an expression with the only two non-zero elements of the scattering amplitude matrix (combine also 2.4.5, 2.6.3 and 2.6.6)

$$\begin{aligned} S_{11}(\Theta, 0; 0, 0) \\ S_{22}(\Theta, 0; 0, 0) \end{aligned} = \frac{i}{k_1} \sum_{n=1}^{\infty} \frac{2n+1}{n(n+1)} \begin{aligned} [a_n \tau_n(\Theta) + b_n \pi_n(\Theta)] \\ [a_n \pi_n(\Theta) + b_n \tau_n(\Theta)] \end{aligned} \tag{2.6.14}$$

$$p(\Theta) = \frac{2\pi}{C_{\text{sca}}} \left[|S_{11}(\Theta, 0; 0, 0)|^2 + |S_{22}(\Theta, 0; 0, 0)|^2 \right], \tag{2.6.15}$$

where $\pi_n(\Theta) = \sqrt{n(n+1)} \frac{d_{01}^n(\Theta)}{\sin\Theta}, \tau_n(\Theta) = \sqrt{n(n+1)} \frac{d}{d\Theta} d_{01}^n(\Theta)$ and d_{01}^n denote the Wigner d-functions, see App. A, Eq. A.0.4.

A rather counter-intuitive asymptotic feature of spherical scatterers is that at the edge of very coarse particles their optical cross section is twice as much the geometrical cross section [19], i.e.

$$\lim_{x \to \infty} Q_{\text{ext}} = 2. \tag{2.6.16}$$

An attempt for a physical explanation is elaborated in [20].

In the previous sections we dilated on the raw foundation of the theory used for this work. Now we would like to take a closer look at our application stepping deeper into the particle properties that will constitute the input data in our algorithm. A great deal of climate variability and uncertainty originates from aerosols, which will replace the idealized scattering object described before. Lidar systems have been monitoring aerosols in routine over the past 30 years, measuring the optical aerosol properties through the lidar equation, which introduces important parameters regarding the shape and size of aerosols. Polarization efficiency in lidars offers an additional powerful feature related to particle non-sphericity.

2.7 Aerosol forcing

"Atmospheric aerosol particles" (aerosols) is an abbreviation for a system of colloidal solid or liquid particles suspended in a gas (e.g. the air). Aerosols stand in the way of the solar radiation, almost quarter of which does not make it to Earth's surface. Their great variability in shape, size, chemical composition, sources, age, and distribution spatially and temporally is underlined by the latest IPCC

reports as being important uncertainties to invest on for a better climate understanding. Indeed, it is known that the so-called aerosol microphysics pulls the strings of the shortwave and longwave radiation give-and-take (owing to scattering and absorption), but they also have an indirect mechanism which alters cloud radiative properties, see e.g. [93]. Besides weather- and climate influence, another straightforward aspect of the aerosol effect is on air quality and thus human health, depending on aerosol size and type.

On the one hand, aerosols can have an originating source, in case they are released from Earth's surface mainly to the planetary boundary layer (lowest part of the atmosphere undergoing turbulence corresponding to changes in surface forcing within an hour) and transported to the free atmosphere, e.g. desert dust (minerals), sea salt, forest fires, combustion of fossil and biomass based fuels (human-made). There are also aerosols reaching the upper troposphere or the stratosphere e.g. through volcanic eruption events. On the other hand there are aerosols formed in the atmosphere from gaseous precursors, e.g. non-sea-salt sulphate, nitrate and ammonium. Both instances of aerosols presence can be affected by natural and anthropogenic involvement, resulting in an extreme range of physical properties and radiative effect, for more details see [59, 64]. Additionally, aging process might involve aggregate formation (coagulation) due to particle collisions or even result in swelling aerosols due to water vapor condensation in the event of high relative humidity, all of which alter obviously the scattering behavior.

Mineral dust has a conspicuous position among aerosols due to its influence on the climate system, mainly through deserts from all over the globe with a regional or a long-range scale. Australian dust storms can be very severe and affect both east and west with occasional extreme events, see [77], the latest being in 2009 across New South Wales and Queensland. Taklamakan and Gobi desert winds and dust (also known as yellow sand) affects the central and east Asia and can reach even the United states, see [61, 151]. Among dust events, Saharan desert and Sahel in North Africa are the main sources of long range airborne dust transportation northwards to Europe and westwards to North and South America in terms of freguency and dust load. This explains the vast documentation in scientific literature in Saharan dust events, with perhaps the epicenter being the SAMUM I and II campaigns [4], where dust was investigated both in its source (Morocco, 2006) and through long-range transport (Cape Verde, 2011). The measurements in Morocco [75] revealed (wide) size ranges of dust differing by an order of magnitude (nm to µm) and identified the main non-spherical components with paricle diameters over 0.5 µm, as being feldspars and clay minerals, quartz and carbonates. Coming discussions about non-spherical particles in this work will largely refer to dust-like particles.

2.8 Aerosol optical properties and lidars

Aerosol forcing is directly related to the net scattering contributions by all aerosol particles. Assuming n_j single scattering objects of type j, each of which having extinction- and backscatter cross sections $(C_{\text{ext}})_j$ and $(C_{\text{bsca}})_j$ are called the *extinction coefficient* α and the *backscatter coefficient* β of the medium respectively and are given by

$$\alpha = \sum_j n_j (C_{\text{ext}})_j, \quad \beta = \sum_j n_j (C_{\text{bsca}})_j. \tag{2.8.1}$$

These parameters are usually referred as the *aerosol optical properties* or *optical parameters*, as they give vital information for aerosol profiling and the atmospheric state. Later on, these relations will be expressed through a continuous model with the help of the Fredholm integral (see Eq. 1.1.2), resulting in the basic working model for the present work. Fortunately, the optical parameters are nowadays directly measurable on a routine basis by lidar systems.

As we saw in previous sections, scattering behavior acts as an identifier for a particle. This is the very feature exploited by the working principle of lidar systems. An artificial beam of (linearly) polarized and coherent light strikes the target aerosol particles and the backscattered radiation is collected by a telescope and analyzed, see Fig. 2.3. *Lidar equation* provides a way to calculate the extinction and backscatter coefficients, by making the link between physical characteristics of the machine itself, and the receiving intensity $\mathscr{I}$ of the returned signal from a distance r from the target object

$$\mathscr{I}(r) = \mathscr{I}_0 f \frac{O(r)}{r^2} \beta(r) e^{-2\tau}, \quad \tau = \int_0^r \alpha(s)\, ds. \tag{2.8.2}$$
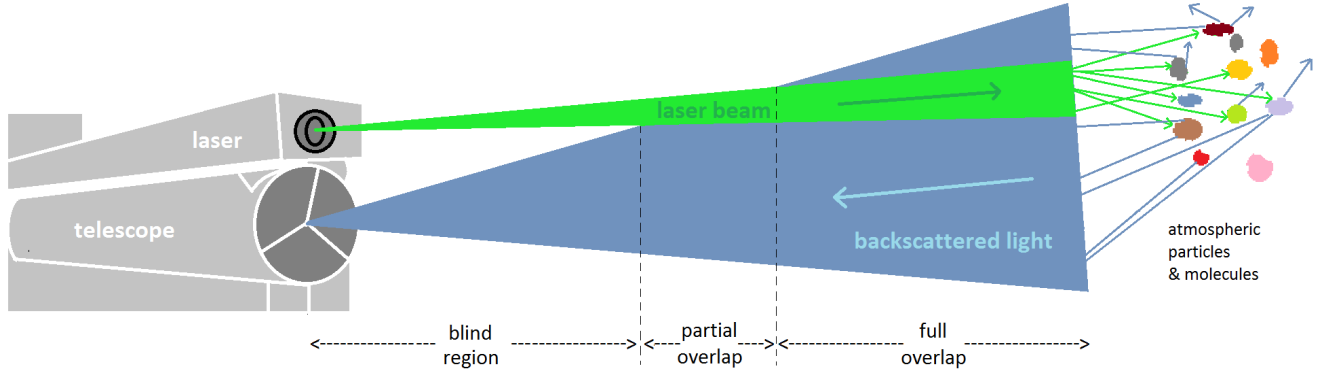
Figure 2.3: Illustration of the lidar principle and the overlap effect. We distinguish 3 regions during the scattering process: the zero overlap (blind region), the partial overlap and the full overlap.

$\mathscr{I}_0$ is the average transmitted laser pulse intensity, f is the (optimized) system factor describing the detection system and the optical efficiency through which the transmitted and scattered light pass. $O(r)$ is the overlap function, responsible for the geometric effects regarding the incident laser beam and the field of view of the telescope (perception angle $\sim \frac{1}{r^2}$). Fig. 2.3 shows an illustration of the overlap effect. If the full overlap is achieved too far from the lidar the signal will already be too weak. The latter is a well-known lidar defect directly affecting signal quality, which needs to be addressed and compensated through overlap profiling on clear sky measurements, see [148]. The attenuation of the laser beam due to the intervention of aerosols and molecules is expressed by the exponential term of Eq. 2.8.2 according to Beer's law [156], introducing another measure of particle extinction called the *optical depth* (τ). The latter is also used in *sun photometer* measurements, and it's dependency from the wavelength λ is often empirically described by the power law $\tau \sim \lambda^{-\mathscr{A}}$, where $\mathscr{A}$ is called the *Ångström exponent*. Another important intensive parameter is the aerosol extinction to backscatter ratio, called the *lidar ratio*. It should be emphasized that lidar ratios and Ångström exponents (AE) are very useful characterization tools labeling concisely the type and size of aerosol particles respectively, see [103, 149]. A small |AE| is linked to large particles whereas a larger |AE| is linked smaller ones. For instance, a typical AE for (Saharan) dust particles is ~ 0.5 and for biomass burning aerosols AE can reach ~ 2.

Generally, the parameters α and β in Eq. 2.8.2 pertain to the total scattering contribution from molecules and aerosols. Meteorological feedback can be used for the molecular backscatter and extinction, therefore the primary concern is the derivation of the aerosol part. *Elastic-backscatter lidars* (EBL) provide profiles of the extinction coefficient estimated using the assumption of a conditionally "constant" lidar ratio, a method developed by J. D. Klett [83] and F. G. Fernald [39]. The need for an estimation of an otherwise strongly size- and morphology dependent lidar ratio is overcome by *Raman-lidars* by additionally measuring the inelastic backscatter by nitrogen and/or oxygen molecules, see [5], and thus retrieving α and β independently. Denoting with the subscript "aer" and "mol" the aerosol- and molecular contributions, with "i" and "s" the incidence- and (shifted) backscatter-related quantities, and with N the nitrogen / oxygen molecule number density, the inelastic lidar equation can be explicit solved with respect to the α_{aer} as follows

$$\alpha_{\text{aer}}(r, \lambda_i) = \frac{\frac{\mathrm{d}}{\mathrm{d}r} \ln \frac{N_{\text{s}}}{r^2 \lambda_{\text{s}}} - \alpha_{\text{mol}}(r, \lambda_{\text{i}}) - \alpha_{\text{aer}}(r, \lambda_{\text{s}})}{1 + \left(\frac{\lambda_i}{\lambda_{\text{s}}}\right)^{\mathscr{A}(r)}}, \tag{2.8.3}$$

where the additional terms involved can be derived by meteorological (e.g. radiosoundings) or from standard-atmosphere data. A multi-wavelength Raman-elastic lidar, e.g. the nowadays most popular Nd:YAG-laser equipped lidar, transmits and collects at 355, 532 and 1064 nm (elastic channels) and additionally detects Raman (inelastic) signals from nitrogen molecules at 387 nm (355 nm primary wavelength - PM) and 607 nm (532 nm PM), and from water-vapor molecules at 660 nm (532 nm PM). This revolutionay method is not without its flaws. Raman scattering is relatively weak, raising the system costs in demand for more powerful lasers and larger telescopes. Moreover, mathematically, the calcu-

lation of the derivative in Eq. 2.8.3 can become unstable in the presence of fluctuations of the Raman signal, so that special methods need to be used, see [121] for a treatment with regularization.

Atmospheric lidar applications have nowadays extended to monitor also the wind (Doppler lidar), and detect atmospheric gases (*Differential Absorption Lidar* - DIAL). Lidar potential was greatly expanded by employing polarization techniques which allows the distinction of the horizontally and vertically polarized backscattered light from a transmitted linearly polarized beam. The ratio of the vertically- $\beta_\perp$ over the horizontally polarized backscatter coefficient $\beta_\parallel$ is called *linear particle (backscattering) depolarization ratio* δ_L and can be calculated via the scattering matrix **F**, see Sec. 2.6 and Eq. 2.6.6

$$\delta_L = \frac{F_{11}(\pi) - F_{22}(\pi)}{F_{11}(\pi) + F_{11}(\pi)}. \tag{2.8.4}$$

This parameter often plays a decisive role as an index of particle non-sphericity. For spherically modelled particles this quantity vanishes. Linear depolarization ratio measurements have been used during the Saharan Mineral Dust Experiment (SAMUM), [4, 42] but also to distinguish dry, liquid and the ice phase of aerosols and clouds. Latest technological advancements on *polarization lidars* allow depolarization ratio profiling at three wavelengths 355, 532 and 1054 nm, see [42].

Chapter 3

Spheres and spheroids: models and algorithms

Foreword

Up to now we have already seen the basic principles behind light scattering acting as an identifying property of the material, which together with the exploitation of polarization by lidar systems can bring us various information about the ongoing atmospheric scene. This chapter is the final theoretical step before entering our application from a practical point of view. Here we meet the basic models from literature regarding the particle size distribution and its relation to the optical properties, and we introduce natural generalizations enabling the exploration of non-sphericity. Subsequently, we will narrow down the particle non-sphericity and limit ourselves to spheroid-modelled particles, prompted by theoretical and experimental evidence related to the phase function. The computational cost and complexity for the purpose of the massive simulations performed later in this work leads to use of a special program (Miescka) for the calculation of the scattering efficiencies and further to a creation of a discretization database. We will further see the link between the mathematical and physical toolbox, presented in the previous chapters, with all practical details about how to solve the microphysical retrieval problem, which constitutes the core of the present work.

3.1 Modelling aerosol optical and microphysical properties

It becomes clear that the distribution of aerosols with respect to their size, i.e. the aerosol size distribution, is very important for aerosol typing. Logarithmic-normal (log-normal) distributions bear a good -continuous- empirical fit to aerosol size distributions. Denoting the total number concentration of particles by $(N_\mathrm{t})_j$, the median radius by $(r_\mathrm{med})_j$, the geometric standard deviation (mode width) by σ_j,

Table 3.1: Notation and units of parameters and variables

Parameter / Variable	Notation	Units
number concentration	$N_\mathrm{t}, n_\mathrm{t}$	$\mathrm{\mu m^{-1} cm^{-3}}$
total volume concentration	v_t	$\mathrm{\mu m^{3} cm^{-3}}$
surface-area concentration	a_t	$\mathrm{\mu m^{2} cm^{-3}}$
radius, median radius, effective radius	$r, r_\mathrm{med}, r_\mathrm{eff}$	$\mathrm{\mu m}$
number distribution	$n(r)$	$\mathrm{cm^{-3}}$
volume size distribution	$v(r)$	$\mathrm{\mu m^{3} \mu m^{-1} cm^{-3}}$
wavelength	λ	nm
extinction coefficient	$\alpha(\lambda), \mathscr{Z}(\lambda)$	$\mathrm{m^{-1}}$
backscatter coefficient	$\beta(\lambda), \mathscr{Z}(\lambda)$	$\mathrm{m^{-1} sr^{-1}}$
extinction cross section	$C_\alpha(\lambda, r; m), C_\alpha(\lambda, r, a; m)$	$\mathrm{m^{2}}$
backscatter cross section	$C_\beta(\lambda, r; m), C_\beta(\lambda, r, a; m)$	$\mathrm{m^{2} sr^{-1}}$

and the particle radius by r, the k-modal log-normal distribution $n(r)$ is a probability density function, defined by

$$n(r) = \sum_{j=1}^{k} \frac{(N_t)_j}{\sqrt{2\pi} r \ln(\sigma_j)} e^{-0.5\left(\log_{\sigma_j} r/r_{med}\right)^2}. \tag{3.1.1}$$

The extinction- (α) and backscatter coefficients (β), both denoted with $\mathscr{L}(\lambda)$ are traditionally related to the aerosol size distribution $n(r)$ through the continuous collection of scattering cross sections $C_{\alpha/\beta}(r, \lambda; m)$ from scatterers over all sizes. This can be expressed with the Fredholm integral of the first kind

$$\mathscr{L}(\lambda) = \int_{r_{min}}^{r_{max}} C_{\alpha/\beta}(r, \lambda; m) n(r) dr, \tag{3.1.2}$$

where m is the refractive index (RI). The integral boundaries typically extend to $[0, \infty)$, but for practical purposes we define the integral (Eq. 3.1.2) over a "sensible" domain $[r_{min}, r_{max}]$ and we consider the rest a part of the total modelling error. The radius domain is part of the initial parameter setup when solving for the microphysical problem, and is usually based on some very rough knowledge on particle size. Details on how this affects the resulting size distributions can be found in [131].

The numerical performance is more stable by using the so-called *volume size distribution* defined by

$$v(r) = \frac{4\pi r^3}{3} n(r). \tag{3.1.3}$$

The log-normal distribution 3.1.1 can be rewritten to its "volume" version using 3.1.3, i.e.

$$v(r) = \sum_{j=1}^{k} \frac{4\sqrt{\pi} r^2 (N_t)_j}{3\sqrt{2} \ln(\sigma_j)} e^{-0.5\left(\log_{\sigma_j} r/r_{med}\right)^2}. \tag{3.1.4}$$

Knowing the size distribution, we can calculate the following microphysical parameters.
The *total volume concentration*:

$$v_t = \int_{r_{min}}^{r_{max}} v(r) dr, \tag{3.1.5}$$

the *number concentration*

$$n_t = \int_{r_{min}}^{r_{max}} n(r) dr = \frac{3}{4\pi} \int_{r_{min}}^{r_{max}} \frac{v(r)}{r^3} dr, \tag{3.1.6}$$

the *surface-area concentration*

$$a_t = 4\pi \int_{r_{min}}^{r_{max}} r^2 n(r) dr = 3 \int_{r_{min}}^{r_{max}} \frac{v(r)}{r} dr \tag{3.1.7}$$

and the *effective radius*

$$r_{eff} = 3 \frac{v_t}{a_t}. \tag{3.1.8}$$

The units for every quantity can be found in Tab. 3.1. Replacing $n(r)$ with $v(r)$ and the $C_{\alpha/\beta}$ with the dimensionless optical efficiencies $Q_{\alpha/\beta}$ (see Eq. 2.6.2), the spherical model Eq. 3.1.2 becomes

$$\mathscr{L}(\lambda) = \int_{r_{min}}^{r_{max}} \frac{3}{4r} Q_{\alpha/\beta}(r, \lambda; m) v(r) dr. \tag{3.1.9}$$

We will often refer to Eq. 3.1.2 and 3.1.9 as the LM-model, referring to the optical efficiencies being calculated by the Lorenz-Mie theory, see Eq. 2.6.9-2.6.13.

This formula describes an inverse ill-posed problem that needs to be solved in order to retrieve the size distribution, from which one can retrieve the microphysical parameters n_t, v_t, a_t and r_{eff}. A series of results with regularized inversion of synthetic and real lidar data results has proved this model reliable for particles approximated by spheres. Tikhonov regularization with the generalized cross validation is used [106, 107, 108], while in [145] the same regularization method is combined with a modified version of discrepancy principle. [86] suggest an evolved two dimensional regularization method in the sense of

a correlation condition between successive height bins. [16] use Padé iteration to regularize the problem and later an adaptive base point approach is added to the iteration by [113]. [14] introduces a data-driven hybrid regularization method to simultaneously benefit from different mathematical features. The problem of automatization of the inversion process for real-life lidar data without manual postprocessing is discussed and methodologically addressed in [131] for pure and aged smoke with continental pollution.

3.2 The need for a non-spherical model over particle ensembles

Eq. 3.1.2 is undoubtedly the most often-used microphysical prescription at least in climate research and even more spread across the lidar community, owing to it's simplicity and the direct connection with the lidar observables α and β. It's range of applicability, the way the optical cross sections depend only from r, λ and m, limits itself to spherically modelled particles, see Eq. 2.6.9-2.6.13. Additionally, it is assumed that the spheres are homogeneous, so that they can be characterized by a single refractive index. The series involved in the spherical cross sections have known convergence criteria which makes them easy to compute and thus by far the most advantageous numerically. As discussed in Sec. 3.1, the sphere-based model in conjunction with several regularization algorithms delivered a satisfying first order approximation over the years. Evidently, spheres cannot be a representative shape for most atmospheric particles, as a result of atmospheric state complexity and variability. Irregularities in particle shape and internal structure bring generally all kinds of unpredictable scattering outcomes, but what matters in a first step is the order of particle size relative to the incidence wavelength, which is where the size parameter (x) comes in (Sec. 2.5). For a much smaller particle size than the incidence wavelength, in the so-called Rayleigh regime, everything "looks" quite spherical, and hence the LM-model is a good approximation. However, for particle sizes comparable to- (resonance region) or much larger than the wavelength ($x \gg 1$) the current consensus points to the insufficiency of the LM-model to reproduce optical characteristics accurately.

Particle non-sphericity is a way too general term and in fact needs to be modelled and then investigated for its sufficiency experimentally. In order to see in practice the spherical-non-spherical scattering differences, let us introduce the *spheroid-particle approximation*. A spheroid is geometrically obtained by the revolution of an ellipse about one of its principle axes. Denoting the semi-minor axis with a, the semi-major axis with b, and their ratio with $\eta = a/b$, called the *aspect ratio*, we can distinguish the only three possible shapes: the oblate spheroid with $\eta < 1$, the sphere with $\eta = 1$ and the prolate spheroid with $\eta > 1$, see Fig. 3.1.
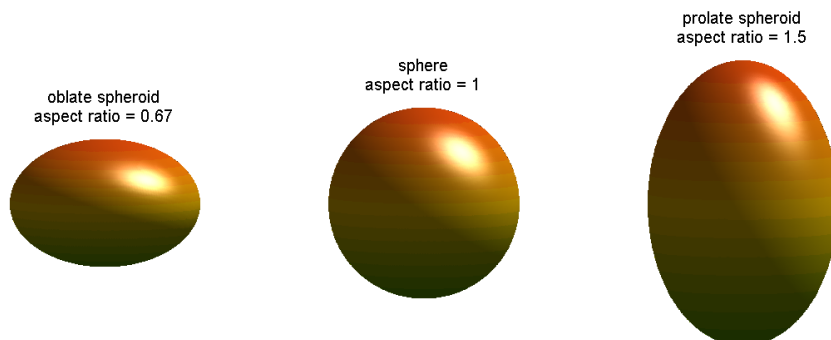
Figure 3.1: Spheroids: Oblate spheroid (left), sphere (middle) and prolate spheroid (right).

The scattering patterns can be investigated through instances of the phase function. In Fig. 3.2 and 3.3 we see examples of surface plots of the phase function with respect to the size parameter $0.02 \le s \le 40$
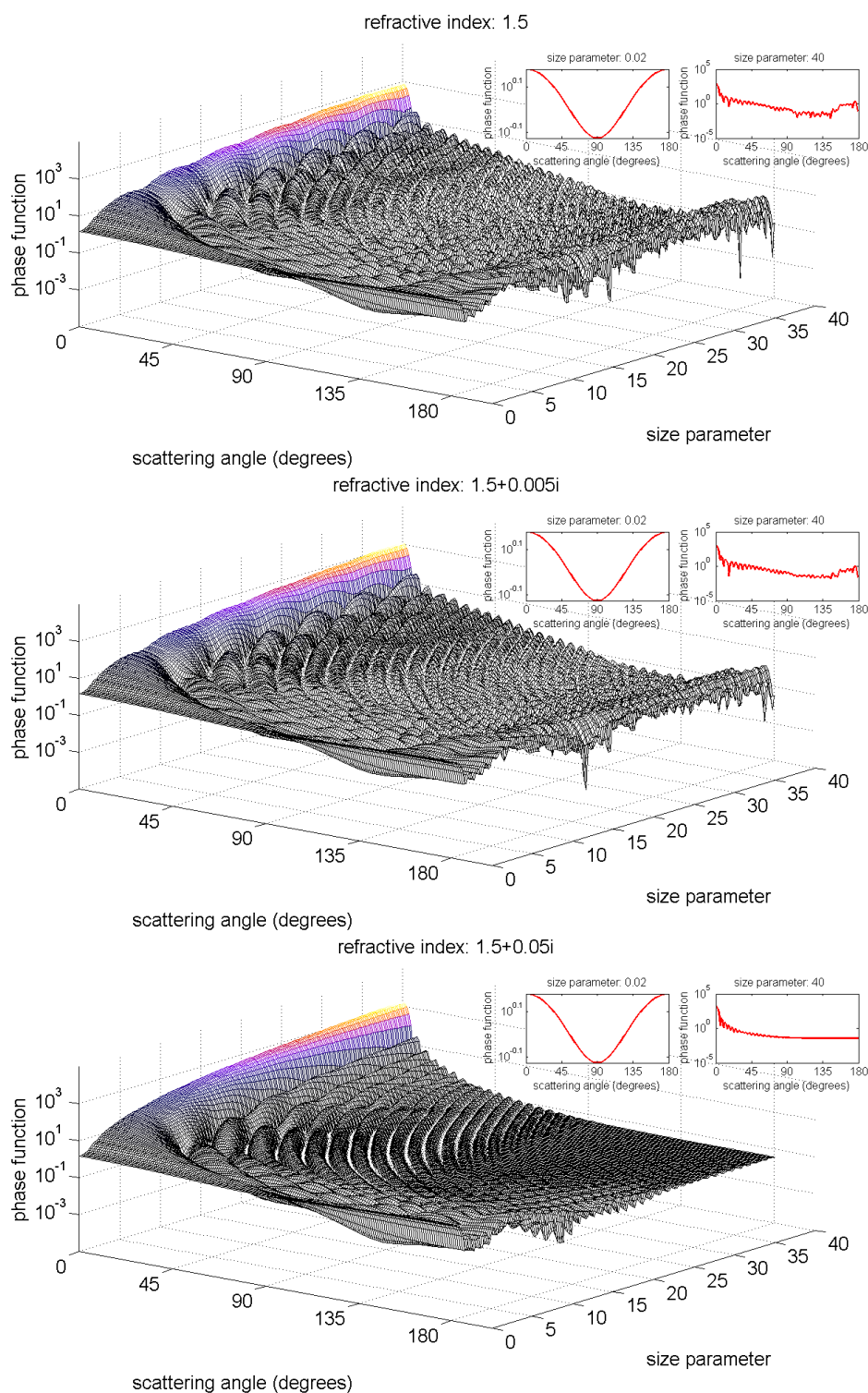
Figure 3.2: 2D-Plots of the phase function for spherical scatterers with respect to the size parameter (x) and the scattering angle with increasing absorption (imaginary part of the refractive index) from top to bottom. Smaller figures in the upper right corner of each plot, display the extreme cases for size parameters 0.02 and 40.

and the scattering angle $0 \leq \Theta \leq 180°$ for spheres and spheroids respectively. The panels in each figure are ordered with increasing absorption level from top to bottom, i.e. imaginary part of refractive index (IRI) $\mathfrak{Im}(m) \in \{0, 0.005, 0.05\}$ and a fixed real part of refractive index (RRI) $\mathfrak{Re}(m) = 1.5$. Moreover,
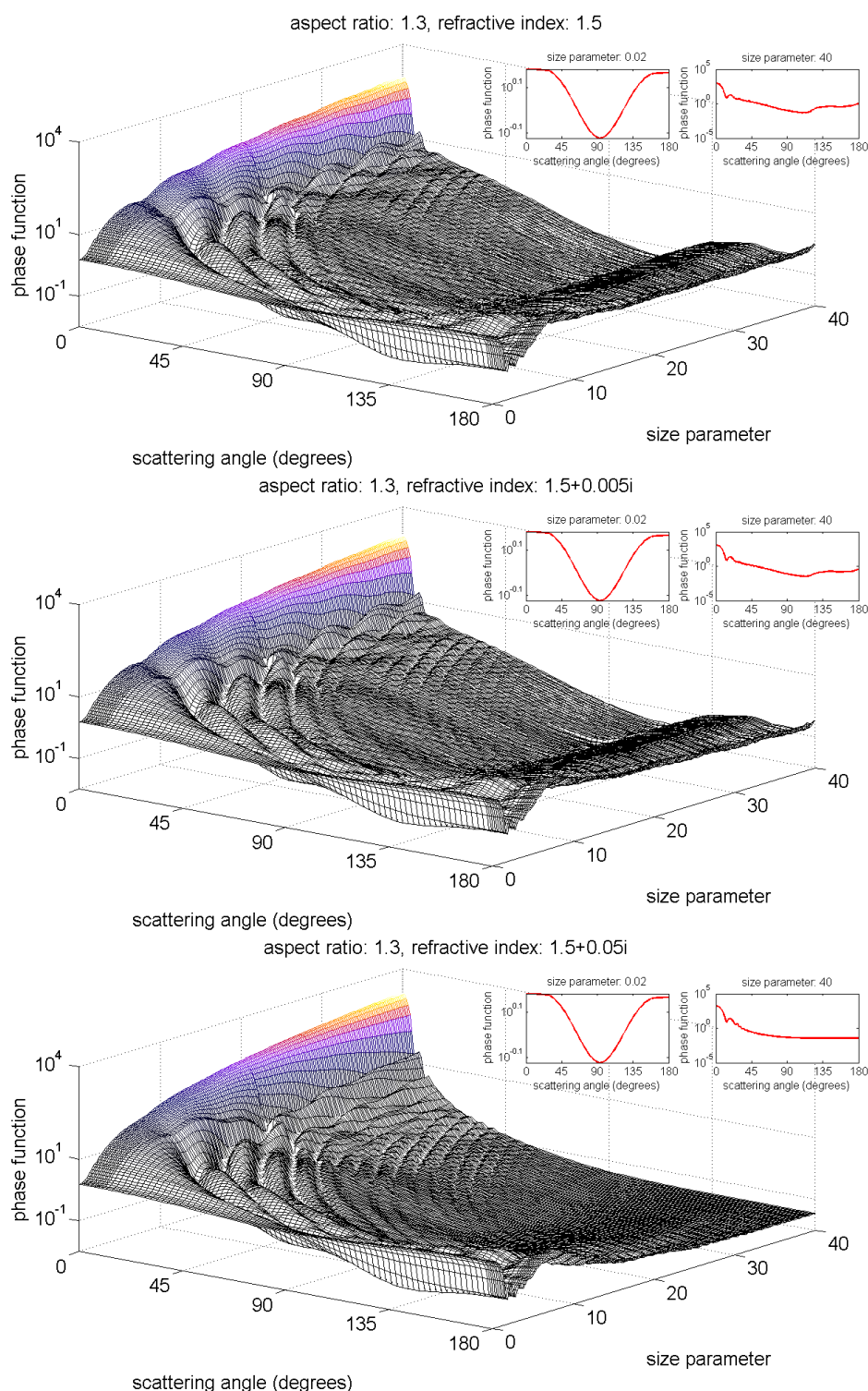
Figure 3.3: 2D-Plots of the phase function for prolate ($\eta = 1.3$) spheroidal scatterers with respect to the size parameter (x) and the scattering angle with increasing absorption (imaginary part of the refractive index) from top to bottom. Smaller figures in the right upper corner of each plot, display the extreme cases for size parameters 0.02 and 40.

in the top right part of each figure there are one-dimensional subfigures containing the boundary cases $s = 0.02$ and $s = 40$. Focusing on relatively small sizes in the vicinity of $s = 0.02$ we see that the scattered light is almost equally distributed in forward- and backward directions regardless of the absorption level

for both spheres and spheroids. Spherical particles have a strong oscillatory behavior for greater sizes in the so-called resonance region (here $s > 0.1$). Looking at the top and middle panels of Fig. 3.2, we observe a small portion of dominant sideward scattering ($< 20°$) against backward scattering which is compensated in a point, even for the absorbing case with $\mathfrak{Im}(m) = 0.005$ especially for large sizes, see subfigures for $s = 40$. While we see only minute differences from $\mathfrak{Im}(m) = 0$ to $\mathfrak{Im}(m) = 0.005$ in the top and middle panels of Fig. 3.2 and 3.3, stronger absorption ($\mathfrak{Im}(m) = 0.05$) seems to level off backward scattering almost entirely both for spheres and spheroids, an effect mostly pronounced as we move away from small particles.

The oscillatory pattern above and beyond the resonance region seems to be a trademark mostly of spheres, since the panels of Fig. 3.3 show a much smoother phase function for spheroids, which appears to match measurement cases. Moreover, comparing Fig. 3.2 and 3.3, we see that backward scattering by spheroids is diminished relative to sideward scattering for larger particles as opposed to spheres, see also [85, 111]. This is not an isolated feature but rather exhibited also for other refractive indices (real parts), as it is confirmed by several one-dimensional versions of the phase function in Fig. 3.4 for $x = 40$, $\mathfrak{Im}(m) = 0.005$ and different RRIs. In addition, an increasing real part of refractive index for larger spheroids results in a upward right shift of the minimum located in $90° < \Theta < 135°$ and also a gradual enhancement of backscattering.

Attempts in literature to replicate the experimental phase function of particles are enlightening in the discussion of spherical-versus-non-spherical shape. What is interesting and perhaps unexpected is
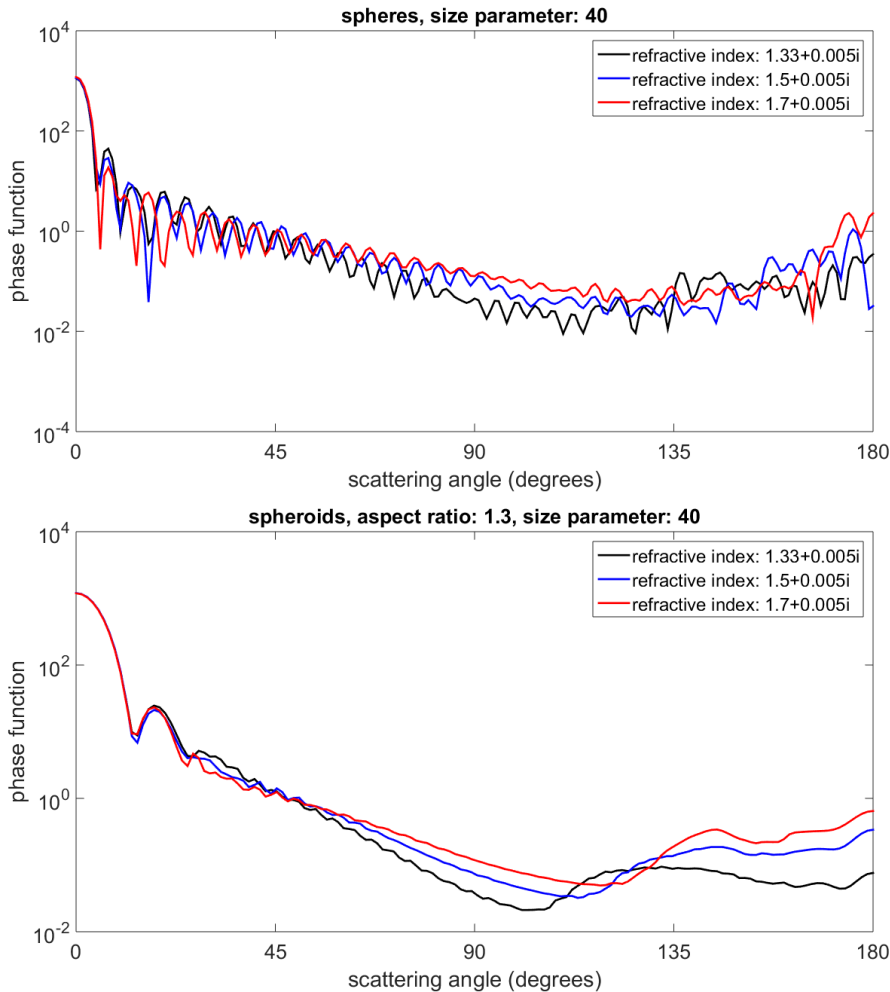
Figure 3.4: Plots of the phase function for spherical- (upper panel) and spheroidal scatterers (lower panel) with size parameter $x = 40$ with respect to the scattering angle for increasing real part of the refractive index.

that phase functions of natural particle ensembles appear to be smooth. When simulating real-life phase functions, it rarely makes sense to consider single size- and/or shape particle ensemble, but rather a polydisperse one expressed by a distribution, over which the phase functions (or other properties) are calculated. This is again a form of averaging which suppresses or even wipes out the resonances for sufficiently large ensembles and can even produce a smoothed spherical phase function. Even so, spheroids have a much better (in some cases perfect) agreement with the observed phase functions. Fig. 3.5 illustrates this with a comparison of experimental phase functions measured by [67] and synthetic spherical and spheroidal phase functions. The dashed curve corresponds to a measured phase function for natural wavelength-sized soil particles, while the normal- and dotted line corresponds to a calculated phase function based on shape distribution of polydisperse, randomly oriented spheroids and surface-equivalent spheres respectively. Other examples of such a comparison of sphere- and spheroid phase function fit with a characteristically featureless experimental phase functions can be found in [109].

The selection of spheroids against spheres is generally supported in literature relying on the much better performance at least for some scattering properties of soil and dust-like particles and by no means on an accurate particle resemblance. Moreover, other reported large differences [99] of this simple non-spherical approximation as compared to spheres, for instance in lidar ratio, hint to the insufficiency of the spherical approximation, therefore the usual underlying assumption of a spherical geometry may lead to wrong results. We note, however, that there are reported similarities in the behavior of spheres and spheroids in other properties e.g. the asymmetry parameter and the single scattering albedo.

Nowadays' consensus on non-spherical aerosol particles comes largely from the spheroid-particle approximation. This is a result of the relatively infant research stage regarding more complicated particle approximations. Despite the lesser extent of experiments involving the latter, the discrepancies in optical properties between sphericity and non-sphericity are still confirmed in general. An example of higher particle complexity are the so-called *Chebychef particles* associated with small-scale surface roughness, see e.g. [71, 102, 126]. However, the strong refractive index dependence of these shapes found in [71] and the poor association of the tested particle morphologies (surface roughness) to simple patterns regarding scattering intensity and polarization add up to additional limitations with regard to involving more complex shapes.

The spherical phase functions were calculated using Eq. 2.6.14-2.6.15 and a Matlab implementation of Bohren and Huffman code [20], while for the spheroidal phase functions the software *Miescka* [125] was used. The latter software was a vital companion for this work, providing the means (kernel function database) to realize the coming microphysical retrievals with the spheroid-particle approximation. More
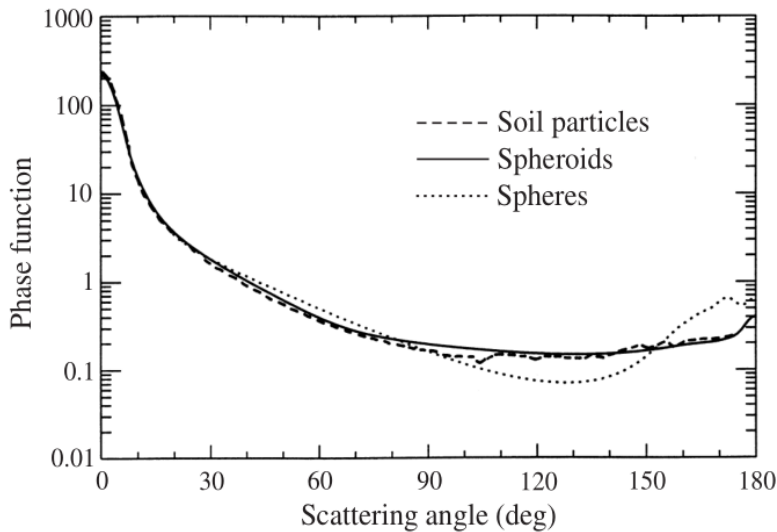
Figure 3.5: Comparison of experimental and synthetic spherical and spheroidal phase function. The dashed curve corresponds to a measured phase function for natural wavelength-sized soil particles, while the normal- and dotted line corresponds to a calculated phase function based on shape distribution of polydisperse, randomly oriented spheroids and surface-equivalent spheres respectively. Plot credit: [67].

details on assets and the limitations of Mieschka pertaining to this work will be given later on (Sec. 3.3). The size parameter resolution used for the plots is 0.2. We note that the use of the boundary size parameter $x = 40$ in Fig. 3.2, 3.3 and 3.4 is quite conservative for large particles, e.g. for the lidar wavelength $\lambda = 355$ nm and a radius $r = 2$ µm (coarse particle size) the size parameter is $s = 35.4$.

3.3 Generalization of the spherical model

The previous analysis indicated that the individual shape contributions are rather not sensed by the experimental result. In particular, we saw that averages over shape and /or size distributions can be used to fit phase functions of naturally formed particles (soil and dust). This brings the idea of a generalization of the LM-model 3.1.2 evolving the particle distribution $n(r)$ to a *shape-size distribution* $n(r, \eta)$, where η may be a set of parameters $a_1, a_2, \ldots, a_{N-1}$ describing the particle physically (geometry & morphology). These parameters will also identify the non-spherical scattering cross sections. This concept is an extension of the generalization first proposed by [18, 112] for $N = 2$, which we will also follow here. More specifically, we will consider a *spheroid-particle approximation*, which needs only one additional parameter, i.e. the aspect ratio η, to be fully defined. It is formalized as follows:

$$\mathscr{L}(\lambda) = \int_{\eta_{\min}}^{\eta_{\max}} \int_{r_{\min}}^{r_{\max}} C_{\alpha/\beta}(r, \lambda, \eta; m) \, n(r, \eta) \mathrm{d}r \mathrm{d}\eta, \tag{3.3.1}$$

where $[\eta_{\min}, \eta_{\max}]$ is again a sensible and sufficiently wide aspect ratio range determined experimentally as part of the initial parameters (as discussed in [131]) of a microphysical retrieval. The radius here makes sense as the one of a sphere with equal volume to a spheroid. The latter is found by $V = 4\pi a^2 b/3$, so that $r = \sqrt[3]{a^2 b}$, where a and b are the semi-minor and semi-major axis respectively.

Regarding the particle distribution, we see that the case of spheroids defines a two-dimensional (2D) generalization, but the optical parameters ($\mathscr{L}$) still remain only wavelength-dependent, which is why we shall consider this a *quasi-2D model*. Furthermore, the reduction to a quasi-ND case with $N - 1$ shape-related parameters (SRP) is easily being formed, extending the averaging and thus the integration of Eq. 3.1.2 over the $N - 1$ parameters (in addition to the size averaging).

The microphysical parameters can be redefined in 2D analogously. Similarly to the 1D-case we set $n(r, \eta) = \frac{3}{4\pi r^3} v(r, \eta)$, where $v(r, \eta)$ is the *volume shape-size distribution*. Through the latter, we define the *number concentration*

$$n_{\mathrm{t}} = \int_{\eta_{\min}}^{\eta_{\max}} \int_{r_{\min}}^{r_{\max}} n(r, \eta) dr d\eta, \tag{3.3.2}$$

the *total volume concentration*

$$v_{\mathrm{t}} = \int_{\eta_{\min}}^{\eta_{\max}} \int_{r_{\min}}^{r_{\max}} v(r, \eta) dr d\eta, \tag{3.3.3}$$

and the *surface-area concentration*

$$a_{\mathrm{t}} = \int_{\eta_{\min}}^{\eta_{\max}} \int_{r_{\min}}^{r_{\max}} \frac{3}{\pi r^3} G(r, \eta) v(r, \eta) dr d\eta. \tag{3.3.4}$$

The effective radius is still calculated by the same formula in Eq. 3.1.8, using Eq. 3.3.3 and 3.3.4 instead. The function $G(r, \eta)$ denotes here the spheroidal geometrical cross section of the particle, which can be explicitly computed as follows

$$G(r, \eta) = \begin{cases} 2\pi \left[a^2 + \frac{b^2}{e} \tanh^{-1}(e)\right], \text{ where } e = \sqrt{1 - b^2/a^2}, & \text{if } \eta < 1, \\ 4\pi r^2, & \text{if } \eta = 1, \\ 2\pi \left[a^2 + \frac{ab}{e} \sinh^{-1}(e)\right], \text{ where } e = \sqrt{1 - a^2/b^2} & \text{if } \eta > 1. \end{cases} \tag{3.3.5}$$

Furthermore some new parameters are introduced here in order to study the shape of the size distribution in greater detail. We define the -volume-weighted- *effective aspect ratio*

$$\mu_\eta^{(v)} = \frac{\int_{\eta_{\min}}^{\eta_{\max}} \eta \int_{r_{\min}}^{r_{\max}} v(r, \eta) dr d\eta}{v_{\mathrm{t}}}, \tag{3.3.6}$$

and the *aspect ratio width*

$$\sigma_\eta^{(v)} = \frac{\int_{\eta_{\min}}^{\eta_{\max}} (\eta - \mu_\eta^{(v)})^2 \int_{r_{\min}}^{r_{\max}} v(r,\eta) dr d\eta}{v_{\mathrm{t}}} \tag{3.3.7}$$

The parameters $\mu_\eta^{(v)}$ and $\sigma_\eta^{(v)}$ give us an estimation and a direct look of a central tendency of the aspect ratio and the spread of the values from this type of mean.

The following parameter specializes in identifying individual spherical-non-spherical contributions (%) in the volume concentration. We define the *non-spherical volume concentration fraction* by

$$\gamma = 1 - \frac{1}{v_{\mathrm{t}}} \int_{1-\chi}^{1+\chi} \int_{r_{\min}}^{r_{\max}} v(r,\eta) dr d\eta, \tag{3.3.8}$$

where χ is a positive small, yet not negligible number called the *shape-transition parameter*. Similarly we call $1 - \gamma$ the *spherical volume concentration fraction*.

Several non-spherical-particle approximations are present in publications regarding optical parameter investigations, while in microphysical-retrieval research, non-sphericity is dominated by spheroids. The commonly cited microphysical-parameter database hosted by AErosol RObotic NETwork (AERONET) is such an example (see Introduction). Aerosols are assumed by AERONET to have both a spherical and a non-spherical component, where the former is modeled by an ensemble of polydisperse, homogeneous spheres, and the latter considers a mixture of polydisperse, randomly-oriented homogeneous spheroids. A customary assumption in non-spherical microphysical retrieval codes, adopted also by AERONET, is that shape and size have negligible effect on each other, so that particle shape is independently described by a separate aspect ratio distribution. It is worth noticing that by contrast no such restriction is being followed in this work. In fact, it appears that there is a connection of aspect ratio distributions with particle size, as it was found during the SAMUM campaign, see [75, 84].

3.4 Technical aspects of the generalized model: Getting ready for the inversion

More often than not particle orientation is unknown and at the same time, as demonstrated in Ch. 2, we can benefit in terms of formulas' relative simplicity by considering averages over particle orientation. The presented theory for randomly oriented non-spherical particles (here spheroids) is our basis for the scattering cross sections calculations in Eq. 3.3.1. Replacing the latter with dimensionless efficiencies $Q_{\alpha/\beta}$ and the number- with volume distribution we can reformulate the generalized model Eq. 3.3.1 to the one we used in practice for our application

$$\mathscr{Z}(\lambda) = \int_{\eta_{\min}}^{\eta_{\max}} \int_{r_{\min}}^{r_{\max}} \frac{3A}{16\pi r^3} Q_{\alpha/\beta}(r,\lambda,\eta;m)\, v(r,\eta) \mathrm{d}r \mathrm{d}\eta, \tag{3.4.1}$$

where A is the particle surface area. Here we used the fact that in a convex particle ensemble the average area per particle is equal to $A/4$, see [142]. The formula 3.4.1 was also derived by [18, 112]. A noteworthy technicality is that when actually solving this equation, the backscatter coefficients, measured in $\mathrm{m}^{-1}\mathrm{sr}^{-1}$, have to be scaled by a factor of 4π (the solid angle of an entire sphere) in order to be compatible (have the same units) with the extinction extinction (m^{-1}), see Table 3.1.

As seen in Sec. 3.3 the primary objective of our microphysical retrieval is the shape-size distribution. After its determination we get to know the rest of the parameters, and therefore we will focus on the retrieval efficiency regarding this decisive function. The first stage in trying to solve Eq. 3.4.1 is, of course, a discretization, which is done here with projection by *quasi-2D collocation* as proposed in Sec. 1.4.2. Formally discretizing the model equation is one thing, but there are two other important practical implications here: (i) the determination of the refractive index (m) and (ii) the calculations of the kernel functions (efficiencies).

The refractive index is actually unknown too, and looking even at the sphere-related formulas, one realizes that it introduces a highly non-linear quest. In order to bypass this difficulty, we will redefine the problem upon a predetermined RI grid (RIG) of viable choices and then solve it for all the combinations of real parts and imaginary parts of RI. This is especially important when dealing with measurement

data, where a non-automatized delicate job is required, as shown in [131], employing sensitivity analyses and imposing physical constraints (if known), which will confine the solution space in an irredeemable way. This is restrictive in a way and might seemingly underestimate the involvement of the RI, but at the same time it empowers the RI as a physical property giving us the chance to clasify the solutions through a (user-specified) post-inversion minimization process. This is a central concept used in our algorithms which are yet to be introduced in Sec. 3.6. The clusters formed by the most-probable solution candidates, see [131] will also become a measure of the efficiency of the algorithm in use. Obviously, a finer resolution of a sensibly chosen RIG, has a bigger chance of revealing patterns and helping us discard numerical artifacts or physically unacceptable (while mathematically probable) solutions. Unfortunately a grid refinement in the case of spheroids is out of our league in the present work, since a fixed grid is part of the limitations of our approach. Furthermore, the common assumption of a wavelength-independent refractive index is followed here, see e.g. [16, 86, 114]. While there are some relevant investigations in literature suggesting the opposite, especially for the imaginary part of the refractive index being a function of wavelength in dust-like particles, e.g. one of the earliest being [120] and the latest [112, 144], we can accept this oversimplification by considering the RI output as a spectral average. Moreover, it appears that the wavelength-dependence has greater effects in very large particles over $> 15\,\mu m$, which is by far larger than our largest-particle considerations within this work. More advanced alternatives, which still avoid spectral dependence, would require further experimental knowledge, e.g. [143] use the ratio $\mathfrak{Im}\,[\mathrm{RI}(355\,\mathrm{nm})]\,/\,\mathfrak{Im}\,[\mathrm{RI}(532\,\mathrm{nm})]$ from in situ measurements, which enables its own limitations.

The most time-consuming part of solving the model equation is the discretization due to the unprecedented computational expense of the kernel-function calculations. The upgrade from spherical to spheroidal shape raises stability- and convergence uncertainties of these quantities to an unpractical point for an additional unstable process (microphysical inversion) to take place. In addition, since there are no global settings for the truncation parameters of the series in the T-matrix formulas, a high level of technical experience is required in order to expedite the process within reason. Instead, a precalculated database will be used, created by the software tool Mieschka, see [125]. Counting over 12 years of existence and development, Miescka software is able to perform scattering-related T-matrix calculations for spherical particles and rotationally symmetric non-spherical particles with a convergence strategy based on [9, 154]. Additionally, it provides an extensive database of scattering quantities for spheroidal geometries, currently also available through an interactive platform of the German Aerospace Center (DLR). Mieschka's look-up tables include scattering efficiencies for a 6×7 ($\mathfrak{Re}(m) \times \mathfrak{Im}(m)$) refractive index grid (a total of 42 RI values), 7 different aspect ratios and a size parameter range $[0.02, 40]$ with a resolution of 0.2. While the maximum size parameter is reasonably large for other applications, its potential cannot be fully exploited here in terms of the radius extent (all working formulas are with respect to r), since the lidar wavelength at 355 nm restricts the maximum radius ($r_{\max}$) to 2.26 µm. We used in our calculations $r_{\max} = 1.2$ and 2.2 µm, see Table. 3.2 for a parameter synopsis. The resolution gap in the aspect ratio needed for the integrations is handled by interpolation to the nearest neighbor; other interpolation techniques, e.g. cubic interpolation, show only tenuous differences in the discretization outputs.

A single inversion (one dataset) of Eq. 3.4.1 requires solving for every refractive index within a predefined grid that suits the problem. Every refractive index is injected in the scattering efficiency function and subsequently the model equation is discretized. Although the calculation of the efficiencies for a specific refractive index, size parameter and aspect ratio is already handled by the look-up tables of Mieschka software, we are still left with the interpolation of these functions and double integration of the discretization procedure, see Sec. 1.4.2. Even for the relatively coarse grid, shown in Table 3.2, it not only very time consuming, but also extremely wasteful to recalculate the very same matrices for another dataset. For reference, it takes about 32 minutes for a normal workstation PC to fulfil a discretization with a 6×7 grid, an 8-point dataset, 9 spline points for the radius, 7 spline points for the aspect ratio, and a spline degree equal to 3 (for both). For this reason another database was created, this time including the discretization matrices with number of spline points from 3 up to 20 combined with spline degree from 2 up to 6. The spline points for the aspect ratio are fixed to 7, the actual number of different aspect ratio values (Table 3.2). This large collection is overqualified for the needs of the present work, covering lots of different discretization dimensions. The integrations involved a two-dimensional Gaussian quadrature integration scheme with a relative tolerance 10^{-3}.

The potential of the LM-model is greatly expanded with the new model (Eq. 3.3.1, 3.4.1) due to the embedded non-sphericity. Not only the shape-size distribution carries wealthier information but we can

Table 3.2: Parameters used from the database of Mieschka software [125]

$\Re\mathfrak{e}(m)$	1.33	1.4	1.5	1.6	1.7	1.8	
$\Im\mathfrak{m}(m)$	0	0.001	0.005	0.01	0.03	0.05	0.1
aspect ratio	0.67	0.77	0.87	1	1.15	1.3	1.5
radius (µm)	0.01		1.2		2.2		
size parameter	0.2		21.2		38.9		
scattering quantities	extinction efficiency		backscatter efficiency $Q_\beta^{\parallel}$		backscatter efficiency $Q_\beta^{\perp}$		single scattering albedo

now also employ depolarization measurements (see Sec. 2.8) including more data points ($\mathscr{L}(\lambda)$). We extend the traditional lidar setup "$3\beta + 2\alpha$" which consists of 3 backscatter coefficients at 355, 532 and 1054 nm and 2 extinction coefficients at 355 and 532 nm, to "$3\beta + 2\alpha + d$", where "d" shall stand for vertically polarized backscatter coefficients ($\beta_\perp$) at 532 nm ($3\beta+2\alpha+1d$), or 355 and 532 nm ($3\beta+2\alpha+2d$), or 355, 532 and 1064 nm ($3\beta + 2\alpha + 3d$). Three depolarization channels are an asset of only the most advanced lidar machines and will be the default setup in our theoretical analysis, although we should note that most of today's depolarization lidars provide $3\beta + 2\alpha + 1d$ optical datasets. The backscatter coefficient (β) in the aforementioned 6-, 7- or 8-point datasets pertains now to the horizontally polarized one ($\beta_\parallel$), which in the case of spheres coincides with the total backscatter coefficient. For brevity we will still use just "β" when there is no risk of confusion.

The calculation of the degree of ill-posedness is not a practically viable choice for the non-spherical case, the way it is done for the spherical case, e.g. in [114, 131]. The Galerkin discretization required by the theory combined with our generalization of the Fredholm equation would require quadruple integral calculations, which is not only time-prohibitive but finally too involved and dubious. On the other hand, it is instructive to analyze the "ill-posedness" of the equations derived by the collocation, which does not directly link to the singular system (see Th. 1.3) of the integral operator but reflects the condition of the linear system which is practically solved. We can still use the discrete form of the Picard condition and also calculate the decay rate of the singular values of the linear system (see Def. 1.1.3) using a non-linear fit. This alternative can sometimes be a more advanced and informative technique than using a static condition number of the matrices, since it enables the use of the noisy dataset and thus allows to involve more physical factors and further to understand better the noise effect. This is advantageous when we study specific retrieval instances and seek an objective way to compare the effect of ill-posedness in them. It should be noted that the ill-posedness at this stage is expected to be milder since the initial equation will have already undergone some sort of regularization from the discretization.

3.5 Spheroidal scattering efficiencies

It is interesting to see how the associated efficiencies $Q_\beta^{\parallel}$, $Q_\beta^{\perp}, Q_\alpha$, and the *backscatter depolarization fraction* $Q_\beta^{\perp}/Q$, where $Q = Q_\beta^{\parallel} + Q_\beta^{\perp}$, respond to the variation of the refractive index and shape. In Fig. 3.6 we restrict to prolate particles with an aspect ratio $\eta = 1.3$ and make multiple plots of scattering efficiencies raising the real- and imaginary part of the RI separately (left and right panels respectively); examples with oblate particles lead to similar results. One can easily infer from all plots that a lower RRI or a larger IRI brings a smoother backscatter- (left panels) or extinction efficiency (right panels). Thus, the refractive index effect is in agreement with what experience with spheres tells us to expect. The smoothing effect, which comes also with a reduction in the efficiency's magnitude is more pronounced in the backscatter- than the extinction efficiencies and is handled differently by the RRI and IRI. The upper pair of plots in Fig. 3.6 shows that an increasing absorption level results in a decrease of local maxima on site, with "silent" changes of the general shape of the graphs. This might eventually lead to a complete suppression of the major oscillations, especially in the case of the backscatter efficiency. On the other hand, a decreasing RRI resembles a wave-like pattern, shifting and spreading simultaneously
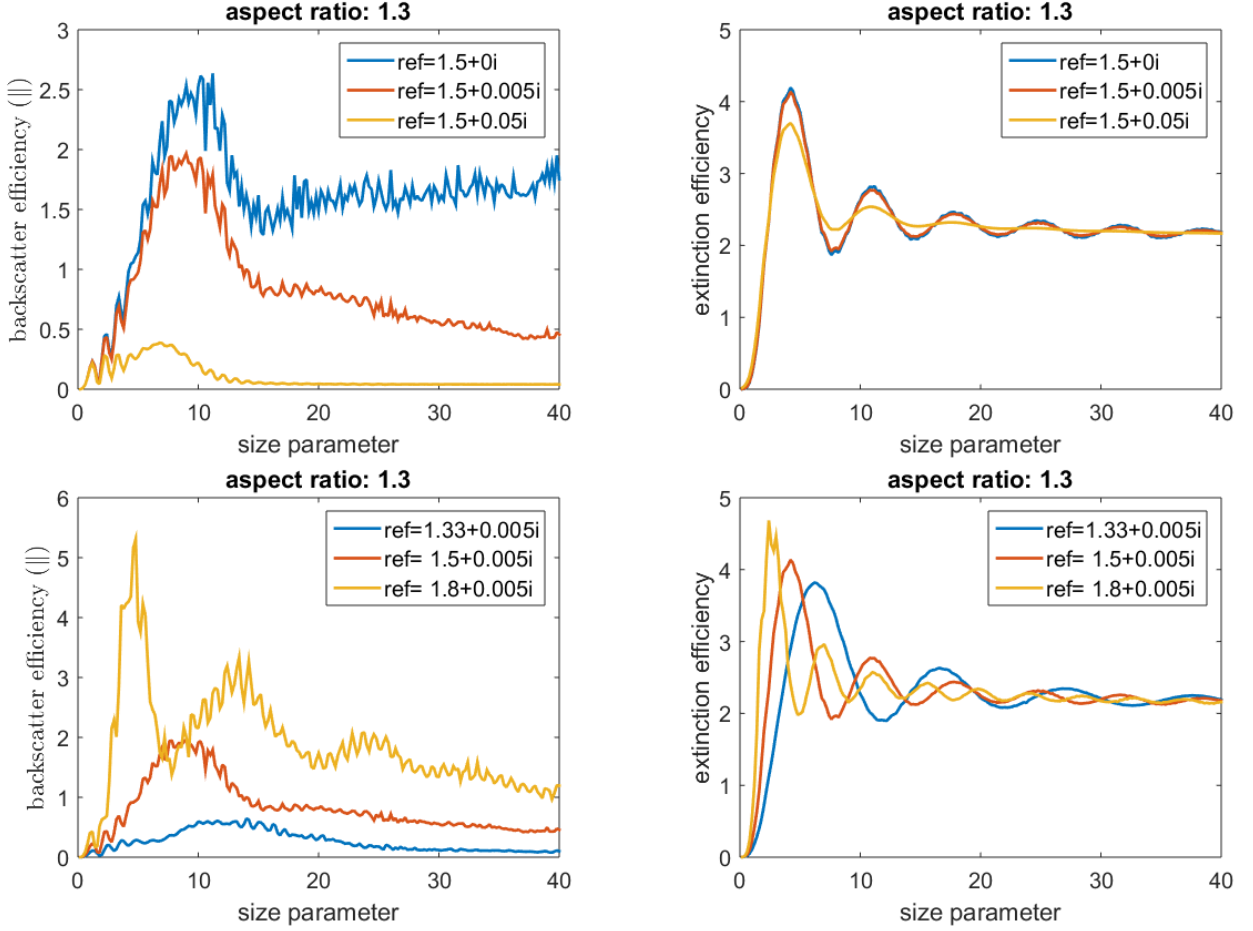
Figure 3.6: Plots of scattering efficiencies for a fixed aspect ratio (1.3) and a variable refractive index. Left panel: backscatter efficiency horizontally polarized ($\parallel$) with fixed $\mathfrak{Re}(m) = 1.5$ (top) and fixed $\mathfrak{Im}(m) = 0.005$ (bottom). Right panel: extinction efficiency with fixed $\mathfrak{Re}(m) = 1.5$ (top) and fixed $\mathfrak{Im}(m) = 0.005$ (bottom).

local maxima (and reducing their peaks), altering distinctly the function shape. Two plots in Fig. 3.7 with the same setting as the lower pair of plots in Fig. 3.6 demonstrate that this is a common behavior also for spheres. Moreover, by comparing Fig. 3.6 and 3.7, we can confirm again, as in the case of phase functions (Sec. 3.2), that spherical scattering efficiencies are in general more oscillatory. In addition, the highest-resonance areas are observed mostly for medium-large shapes (size parameter $0 < x < 20$) and much less for larger shapes. The case of the spherical backscatter efficiency with $m = 1.8 + 0.005i$ in Fig. 3.7 seems to be an exception, but the function actually starts going down for $x > 30$ on average and oscillates close to zero for $x > 150$ (not shown here).

It is quite clear from the previous analysis that shape is itself a smoothing factor too. In order to watch closely the shape involvement we made two-dimensional plots of the scattering efficiencies with respect to size parameter and the aspect ratio, see Fig. 3.8. The fixed refractive index $1.5 + 0.01i$ was chosen as a kind of "central" value from the available refractive index grid in Mieschka's database, see Table 3.2. The backscatter efficiency $(Q_\beta^\parallel)$ suffers greater oscillations in the neighbourhood of $\eta = 1$, but these are conspicuously reduced as we move to pure spheroidal geometries (oblate or prolate), see top left plot of Fig. 3.8. On the other hand, the extinction efficiency (bottom right plot) while generally smooth, it is neutral regarding the aspect ratio, showing a potential inability to give information about shape. Especially for large size parameters Q_α becomes entirely featureless, an effect also visible in $Q_\beta^\parallel$ in lesser degree. Interestingly, the vertically polarized backscatter efficiency, see top right plot in Fig. 3.8, shows more complicated shape-dependence. The capacity of prolate-spheroid depolarization (PSD) seems larger and is more localized for medium-large sizes than oblate-spheroid depolarization (OSD), the

44
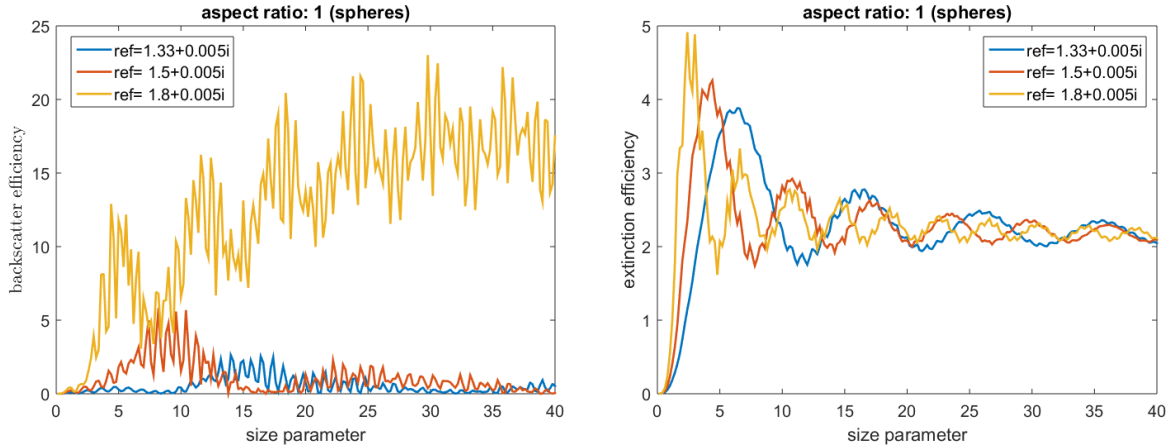
Figure 3.7: Plots of scattering efficiencies for spheres with a fixed $\mathfrak{Re}(m) = 1.5$ and a variable IRI. Left: backscatter efficiency. Right: extinction efficiency.

action field of which appears more spread out with respect to size. Again, a higher or extreme absorption (not shown here) clears plenty of the resonances and has greater effects on OSD, leaving back only minute traces (of OSD). This should not leave the impression of a generally insignificant OSD. Indeed, "mild" cases with small absorption (IRI) and large RRI, e.g. $m = 1.8 + 0.001i$, show a very distinct OSD of equal or slightly larger strength than PSD but located in large sizes (not shown here), but these cases are more rare in our physical scenery. Perhaps it is easier and more representative to watch OSD-PSD differences from the relative perspective of the backscatter depolarization fraction $Q_{\beta}^{\perp}/Q$, see Fig. 3.8, bottom left plot. The latter follows the general behavior of $Q_{\beta}^{\perp}$ and we can see that slightly less than 40% of the total backscatter efficiency is (vertically) depolarized by prolate spheroids for size parameters $x < 10$, which then continue to be dominant for $x < 20$ but with smaller aspect ratios and for larger sizes both oblate and prolate spheroids contribute about 20-30%. In addition, one can actually see the steep discontinuity at $\eta = 1$ (characteristic $\boldsymbol{r}$- or $\boldsymbol{v}$-shaped surface in Fig. 3.8 bottom left plot), demonstrating by contrast the wealth of information one gets by taking into account (non-spherical) particle depolarization.

The smoother the backscatter- and extinction efficiencies the more problematic the retrieval might be, especially for very noisy data, since errors will be magnified during the inversion process, see Ch. 1, Remark 2. Therefore, cases where there is hint of high absorption, or low RRI should be handled with extra caution by non-purely data-driven regularization.

3.6 Retrieval algorithms

After discretizing the model Eq. 3.4.1 we solve the resulting linear system with regularization, which is the first big step to counteract the ill-posedness of this inverse problem. Having usually no further information about the data error, makes it difficult to choose an optimal regularization parameter which will guarantee physical adequacy. This weakness can be dealt by imposing several mathematical constraints and producing extended solution spaces. Ordering then the solutions with respect to refractive index (as a physical constraint) based on forward-error calculations, gives the chance to watch closely their variability and the clusters they potentially form. Therefore in the case of simulations, rerunning the model in the forward direction, we can use the vicinity to the initial dataset as a guide (through minimization) to decide for the quality of a solution. The latter will be an average from a candidate solution cluster which passes the error-criteria. This way we are able to test a particular regularization technique with respect to its accuracy and the ability to form "good" solution clusters. By experimenting further with several random distributions of a specific error level imposed in the dataset, and subsequently for different error levels, we can test the stability and become accordingly confident about the method used.

The latter approach is particularly useful for another important reason too. Prior to the regularization, the problem has to be projected in a space of finite dimension, to be able to be solved in the first place. Finding a suitable dimension is the key as shown in [131] and it is often problematic to pick one dimension as a global setting to handle datasets which correspond to very different atmospheric scenar-
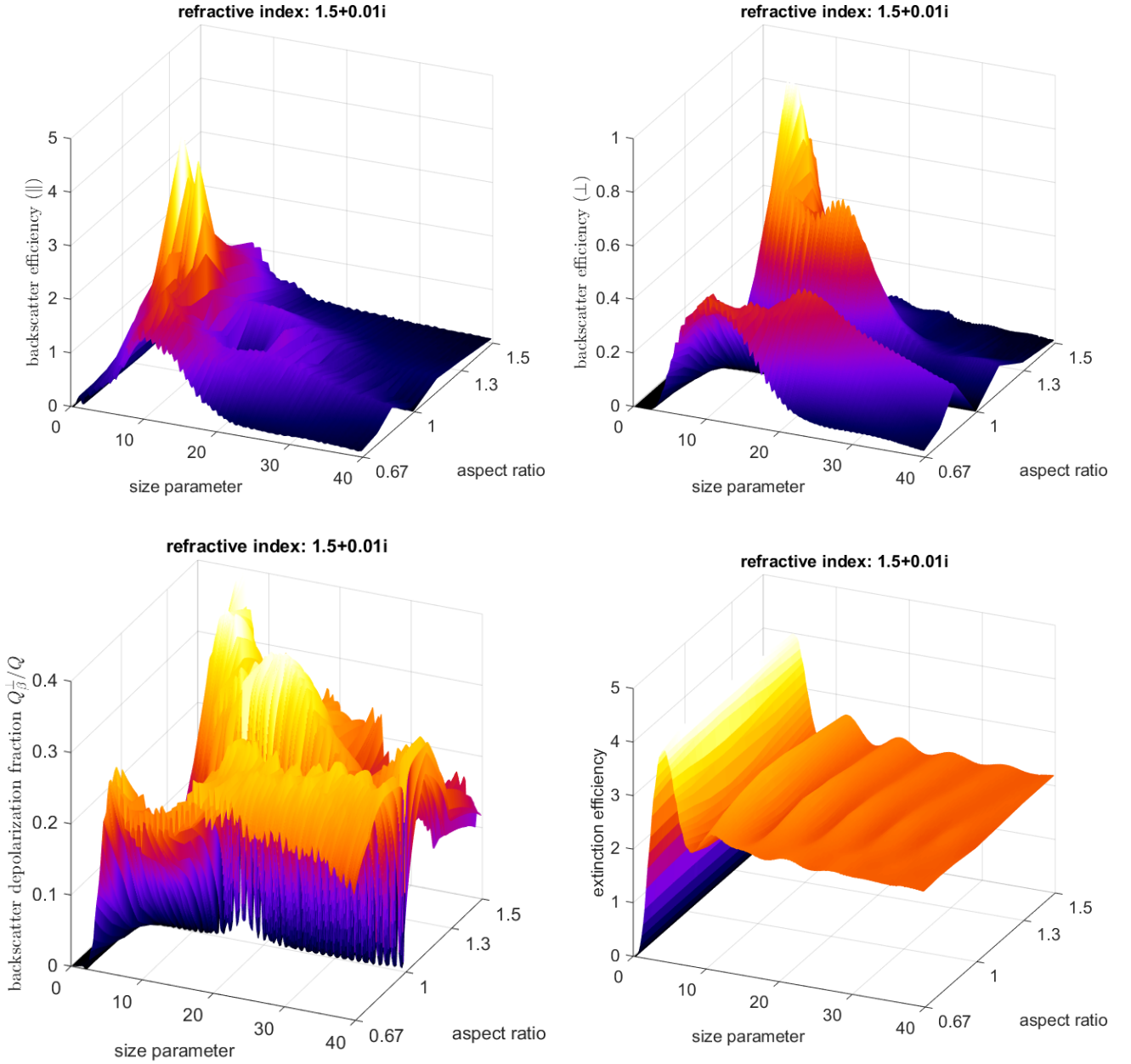
Figure 3.8: 2D-Plots of scattering efficiencies with respect to the size parameter and the aspect ratio for a fixed refractive index 1.5+0.01i. Upper panel, left: backscatter efficiency horizontally polarized ($\parallel$). Upper panel, right: backscatter efficiency vertically polarized ($\perp$). Lower panel, left: backscatter efficiency fraction ($Q_{\vec{\beta}}^{\perp}/Q$). Lower panel, right: extinction efficiency.

ios. Therefore, the mathematical constraint we will use in this work are the spline features (number of spline points and spline degree) which are associated with the dimension of the produced linear system. Previous work done with real-life data in [14, 114, 115, 131] in parallel with several early simulations for this work, showed the benefit of such *hybrid algorithms*, the concept of which is the leading approach of the present work as well.

We often encounter a situation where the actual solution coefficients are zero (or nearly zero), but might, nevertheless, turn to negative values due the noise presence (e.g. measurement errors). This is apparently an undesired eventuality from physical point of view, which we prevent by setting all strictly negative coefficients to zero. This decision is a result of early numerical experiments for this work

leading to a superior algorithm performance. Especially for Padé iteration, we apply the non-negativity constraint to the solution in each iteration.

We summarize the two basic algorithms which we will use for throughout this work, depending on whether we know or not the refractive index as follows. The reader is reminded that the primary unknowns of the resulting linear systems are the spline coefficients of the shape-size distribution (and not the function itself) with respect to the specified projection space.

Solution algorithm 1 (SA1) with a fixed refractive index:

1. Specify the range of the number of spline points and the range of spline degrees.

2. Discretize for every number of spline points, every spline degree and the fixed refractive index. (Use of database of precalculated discretization matrices (T))

3. Choose a regularization method and a parameter choice rule to solve the linear systems for a given (error-) dataset (g) applying the non-negativity constraint.

4. For all sets of solution coefficients v, make the forward calculation $\tilde{g} = Tv$ and estimate the residual error $\|\tilde{g} - g\|$.

5. Calculate the solutions (shape-size distributions) with respect to the corresponding projection spaces.

6. Calculate the mean solution out of a few least-residual solutions.

Solution algorithm 2 (SA2) with unknown refractive index:

1. Specify the refractive index grid.

2. Specify the range of the number of spline points (s) and the range of spline degrees (d).

3. Discretize for every number of spline points, every spline degree and every refractive index. (Use of database of precalculated discretization matrices (T))

4. Choose a regularization method and a parameter choice rule, fix a projected dimension $n = s+d-1$ and solve the linear systems for every refractive index and a given (error-) dataset (g) applying the non-negativity constraint.

5. For all sets of solution coefficients v, make a forward calculation $\tilde{g} = Tv$ and estimate the residual error $\|\tilde{g} - g\|$.

6. Pick the refractive index with the least residual.

7. Repeat 4 (with the same method) and 5 until all the combinations $s \times d$ are exhausted.

8. Calculate the solutions (shape-size distributions) with respect to the corresponding projection spaces.

9. Calculate the mean solution out of a few least-residual solutions.

The most complete of the two algorithms is obviously SA2, which also predicts the refractive index in addition to the shape-size distribution. In the trivial case where the grid in SA2 is inhabited by only one refractive index, the minimization with respect to the refractive index is redundant and SA2 and SA1 coincide. It is essential to realize that the last step (9) in SA2 considers solutions which are (possibly) different not only with respect to the spline-point number and degree (as in SA1, 6) but also with respect to the refractive index.

The regularization methods and the parameter choice rules that both algorithms require to use, are chosen among the following ones.

(i) Truncated singular value decomposition with the discrepancy principle (TSVD-DP),

(ii) Tikhonov regularization with the L-curve method (Tikh-LC),

(iii) Padé iteration with the discrepancy principle (Pade-DP),

(iv) Tikhonov regularization with the generalized cross validation method (Tikh-GCV),

(v) Tikhonov regularization with the discrepancy principle (Tikh-DP), and

(vi) Padé iteration with the L-curve (Pade-LC).

The methods in i, ii, iv and v are well studied regularization methods and parameter choice rules which have been widely used with the Lorenz-Mie model, e.g. [14, 107] and it is interesting to see their efficiency for the new non-spherical model as well. Similarly we investigate the lesser known Padé iteration as a regularization method, first used in the lidar-data inversion by [16], here combined with the discrepancy principle (v), and for the first time with L-curve method (vi). The parameter choice rules are also common in bibliography and while they operate very differently, the primary reason of their use here is the presence (DP) or lack of a-priori error knowledge (LC, GCV).

TSVD-DP (i) is implemented using the theory directly from 1.2.1 and 1.3.1. We start by including all the terms in the SVD-description of the solution (see also Eq. 1.2.8) and remove them one by one till the discrepancy principle is fulfilled or we arrive at a single term. Apparently, the assumed discrepancy (perhaps multiplied by a safety factor) cannot be smaller than the residual error with all the SVD-terms included. In other words, we cannot demand a better approximation than the best we have.

The Padé approximants (see Eq. 1.2.24) for Padé iteration (iii, vi), were calculated using a routine implemented by [80] which was integrated in the code. Pade-DP is implemented simply by fixing a maximum number of iterations (MNI) and checking if the assumed discrepancy is interposed between the corresponding residual terms of two successive iterations, see also 1.3.1. The iteration is stopped either by the satisfaction of the DP or by reaching the MNI. For Pade-LC (vi) we use a discrete implementation of L-curve with respect to the number of iterations the following way.

- Fix a maximum number of iterations (m) and run Padé iteration for each number $1, \ldots, m$. (m independent times in total)

- Store the residual error $\|\tilde{g} - g\|^2$ and the regularity term $\|v\|^2$ for each number of iterations.

- Build the L-curve with cubic spline interpolation from the points $(\|\tilde{g} - g\|^2, \|v\|^2)$.

- Locate the point of maximum curvature of the L-curve $m^\star$.

- Take as the solution the output of Padé iteration with $m^\star$ iterations.

For Tikh-LC (ii), Tikh-GCV (iv) and Tikh-DP (v) we used modified versions of routines used in the software package *Regularization Tools* by P. C. Hansen [57].

3.7 The method Padé-L-curve

Before proceeding to the simulations of the next chapter involving all the methods discussed, we will demonstrate that Pade-LC does indeed produce regularized solutions practically out of the context of the algorithms SA1 and SA2. For this purpose we conducted the following preliminary synthetic retrievals for a variety of test problems and finally for the microphysical retrieval problem in the spherical setup $3\beta + 2\alpha$. For all inversions we use the (2,1)-Padé iteration (see 1.2.24 for the notation) with a maximum number of 100 iterations and the relaxation parameter set to 100. These values resulted from experience with earlier simulations and they are also in accordance with findings in [112, 113]. The discretization dimension is fixed to 11, considering 9 spline points and 3rd-degree splines. The initial- and retrieved size distributions were derived using a 200-point resolution. The spherical kernel functions were calculated through a Matlab implementation of Bohren and Huffman code [20].

The first examples involve the test-ill-posed problems "shaw", "phillips", "gravity" and "deriv2" from Regularization Tools in [57]. Especially for the very ill-posed problem of gravity surveying ("gravity"), two different exact solutions ("2" and "3" from [57]) are used which we will denote "gravity2" and "gravity3", see 3rd and 4th plot on Fig. 3.9 left. For each of these problems we consider 15 dataset-instances with 10% input data error, which are subsequently inverted. The solutions are finally averaged to get a single one (mean), for which we calculate the standard deviation to use it as an errorbar. The left column of subplots in Fig. 3.9 shows the results of these inversions and the right column contains individual (not mean) L-curve plots corresponding to a random but representative dataset from the test

problem on its left. Additionally a circle marks the corner obtained by the L-curve algorithm as well as the number of iterations as the regularization parameter corresponding to it, which is also given for different parts of the L-curve. Each subplot in the left column shows also the exact solution of the corresponding test problem. The discretization dimension used for all the test problems was 60. Note that the non-negativity constraint was not applied for these examples since the problems pertain to different physical quantities which are not analyzed here.

A general observation from Fig. 3.9 is that Pade-LC manages to reconstruct the exact solutions with very good precision almost in every case, despite the relatively high error level. The most problematic cases are gravity3 (4th plot, left column) where Pade-LC follows the general trend of the exact solution but less accurately, and deriv2 (5th plot, left column), where we see a larger variation of the solutions compared to the other test problems. Retrievals with 1% and 5% were performed in the same manner as well (not shown here) revealing the same efficiency and even smaller (in some cases indistinguishable) errorbars. The L-curve corners are correctly identified in a general sense and the iteration number does not exceed 5, which is common for high error levels, as prior experience showed. In case of 5% errors the algorithm reaches up to 15 iterations and for 1% errors we usually get more than 40. Obviously, the lack of knowledge of the true error level is an important obstacle for a retrieval with real-life (non-synthetic) data, but it is hypothetically avertable with a data-driven method like Pade-LC. Therefore the ill-posedness is a more relevant issue, as we will see next in the problem of microphysics. The whole numerical experiment was also repeated using Tikh-LC, but the outcome was almost identical to Pade-LC, resulting in equivalence between them.

Now let us investigate briefly the efficiency of Pade-LC in the microphysical retrieval problem, but for spherical particles, a case that is relatively easier than the non-spherical one, but still much harder compared to the test problems presented before. The focus of the simulations here is the reconstruction of the size distribution. We experiment with different atmospheric scenarios artificially produced with the log-normal-distribution parameters and refractive indices shown in Table 3.3. Through these parameters we create datasets with input white noise 1%, 5% and 10% and repeat the experiment 15 times with different random distribution for each error level. In addition to Pade-LC, we solve also with Pade-DP for comparison and present the results for the cases 1-5 in Fig. 3.10 and B.1. The title of each plot shows also the mean reconstruction error and the median of the iteration numbers found in the (15) individual retrievals.

First let us focus on the cases No 1-3 (Fig. 3.10) which involve monomodal log-normal distributions. The uppermost set of plots (case No 1) pertains to particles of small median radius (0.1), which are handled better by Pade-LC for small input error. This is achieved by choosing a much less conservative iteration (9) number than Pade-DP (100) which is responsible for the large second-mode artifact in the rightmost part of the plot Pade-DP, 1%. Pade-LC has also better response for larger errors (5%) while even higher error levels result in large discrepancies from the exact solution for both methods. The performance of Pade-LC is decent, but not perfect despite the relatively moderate absorption level ($1.4 + 0.005i$), revealing a potential weakness for very small particles. For case No 2 with larger and more absorbing particles ($1.5 + 0.01i$) we get a kind of the same pattern but both methods operate a lot better managing to lower the reconstruction errors, especially for higher data errors. Pade-LC continues to have milder artifacts than Pade-DP, obviously due to a better control of the iteration number. The last monomodal-distribution case (3) pertaining to very absorbing particles ($1.7 + 0.05i$) is the most successful for these methods. Indeed both of them deliver a equivalently precise reconstruction, with Pade-DP being only marginally better for the case of 10% data-error. Moreover, compared to the cases 1 and 3, we see here the lowest reconstruction errors with respect to any error level. However, we should note that smaller scale experiments (not included here) showed that for the particular size distribution but higher absorption and/or smaller real part of the refractive index (i.e. theoretically more ill-posed cases), Pade-DP appears superior mainly for low data errors.

The next part of numerical experiments involves the much harder task of reconstructing bimodal size distributions. The plots are shown in App. B, Fig. B.1. Case No 4 involves a large coarse mode and a more silent fine mode, and the results are really remarkable even in the case for 10% errors. The general pattern of the exact bimodal distribution is achieved by both methods, while the coarse mode of the Pade-DP solutions for larger errors is under higher oscillatory behavior. On the contrary, the last set of plots in Fig. B.1 related to case No 5 depict a much bigger fine mode relative to the coarse mode. The methods are struggling more here to retrieve especially the coarse mode, with Pade-LC prevailing overall also in this example. Despite the evident noise for 5 or 10% data error, Pade-LC's solutions are
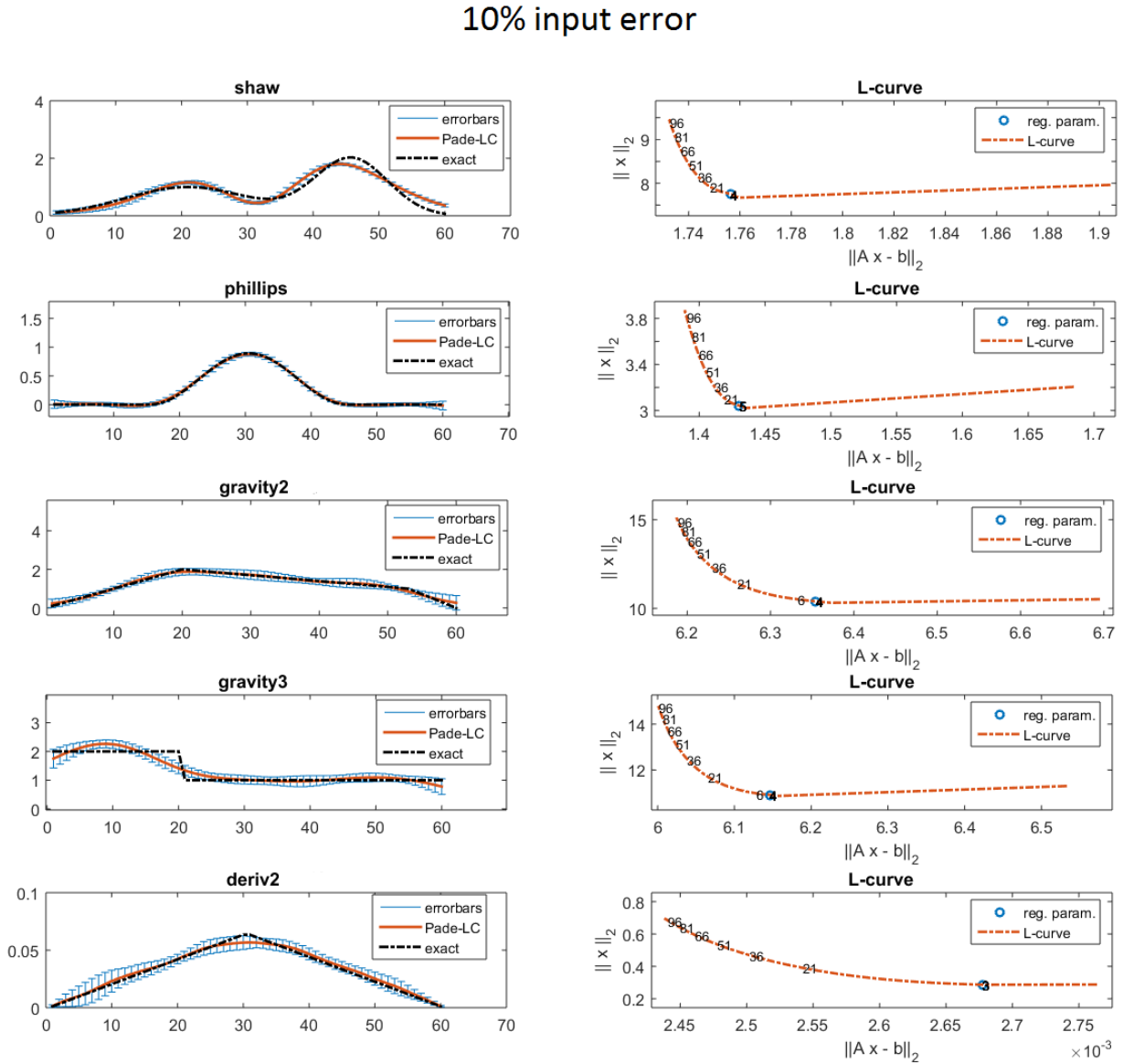
Figure 3.9: The test problems "shaw", "phillips", "gravity" and "deriv2" (top down) from [57] solved 15 times for 10% data error with Pade-LC. Each subplot on the left shows the exact solution (dash-dot line) and the mean solution (red line) with respect to the discretization index (x-axis), and the errobars (blue) obtained by the standard deviation of the solutions. The right column of subplots contains L-curve plots in log-log scale in which we have marked with a circle the located corner as well as the regularization parameter (number of iterations) corresponding to it. The latter plots are random but representative individual instances corresponding to the test problem on their left.

still decent getting right the most part of the initial distribution.

Summarizing the results, we could conclude that Pade-LC provides in practice regularized solutions to a variety of problems. Regarding the microphysical retrieval problem, it further works generally better than Pade-DP in size distribution reconstructions and since both methods share the same regularization standpoint (Padé iteration) and the same parameter configuration, the parameter choice rule (L-curve) makes all the difference. Indeed we observe large differences in the median of iterations between LC- and DP-solutions in the vast majority of the cases No 1-5, see e.g. case No 1, 2 and 5 with 1% errors. This result is not taken for granted later on for the non-spherical case where these methods are re-tested in
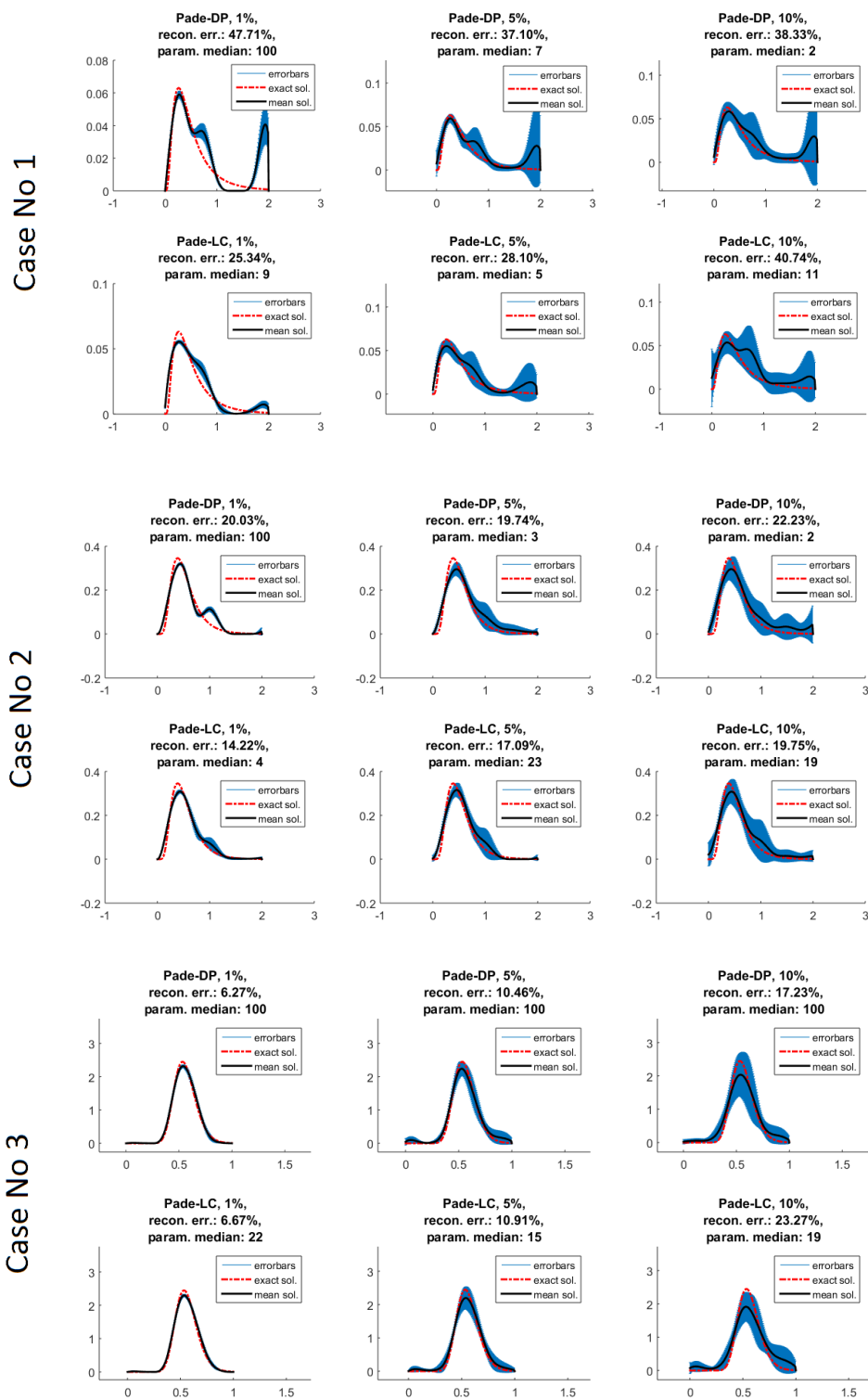
Figure 3.10: Reconstructions of monomodal size distributions. Every set of (6) plots corresponds to Pade-DP solutions (top) and Pade-LC solutions (bottom) and to a specific case (1, 2, 3) from Table 3.3, designated on the left side of the set. The title in each plot shows additionally the input error level, the mean reconstruction error and the median of the iteration numbers (param.) used by the (15) individual retrievals.

Table 3.3: Simulation parameters for preliminary tests for spherical particles

Case No	radius interval	median radius	mode width	number concentration	refractive index
1	$[0.001, 2]$	0.1	2	1	$1.4 + 0.005i$
2	$[0.001, 2]$	0.25	1.6	1	$1.5 + 0.01i$
3	$[0.001, 1]$	0.5	1.2	1	$1.7 + 0.05i$
4	$[0.001, 2]$	$[0.1, 0.7]$	$[1.6, 1.3]$	$[20, 1]$	$1.5 + 0.01i$
5	$[0.001, 1]$	$[0.1, 1]$	$[1.6, 1.3]$	$[400, 1]$	$1.5 + 0.01i$

a much larger scale and since the purpose of the examples here was mainly to demonstrate Pade-LC's reasonable regularization behavior. It should be finally noted that the extent of the radius range ($r_{\max}$) plays an important role to the retrievals as well, as it was underlined in [131]. In fact, a reconstruction can be very vulnerable to either oversee a mode (mainly coarse) or create artifacts where the distribution is essentially zero. This behavior is hinted e.g. in case No 1 or 5, Pade-DP 1% where an additional mode is being built and then steeply forced to zero. However, the full potential of these methods was dormant since we had a fixed discretization dimension which could ideally handle better these difficulties.

Regarding the computational time, Pade-LC has a clear downside as compared to the other methods we are going to use here. In order for Pade-LC to build the L-curve, it runs the iteration the same amount of times as the fixed number of iteration (here: 100). This is of no concern for "every-day" microphysical retrievals but it can be a real issue for massive synthetic retrievals and especially in conjunction with algorithm SA2. It should be noted that the main reason for the proposal of this method is the great potential in marrying a powerful iterative regularization method (successfully tested e.g. in [18, 82, 113]) with a parameter choice rule which does not presuppose error knowledge.

Chapter 4

Synthetic microphysical retrievals for non-spherical particles

Foreword

At this point we are equipped with all available tools to test the efficiency of our methods and algorithms. In the following sections we perform numerical experiments with artificial data simulating several atmospheric scenarios. These retrievals will give valuable feedback which will be used subsequently for real-life data directly from lidar measurements in Ch. 5. Here, we are interested in answering theoretical questions about retrieval behaviors and patterns which will help us differentiate the suitability of the methods used under certain circumstances. A crucial discussion, missing almost entirely to our knowledge from this research field in a systematic way, is a minimum first stage evaluation of inversion algorithms by means of different types of uncertainties regarding the retrieval accuracy, the variability of a solution space and the confidence level of getting similar results when we repeat an experiment for random error instances. These issues are addressed here, providing analyses in statistical terms for the competing methods and more importantly a general framework under which we can test the efficiency of any projection-type regularization method. Moreover, a more palpable aspect of our synthetic-data retrievals is the investigation under the same methodology of the theoretical efficiency of current and potential future lidar technology in terms of additional channels. A tremendous computational relief for Ch. 4 and 5 was the use of the software tool *SphInX* (Spheroidal Inversion eXperiments), a graphical-user-interface program designed by the author exclusively for this purpose. A detailed guide of the current version can be found in App. D. In the simulations that follow, the data are analyzed using tables and figures extensively. Only a relatively small portion of the latter is given within this chapter and the rest of it is shown in App. B and C. Our investigations, analyses, and results were realized with a Windows 10 workstation PC of 16 GB RAM and a 2.40 GHz quad-core processor.

4.1   General configuration with a fixed refractive index

Preliminary numerical experiments were conducted with synthetic two-dimensional distributions with small input errors using the methods i-vi in conjunction with the algorithm SA1 (Sec. 3.6), i.e. considering a fixed refractive index. These tests indicated that all methods are almost equally successful in reproducing the conventional microphysical parameters, number concentration, surface-area concentration, volume concentration and the effective radius (a-d) for relatively small particles with effective radius $0.05 < r_{\text{eff}} < 0.20$ (µm) and oblate, prolate, or mixed sphere-spheroid particle ensembles. This method "equivalence" was actually even more deceiving when we pushed the input error to higher levels or vary the refractive index to create stronger or weaker ill-posedness, driven by the expected effect we meet in the spherical-particle case. As we kept changing the physical picture, i.e. enabling various combinations of size, shape, refraction and data error, certain behaviors and assets of methods individually became more apparent, but the landscape became more fuzzy as to which method could generally have a leading role as a total.

4.1. General configuration with a fixed refractive index (Synthetic microphysical retrievals for non-spherical particles)

It is very helpful to know which method suits specific atmospheric scenarios when additional information is available, but it is often the case that we have a poor idea of what is going on in the atmosphere, and thus an overall well-functioning method offers more flexibility. The motivation of this section is to treat these aspects through a comparison over multiple atmospheric cases which constitute the general configuration of our simulations. For this we will study the efficiency of a method in accuracy and stability as a total rather than examining single-parameter retrievals. In this sense, the initial task will be a blind comparison of the methods which will lead to a better understanding of both the two-dimensional microphysical problem and the methods' operation.

Here we will use the solution algorithm 1 (SA1, Sec. 3.6) and thus assume exact knowledge of the refractive index. The more complicated endeavor of seeking also the refractive index will take place in the next section (4.2), when we will have narrowed down the method candidates based on these section's massive retrievals. The data for the simulation are generated by defining a volume shape-size distribution and then running the model Eq. 3.4.1 in the forward direction to produce a dataset. Details for every parameter for the simulation configuration and inversion, which we will discuss subsequently, are provided in Table 4.1. Parameters below the labels "Distribution data generated with", "Optical data gererated with" and "Optical data inverted with" are combined with each other to perform the corresponding action.

We will consider 8-point synthetic datasets, i.e. $3\beta + 2\alpha + 3d$ (see Sec. 3.4) associated with optical products of the most advanced polarization lidars in the present time. The shape-size distribution $v(r, \eta)$ is formed by multiplying a log-normal distribution $v(r)$ with an aspect ratio distribution $a(\eta)$

$$v(r, \eta) = v(r)a(\eta). \tag{4.1.1}$$

The aspect ratio distribution $a(\eta)$ is given by the simple model

$$a(\eta) = \begin{cases} p_1, & \text{if } \eta = \eta_1, \\ p_2, & \text{if } \eta = \eta_2, \\ \vdots & \vdots & \vdots \\ p_\nu, & \text{if } \eta = \eta_\nu, \end{cases} \tag{4.1.2}$$

where $0 \leq p_j \leq 1$, $j = 1, 2, \ldots, \nu$ and $p_1 + p_2 + \ldots + p_\nu = 1$. The selected aspect ratio distributions cover the three most interesting cases: (i) oblate ensembles, (ii) sphere-spheroid mixtures and prolate ensembles, see Table 4.1 for the specific used values. The associated case-aspect ratios $(\eta_j, j = 1, 2, \ldots, \nu)$ are selected from the exact available ones in Mieschka's database, see Table 3.2. The intervals, either for the distributions or for the integration are $[0.01, 1.2]$ or $[0.01, 2.2]$ for the radius and $[0.67, 1.5]$ for the aspect ratio. Fig. 4.1 shows some examples of shape-size distributions from Table 4.1.

The combination of the (four) log-normal distributions with the (three) aspect ratio distributions from Table 4.1 yield an effective-radius range of 0.26 to 0.95 µm, calculated using Eq. 3.1.8, 3.3.3 and 3.3.4. The aforementioned sizes cover many interesting cases of aerosol particles and fall within the range of fine and medium-coarse dust-like particles but do not span, of course, the whole physically occurring range.

For the discretization of the model Eq. 3.4.1, the refractive index and the projected dimension (splines) are necessary. The fixed refractive index for the scattering efficiencies takes the values $1.33 + 0.001i, 1.4 + 0.005i, 1.5 + 0.01i, 1.6 + 0.001i$ and $1.7 + 0.05i$ (one at a time). The number of spline points and spline degrees take over values from the ranges 6 up to 14 and 2 up to 5 respectively, resulting in projection dimensions from 7 up to 18. The lowest dimension (7) used here was found also in [131] to be marginally sufficient, while a larger dimension than 18 might result in a systematic behavior in the retrieval because the linear systems end up highly underdetermined. We should note that the spline-ranges are not absolute in the general sense especially for measurement cases, meaning that a preliminary sensitivity analysis is advised in order to avoid undesired systematic behaviors.

Once the optical dataset is created with a forward run of Eq. 3.4.1, we add to it gaussian white noise, with relative error levels 1%, 5% and 10%. Every dataset is randomly generated 15 times for the same error level. Finally, the produced linear systems are solved with the following (3) regularization methods and (3) parameter choice rules:

1. Truncated singular value decomposition with the discrepancy principle (TSVD-DP),

4.1. General configuration with a fixed refractive index (Synthetic microphysical retrievals for non-spherical particles)
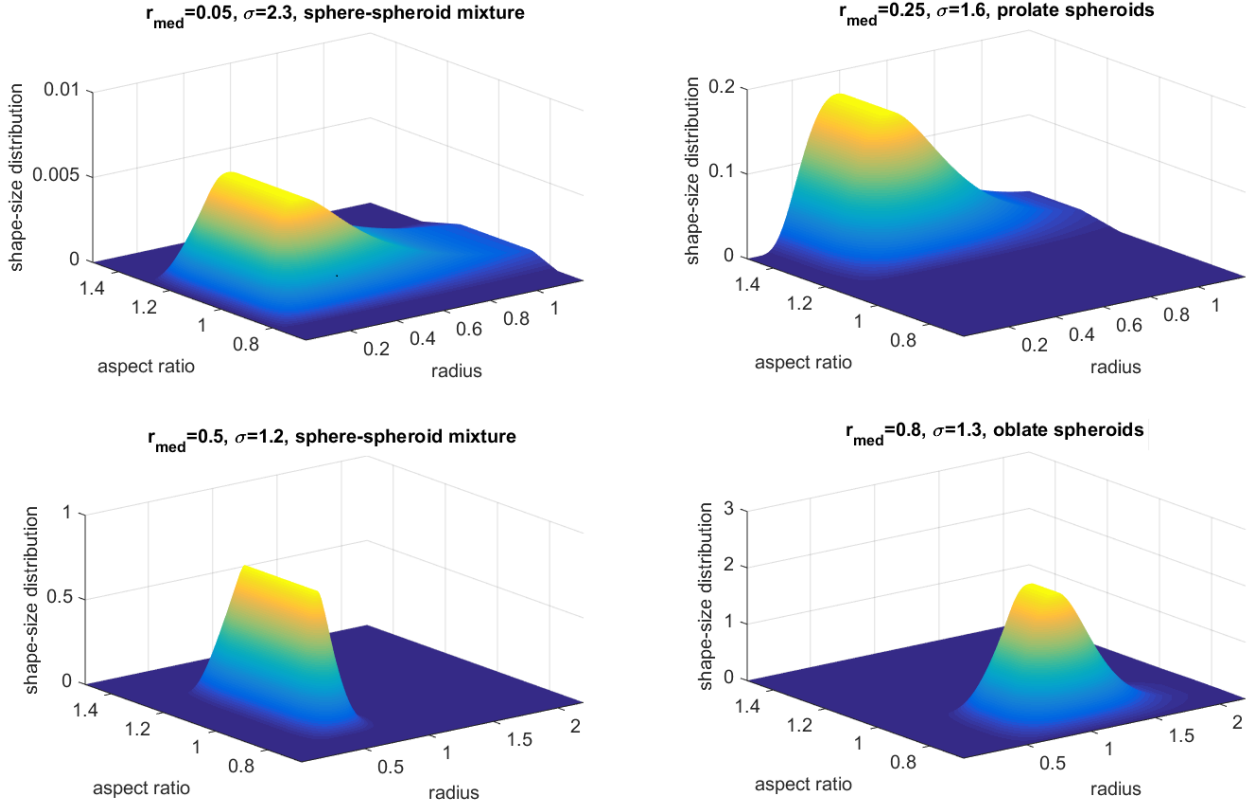
Figure 4.1: 2D-Plots of synthetic shape-size distributions produced by combinations of log-normal distributions and aspect ratio distributions from Table 4.1, see the corresponding title above each plot.

2. Tikhonov regularization with the L-curve method (Tikh-LC),

3. Padé iteration with the discrepancy principle (Pade-DP),

4. Tikhonov regularization with the generalized cross validation method (Tikh-GCV),

5. Tikhonov regularization with the discrepancy principle (Tikh-DP), and

6. Padé iteration with the L-curve (Pade-LC).

The discrepancy (δ) for TSVD-DP, Pade-DP and Tikh-DP is automatically computed for a simulation from the known error level (ϵ) by $\delta = \epsilon \|g\|$, where g is the error-free dataset, and the safety factor is set to be unit. The (m, n)-Padé iteration scheme used here is $(2, 1)$, which was found suitable for regularization in [16, 80, 113, 114]. The maximum number of iterations for Pade-DP/-LC (methods 3 and 6) is fixed to 100 and the relaxation parameter is fixed to 100. After the shape-size distribution is found, we compute the following parameters:

(a) the number concentration (n_t),

(b) the surface-area concentration (a_t),

(c) the volume concentration (v_t),

(d) the effective radius (r_{eff}),

(e) the effective aspect ratio (a_{eff}),

(f) the aspect ratio width (a_{var}), and

(g) the spherical volume concentration fraction ($svcf$).

4.1. General configuration with a fixed refractive index (Synthetic microphysical retrievals for non-spherical particles)

The shape-transition parameter for *svcf* (g), see also Eq. 3.3.8, is assumed here $\chi = 0.1$. The calculation of the single scattering albedo is omitted here, since its quality is highly dependent on the refractive index, which is fixed at this point.

The rationale behind the coming thorough analysis with an abundance of methods in the numerical experiments that follow, is the pursuit of a method that behaves "well" overall. More specifically all methods (1-6) will compete in the following *error-related quantities* (ERQ), all of which are calculated as a percentage (%) using the standard deviation.

1. Difference from exact value (Dif) . This is simply the proximity of the mean solution to the exact synthetic values, or in other words $\text{Dif} = 1 - \text{accuracy}(\%)$. This is probably the first percentage to look at, but clearly it should be backed by other stability evidence to acquire statistical significance. Throughout the thesis we will refer to this ERQ as "accuracy" too, when there is no risk of confusion.

2. Variability of the solution space (Var). The algorithms SA1 and SA2 are completed by ordering the solutions with respect to increasing error level and choosing a few of the first ones (step 6 or 9). This uncertainty percentage (2) is the standard deviation of a sought parameter, which is derived by the chosen best solutions, divided by the mean value of the parameter. It describes how much a mean value of a parameter varies from all best solution solutions in the same solution space i.e. for a specifier error level ϵ. In this regard there are two interpretations of such a statistical measure, both of which have to do with potential solution clusters. We rely on these clusters to find physically meaningful solutions, since previous experience with the sphere-particle approximation, showed that most of the mathematically acceptable solutions do not qualify physically. Therefore, on the one hand, the solution space should be variable enough in its full extent (all solutions), i.e. to produce clusters of more physically probable solutions. On the other hand, there should be a relative homogeneity for a small sample of "best" solutions (small residual error), reflecting the ability of the examined method to recognize such clusters. More details on clusters and patterns in solutions spaces for real-data inversions can be found in [131]. For more than one datasets, Var represents the mean variability of all produced solution spaces.

3. Randomness uncertainty (Unc). This is related to the stability of the examined method with respect to several repetitions of a numerical experiment of the same simulated atmospheric scenario but with different (random) instances of the same error level. By extension, this obviously characterizes the capacity of the method to reproduce well a possibly accurate result (low ERQ 1 -Dif-). The value of Unc is derived by first calculating the mean value of a parameter for every dataset of different data error, and then divide the standard deviation of these values by their mean. In other words, Unc is a form of Var with respect to the different-error datasets.

Each solution space here owns 36 solutions (9 splines-point numbers $\times$ 4 spline degrees), 5 of which are selected as the least-residual error solutions and are involved in the variability percentage (2). This amount of "best" solutions came up as a reasonable choice, since, at least for the spherical case in [131], less than 10% of the total amount of solutions are found to be useful. 15 mean values are calculated for each microphysical parameter (a-g), which then become the input for the randomness uncertainty (3). Combining every bit of the parameters in Table 4.1, we ended up with 60 different error-free datasets, which turn to 2700 noisy ones, and are finally inverted to a huge total of 583.200 solutions and 4.082.400 parameter calculations. Regarding the shape-related parameters (SRP) e-g, especially for the case of prolate ensembles (Table 4.1, $\eta = 1.3$ or 1.5), the initial *svcf* is zero, therefore we compute and compare absolute differences instead of relative ones for the ERQ.

The uncertainty and variability percentages can also be used for the reconstructions of the shape-size distribution to provide the respective levels of confidence we have for the retrieved distributions. The relative difference (Dif), on the other hand, may not suit in our case as a measure to quantify precisely the vicinity of the approximation to the initial distribution. This is due to the different resolution between the initial and the retrieved shape-size distribution which will make an additional 2D-interpolation necessary in order to compare them. Indeed the initial distribution is formed with only 7 points with respect to the aspect ratio because of the limited values provided by the database of Mieschka program, while for the retrieved one we use a symmetrical $r \times \eta$ grid of 30×30 points. However, we will use the absolute difference to measure the distance (Dist) of the retrieved distribution from the initial in order only to compare different retrieved distributions with one another.

4.1. General configuration with a fixed refractive index (Synthetic microphysical retrievals for non-spherical particles)

A *complete retrieval* consists here of the shape-size distribution and the set of (7) microphysical parameters a-g. The criteria for a method to be more suitable than another in the following analysis will be a generally better performance to retrieve the parameters a-d and the shape-related parameters e-g separately, always with respect to the error-related quantities (ERQ) 1-3. More specifically, for every complete retrieval the three "best" methods, namely one for each of the ERQ, are distinguished for every parameter, and the appearances of each method as "best" are counted. In principle we prioritize the frequency of appearances of a "best" method in accuracy as long as the appearances for Unc and Var are in a satisfying level too. We additionally investigate the *overall performance* of a method in each complete retrieval, counting the frequency of appearances of a "best" method in general indistinctly (adding up the appearances for all the ERQ). The best-method rules are summarized as follows:

1. Smaller difference from the exact value in both parameter-subsets a-d, and e-g separately.

2. Lower randomness uncertainty of the parameters and/or lower variability of solutions.

The best method should satisfy both 1 and 2 with an "and" in as many cases as possible. However, it is hard to characterize a method as "absolutely" best, i.e. to simultaneous satisfy of rules 1 and 2, in every occasion and this is why we appeal to an abundance of simulated atmospheric scenarios to make up our mind. What we seek here through the blind experiment that follows, is to identify (i) what are the main assets and defects of the methods and (ii) to find out which of them have a better balance between accuracy and stability and treat a wide spectrum of atmospheric setups reasonably enough. For this we define the *stability-to-accuracy ratio* of appearances

$$\text{UVDR} = \frac{\text{Unc} + \text{Var}}{2\text{Dif}}, \tag{4.1.3}$$

which measures the confidence in the efficiency of a specific method and should ideally be near the unit (1). The reasoning behind this is that stability (Unc+Var) and accuracy should have a fair share ($\sim 1/2$). A very small UVDR ($\ll 1$) means a higher level of uncertainty while a very large UVDR ($\gg 1$) means a lower level of accuracy. Of course, since the discussion is about the best method in terms of appearances, the latter rules tell us nothing about the actual Dif-, Var- and Unc-rates.

We will partly demonstrate this decision-making methodology with Fig. 4.2, which shows an example from Table (4.1) of retrievals of the parameters a-d (upper panel) and e-g (lower panel). We use a shape-size distribution synthesized by $r_\text{med} = 0.05$ and $\sigma = 2.3$ (log-normal) and a sphere-spheroid particle mixture and a refractive index $1.33 + 0.001i$. The datasets are produced 15 times with 10% error and inverted with Pade-LC and Tikh-GCV, using the whole span of spline features from Table 4.1, and as mentioned we pick 5 least-residual solutions in each complete retrieval. The plots depict errorbars corresponding to the randomness uncertainty computed by (15) retrievals for every parameter shown and every method, i.e. both panels host 30 complete retrievals (i.e. 15×2 methods). In addition, above each parameter we mark the "best" method with respect to Unc, Dif, and Var bottom up and compute the associated values, and the title above each panel shows the number of method appearances for Unc, Dif, Var and Unc+Dif+Var, which we will call *Overall*. For instance, focusing on the upper panel of Fig. 4.2, we see that the parameter a_t is retrieved with better accuracy by Pade-LC with 88.53% (Dif: 11.47%), vs Tikh-GCV's 72.6% (not shown) and better randomness uncertainty with 24.79%, but the variability is better with Tikh-GCV with 5.67% vs Pade-LC's 7.19% (not shown). A similar situation is also observed for the parameter r_eff and while Pade-LC is better in accuracy for all parameters a_eff, a_var and *svcf* (lower panel), Tikh-GCV appears nonetheless better in Unc and Var. Pade-LC appears "best" in accuracy 6 times in total, i.e. 3 times in the parameters a-d and 3 times in the parameters e-g, in contrast to Tikh-GCV which appears only once and zero times respectively. Tikh-GCV checks off the list the rule 2 appearing better at Unc and Var, but it is minor in accuracy (rule 1), which is reflected by its UVDR: $5 \gg 1$. On the other hand, Pade-LC's UVDR is 4/12 (≈ 0.33) therefore we conclude that Pade-LC is more suitable for this particular example. Obviously the decision could vary if we change what we look for, e.g. if we focus on specific parameters, but the significance of such a result (not for this particular example) will make more sense for the larger-scale experiment we are about to perform.

4.1.1 Retrieval results with respect to particle size

In this experiment we will test and intercompare the overall performance of the methods 1-6, with respect to all the different sizes, shapes, refractive indices (Table 4.1) and the retrieved parameters a-g.

4.1. General configuration with a fixed refractive index (Synthetic microphysical retrievals for non-spherical particles)

Table 4.1: Simulation- & inversion setup for retrievals with a fixed refractive index. Parameters below the labels "Distribution data generated with", "Optical data gererated with" and "Optical data inverted with" are combined with each other to perform the corresponding action.

Distribution data generated with

log-normal distribution

No	1	2	3	4
median radius (r_{med})	0.05	0.25	0.5	0.8
mode width (σ)	2.3	1.6	1.2	1.3
radius range (µm)	[0.01, 1.2]	[0.01, 1.2]	[0.01, 2.2]	[0.01, 2.2]
number concentration (N_{t})	1	1	1	1

aspect ratio distribution

(a) oblate	(b) sphere-spheroid mixture	(c) prolate
$\begin{cases} 1/2, & \text{if } \eta = 0.77, \\ 1/2, & \text{if } \eta = 0.87, \end{cases}$	$\begin{cases} 1/3, & \text{if } \eta = 0.87, \\ 1/3, & \text{if } \eta = 1, \\ 1/3, & \text{if } \eta = 1.15, \end{cases}$	$\begin{cases} 1/2, & \text{if } \eta = 1.3, \\ 1/2, & \text{if } \eta = 1.5, \end{cases}$

Optical data generated with

refractive index	(i) $1.33 + 0.001i$, (ii) $1.4 + 0.005i$, (iii) $1.5 + 0.01i$, (iv) $1.6 + 0.001i$, (v) $1.7 + 0.05i$
number of spline points	$6, 7, 8, 9, 10, 11, 12, 13, 14$
spline degree	$2, 3, 4, 5$
relative error level ($\times 15$ repetitions)	$1\%, 5\%, 10\%$

Optical data inverted with

regularization methods & parameter choice rules

TSVD-DP	Tikh-LC	Pade-DP	Tikh-GCV	Tikh-DP	Pade-LC

Since shape and size are variables of primary concern in literature we divided the retrieval to four parts according to the (log-normal) size distributions from Table 4.1 and the only distinction for comparisons among parameters will be the shape (parameters e-g) and the effects of the transition to higher error levels. This means that we will not test the efficiency of a method to particular parameters, but the argument for the most suitable ones will be based on collective performance as explained in Sec. 4.1. The analysis will be based in retrieval results lying in Tables 4.2 and 4.3. The numbers represent the appearances of a method as "best" (least residual-error) with respect to an ERQ for a complete retrieval, i.e. for all the parameters a-g. The columns "R", "S" and "T" separate the sum of appearances of the parameters a-d (*R-parameters*), from those of e-g (*S-parameters*) and those of the sum of appearances of R and S respectively. We will call *RA*, *SA* and *TA* the appearances (table entries) related to R, S and T respectively. For every ERQ, there are 3 lines corresponding to the error levels 1%, 5% and 10% top down and one more line (with a separator) showing the sum along the lines (of different error) of the respective R, S and T columns. The sum of every single element in each column is also given, in the row designated by the label "In total". Fixing an ERQ, a line and a method, a table entry counts the sum of appearances

4.1. General configuration with a fixed refractive index (Synthetic microphysical retrievals for non-spherical particles)
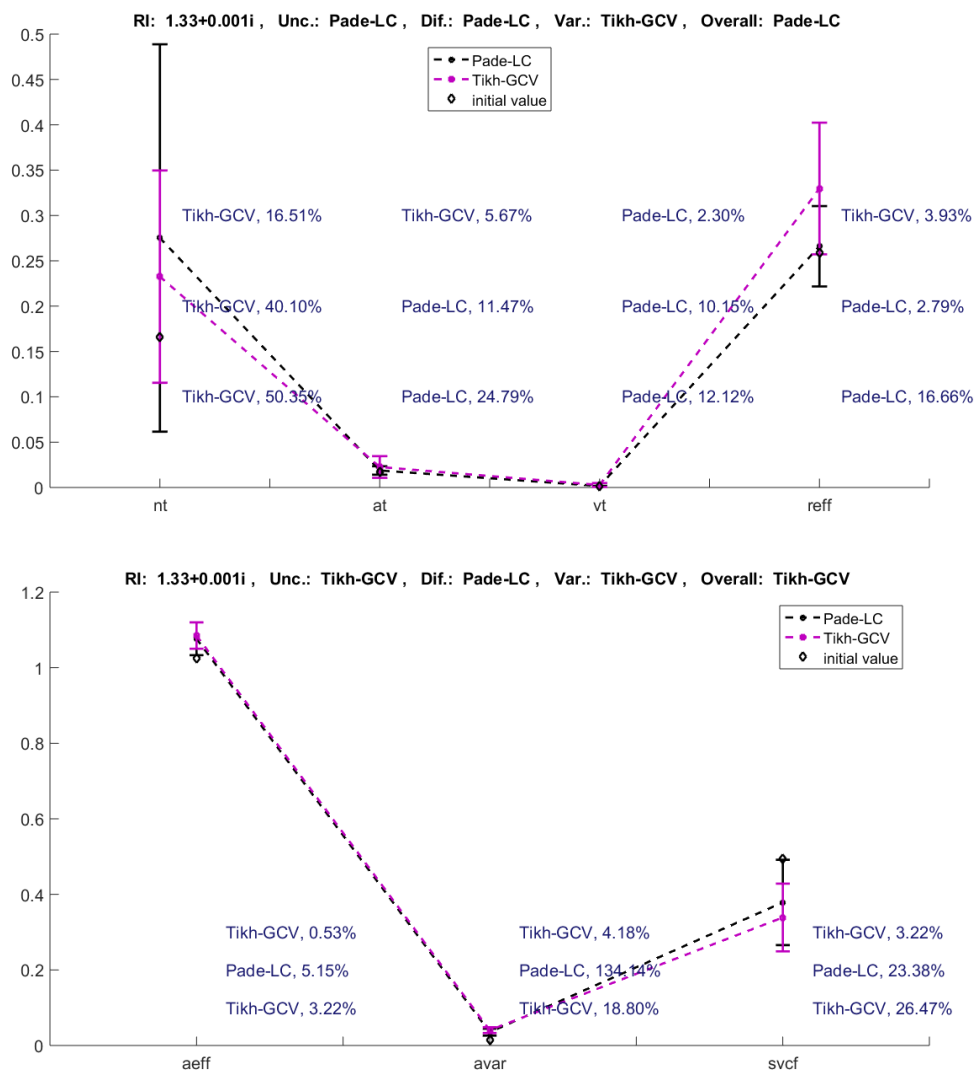
Figure 4.2: Errorbar plot of the microphysical parameters with respect to the randomness uncertainty and illustration of the methodology of counting the appearances of a "best" method with respect to all error-related quantities. Above each parameter the "best" method is marked with respect to Unc, Dif, and Var bottom up with the associated percentage values. The title above each panel shows the method with the largest number of appearances for Unc, Dif, Var and Overall (Unc+Dif+Var).

with no distinction in terms of the refractive index and the aspect ratio distribution used to produce the retrieval products, or a particular parameter from a-g. Hence each entry is the contribution of a "best" method from a total of 15 retrievals -derived by 3 aspect ratio distributions × 5 refractive indices-, and thus RA and SA have a maximum of 60 and 45 respectively. Note that these (15) retrievals are already averaged by means of Var and Unc, so there are actually 5(solutions) × 15(repetitions) retrievals implied for each parameter and each method. The same applies for "Overall", which counts the sum of RA and SA with no distinction in the ERQ but within a specific retrieval. If there are ties in method appearances, e.g. say one method is simultaneously best at n_t and a_t and another is best at v_t and r_{eff}, then the additional point is added to both of them, in this case in the RA.

For instance, focus on the upper sub-table of Table 4.2 and particularly at the Uncertainty-rows and the method (Tikh-LC). The numbers 5, 8 and 13 on the first line, associated with 1% data error, correspond to the appearances of Tikh-LC as a "best" method (among all six) with respect to Unc for the parameters a-d, e-g, and their sum (5+8) respectively. The second line corresponding to 5% data error shows a dramatic reduction with only one RA and zero SA, while the third line for 10% data error shows

a tenuous raise of SA to 1. We emphasize that a rising or diminishing RA, SA, or TA when moving along lines (different errors) does not translate necessarily into a raise or reduction of the associated ERQ; one can only argue in favor or against a method, observing the related entries for the rest of the methods. Let us now see in greater detail the response of all methods through the different atmospheric scenarios being simulated in this numerical experiment. In what follows, the reference to a *total* UVDR means that the number of appearances taking part to the ratio are the TA.

Size distribution No 1, upper sub-table in 4.2

This is the case of finest-size particles under examination. Arguably Pade-LC is the most accurate method (total Dif: 47) and in fact about 74% better (more often met) than the second more accurate Tikh-DP (total Dif: 27). However, Pade-LC has very poor performance in Unc and Var (also TSVD-DP and Tikh-GCV), while Tikh-DP is multiple times superior in Unc (total Unc: 58) than any other method and has satisfying performance in Var, as compared to TSVD-DP and Tikh-GCV, ranking third after Pade-DP and Tikh-LC. The latter two methods have greater uncertainty than Tikh-DP judging by their TA (Unc, Var): (16, 44) and (16, 38), especially in R-parameters (total). A caveat of Pade-DP and the rest of the methods is the mere absence of appearances in accuracy of the SRP for higher errors 5% and 10% (Dif: 0), where Pade-LC is exceptionally better. Looking at the overall appearances within a complete retrieval, Tikh-DP with a total of 57 is twice as good as Pade-DP. Tikh-GCV is evidently the least efficient method, along with TSVD-DP which actually demonstrates an equally good performance in accuracy as Pade-DP but this asset is not supported by the much lower TA Unc: 1 and Var: 3. The UVDR of Tikh-DP is 1.33, which is a more reasonable value than Pade-LC's 2.14. Hence, an overall better performance can be attributed to Tikh-DP.

Size distribution No 2, lower sub-table in 4.2

Tikh-DP does not handle equally well in terms of accuracy the larger (but still relatively fine) particles described here. Indeed Tikh-DP, while being about as good as Pade-DP in Unc and Var, it downgrades to the 4th place regarding total-accuracy appearances (TA Dif: 12). Tikh-DP is slightly better than Tikh-LC looking at their individual performances in (TA) Unc, Dif, and Var and their UVDR: 2.625 and 3.35 respectively. The largest performance change is the one of Tikh-GCV, which appears to be enhanced, relative to the size No 1, both in accuracy and stability. The latter is a little better in accuracy than Tikh-DP and Tikh-LC, but much less efficient in Unc and Var, although it has a consistent (vicinal to 1) total UVDR: 0.77. Pade-LC demonstrates again supremacy in accuracy, the highest rates coming from SA, which also outweighs the rest of the methods. On the other hand, it performs only tenuously better in Unc and Var than in the case of finer particles (size No 1), and still has much smaller contributions comparing to Pade-DP and Tikh-DP, but similar to TSVD-DP. This results in a small total UVDR: 0.06 relative to the one of the second more accurate method, Pade-DP, with 0.87. Therefore Pade-DP is acknowledged in this case as a more appropriate method.

Size distribution No 3, upper sub-table in 4.3

This sub-case pertains to medium-coarse particles. It is straightforward to realize that Tikh-LC exhibits outstanding stability and is by far more dominant in this regard than any other method with TA (Unc,Var): (65, 51). The second more stable is Tikh-DP with (27, 25) and Pade-DP follows with only (9,11). Nevertheless, the best option for accuracy is Pade-DP, which appears 80% more frequently than Tikh-LC (TA Dif: 45 vs 25), while Pade-LC is a little better than Tikh-LC with TA Dif: 30 and 25 respectively. Pade-LC does not show much of an improvement in TA (Unc, Var)=(6, 5) from the previous simulation part (size No 2) and its accuracy, while it is the 2nd best method, is compromised as well being only a little better than Tikh-LC (3rd best). Moreover Pade-DP and Pade-LC are better in shape approximation than Tikh-LC, to which it has very little contribution, but they also share close but rather small UVDRs (0.22, 0.18) compared to Tikh-LC's 2.32. Tikh-LC is only the third most accurate method, thus finally, we are inclined to favor Pade-DP as a more efficient method for this example. In the final method evaluation we will provide a reason for Tikh-LC's undesired behavior, namely the high deviation between TA Dif and TA (Unc, Var), which is met also in the largest-particle size (No 4). Finally, Tikh-GCV and especially TSVD-DP are in this example the least suitable methods in almost all respects.

Table 4.2: Evaluation and comparison regularization methods (RM) with respect to accuracy and stability for the size distributions with $r_{med} = 0.05, \sigma = 2.3$ (upper sub-table) and $r_{med} = 0.25, \sigma = 1.6$ (lower sub-table), see Table 4.1. The numbers represent the appearance of a method as "best" (least residual-error) with respect to an error-related quantity (ERQ) in the table for a complete retrieval, i.e. for all the parameters a-g. The columns "R", "S" and "T" stand for the sum of appearances related to the parameters a-d, e-g and the sum of appearances of R and S respectively. For every ERQ, there are 3 lines corresponding to the error levels 1%, 5% and 10% top down and one more line (with a separator) showing the sum along the lines (of different error) of the respective R, S and T columns. In addition, the sum of every single element in each column is given in the row-field "In total". Fixing an ERQ, a line and a method, a number counts the sum of appearances with no distinction in terms of the refractive index, the aspect ratio distribution or a particular parameter from a-g. The same applies for "Overall", counting the sum of appearances of R- and S-parameters with no distinction in the ERQ but within a specific complete retrieval.

ERQ/RM	TSVD-DP			Tikh-LC			Pade-DP			Tikh-GCV			Tikh-DP			Pade-LC		
							$r_{med} = 0.05$			$\sigma = 2.3$								
	R	S	T	R	S	T	R	S	T	R	S	T	R	S	T	R	S	T
Unc/ty	0	1	1	5	8	13	5	4	9	0	0	0	5	2	7	0	0	0
	0	0	0	1	0	1	0	7	7	0	0	0	14	8	22	0	0	0
	0	0	0	1	1	2	0	0	0	0	0	0	15	14	29	0	0	0
	0	1	1	7	9	16	5	11	16	0	0	0	34	24	58	0	0	0
Dif/ce	3	5	8	2	1	3	4	1	5	2	1	3	4	2	6	3	9	12
	1	1	2	2	1	3	4	0	4	0	2	2	8	2	10	5	13	18
	4	2	6	5	1	6	5	0	5	2	3	5	9	2	11	2	15	17
	8	8	16	9	3	12	13	1	14	4	6	10	21	6	27	10	37	47
Var/ty	2	1	3	7	8	15	1	3	4	1	3	4	5	4	9	0	0	0
	0	0	0	6	6	12	12	9	21	0	1	1	2	1	3	0	0	0
	0	0	0	7	4	11	8	11	19	0	1	1	1	1	2	0	0	0
	2	1	3	20	18	38	21	23	44	1	5	6	8	6	14	0	0	0
Overall	0	3	3	6	7	13	4	4	8	0	0	0	7	3	10	1	2	3
	0	0	0	0	2	2	2	9	11	0	0	0	14	7	21	0	2	2
	0	0	0	2	2	4	3	6	9	0	0	0	14	12	26	0	4	4
	0	3	3	8	11	19	9	19	28	0	0	0	35	22	57	1	8	9
In total	10	13	23	44	41	85	48	54	102	5	11	16	98	58	156	11	45	56
							$r_{med} = 0.25$			$\sigma = 1.6$								
	R	S	T	R	S	T	R	S	T	R	S	T	R	S	T	R	S	T
Unc/ty	1	1	2	5	5	10	4	6	10	1	0	1	6	3	9	2	0	2
	0	0	0	4	4	8	7	7	14	1	0	1	10	4	14	0	0	0
	1	0	1	4	4	8	5	2	7	0	0	0	10	9	19	0	0	0
	2	1	3	13	13	26	16	15	31	2	0	2	26	16	42	2	0	2
Dif/ce	1	5	6	1	0	1	6	4	10	0	2	2	0	0	0	8	10	18
	1	3	4	3	0	3	12	1	13	4	3	7	4	3	7	7	11	18
	0	1	1	5	1	6	10	1	11	3	3	6	3	2	5	5	13	18
	2	9	11	9	1	10	28	6	34	7	8	15	7	5	12	20	34	54
Var/ty	0	0	0	7	6	13	4	3	7	4	8	12	7	3	10	2	1	3
	0	0	0	6	7	13	7	4	11	0	4	4	4	2	6	1	0	1
	1	0	1	9	6	15	3	7	10	1	4	5	5	0	5	0	0	0
	1	0	1	22	19	41	14	14	28	5	16	21	16	5	21	3	1	4
Overall	0	1	1	3	5	8	4	5	9	0	3	3	4	3	7	6	0	6
	0	1	1	4	5	9	6	8	14	0	3	3	6	2	8	1	0	1
	0	0	0	6	4	10	3	4	7	0	3	3	8	9	17	0	4	4
	0	2	2	13	14	27	13	17	30	0	9	9	18	14	32	7	4	11
In total	5	12	17	57	47	104	71	52	123	14	33	47	67	40	107	32	39	71

Size distribution No 4, lower sub-table in 4.3

This is the last and perhaps the most interesting sub-case, as it pertains to coarser particles which are often met in lidar measurements for dust-like particles. The scenery is similar to the previous case (No 3), with Tikh-LC demonstrating mainly stability (Unc, Var) and Pade-LC and Pade-DP prevailing by far in accuracy. The latter methods show some improvements in Unc, Var and Overall (TA) which are

still hardly comparable to the ranking of Tikh-LC with 57, 50 and 57 respectively. Furthermore Pade-LC appears once more to suit better for the accuracy of shape-related parameters especially for higher error levels and is better in general from Pade-DP with TA Dif: 54 vs 36. In terms of stability Pade-DP with TA (Unc, Var): (13, 14) is a little better than Pade-LC with (9, 5). These observations are directly reflected by Tikh-LC's large total UVDR: 6.69 relative to the one of Pade-DP with 0.38 and Pade-LC with 0.12, which promotes Pade-DP to be the most suitable method here.

Table 4.3: Evaluation and comparison of methods with respect to accuracy and stability for the size distributions with $r_{\mathrm{med}} = 0.5, \sigma = 1.2$ (upper sub-table) and $r_{\mathrm{med}} = 0.8, \sigma = 1.3$ (lower sub-table), see Table 4.1. The explanation of the numbers here follow the conventions of Table 4.2.

ERQ/RM	TSVD-DP			Tikh-LC			Pade-DP			Tikh-GCV			Tikh-DP			Pade-LC		
							$r_{\mathrm{med}} = 0.5$			$\sigma = 1.2$								
	R	S	T	R	S	T	R	S	T	R	S	T	R	S	T	R	S	T
Unc/ty	0	0	0	10	13	23	3	0	3	0	0	0	2	2	4	2	0	2
	0	0	0	11	11	22	4	0	4	1	0	1	7	4	11	3	0	3
	1	0	1	9	11	20	2	0	2	0	0	0	8	4	12	1	0	1
	1	0	1	30	35	65	9	0	9	1	0	1	17	10	27	6	0	6
Dif/ce	0	0	0	5	0	5	8	14	22	0	0	0	1	2	3	3	3	6
	1	0	1	9	1	10	3	11	14	1	0	1	2	1	3	7	6	13
	1	1	2	9	1	10	3	6	9	1	0	1	5	0	5	2	9	11
	2	1	3	23	2	25	14	31	45	2	0	2	8	3	11	12	18	30
Var/ty	0	0	0	10	11	21	5	0	5	1	5	6	0	3	3	1	0	1
	0	0	0	7	8	15	4	1	5	0	7	7	2	5	7	3	0	3
	0	1	1	6	9	15	1	0	1	0	3	3	9	6	15	1	0	1
	0	1	1	23	28	51	10	1	11	1	15	16	11	14	25	5	0	5
Overall	0	0	0	10	13	23	4	0	4	0	1	1	0	1	1	1	0	1
	0	0	0	9	11	20	2	1	3	0	2	2	2	4	6	3	0	3
	0	0	0	8	11	19	0	0	0	0	0	0	7	5	12	0	1	1
	0	0	0	27	35	62	6	1	7	0	3	3	9	10	19	4	1	5
In total	3	2	5	103	100	203	39	33	72	4	18	22	45	37	82	27	19	46
							$r_{\mathrm{med}} = 0.8$			$\sigma = 1.3$								
	R	S	T	R	S	T	R	S	T	R	S	T	R	S	T	R	S	T
Unc/ty	0	0	0	13	13	26	1	0	1	2	1	3	1	1	2	1	0	1
	0	0	0	6	10	16	4	1	5	0	0	0	5	4	9	4	0	4
	1	2	3	6	9	15	6	1	7	0	0	0	8	5	13	4	0	4
	1	2	3	25	32	57	11	2	13	2	1	3	14	10	24	9	0	9
Dif/ce	0	3	3	2	1	3	9	10	19	3	0	3	0	0	0	7	5	12
	1	2	3	3	0	3	6	2	8	1	1	2	3	0	3	11	12	23
	0	2	2	1	1	2	7	2	9	0	2	2	3	0	3	8	14	22
	1	7	8	6	2	8	22	14	36	4	3	7	6	0	6	26	31	57
Var/ty	0	1	1	12	8	20	4	4	8	0	3	3	0	5	5	2	2	4
	0	1	1	6	8	14	4	1	5	2	5	7	3	2	5	1	0	1
	1	1	2	8	8	14	0	1	1	1	6	7	7	1	8	0	0	0
	1	3	4	26	24	50	8	6	14	3	14	17	10	8	18	3	2	5
Overall	0	0	0	11	12	23	3	3	6	1	1	2	0	1	1	0	0	0
	0	0	0	5	10	15	4	1	5	0	2	2	2	4	6	4	3	7
	0	1	1	9	10	19	4	1	5	0	3	3	5	4	9	2	2	4
	0	1	1	25	32	57	11	5	16	1	6	7	7	9	16	6	5	11
In total	3	13	16	82	90	172	52	27	79	10	24	34	37	27	64	44	38	82

Method stocktaking and conclusion

A straightforward observation from Tables 4.2 and 4.3 is that TSVD-DP and Tikh-GCV are the least efficient methods and may be ruled out. The most probable cause of this behavior is the overestimation or underestimation of the regularization parameter leading to oversmoothed or undersmoothed solutions. We can see this by estimating the average regularization parameter for multiple retrievals, which is more effective to demonstrate through the retrievals of TSVD-DP. It is easily noticed that the number of total accuracy appearances of the latter undergo a reduction with increasing particle size (cases $1 \to 4$). As an example, we focus on the simulation part with size distribution No 1 and 4 with error level 1%, which

correspond to the upper- and lower panel of Fig. 4.3 respectively. Every plot shows the TSVD-DP regularization parameter (cut-off level) with respect to the 5 least-residual solutions for each of the 15 error-retrievals. Along a row, the depicted plots correspond (for both panels) to a fixed aspect ratio distribution combined with the 5 refractive indices (RI) from Table 4.1. The title above each plot shows the median of all the regularization parameters involved. For size No 1, we see that the best TSVD-DP solutions are produced with an average of 5 SVD-terms in the majority of cases (see upper panel of Fig. 4.3). On the other hand, size No 4 shows that most of these solutions basically remain unregularized, keeping all 8 SVD-terms (see lower panel of Fig. 4.3). It could be argued that the small input error does not contaminate much of the solution and therefore not much of the solution has to be cleared (either 1 or no SVD-terms). However, it is suspicious that this happens so frequently in size No 4 and not at all in size No 1, therefore one has to look carefully at the degree of ill-posedness for the two cases.

As explained in Sec. 3.4, a potentially helpful approach for the of ill-posedness of our problem is studying the singular value decomposition of the linear systems solved after the discretization of the model equation. Fig. 4.4 shows representative instances of the so-called Picard-plot of several simulation cases with 1% data error to illustrate the involvement of on the size-, shape- and refractive index by fixing one of them at a time. The number of spline points and the spline degree, 14 and 3 respectively, correspond to the best solution most frequently found, but the plot trends are similar with spline setups of any of the 5 least-residual solutions. The plots depict the singular values of discretization matrix in the same axes with the SVD-coefficients $U^T b$, where U follows the notation of Th. 1.11 and b denotes the noisy dataset. A common characteristic of these plots is that the smallest singular values are actually conservatively low, which is a sign of the smoothing imposed by the discretization process. This is indeed optimistic, but we are more concerned about the competition of the decay rates between the two depicted quantities. Let us focus on the uppermost Picard-plots with variable size, i.e. cases No 1 (left) and 4 (right), a fixed prolate shape and a fixed refractive index equal to $1.5 + 0.01i$. The small-particle case (left plot) essentially proves that the Picard condition is satisfied, and in fact there is virtually no peril that the inversion is severely compromised. The large-particle case (right plot), by contrast, shows that there is actually very little hope that one might get a more meaningful solution by subtracting any number of terms, i.e. applying the TSVD-algorithm. This shows that TSVD-DP is rather not sufficient for larger particles as compared to methods which can modify the matrix spectra. Analogous analysis for cases No 2 and 3 shows that they are treated by TSVD-DP close to the cases No 1 and No 4 respectively. A hint for this is given by the plots on the middle and bottom panels in Fig. 4.4 corresponding to examples for size No 2 and No 3 respectively. Even though we examine different cases of shape and refraction we see an indication of the decay rate of singular values gradually increasing for size No 3 vs 2. This rather confirms the sense we had from Tables 4.2 and 4.3 about the efficiency discontinuation of this method, marking the particle size $0.43 \leq r_{\text{eff}} < 0.54$ (sizes No 2 and 3) as a probable transition barrier for TSVD-DP's efficiency.

We witness a similar behavior with Tikh-GCV with a systematic underestimation of the Tikhonov regularization parameter (TRP) as compared to Tikh-DP, which is a much better method in an overall fashion. For instance, for size No 1, for 1% data errors Tikh-GCV has a mean TRP (calculated the same way as the cut-off level median for TSVD-DP) which is 2 to 4 times smaller from the one derived by Tikh-DP. The same pattern is observed for 10% error level, even though the mean TRP for both methods grows 5-12 times. The third best alternative we have for size No 1, Tikh-LC, is close to Tikh-DP's standards for 1% errors but ends up with a parameter underestimation too (twice as small mean TRP) for 10% errors. The most accurate method for size No 1, Pade-LC, has an average (median) number of iterations of 89, 82 and 54 for 1%, 5% and 10% data error respectively, while Pade-DP differs distinctly performing runs with only 4, 2, and 2 iterations, obviously producing oversmoothed solutions. We should point out that the average regularization parameter used here does not constitute a quantity bound with precision for a practical purpose, other than the rough statistical context through which we can distinguish prominent differences between methods and insistent behaviors that are also supported by other arguments.

Size distribution No 1
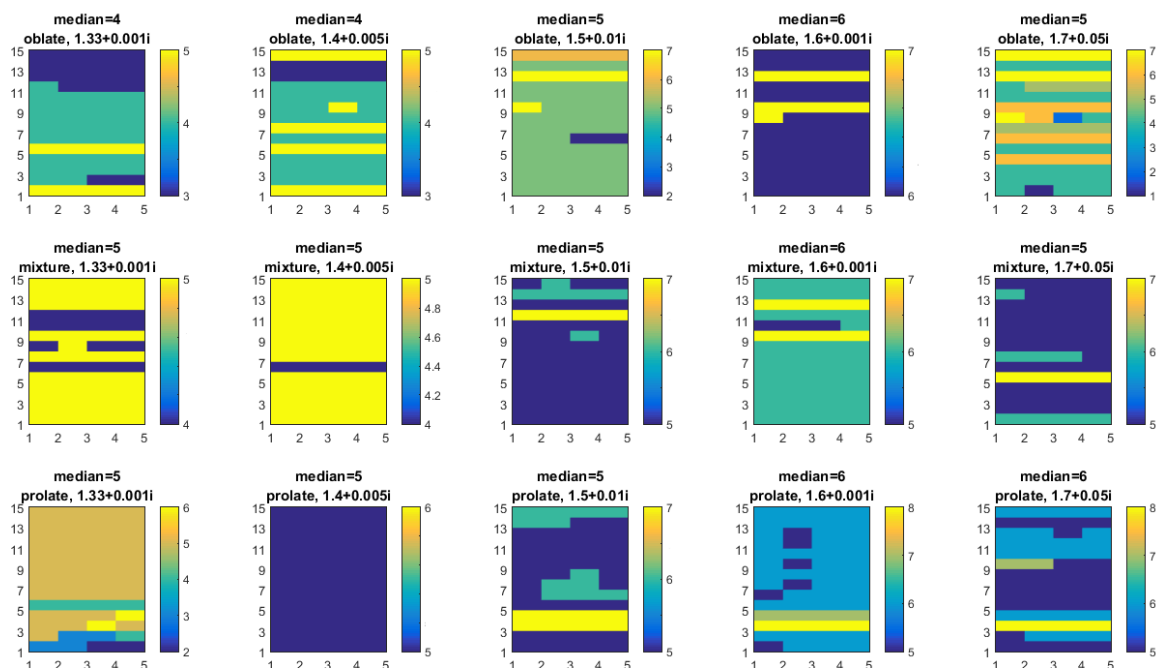
Size distribution No 4
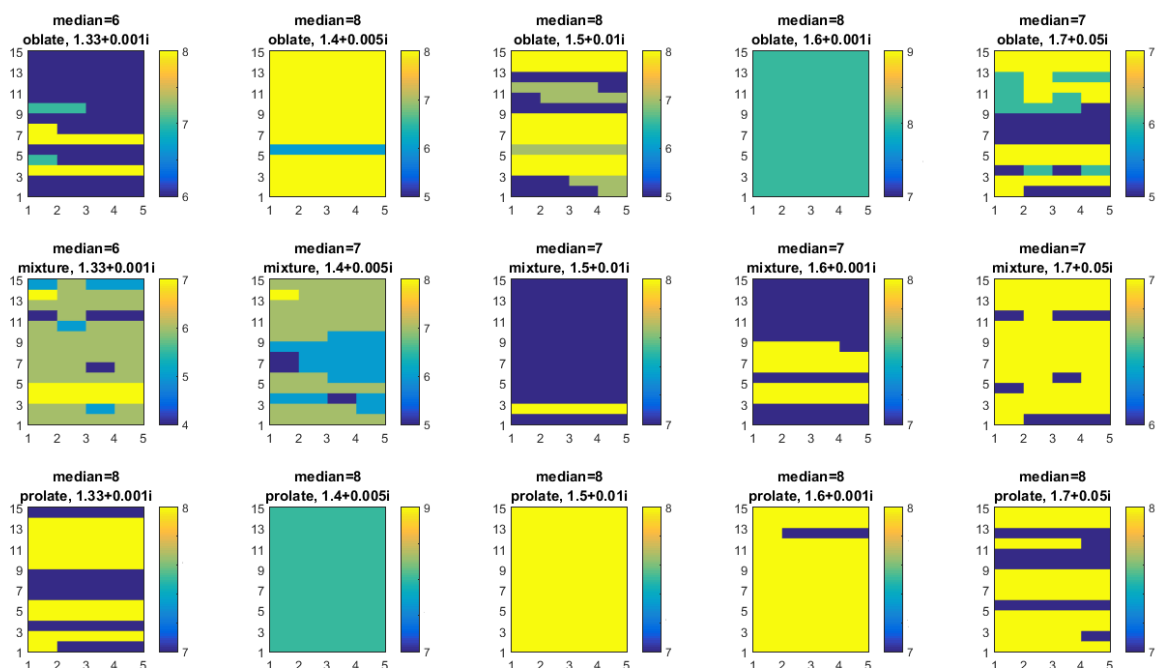
Figure 4.3: Illustration of the development of the average regularization parameter of TSVD-DP for an increasing particle size: size No 1 (upper panel) and 4 (lower panel). Every plot shows the TSVD-DP regularization parameter (cut-off level) with respect to the 5 least-residual solutions for each of the 15 error-retrievals. The depicted 15 plots (for each panel) correspond to the combination of the 5 RI with the 3 aspect ratio distributions (oblate, mixture, prolate, one per row) from Table 4.1. The title above each plot includes the median of all the regularization parameters involved, found first with respect to the best solutions and subsequently with respect to the different datasets.
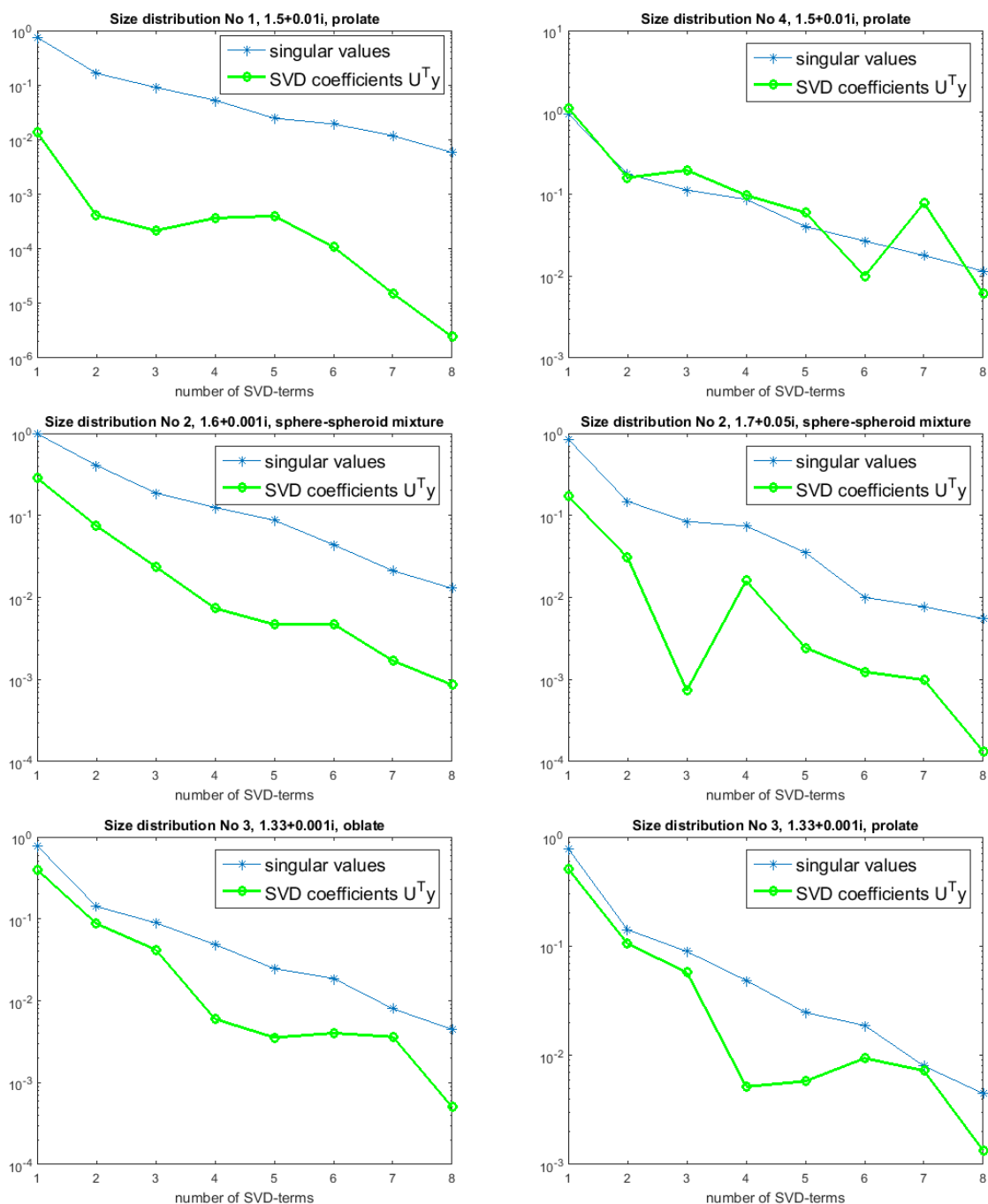
Figure 4.4: Picard plots of several simulation cases with 1% data error focusing on the size-, shape- and refractive index involvement. The plots on the upper panel plots have fixed shape (prolate) and RI $(1.5 + 0.01i)$ and variable size (No 1 and 4). The plots on the middle panel have fixed size (No 2) and shape (sphere-spheroid mixture) and variable RI $(1.6 + 0.001i$ and $1.7 + 0.05i)$. The plots on the lower panel have fixed size (No 3) and RI $(1.33 + 0.001i)$ and variable shape (oblate and prolate) The notation "U" stems from Th. 1.11 and b denotes the noisy dataset. The fixed spline configuration (No points: 14, degree: 3) used for the discretization is the one corresponding to the best solution.

Table 4.4: Assessment of the total performance of methods. The table elements yield by summing the partial (with respect to a size distribution) RA, SA and TA for the respective ERQ, Overall or In total from Tables 4.2 and 4.3.

Total method performance

ERQ/RM	TSVD-DP			Tikh-LC			Pade-DP			Tikh-GCV			Tikh-DP			Pade-LC		
	R	S	T	R	S	T	R	S	T	R	S	T	R	S	T	R	S	T
Unc/ty	1	2	3	33	39	72	13	10	23	3	1	4	14	8	22	5	0	5
	0	0	0	22	25	47	15	15	30	2	0	2	36	20	56	7	0	7
	3	2	5	20	25	45	13	3	16	0	0	0	41	32	73	5	0	5
	4	4	8	75	89	164	41	28	69	5	1	6	91	60	151	17	0	17
Dif/ce	4	13	17	10	2	12	27	29	56	5	3	8	5	4	9	21	27	48
	4	6	10	17	2	19	25	14	39	6	6	12	17	6	23	30	42	72
	5	6	11	20	4	24	25	9	34	6	8	14	20	4	24	17	51	68
	13	25	38	47	8	55	77	52	129	17	17	34	42	14	56	68	120	188
Var/ty	2	2	4	36	33	69	14	10	24	6	19	25	12	15	27	5	3	8
	0	1	1	25	29	54	27	15	42	2	17	19	11	10	21	5	0	5
	2	2	4	30	27	57	12	19	31	2	14	16	22	8	30	1	0	1
	4	5	9	91	89	180	53	44	97	10	50	60	45	33	78	11	3	14
Overall	0	4	4	30	37	67	15	12	27	1	5	6	11	8	19	8	2	10
	0	1	1	18	28	46	14	19	33	0	7	7	24	17	41	8	5	13
	0	1	1	25	27	52	10	11	21	0	6	6	34	30	64	2	11	13
	0	6	6	73	92	165	39	42	81	1	18	19	69	55	124	18	18	36
In total	21	40	61	286	278	564	210	166	376	33	86	119	247	162	409	114	141	255

From the split analysis in the previous subsections (size distributions No 1-4) we saw that Tikh-DP is much more stable than accurate, Pade-LC is much more accurate than stable and Pade-DP seems to find middle ground. We can get the same sense more emphatically by looking at Table 4.4, which contains a raw synopsis of all methods' performance for all cases No 1-4 obtained by summing RA, SA and TA from Tables 4.2 and 4.3 for the respective sections Unc, Dif, Var, Overall and In total. Pade-LC is the only true competitor in accuracy with a total of all TA Dif: 188 vs 129 of Pade-DP, a great deal of which is attributed to the shape-related parameters as expected from the simulation parts analyzed previously. In addition, it is interesting that Pade-LC's SA contribution (120) is more than twice the one of Pade-DP, while Pade-DP's total RA contribution is only slightly larger. However, in turn Pade-LC is more unpredictable in terms of stability especially in smaller-particle cases which shrinks its total UVDR to 0.08 (Table 4.4). Pade-DP seems also to be relatively less advantageous for the smallest particles simulated (size No 1, upper sub-table in Table 4.2), a problem already hinted through the preliminary simulations in Sec. 3.7, but overall manages to be less uncertain than Pade-LC, with a UVDR: 0.64.

Besides TSVD-DP, a more obscure monotone behavior with respect to particle size is demonstrated by Tikh-DP and conversely with respect to Unc and Var by Tikh-LC. These methods keep by far the highest level of certainty of the solutions they produce among all methods. However, they are outweighed in accuracy by Pade-DP and Pade-LC whose TA Dif are way over twice and three times larger respectively. According to their total UVDR from Table 4.2, Tikh-DP with 2.05 appears less systematic than Tikh-LC with 3.13. The two less effective methods, Tikh-GCV and TSVD-DP share very close number of appearances with respect to accuracy and Unc but Tikh-GCV tends to produce solutions with lower variability (TA Var: 60 vs 9) more often, and further it appears as "best" more often within a specific physical setup (TA Overall: 19 vs 6).

4.1.2 The retrieved microphysical parameters with a fixed refractive index

The blind numerical experiment of the previous section with respect to the specific parameters we retrieved would give less credit to a method distinction, if despite the analysis over multiple criteria, the accuracy differences between them are low and/or the uncertainties too high. Fortunately none of these occasional occurrences are the rule here. We can demonstrate through specific examples that the differences between the methods grow in significance with increasing particle size. As discussed in the beginning of Sec. 4.1, for relatively small particles the differences between the methods are relatively small. This is now further confirmed by looking at Tables 4.5 and 4.6 which show the microphysical parameter retrievals for the size No 1 (smallest particles examined), with the refractive index $1.5 + 0.01i$, 1% data error and either prolate or oblate particle ensembles respectively. The retrievals depicted here show small differences for Table 4.5 and marginal for Table 4.6. Indeed, all parameters are retrieved by all methods with very satisfying accuracy, variability and uncertainty levels. The error appearing in the rightmost part of the tables is the mean relative residual error and one can see its extremely low levels.

Focusing on the number concentration n_t in Table 4.5, best retrieved by Tikh-DP, we see that it is the parameter of highest variability (and uncertainty) for all methods which still has a reasonable range of 8.06-33.50% (lowest by Tikh-LC). In fact, it has been shown plenty of times in literature that n_t is one of the most difficult parameters to retrieve, even for the spherical case, therefore we can not stress enough how important this achievement is. This efficiency is repeated in the case of oblate spheroids, as we see in Table 4.6, with better uncertainties and lesser accuracy, but still in very reasonable levels. These are very limited but not isolated instances, more of which we will explore later, realizing that Padé iteration actually carries the best chance among the other methods of predicting n_t. The rest of the parameters are retrieved with much lower uncertainties generally, with an exception in *svcf* by Pade-DP and Pade-LC in Table 4.5, which are generally the most accurate methods for the shape-related parameters as shown earlier. The accuracy standards for *svcf* are more loosely defined as the point which allows us to deduce a tendency towards sphericity or non-sphericity matching the one of the original value. Therefore in this particular case with an initial value of 0.0%, the lowest retrieved values, 7.44% and 9.72% retrieved by Pade-LC and Pade-DP respectively, are largely a success as well. A fair reproduction of the initial *svcf* (0.18) is also achieved in the case of oblate spheroids (Table 4.6) by all methods (about 0.34). Pade-LC and Pade-DP are much closer to the initial effective aspect ratio than the rest of the methods -as expected- for prolate particles, while all methods retrieve this parameter with very small uncertainties. On the other hand, a_{eff} is falsely predicted as being mostly spherical in the case of oblate spheroids by all methods, which reflects a more general problem of our retrievals with purely oblate spheroidal

shapes. The aspect ratio width (a_{var}) is the parameter of smallest variation among the methods, but it is actually quite problematic in our retrievals due to its high sensitivity in the noise level, e.g. here it is retrieved 6 times larger than the original value. However, if the effective aspect ratio is accurately found, the retrieved shape-size distribution often reveals the parts which underwent any artifacts and enlarge a_{var}. Fig. B.2 (App. B) shows the average shape-size distributions retrieved by all methods against the initial shape-size distribution shown on the top left panel. The best retrieved distributions, i.e. by Pade-LC and Pade-DP, make a quite clear distinction of the "healthy" distribution parts and its "ill" counterparts which add up to a noisy a_{var}. Moreover, we see that the differences between the methods are more prominent when it comes to the distribution reconstructions. This is expected since all parameter calculations involve shape-size distributions as integrands and thus the smoothing effect conceals parts of the oscillations.

Now let us see what happens to the retrievals with larger particles through another example keeping the same RI and data error and combining the size distribution No 3 with either prolate or sphere-spheroid particle ensembles, shown in App. C, Tables C.1 and C.2 respectively. In this simulation scenario the differences between methods are much more pronounced. First of all, the only viable options for the number concentration for the prolate-particle case appear to be Pade-DP and Pade-LC. This is not the case for the sphere-spheroid mixture where no method offers a reasonable approximation for n_{t}, but the high level of disagreement between the values of Pade-DP, Pade-LC and the rest of methods indicates that the latter have a bigger problem handling the amplification of errors imposed by the ill-posedness. Oddly enough the surface-area concentration and the volume concentration retrieved by TSVD-DP, Tikh-GCV and Tikh-DP are deviating from the respective initial values in close proportions so that they are cancelled out producing eventually good approximations of the effective-radius ($\sim v_{\text{t}}/a_{\text{t}}$). Contrary to the prolate-particle case, the sphere-spheroid mixture does not compensate the lost precision between a_{t} and v_{t}, so that r_{eff} is less accurate in this instance. Pade-DP has an astounding performance in the SRP, it is followed by Pade-LC, and both have leading roles in this respect in the sphere-spheroid-particle case too. Indeed the initial shape-size distribution, found in the top left plot of Fig. B.3 (App. B), pertaining to the sphere-spheroid case, is reconstructed very well by the latter and much better than the rest methods. It is noteworthy to observe that TSVD-DP and Tikh-LC retrieve the parameters $svcf$, a_{eff} and a_{var} with almost the same efficiency (Table C.2) and yet they have distinct graphical differences in the distribution reconstruction. Finally, the residual errors are essentially larger for both shapes (prolate and sphere-spheroid mixture) than in the fine-particle case we analyzed before.

The variation of the retrieved data and the mathematical hint we briefly saw through the example in Fig. 4.4, point to particle size as a plausible underlying cause for the lack of predictability of the treatment of ill-posedness for larger particles. We should note though that this does not exclude the involvement of other physical properties (e.g. shape, RI) as additional factors, since their correlation with size in non-spherical particle geometries is not fully understood although known for its creative scattering outcomes. These factors will be explored subsequently in greater detail, both theoretically and statistically through the retrievals of Pade-DP.

4.1.3 A closer look at the retrievals of Padé iteration

Let us continue the parameter analysis with the most efficient method, Pade-DP, comparing with its main antagonists Pade-LC and Tikh-DP in lesser extent. Since it is impossible to show the range of efficiency for every single parameter, shape, size, refractive index and error level, we will restrict from now on mainly to the smaller combination collection from Table 4.1, X1: $(2) \times (a, b, c) \times (\text{iii}, \text{iv}, \text{v})$, X2: $(3) \times (a, b, c) \times (\text{i}, \text{iii}, \text{v})$ and X3: $(4) \times (a, b, c) \times (\text{ii}, \text{iii}, \text{v})$ with all error levels for every case. As mentioned in the previous section (4.1.2), while the aspect ratio width (a_{var}) provides a useful tool for the comparison of different methods, it is approximated with more than 60% accuracy only in some of the cases associated with the sphere-spheroid mixture. Other than these occasions, it is largely overestimated up to 8 times the initial value in the majority of the retrievals for the oblate and prolate ensembles and will be omitted from subsequent analyses. A detailed exposure of the results is found in App. C in Tables C.3, C.6 and C.9 for Pade-DP and Tables C.12, C.15 and C.18 for Pade-LC. The tables correspond to the cases X1, X2 and X3 and include the Difference, Variability and Uncertainty percentages for every parameter and each error level shown vertically on the left side of each sub-table. Note that in this section we will use the abbreviations Dif, Var and Unc to denote the actual rates % (not appearances) for the respective ERQ. A synopsis of the retrieval ranges of a_{t}, v_{t}, r_{eff}, $svcf$ and a_{eff} for all ERQ (except Dif for $svcf$) is

4.1. General configuration with a fixed refractive index (Synthetic microphysical retrievals for non-spherical particles)

Table 4.5: Microphysical parameters retrieved with all methods for size distribution No 1, prolate particles, data error: 1% and RI: $1.5 + 0.01i$. The rightmost indication "error" corresponds to the mean relative residual error found with a forward calculation.

Parameters	n_t	a_t	v_t	r_{eff}	$svcf$	a_{eff}	a_{var}	error
Synthetic	0.1690	0.0172	0.0015	0.2588	0.000	1.3592	0.0073	1.36e-04
T S V D - D P								
Average	0.2142	0.0188	0.0017	0.2788	0.1340	1.1958	0.0434	0.0041
Var/ty	19.35%	4.46%	2.42%	2.69%	9.78%	0.31%	1.21%	9.98%
Unc/ty	24.42%	6.91%	5.38%	3.51%	13.94%	0.82%	1.77%	55.00%
T i k h - L C								
Average	0.1809	0.0163	0.0014	0.2560	0.2328	1.1290	0.0462	0.0345
Var/ty	8.06%	1.45%	0.39%	1.09%	4.06%	0.30%	1.60%	2.04%
Unc/ty	5.61%	1.15%	0.91%	1.08%	2.50%	0.23%	0.62%	9.66%
P a d e - D P								
Average	0.1277	0.0158	0.0015	0.2780	0.0972	1.2334	0.0410	0.0098
Var/ty	30.32%	4.34%	0.91%	3.30%	15.60%	0.96%	2.66%	0.56%
Unc/ty	17.47%	2.41%	1.37%	3.04%	36.13%	2.57%	8.14%	1.85%
T i k h - G C V								
Average	0.1664	0.0173	0.0016	0.2842	0.1187	1.1968	0.0440	0.0949
Var/ty	13.79%	2.32%	0.75%	1.68%	2.56%	0.12%	0.50%	6.03%
Unc/ty	11.49%	2.23%	3.23%	3.06%	16.53%	0.89%	1.93%	22.91%
T i k h - D P								
Average	0.1668	0.0169	0.0016	0.2775	0.1351	1.1852	0.0453	0.0611
Var/ty	16.09%	2.84%	0.96%	1.95%	1.76%	0.11%	0.33%	8.97%
Unc/ty	8.32%	1.63%	2.52%	2.39%	12.11%	0.80%	1.57%	26.35%
P a d e - L C								
Average	0.1269	0.0158	0.0015	0.2760	0.0744	1.2559	0.0387	0.0123
Var/ty	33.50%	4.39%	0.90%	3.39%	20.30%	0.53%	2.06%	11.28%
Unc/ty	16.16%	2.86%	1.91%	2.46%	23.86%	1.20%	6.07%	30.22%

shown in Table 4.8 for Pade-DP and in Table 4.9 for Pade-LC. Moreover, in order to specify a case from the tables we will refer to it in the compact form *(size, shape, RI, error level, parameter, ERQ)* using the numbering from Table 4.1. For instance the case (2, a, iii, 5%, v_t, Dif), focuses on the Dif % of the volume concentration related to the combination, size distribution No 2 with an oblate ensemble (a), RI: $1.5 + 0.01i$ (iii) and 5% error level. Note, that more than one values of the same kind imply multiple compact forms, e.g. (2, b, a_t, v_t), expands to (2, b, a_t) and (2, b, v_t) and, further, missing pieces of information (if any) in this form from the total of 6 will be clearly mentioned separately. Exceptionally for the parameter *svcf*, Dif is given by the absolute difference from the initial value, since the latter is zero for the prolate spheroid ensemble (Table 4.1, c). A variation less than $< 3\%$ in the ERQ is generally considered of minor significance taking into account all possible errors that are involved.

Retrieval of the R-parameters

The results show that Pade-DP retrieves the parameters a_t, v_t and r_{eff} astonishingly well. The latter are approximated with more than 85% accuracy on average, that is, for any shape, size, RI, and error level, with very few exceptions. The important microphysical parameter r_{eff} is retrieved with Dif ranges $1.00 - 13.23\%$, $0.16 - 16.37\%$ and $0.04 - 19.86\%$ for X1, X2 and X3 respectively, which include every possible combination of cases. The lowest and highest rates in each of these ranges correspond to 1% and 10% error levels, reflecting the general trend of a less accurate retrieval with increasing error level. Similarly, a_t is retrieved with Dif ranges $0.89 - 17.56\%$, $4.38 - 43.68\%$ and $0.32 - 31.25\%$, and v_t with $0.15 - 13.09\%$, $0.32 - 39.84\%$ and $0.04 - 18.11\%$, see Table 4.8. The upper range bounds, i.e. 43.68%, 31.25% and 39.84%, are isolated cases, as one can see from the respective average values 14.74%, 10.53% and 14.90% and correspond to the cases (3, iii, b, 10%, a_t), (4, ii, a, 10%, a_t) and (3, i, b, 10%, v_t)

4.1. General configuration with a fixed refractive index (Synthetic microphysical retrievals for non-spherical particles)

Table 4.6: Microphysical parameters retrieved with all methods for size distribution No 1, oblate particles, data error: 1% and RI: $1.5 + 0.01i$. The rightmost indication "error" corresponds to the mean relative residual error found with a forward calculation.

Parameters	n_t	a_t	v_t	r_{eff}	$svcf$	a_{eff}	a_{var}	error
Synthetic	0.1321	0.0134	0.0012	0.2588	0.1802	0.8290	0.0050	1.08e-04
T S V D - D P								
Average	0.2024	0.0142	0.0012	0.2480	0.3626	1.0653	0.0386	0.0050
Var/ty	9.59%	2.68%	1.78%	1.29%	1.97%	0.35%	2.82%	7.97%
Unc/ty	11.30%	2.56%	3.34%	3.80%	7.40%	1.44%	7.96%	38.22%
T i k h - L C								
Average	0.1962	0.0139	0.0011	0.2445	0.3353	1.0776	0.0402	0.0082
Var/ty	6.19%	1.68%	0.30%	1.39%	1.15%	0.14%	1.29%	1.65%
Unc/ty	13.20%	3.15%	1.04%	3.14%	3.87%	0.65%	3.41%	36.10%
P a d e - D P								
Average	0.1870	0.0138	0.0011	0.2458	0.3243	1.0835	0.0408	0.0072
Var/ty	7.08%	1.74%	0.26%	1.55%	1.46%	0.18%	1.12%	1.28%
Unc/ty	6.39%	1.62%	1.05%	1.99%	3.66%	0.59%	1.95%	22.62%
T i k h - G C V								
Average	0.1967	0.0139	0.0011	0.2466	0.3474	1.0705	0.0395	0.0092
Var/ty	5.98%	1.56%	0.31%	1.41%	1.71%	0.18%	1.88%	6.00%
Unc/ty	14.76%	3.50%	1.37%	3.52%	8.80%	1.43%	7.27%	76.48%
T i k h - D P								
Average	0.1992	0.0139	0.0011	0.2444	0.3219	1.0833	0.0411	0.0100
Var/ty	11.33%	2.81%	0.51%	2.31%	2.35%	0.21%	2.04%	0.00%
Unc/ty	5.97%	1.68%	1.06%	1.96%	5.59%	0.83%	3.50%	0.39%
P a d e - L C								
Average	0.1842	0.0136	0.0011	0.2468	0.3587	1.0686	0.0389	0.0029
Var/ty	8.34%	1.93%	0.38%	1.57%	1.59%	0.20%	2.08%	11.24%
Unc/ty	14.37%	3.65%	2.17%	3.52%	8.10%	1.31%	7.08%	47.47%

(Tables C.6-C.9) respectively. The variability and the uncertainty are also vastly low, in almost all cases for a_t, v_t and r_{eff}. Taking again the effective radius as an example, combined with any other instance (shape, RI, error level), we have Var: $0.52 - 3.45\%, 0.42 - 6.32\%$ and $0.53 - 5.65\%$ and Unc: $1.04 - 12.94\%, 0.71 - 14.56\%$ and $0.83 - 21.70\%$, for X1, X2 and X3 respectively. Evidently Var has a small variation (and much smaller than Unc), which shows the kind of desired homogeneity (solution clusters) expected from a stable method in a deliberately small solution space. The case X2 (size no 3) constitutes a worst case scenario owning in general the largest values and variation of the ERQ with respect to the different error levels.

Pade-LC is almost as good as Pade-DP in accuracy on average at the retrieval of the R-parameters, as demonstrated by the blind experiment earlier (Tables 4.2, 4.3 and 4.4), but with a few more isolated blow-up-incidences. For instance, r_{eff} is retrieved with Dif ranges $2.15 - 15.40\%$, $0.02 - 15.52\%$ and $0.02 - 15.09\%$ and v_t with $0.13 - 16.72\%$, $0.16 - 39.44\%$ and $0.23 - 19.15\%$ for X1, X2 and X3 respectively, see Table 4.9. The disagreement with Pade-DP on average is of order $\sim 1\%$, see r_{eff} and v_t in Table 4.8. A larger disagreement is found on a_t in X1 where Pade-LC has Dif: $0.08 - 36.05\%$, which is by 4.91% larger on average than the one of Pade-DP. A similar situation is to be found for the uncertainties (Unc, Var) of Pade-LC. Although the ranges are often larger (on the right side), the mean values have mostly less than 1% discrepancy from the ones of Pade-DP. For instance, the Var-range of r_{eff} in X3, is $0.50 - 12.32\%$ with a mean: 2.63% which is 0.61% more than the one of Pade-DP, see Table 4.8, X3, r_{eff}. The main counterexample is again the surface-area concentration in X1, where the Unc-range is highly expanded from the side of Pade-LC with $0.43 - 31.69\%$ (mean: 8.48%), whereas Pade-DP has $0.38 - 4.88\%$ (mean: 2.71%). There are also more rare converse examples, where Pade-DP has larger ranges (in any of the ERQ), yet its mean values are always close to Pade-LC (or lower); the most characteristic are X2, a_t, Dif and $X3, v_t$, Unc, see Table 4.8. To illustrate the comparison between Pade-LC and Pade-DP and the

relative rarity of high ERQ in general, we show in Fig. 4.8 all (27) parameter retrievals of a_t, v_t and r_{eff} for X1, X2 and X3 with respect to their Dif (upper panel) and Var (lower panel). The numbers $1 - 27$ on the x-axis correspond to the order of the results, as seen top down, in any of the Tables C.3-C.9 or C.12-C.18 top down. All parameters of the same particle size (X1, X2, or X3) appear vertically (3×3 in total) on the plots with the same symbol and no further distinction. We see clearly that most of the parameters are gathered below 15% Dif for both methods and there are only a few upward shifts from the side of Pade-LC (right plot) to higher Dif levels mostly for X1 which do not change the overall picture. Focusing now on the lower panel of Fig. 4.8 while we can see again that for both methods most of the retrieved parameters accumulate to less than 5% Var, Pade-LC has shifted a fair amount of instances to higher variability, with the most extreme discrepancies attributed to prolate-particle cases (No 18-27). The differences for Unc (not shown graphically) occur in even more irregular basis and most of them relate to the parameter a_t in X1.

The number concentration is a major struggle of the retrievals of Pade-DP showing high but mostly reasonable uncertainties (Var, Unc) for error levels 1% and 5% and at the same time the greatest accuracy losses. The best approximations of n_t belong to size No 1, partly shown on Tables 4.5-4.6. For 1% error level we have the ranges (Dif) $4.89 - 88.44\%$ (mean: 41.43%), Var: $2.82 - 23.99\%$ (mean: 12.68%), and Unc: $6.35 - 21.99\%$ (mean: 13.02%). Other than the cases for size No 1, there are limited cases of accuracy $\gtrsim 50\%$, namely (2, c, iii, 1%), (3, a, i, 1%, 5%), (3, b, i, 1%, 5%), (3, c, i, 1%). Some of these are presented in Fig. 4.9 but have been excluded from the previous thorough parameter analysis, since there are plenty of cases in which the retrieved value is hugely divergent ($\gg 2\times$) leading to very low confidence regarding its retrieval reliability. Moreover, in contrast to the other retrieved parameters, the uncertainties for n_t grow prohibitively ($>50\%$) for a 10% error level. Pade-LC shows often greater efforts in accuracy but does not really make it up, mainly due to its larger uncertainties. However, Padé iteration is the only method from the ones available here that has a better chance of providing even such approximations of n_t. Fig. 4.9 illustrates this very situation, showing an intercomparison between the Pade-DP, Pade-LC and Tikh-DP with respect to the accuracy and Unc (errorbars) of the retrieved values for the parameters n_t, a_t, r_{eff}, $svcf$ and a_{eff} through several examples. Evidently, the only instances that Tikh-DP really competes Padé belong to size No 1 (top 2 plots), which is expected since Tikh-DP is indeed the best method for this particle size, as shown earlier. However, there is mostly a quite large accuracy gap in n_t between Tikh-DP and Padé iteration (-DP / -LC) which greatly magnifies for the case X3, see Fig. 4.9 example (4, b, iii, 1%). Secondly, we investigated separately the root of the great instability that n_t undergoes and found out that it is almost entirely a numerical issue. Even tiny oscillations due to noise of any kind, come out as blow-ups in the calculation of n_t because of the function discontinuities that might occur with very small radii (see Eq. 3.1.3). Knowing this in advance, it creates an unprecedented advantage and can save us from a completely meaningless retrieval of n_t. For this reason, we can make an additional check in the norm of the very first distribution elements and exclude these contributions if they are above a point (by a measure of some norm) we gained from experience. Doing so, the retrieval of n_t goes back to "normal", e.g. (1) for Pade-DP in Table C.2, the corrected n_t is found $0.157 \, \mu m^{-1} cm^{-3}$ with Var: 15.59% and Unc: 1.43%, (2) for Pade-LC case (4, c, v, 10%), with no correction we would have Dif: 3737%, Var: 51.99% and Unc: 76.88%, and now Dif: 32.22%, Var: 12.90% and Unc: 22.18%; these quite outstanding results were chosen completely randomly. From now on, whenever n_t is included in the retrieval (Ch. 5) we will consider this correction when necessary. We note that a good indication of a potential blow-up of n_t in synthetic or real data is the pronounced difference in the order of magnitude with the surface-area concentration (a_t). The latter is the second parameter of largest disagreement between Tikh-DP and Padé iteration with the most significant differences observed in cases X2 and X3, see examples (3, c, iii, 1%) and (4, b, iii, 1%) in Fig. 4.9.

Retrieval of the shape parameters and reconstructions of shape-size distribution

We have already seen quite a few examples of reconstructions of the shape-size distribution in the context of inversion by all methods and now we are going to expand this a bit more. First of all, there is a clear limitation on the expectation of this endeavor as compared to the retrieval of the microphysical parameters. The latter are basically continuous averages weighted by the shape-size distribution, and as such, they leave out a fair amount of the distribution detail with the process of smoothing. This is

precious on the one hand since we can still get the non-shape parameters (n_t, a_t, v_t, r_{eff}) right within a reasonable tolerance even if the distributions are less precise in shape, as we saw through the diversity of distributions in Fig. B.2 and B.3 as compared to the well-retrieved data of all methods in Tables 4.5 and C.2. On the other hand, a very precise reconstruction of this two-dimensional distribution, especially in terms of shape, would require a much higher level of knowledge of the kernel functions with respect to the aspect ratio and not limit to 7 discrete values (Mieschka's database), which is the case here. Nevertheless, the reconstructions are very decent even under these circumstances. We will explore more cases of reconstructions of monomodal shape-size distributions and then we will show for the first time in literature reconstructions of bimodal shape-size distributions. First let us continue the parameter analysis of the previous section, turning to the shape-related parameters.

Regarding the shape parameters, the outcome is generally optimistic as well. The parameters $svcf$ and a_{eff} are approximated most efficiently for sphere-spheroid mixed particles and then follow prolate and oblate particles. Especially the ones related to the mixed ensemble are retrieved with near-perfect precision, see e.g. the cases (4, b, 1%, 5%, 10%, $svcf$) with $1.5 + 0.01i$ (or any RI) in Table C.9, which have the range of accuracy $80.88 - 99.29\%$ with respect to the error levels (1, 5, 10%). This is very promising taking into account that a mixture, not with the given proportions necessarily, is often a more realistic atmospheric scenario as opposed to pure non-spherical ensembles. The effective aspect ratio is retrieved steadily for all cases within the range (Dif) $0.04 - 34.20\%$, which is the union of ranges in Table 4.8 for X1, X2 and X3 (Tables C.3-C.9). However, this range might be misleading since it basically contains three extreme retrieval incidences whose Dif are not close on average, namely the range for sphere-spheroid mixtures which is very low, the one for prolate particles which is reasonable and the one for oblate particles which is only moderately good. On the one hand, for sphere-spheroid mixtures a_{eff} has the Dif-range $0.04 - 8.56\%$ (mean: 2.64%), where the boundary values correspond to the cases (2, iv, 1%) and (3, i, 10%), and for prolate particles it is retrieved within the range $2.41 - 18.64\%$ (mean: 11.17%), where the boundary values correspond to the cases (2, iv, 1%) and (4, ii, 10%). On the other hand, for oblate particles we get $11.89 - 34.20\%$ (mean: 26.85), where the boundary values correspond to the cases (3, i, 10%) and (4, ii, 1%) in Table C.6 and C.9 respectively. Although the ranges for oblate particles seem reasonable and are further associated with low uncertainties as well (see Table 4.8), the relative difference (Dif) should be less than 20% for this initial effective aspect ratio (~ 0.82) otherwise the retrieved value exceeds the value 1 and therefore the ensemble is misinterpreted as a spherical one. The parameter $svcf$ has similar behavior, i.e. there are very good approximations for the sphere-spheroid-mixed- and the prolate-particle case and mediocre ones with oblate spheroids. However, even the case of more than a 100% overestimation, e.g. the case (4, iii, 1%), Table C.9, it still conveys the message of a reduced sphericity chance ($\sim 30\%$) and therefore is useful in that sense. In general, such deviations from the initial value end up being a defect since they are immediately felt by the distribution reconstruction as we saw earlier in Fig. B.3. There are only small differences in accuracy between Pade-DP and Pade-LC, mostly in favor of Pade-LC, in the shape parameters $svcf$, a_{eff} and in a_{var} (not shown), which occasionally account to a better distribution reconstruction than the one produced by Pade-DP. However, the parameter uncertainties (Var, Unc) are on average better with Pade-DP especially in $svcf$, e.g. compare the $svcf$ of X1 (most pronounced disagreement) in Tables 4.8, 4.9 and see also for instance the cases (1, c, v, 10%) and (2, a, iii, 1%) in Fig. 4.9. The differences between Tikh-DP and Pade-DP/-LC in the shape parameters $svcf$ and a_{eff} are essentially milder than those in a_t, v_t and r_{eff}, but Tikh-DP is finally inferior in accuracy while having at the same time lower uncertainties than Pade-LC.

The distribution reconstruction is not limited to shape influence, as we showed through Fig. B.2 in Sec. 4.1.2 but it is affected by both shape and size as well as the refractive index. The reconstructions follow the same pattern described up to now, i.e. a greater accuracy potential in Padé iteration occasionally blocked by high uncertainties especially in the presence of large data errors. As mentioned earlier in Sec. 4.1, a sense of the reconstruction accuracy is obtained here with Dist and similarly the uncertainties are obtained with ratios of the same notion of Var and Unc used up to now. Fig. 4.5 and B.4 (App. B) show the error-level evolution of the produced reconstruction by Pade-DP, Pade-LC and Tikh-DP (left to right) for the cases (2, c, iii) and (4, a, ii) respectively for 1% (2nd row) and 10% (3rd row) error level; the initial shape-size distribution is shown in the uppermost plots for both figures. In addition, the triple (Unc, Dist, Var) is given in the title of each reconstruction. Pade-DP and Pade-LC achieve a more accurate reconstruction than Tikh-DP in both cases (2, c, iii) and (4, a, ii) and both error levels. Indeed, Padé iteration has less pronounced artifacts than Tikh-DP and preserves the location of

the peak (see also colorbars) and its width better. For instance, the case (2, c, iii, 1%) in Fig. 4.5 Dist is larger for Tikh-DP and the reconstruction has a stronger spread in the radius axis and more artifacts in the bottom of the graph. Pade-LC achieves a much better reconstruction for the same case but 10% error level, see lowermost panel of Fig. 4.5, but it has a dubious uncertainty (Unc) of 66.45%, which is more than twice the ones of Pade-DP and Tikh-DP. The case (4, a, ii) in Fig. B.4 essentially reconfirms the situation in another setting. The Tikh-DP reconstruction presents much stronger elongation in the aspect-ratio axis as well as the radius axis, and there is also some otherwise negligible noise in the beginning (leftmost) of the graph. However, in the case of 10% error level there is a reduced chance of $\sim 50\%$ (Unc) from the side of Pade-DP/-LC of reaching this accuracy, which is much more than the one of Tikh-DP (23.50%), see lowermost panel of Fig. B.4. Furthermore, the variability is considerably lower for Tikh-DP. However, a simple rough calculation for the worst-case scenario (high deviation from the average accuracy) for Padé iteration accounting both Var and Unc shows that it is still better than the one of Tikh-DP, which is the rule for many of the cases.

There is a milder but noteworthy competition between Pade-DP and Pade-LC in distribution reconstructions mostly expressed for 5% or 10% error level. Fig. 4.6, shows several examples of reconstructions for a comparison between Pade-DP and Pade-LC, through which we can also see noisy or less trustworthy outcomes for both methods. For instance, focusing on the uppermost row of plots, i.e. the case (2, c, i, 5%), Pade-LC demonstrates again better accuracy but much higher uncertainty (Unc: 51.54%) than Pade-DP (Unc: 13.81%), which essentially fails to capture the shape of the initial distribution in greater detail. We note that there are plenty of cases with very smooth and nice distribution results that are not shown here, but instead the chosen cases cover mostly difficult encounters for Padé iteration, which may be of practical interest in a real application. Evidently a high error level damages the reconstructions very distinctly. The mildest effect is expressed through the aforementioned spread in radius- or aspect ratio axis, while stronger noise involves additional "modes" (artifacts), see e.g. the lowermost panel of Fig. 4.5. However, it is important to realize that in an experimental case (real data) multimodality is quite a probable scenario and our intuition about what is noise or a real extra mode has to be conformed accordingly. As a general remark, the location of the peak in the radius axis is best reproduced, as compared to the (radius) mode width, the aspect ratio width and the height of the peak, i.e. the volume distribution (colorbar). Indeed even in cases of mistreatment of the shape (aspect ratio) the location of peak in the radius axis is still obtained, see e.g. the uppermost or lowermost panel of Fig. 4.6. The plots in Fig. B.4 for Padé iteration correspond to the best we can do for a case with oblate spheroids; most often the distributions are falsely shifted upwards, resembling those of the sphere-spheroid mixture. The refractive index, obviously plays a crucial role in the inversion even if the initial shape- and size settings are the same, since the kernel functions impose different levels of smoothing depending on its value. We can see this through the examples on the 2nd and 3rd row of plots in Fig. 4.6 referring to the cases (3, c, iv, v, 10%). These instances show the reconstruction of same shape-size distribution for the extreme cases of weakly absorbing particles (RI : $1.6 + 0.001i$) and very absorbing particles (RI : $1.7 + 0.05i$), illustrating the infiltration of noise and the enhanced difficulty for an approximation associated with the absorbing case.

Bimodal shape-size distributions

In this section we would like to show the potential of our approach in retrieving bimodal shape-size distributions, restricting to reconstructions produced by Pade-DP. Multimodality in a two-dimensional aerosol distribution has never been studied, as a result of the mere absence of a 2D-representation of the distribution itself from contemporary bibliography for the sake of simplicity. Indeed, in order to even build a shape-size distribution of desired modes (location, peak, etc), experience of some level is required as compared to the case of a usual size distribution since there is no standard model and the additional dimension (aspect ratio) expands significantly the possible outcomes. The construction of such distributions is based here again on simple multiplication of independent log-normal size distributions and aspect ratio distributions. The parameters used to create the synthetic data and distributions are shown in Table 4.7 (BMD: 1-6). We will investigate shape-size distributions which have two distinct modes either on the radius axis formed by a bimodal log-normal distribution (BMD: 1-4) or on the aspect ratio axis (BMD: 5, 6) with greater emphasis on the latter.

The new inversion examples were ran 15 times for 1% error level, choosing as usual 5 best solutions (out of 36) for each run and the reconstruction plots are shown in Fig. 4.7 and B.5 (App. B) containing

4.1. General configuration with a fixed refractive index (Synthetic microphysical retrievals for non-spherical particles)
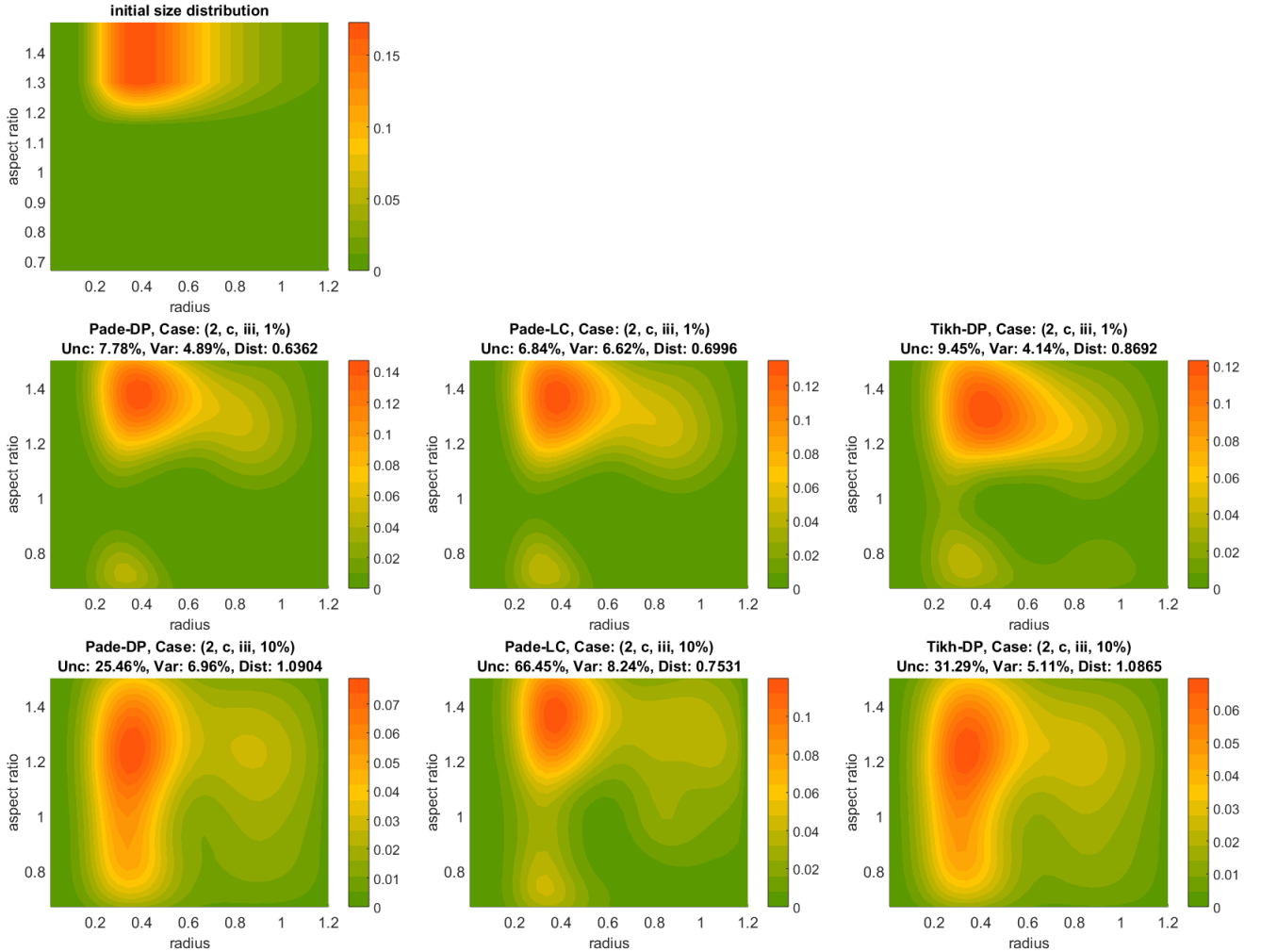
Figure 4.5: Shape-size distribution reconstructions produced by Pade-DP, Pade-LC and Tikh-DP (left to right) for the case (2, c, iii) respectively for 1% and 10% error level. The uppermost plot corresponds to the initial shape-size distribution. The triple (Unc, Dist, Var) in the title of each plot refers to error-related quantities of shape-size distribution described in Sec. 4.1.

also information about the involved uncertainties in their titles. The top first and second panels of Fig. 4.7 depict examples of a fixed mixture of oblate and spherical particles combined with very diverse bimodal log-normal distributions, each of which marrying fine (BMD 1) and very fine absorbing particles (BMD2) with coarse ones, see Table 4.7. In both of these cases the reconstructions are remarkably good at making out the different modes not only locating the peaks but also the transition between the modes. This detail is especially pronounced in the BMD 2, see the smaller 3D plots within the main plots. The radius-width and the aspect ratio width are reproduced with good accuracy as well, with BMD 1 allowing more noise into the plot. The third plot from the top of Fig. 4.7 (BMD 3) relates to a case of prolate particles where both modes pertain to coarse particles. The reconstruction faces greater difficulty but all in all has similar characteristics, i.e. identifying two modes which overall resemble the initial trends. The second mode (right), however, appears to be noisier and its peak is shifted on downward and right and we further observe a height suppression of the peaks and some artifacts in the bottom of the graph. The modes on the last plot (BMD 4) pertain to very coarse particles combined with the sphere-spheroid mixture used extensively in the previous simulations. Here, in addition to the overall good response of the method, we can see that the reconstruction senses also the small height difference between the mode peaks. The second mode (again) suffers bigger errors but within a reasonable level.

Shape bimodality appears to be more problematic, probably as a result of the limited access we have on kernel values with respect to the aspect ratio. Fig. B.5 shows our attempts to reproduce two

74

4.1. General configuration with a fixed refractive index (Synthetic microphysical retrievals for non-spherical particles)
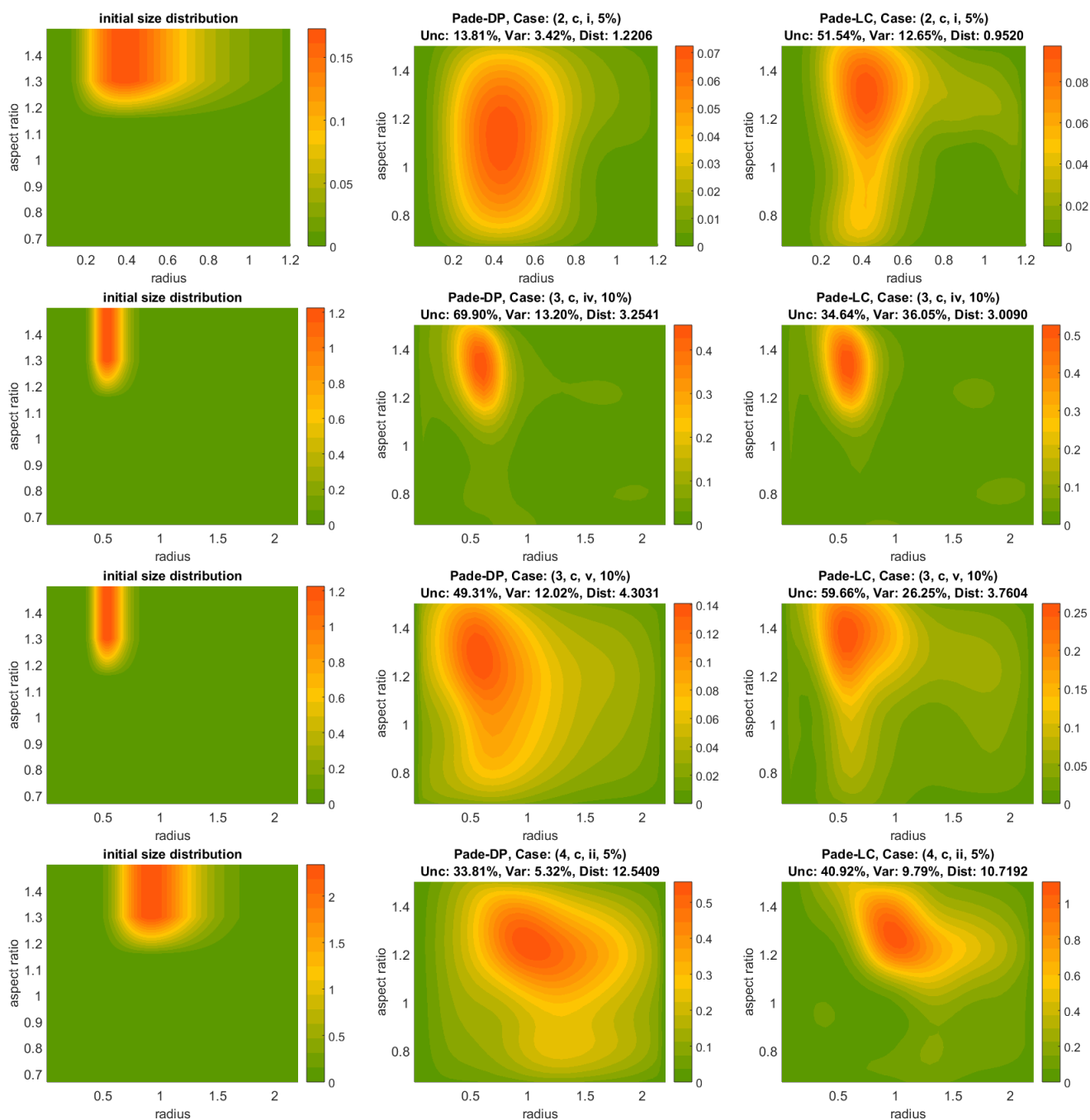
Figure 4.6: Shape-size distribution reconstructions produced by Pade-DP, Pade-LC for several cases. From left to right: initial shape-size distribution, Pade-DP-reconstructed distribution, Pade-LC-reconstructed distribution. The triple (Unc, Dist, Var) in the title of each plot refers to error-related quantities of shape-size distribution described in Sec. 4.1.

atmospheric settings (BMD 5, 6 in Table 4.7) of a fixed particle size combined with a mixed ensemble consisting of oblate and prolate particles. The example BMD 5 (upper panel) shows correct identification and detection of the two modes (location, radius width) but the strength of the modes (peak heights) is reversed. The second example, BMD 6 (lower panel) pertains to weakly absorbing particles (in contrast to BMD 5) with much larger radius width. The relative strength of modes and their separation is well felt by the reconstruction, but the upper mode is noisy and the peak of the lower mode is shifted downward. Bimodal distributions with vicinal shape modes, e.g. using a prolate ensemble with $\eta = 1.15$ and $\eta = 1.5$,

are often misrepresented after the inversion, showing the two modes merged to a single wider one and thus revealing a shortcoming in sensitivity. We should underline that the right choice of spline number and degree by the algorithm (SA1) seems to be more delicate when the bimodality is on the aspect ratio axis. In this case, further simulations showed that a smaller projection dimension is often needed, i.e. a small number of spline points and/or degree, in order to better identify the two modes.

As demonstrated, the results are generally very optimistic also for the case of bimodalities. The reconstructions of such shape-size distributions are quite obviously associated with more limitations than the ones with a single mode. High error levels can have a devastating effect in the reconstruction, causing distinct (mode-like) artifacts, shifting, conflation or even disappearance of a mode. Similar effects are to be observed for a higher absorption level, which further has a stronger impact as compared to monomodal distributions. The results shown here are relatively limited as compared to the range of synthetic possibilities that a two-dimensional distribution can offer. Furthermore it is unknown what is the exact connection and implications regarding bimodal two-dimensional distributions and real atmospheric scenarios involving aerosols and future field work is needed to explore this experimentally.

Table 4.7: Simulation setup for the reconstruction of bimodal shape-size distributions (BMD) with a fixed refractive index and 1% error level. The following combinations were used: BMD 1: (1, a, iii) , BMD 2: (2, a, iii) , BMD 3: (3, e, ii) , BMD 4: (4, d, i) , BMD 5: (3, b, iii) , BMD 6: (4, c. i).

log-normal distribution

No	1	2	3	4	5	6
median radius	$[0.05, 1.4]$	$[0.2, 1]$	$[0.5, 1.6]$	$[0.8, 1.7]$	0.5	0.8
mode width	$[2.3, 1.2]$	$[1.6, 1.4]$	$[1.3, 1.2]$	$[1.2, 1.2]$	1.2	1.4
radius range (µm)	$[0.01, 2.2]$	$[0.01, 2.2]$	$[0.01, 2.2]$	$[0.01, 2.2]$	$[0.01, 2.2]$	$[0.01, 2.2]$
number concentration	$[600, 1]$	$[30, 1]$	$[12, 1]$	$[6, 1]$	1	1

aspect ratio distribution

$$(a) \quad \begin{cases} 1/2, & \text{if } \eta = 0.87, \\ 1/2, & \text{if } \eta = 1, \end{cases} \qquad (b) \quad \begin{cases} 1/3, & \text{if } \eta = 0.77, \\ 2/3, & \text{if } \eta = 1.3, \end{cases} \qquad (c) \quad \begin{cases} 1/3, & \text{if } \eta = 0.87, \\ 2/3, & \text{if } \eta = 1.3, \end{cases}$$

$$(d) \quad \begin{cases} 1/3, & \text{if } \eta = 0.87, \\ 1/3, & \text{if } \eta = 1, \\ 1/3, & \text{if } \eta = 1.15, \end{cases} \qquad (e) \quad \begin{cases} 1/2, & \text{if } \eta = 1.3, \\ 1/2, & \text{if } \eta = 1.5, \end{cases}$$

refractive index

(i) 1.33+0.001i   (ii) 1.4+0.005i   (iii) 1.5+0.01i

4.1.4 Collateral retrieval statistics

We can get some useful generalizations, by taking the mean of the ERQ over all parameters with respect to the factor we want to examine (error, shape, size and RI). The parameter *svcf* is excluded from the mean of Dif (%), but included in the mean of Var and Unc, and n_t is entirely left out. We emphasize that the mean is computed by the values in Tables C.3-C.9 and not as the mean of the mean values from the synoptic Table 4.8. All the following analysis refers exclusively to Pade-DP.

On average the effective aspect ratio for oblate particles gets better approximations for larger sizes reducing their Dif from 29.24% (size No 2) to 23.33% (size No 4), and prolate ones get worse approximations raising their Dif from 10.24% to 12.52%. The parameter *svcf* for prolate particles also gets worse on average with absolute Dif range $0.9697 - 1.6290$ for larger sizes but for oblate ones it increases and then drops again with 0.1699, 0.2022, 0.1794 for the sizes No 2, 3 and 4 respectively. The uncertainties
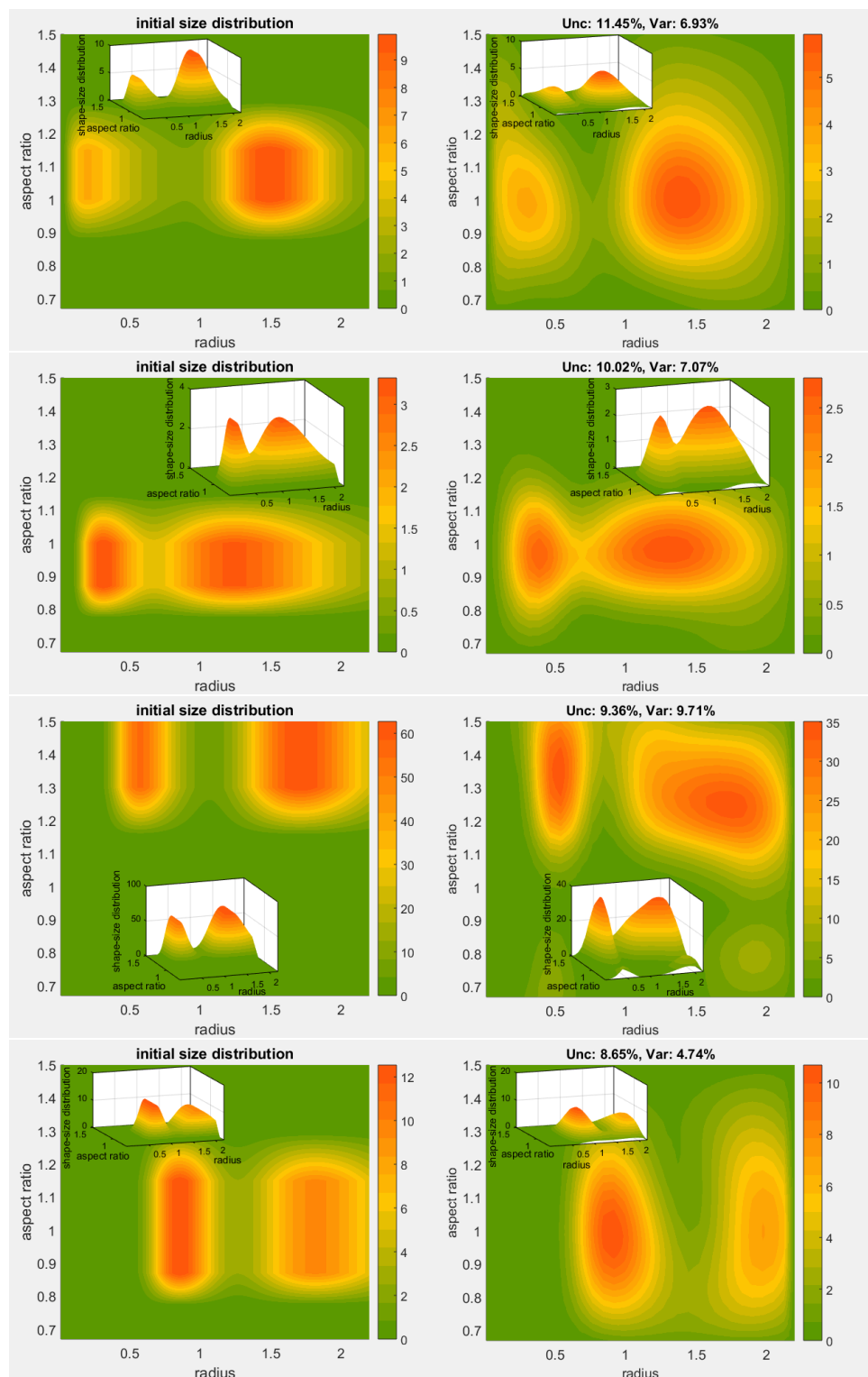
Figure 4.7: Reconstructions of bimodal shape-size distributions with two distinct radius-modes. Top down, right: reconstructions corresponding to the BMD 1-4 from Table 4.7. Left: Initial shape-size distributions for the reconstructions on the right. Smaller plots within the main plots show the shape-size distribution in 3D.

for a_{eff} belong on average within the Unc-range 1.39-4.05% for all sizes, with the prolate shapes in size No 2 having slightly the largest values (Unc); the variability with less than 1% on average is considered

77
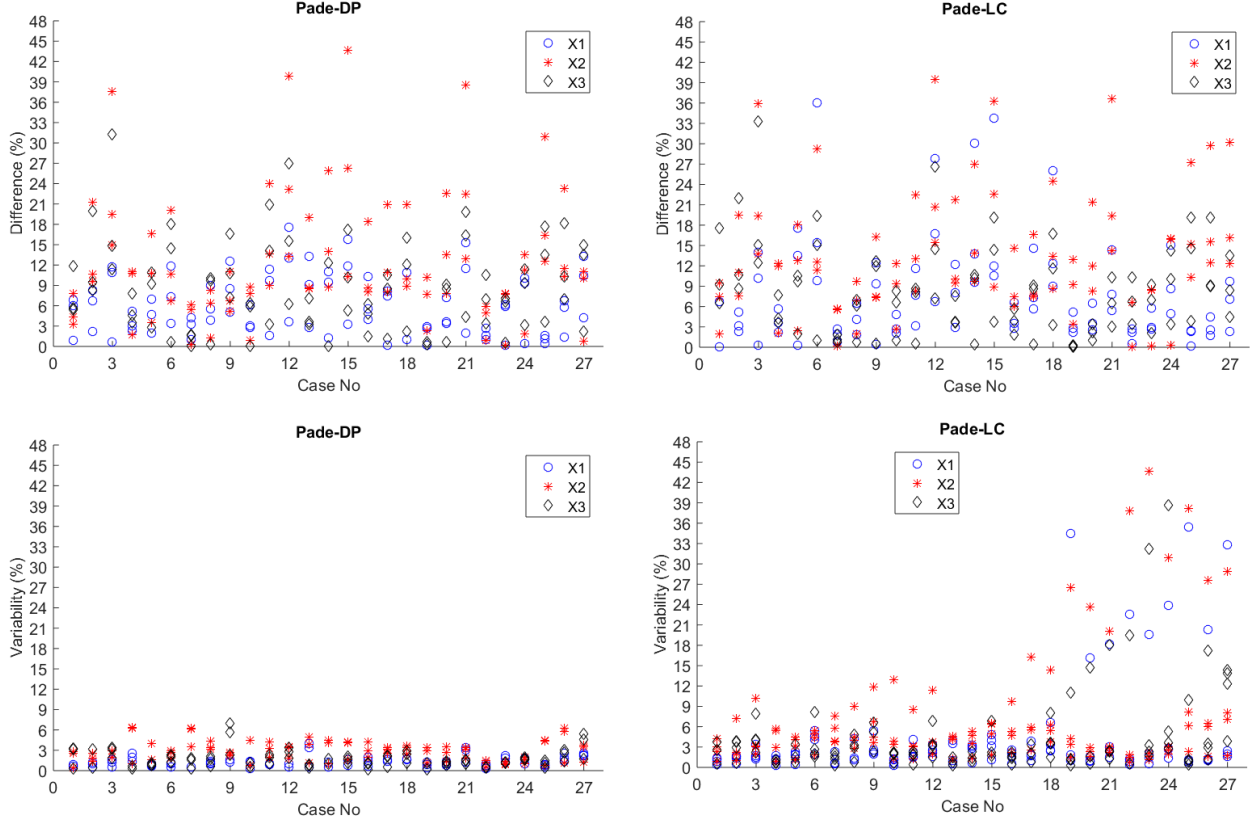
Figure 4.8: All parameter retrievals of Pade-DP (left) and Pade-LC (right) for a_t, v_t and r_{eff} for X1, X2 and X3 with respect to their Dif (upper panel) and Var (lower panel). The numbers $1-27$ on the x-axis correspond to the order of the results as seen top down in any of the Tables C.3-C.9 or C.12-C.18

insignificant. On the other hand the uncertainties for *svcf* are much more significant on average, with Unc: $[7.11\%, 6.46\%, 34.18\%]$ for X1, $[15.82\%, 15.05\%, 39.15\%]$ for X2 and $[13.52\%, 13.65\%, 26.46\%]$ for X3, where every triple refers to oblate, sphere-spheroid-mixed and prolate particles respectively. We see that Unc essentially doubles for larger sizes (size No $2 \to 3, 4$) between oblate and sphere-spheroid-mixed particles, and prolate particles have by far the largest rates for all sizes. The variability also follows a similar pattern but with much lower values, i.e. $[2.22\%, 2.18\%, 15.18\%]$ for X1, $[5.78\%, 7.25\%, 17.74\%]$ for X2 and $[4.01\%, 3.43\%, 11.08\%]$ for X3.

Now, we would like to quantify the effect of the initial data noise to the retrieved values. The transition to higher error levels for the parameters a_t, v_t, r_{eff} and a_{eff} costs on average less than 4% increase in accuracy, while the mean range for all error levels and all cases is $5.69 - 16.48\%$ (Dif). For instance, in Table 4.8 we see that a_t is retrieved on average 8.17%, 14.74% and 10.53% for X1, X2 and X3 which fall within the aforementioned range. More specifically, using Tables C.3-C.9 we find that its Dif for 1%, 5% and 10% error level is $[4.59\%, 7.45\%, 12.46\%]$ for X1, $[10.30\%, 14.16\%, 19.75\%]$ for X2 and $[4.00\%, 11.21\%, 16.38\%]$ for X3. Notice that the greater accuracy losses occur for the cases X2 and X3, which is a more general feature of larger particles, see Table 4.8. The average range for Unc for all error levels and all parameters is $1.35 - 12.67\%$ with an average of 4.27% and 5.15% for the data-error transitions $1 - 5\%$ and $5 - 10\%$ respectively. For instance, v_t is retrieved with mean Dif $[1.35\%, 5.07\%, 8.95\%]$ for X1, $[2.00\%, 6.92\%, 11.40\%]$ for X2 and $[1.38\%, 5.57\%, 12.67\%]$, where the triples refer to the transition $1\% \to 5\% \to 10\%$ in sequence. The variability is very low, as we have seen previously, and surprisingly the different error levels do not change this significantly so that we have an average range of $1.78 - 4.12\%$ for every case.

4.1. General configuration with a fixed refractive index (Synthetic microphysical retrievals for non-spherical particles)
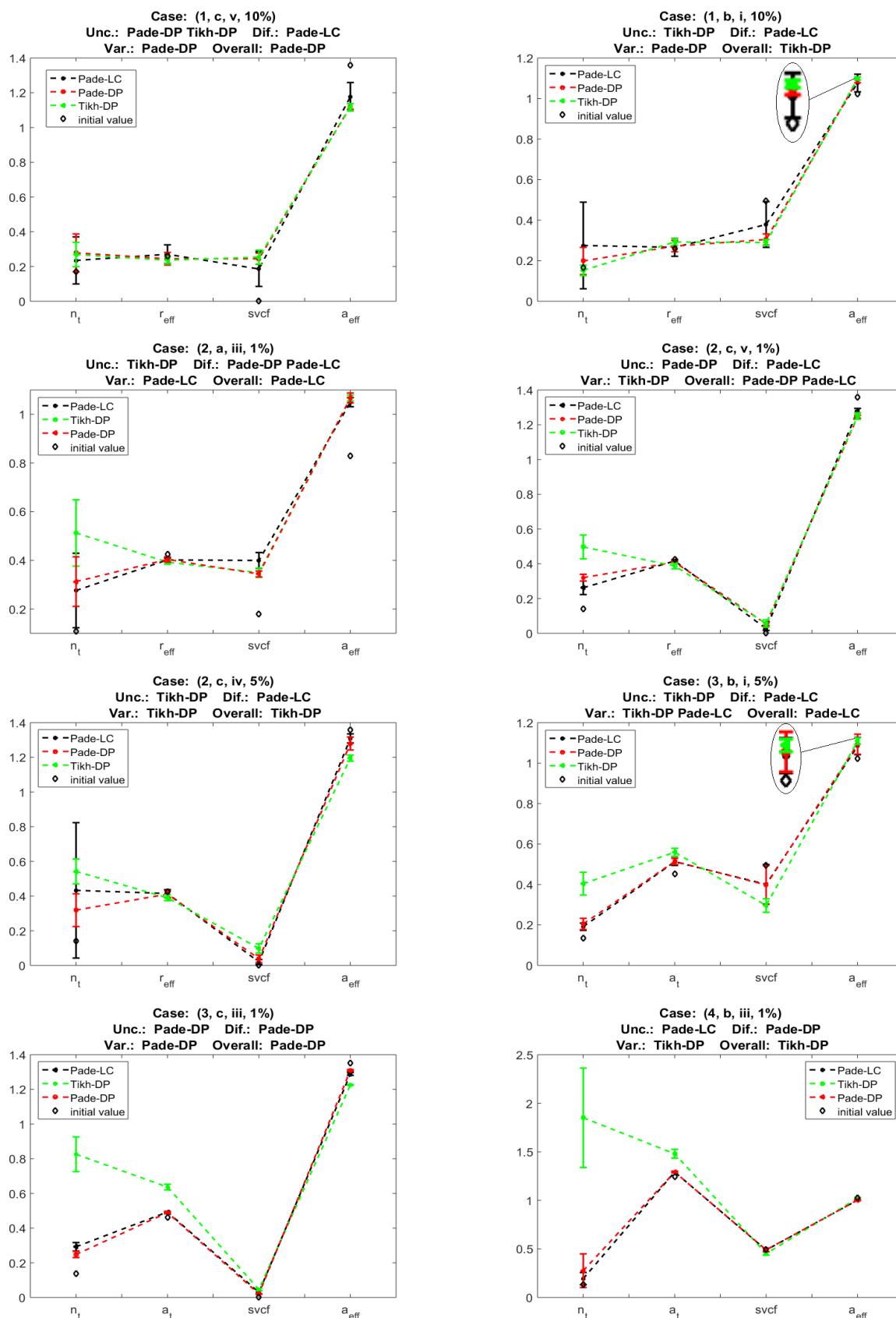
Figure 4.9: Comparison with respect to the accuracy and uncertainty of n_t, r_{eff}, *svcf* and a_{eff} between Pade-DP, Pade-LC and Tikh-DP through several simulation examples. The title of each plot identifies the specific example and it further reports the "best" method found for these parameters in total with respect to Unc, Dif, Var and Overall.

4.1. General configuration with a fixed refractive index (Synthetic microphysical retrievals for non-spherical particles)

Table 4.8: Synopsis of regularization results shown in Tables C.3-C.9 (Pade-DP). The parenthesized terms show the mean value of the respective ERQ within the specified range.

Cases: (2, a-c, iii-v, 1%, 5%, 10%) (X1)

Parameters	a_t	v_t	r_{eff}	$svcf$	a_{eff}
Difference	$0.89-17.56\%$ (8.17%)	$0.15-13.09\%$ (3.68%)	$1.00-13.23\%$ (6.29%)	$-$	$0.04-30.79\%$ (13.92%)
Variability	$0.53-3.95\%$ (1.53%)	$0.27-2.51\%$ (0.98%)	$0.52-3.45\%$ (1.42%)	$0.95-29.14\%$ (6.52%)	$0.11-2.07\%$ (0.54%)
Uncertainty	$0.38-4.88\%$ (2.71%)	$0.75-13.51\%$ (5.13%)	$1.04-12.94\%$ (5.29%)	$3.20-61.48\%$ (15.92%)	$0.48-5.90\%$ (1.77%)

Cases: (3, a-c, i, iii, v, 1%, 5%, 10%) (X2)

Parameters	a_t	v_t	r_{eff}	$svcf$	a_{eff}
Difference	$4.38-43.68\%$ (14.74%)	$0.32-39.84\%$ (14.90%)	$0.16-16.37\%$ (7.78%)	$-$	$0.53-34.20\%$ (13.96%)
Variability	$0.74-6.29\%$ (3.02%)	$0.98-6.24\%$ (2.94%)	$0.42-6.32\%$ (2.73%)	$2.82-27.71\%$ (10.25%)	$0.27-2.81\%$ (1.27%)
Uncertainty	$0.73-15.88\%$ (4.91%)	$0.75-14.47\%$ (6.78%)	$0.71-14.56\%$ (6.15%)	$2.44-84.41\%$ (23.34%)	$0.32-8.21\%$ (2.97%)

Cases: (4, a-c, ii, iii, v, 1%, 5%, 10%) (X3)

Parameters	a_t	v_t	r_{eff}	$svcf$	a_{eff}
Difference	$0.32-31.25\%$ (10.53%)	$0.04-18.11\%$ (6.79%)	$0.04-19.86\%$ (8.69%)	$-$	$0.65-31.50\%$ (12.79%)
Variability	$0.17-3.43\%$ (1.44%)	$0.17-6.98\%$ (1.64%)	$0.53-5.65\%$ (2.02%)	$1.22-25.08\%$ (6.17%)	$0.15-1.64\%$ (0.66%)
Uncertainty	$0.67-10.94\%$ (4.09%)	$0.91-\%28.50$ (6.54%)	$0.83-21.70\%$ (6.05%)	$3.18-61.10\%$ (17.87%)	$0.44-5.38\%$ (2.51%)

Dependency on shape, size, and refractive index

Looking back to the discussion started in Sec. 4.1.1 with the upper panels of Fig. 4.4 and also the analysis from Tables 4.2-4.3, we have established that particle size makes an essential distinction regarding the condition of the linear systems involved and the efficiency with which the parameters are retrieved. Moreover, we have previously demonstrated in Sec. 3.5 the smoothing effect of shape and refractive index via the scattering efficiencies, which ultimately translates to ill-posedness in the inversion. We would like to explore further the strength of these factors relative to one another and with respect to the retrieved data. The effects of ill-posedness on spherically modelled particles (3.1.9), most suitably used to model small particles, are usually quite distinct following the general rule of increasing deficiency with increasing imaginary part and/or decreasing real part of the RI and/or particle size. It is not striking that the complexity of non-spherical geometries and the additional smoothing that is imposed by the generalization of the Lorenz-Mie model (additional integration) will make it hard to make sense of possible patterns. An SVD-analysis is an attempt for a theoretical answer.

The plots on the middle panel of Fig. 4.4 depict Picard-plots with variable refractive index, i.e. $1.6+0.001i$ (left) and $1.7+0.05i$ (right), and a fixed shape-size distribution formed by the sphere-spheroid mixture in Table 4.1 and the size distribution No 2. The plots show that the decay of SVD-coefficients is markedly disturbed for the much more absorbing case with $1.7+0.05i$. However, the falling trend remains in a safe position with respect to the singular values and does not seem to yield a much bigger risk. Further examples show that oscillations in the decay rate of the SVD-coefficients, are a general characteristic of additional ill-posedness, here imposed by absorption, and can be more aggressive than the ones depicted. Shape alteration produces a similar effect to the refractive index, see the Picard-plots in the lowermost panel of Fig. 4.4 for oblate (left) and prolate spheroids (right). Here we used the size distribution No 3 and a refractive index fixed to $1.33+0.001i$. In this particular example, prolate particles are slightly more likely to compromise the retrieval. The differences of oblate vs prolate spheroids start to grow large when we add more absorption (not shown), whereby we observe a more rapid change from the side of prolate spheroids. The response to the case of sphere-spheroid mixture is much more unpredictable in the general case, but in many cases follows the trend of the less oscillatory of the two shapes (oblate or prolate).

4.1. General configuration with a fixed refractive index (Synthetic microphysical retrievals for non-spherical particles)

Investigating more examples leads to the realization that particle size has the most drastic signature, as strongly indicated by the upper panel of Fig. 4.4. Indeed, varying the combinations of shape and refractive index for a fixed size, does not alter in an essential manner the relation between the decay rates of the singular values and the SVD-coefficients. Thus, particle size poses a greater risk in theory in the presence of errors as opposed to shape and refractive index. The risk increases with increasing particle size, and as we saw, particles with effective radius $\sim 0.95\,\mu m$ (X3) have already reached the point where the Picard condition is not satisfied. We performed limited experiments (not shown) and even larger particles with $r_{\mathrm{eff}} = 1.2$ and $1.4\,\mu m$, in which we assured that this was not just a worst case scenario, but the rule. These instances showed that the SVD-coefficients get overwhelmed by errors and oscillate over the graph of the singular values regardless of the shape or the refractive index. This does not mean that the method (Pade-DP) is most likely to fail but rather that when it fails, the solutions will be more assailable to errors than they would be for smaller sizes. This might explain why the ranges of the uncertainties are mainly spreading for the largest particles (No 2 and 3). For example, the volume concentration has the Unc ranges $0.75 - 13.51\%$, $0.75 - 14.47\%$ and $0.91 - 28.50\%$ for X1, X2, and X3 respectively, see Table 4.8. We note though, that retrievals with size No 2 have smaller Unc only by 1.25% and 2.67% on average from the sizes No 4 and 3 respectively.

Yet, it remains inconclusive from the SVD-analysis, if any of the two other factors, namely shape and refraction, or any combination of the latter with size, has greater effects, which suggests that these parameters are too involved and span a greater range of non-trivial possibilities of response. The theoretical hints are mainly applicable whenever the regularization effects are milder, and since Pade-DP handles robustly most of the occasions, we do not expect to see clearly the aftermath of the effects discussed. A number of examples indicates that shape restricts or suspends the effect of absorption in favor of the retrieval. Let us consider cases with 1% error level to minimize the error involvement, e.g. $(2, a\text{-}c, r_{\mathrm{eff}})$ in Table C.3. Then, the order of Dif (min-to-max) is $1.6 + 0.001i \lesssim 1.5 + 0.01i < 1.7 + 0.05i$ for oblate ensembles, $1.6 + 0.001i < 1.7 + 0.05i < 1.5 + 0.01i$ for sphere-spheroid mixed ensembles, and $1.6 + 0.001i \lesssim 1.7 + 0.05i \lesssim 1.5 + 0.01i$, for prolate ensembles; the differences in Var and Unc are very subtle to analyze. The converse, i.e. fixing a refractive index and observing the oblate vs prolate instances interchange in retrieval efficiency, is also encountered. For instance, the cases $(3, a_{\mathrm{t}}, v_{\mathrm{t}}, r_{\mathrm{eff}})$ in Table C.9 are found to be more troublesome (higher Dif) for prolate than oblate spheroids for the most absorbing case $1.7 + 0.05i$, supporting the theoretical expectation we saw before (SVD). However, for $1.33 + 0.001i$ we observe the opposite effect and for $1.5 + 0.01i$ we have equivalence.

The seemingly undirected ill-posedness between shape, size and refraction can be addressed again in statistical terms in the retrievals of Pade-DP. The largest variation on average in accuracy occurs with respect to the refractive index, having the Dif range $9.82 - 15.64\%$ and the order of increasing Dif is as follows, $1.6 + 0.001i < 1.5 + 0.01i \lesssim 1.7 + 0.05i < 1.4 + 0.005i < 1.33 + 0.001i$. The first thing to notice is that, the less accurate case on average is the one with the smallest real part of RI (1.33) and not the one with the largest imaginary part of RI (0.05). Moreover, this order conforms in the most part with the one found on average by arranging (min-to-max) the examined refractive indices according to the condition numbers of the discretization matrices using the best solutions of Pade-DP. The exception is the interchange of 1.7+0.05i, 1.5+0.01i, which is a negligible discrepancy since they have vicinal condition numbers. Shape and size are the next in order, and for all parameters we have Dif range $8.99 - 12.95\%$ with $b \lesssim c < a$, and $8.02 - 12.85\%$ with No 2 < No 4 < No 3, where we used the notation from Table 4.1. On the other hand, the uncertainty (Unc) is varying more with respect to shape $5.10 - 10.85\%$ on average and $a \lesssim b < c$ and then follow the RI with $6.52 - 9.40\%$ and size with $6.16 - 8.83\%$; the order with respect to RI and shape remain the same. The variability, as already shown, is more subtle and has the average range 2-4% for all ERQ and the RI-order $1.6 + 0.001i < 1.4 + 0.005i < 1.5 + 0.01i \lesssim 1.7 + 0.05i < 1.33 + 0.001i$, and the same order of shape and size with Unc.

Summarizing the previous analysis, we saw that retrievals with larger particle size appear to be more susceptible to errors inherently, while in practice for Pade-DP the refractive index and shape are associated with the largest losses in accuracy and higher uncertainties on average. The refractive index $1.33 + 0.001i$ and the size No 2 appear to be the most problematic on average. Prolate shapes raise the level of uncertainties on average and oblate ones lower the level of accuracy. Evidently, size, shape and RI are benchmarks for the retrieval efficiency and even partial knowledge allows to some extent a better judgement of the difficulty and the odds of a successful retrieval.

4.1. General configuration with a fixed refractive index (Synthetic microphysical retrievals for non-spherical particles)

Table 4.9: Synopsis of regularization results shown in Tables C.12-C.18 (Pade-LC). The parenthesized terms show the mean value of the respective ERQ within the specified range.

Cases: (2, a-c, iii-v, 1%, 5%, 10%) (X1)

Parameters	a_t	v_t	r_{eff}	$svcf$	a_{eff}
Difference	$0.08-36.05\%$ (12.08%)	$0.13-16.72\%$ (4.98%)	$2.15-15.40\%$ (6.09%)	–	$0.33-33.10\%$ (12.51%)
Variability	$0.67-5.44\%$ (2.19%)	$0.25-2.54\%$ (1.07%)	$0.48-4.14\%$ (1.86%)	$0.61-35.38\%$ (10.34%)	$0.18-1.59\%$ (0.78%)
Uncertainty	$0.43-31.69\%$ (8.48%)	$1.29-14.65\%$ (6.40%)	$1.06-23.10\%$ (8.96%)	$4.78-86.85\%$ (33.34%)	$0.50-6.87\%$ (3.82%)

Cases: (3, a-c, i, iii, v, 1%, 5%, 10%) (X2)

Parameters	a_t	v_t	r_{eff}	$svcf$	a_{eff}
Difference	$5.64-36.29\%$ (15.66%)	$0.16-39.44\%$ (15.81%)	$0.02-15.52\%$ (8.45%)	–	$0.10-31.56\%$ (14.02%)
Variability	$1.57-6.53\%$ (3.59%)	$0.85-8.11\%$ (3.63%)	$0.72-7.04\%$ (3.28%)	$2.93-43.69\%$ (15.70%)	$0.48-4.10\%$ (1.85%)
Uncertainty	$0.79-12.10\%$ (4.41%)	$0.73-18.05\%$ (6.50%)	$0.57-18.86\%$ (6.52%)	$2.16-66.77\%$ (24.57%)	$0.36-6.06\%$ (2.88%)

Cases: (4, a-c, ii, iii, v, 1%, 5%, 10%) (X3)

Parameters	a_t	v_t	r_{eff}	$svcf$	a_{eff}
Difference	$0.24-33.34\%$ (10.95%)	$0.23-19.15\%$ (6.42%)	$0.02-15.09\%$ (7.17%)	–	$0.35-29.82\%$ (11.88%)
Variability	$0.29-4.05\%$ (1.82%)	$0.26-14.31\%$ (2.26%)	$0.50-12.32\%$ (2.63%)	$1.16-38.68\%$ (9.27%)	$0.26-3.07\%$ (0.90%)
Uncertainty	$0.58-9.85\%$ (4.07%)	$0.84-20.78\%$ (5.95%)	$0.75-18.85\%$ (6.32%)	$2.69-70.74\%$ (22.26%)	$0.42-6.51\%$ (2.71%)

4.1.5 The ideal lidar setup

There is a sort of ongoing debate nowadays between people in the lidar industry and researchers about whether or not the optical products offered by lidars at the present moment are sufficient in order to carry out the microphysical inversion. The lidar setup $3\beta + 2\alpha$, with 3 backscatter coefficients in 355, 532 and 1064 nm and 2 extinction coefficients in 355, 532 is established to be the minimum requirement to study at least spherically modelled particles, with a rather rich literature backing it, e.g. [14, 86, 107, 113, 131], so that those 5 channels are part of virtually any Elastic lidar nowadays. Furthermore, recent research studies confirmed that depolarization signals have to be incorporated in the usual $3\beta + 2\alpha$ in order to study non-spherically modelled particles, see [18, 112]. Lately this debate was reduced to how many depolarization channels are sufficient, at least among the already existing ones in today's lidar technology, i.e. the 355, 532 and 1064 nm horizontally polarized backscatter. Although our investigations targeted this very question in the beginning, soon it was updated to "what is the ideal channel combination", as it was early realized that certain combinations might be detrimental or less advantageous. Moreover, numerous results from campaigns (e.g. SAMUM) underline the necessity of the use of depolarization information in order to differentiate between particle non-sphericity levels. This is why all Raman-Elastic lidars are equipped currently with at least 1 depolarization channel (d), usually in 532 nm, and therefore the setup $3\beta + 2\alpha + 1d$ is a minimum is our tests here.

The simulations are conducted with Pade-DP and cover the following lidar setups:

$$(1) \quad 3\beta + 3\alpha + 3d \quad (333),$$
$$(2) \quad 3\beta + 3\alpha + 1d(532) \quad (331),$$
$$(3) \quad 3\beta + 2\alpha + 3d \quad (323)$$
$$(4) \quad 3\beta + 2\alpha + 2d(355, 532) \quad (322),$$
$$(5) \quad 3\beta + 2\alpha + 1d(355) \quad (321^1),$$
$$(6) \quad 3\beta + 2\alpha + 1d(532) \quad (321^2),$$

where the parenthesized terms on the right are abbreviations of the given setup. Apart from the lack of any coverage in literature of any such experiment for non-spherical particles, the novelty lies also within

4.1. General configuration with a fixed refractive index (Synthetic microphysical retrievals for non-spherical particles)

the first two setups with the indication "3α". The latter involve an additional extinction coefficient at 1064 nm, a technology not yet available but discussed in scientific circles as one of the next steps in lidar advancement. Altering the lidar setup is nothing more than a regularized inversion varying the optical data vector from 6 up to 9 data points (here) depending on the specified setup (1-6). From mathematics's perspective it should be beneficial in principle to add more data points, at least for stability, but due to the ill-posedness and model limitations we cannot foresee if such a step is a real improvement. For instance older experiments for spherical particles with the additional wavelengths in 400, 710 and 800 nm (so-called $6\beta + 2\alpha$ setup) in [14, 105, 107] did not give compelling reasons as opposed to the use of the $3\beta + 2\alpha$ setup. Moreover, it is unknown if there is an essential difference in using the same amount of data points but occupy different lidar channels, e.g. setups $331 - 322$, and $321^1 - 321^2$. It should be noted that the profuse (mathematically) addition of 1-4 data points, requires a very high level of lidar sophistication, from engineering and implementation point of view, in order for the extra channels to provide whole extinction or polarization profiles in the aerosol layer under examination. Therefore such theoretical analyses are really crucial for the future of lidars. The procedure followed here to compare the different setups is the same as the one used for the comparison of the methods in Sec. 4.1, i.e. we count appearances for the best setup among the ones under comparison in terms of Dif, Var and Unc in every complete retrieval. A huge amount of synthetic retrievals took place also here, which is constituted by the complete setting of the central particles sizes No 2 and 3, i.e. cases (2-3, i-v, a-c, 1%, 5%, 10%) in Table 4.1 reran for all (6) the aforementioned setups. Since Pade-DP is proved to be generally accurate and stable in a variety of instances, this comparison is expected to be more delicate than the one conducted with respect to the different methods.

A first aspect of this attempt involved comparing all the setups 1-6 at once, which further guided the next steps. Fig. 4.10 summarizes the results for size No 2 (upper panel) and 3 (lower panel) through pie charts, which are given from left to right with respect to Unc, Dif, and Var for all parameters (R- and S-parameters). Each piece of a specified chart represents the percentage of occurrences that a setup appeared as the one among the six of them with the lowest respective ERQ, for all parameters (R+S), refractive indices (i-v), shapes (a-c) and error levels (1%, 5%, 10%). This means that the rates (%) are calculated over a total of 180 ($5 \times 3 \times 3 \times 4$) RA, plus 135 ($5 \times 3 \times 3 \times 3$) SA, see the notation of Sec. 4.1.1. A quick look at the distribution of percentages in the pie charts indicates conservative disagreements in accuracy and more essential ones in uncertainties (Unc and Var). More specifically, for particle size No 2, the setup 333 is leading in (Unc, Var) with (38%, 29%) followed by 323 with (25%, 18%). Especially for Unc, this trend is the result of a big gap found in R-parameters between 333 (43%), 323 (34%), and the rest of the setups lying within only 3-9% of the total appearances (not shown here). Focusing on accuracy, 323 comes first and 333 is only third but very close to the second in ranking, 321^2. Again looking at only the R-parameters (not shown here), there is virtually no distinction between the leading setups (RA Dif: 18-22%), except that 321^1 and oddly 333 find themselves as the very last in Dif RA scale (13%, 7%). The differences in variability between the three leading setups, 321^2, 331 and 333 are marginal as well with RA Var: 21-22%. This is not the case for the shape parameters (not shown) where 323 is found more often most accurate (33%) than 333 (24%) and 321^2 (17%). Moreover 333 prevails in (SA) Var with 40% vs 21% of 323, and in lesser degree in Unc with 30% vs 27% of 321^2. Regarding the results on the larger particle size No 3 (Fig. 4.10, lower panel) we observe that, conversely, 323 now gains the upper hand in Unc with 33% vs 333 with 25%, and 333 prevails in accuracy with 23% vs 323 with 16% but with very small difference from 331 with 21%. Furthermore, there are small differences in variability between the setups in general e.g. the leading setups are 321^2 with 23% and 333 with 20%.

We now got the sense that 323 and 333 have an overall greater potential in Unc and Var, but their advantage in accuracy, especially 333, is somewhat controversial. Moreover 322 and 321^1 appear as the least competent and 331 and 321^2 have rather dubious appearances. It is sensible enough to consider 323 and 333 as the safest options, and there is further no indication that any of these setups is disastrous or far worse from the others. It is difficult, though, with this process to get closer to definite answers to the topics discussed before, e.g. how many and which depolarization data are worth using. In order to differentiate in greater detail the algorithm's behavior and preferences in the different setups we conducted the following one-to-one direct comparisons: $333 - 331$, $333 - 323$, $333 - 322$, $333 - 321^2$, $331 - 322$, $331 - 321^1$, $331 - 321^2$, $323 - 322$, $323 - 321^2$, $322 - 321^2$ and $321^1 - 321^2$. The results for sizes No 2 and 3 are similar in great extent and only the ones for size No 3 are given here in Table 4.10. All percentage rates (%) in this table count the number of appearances of a setup as best within a specified pair ($* - *$) whose counterparts add up to 100% and correspond to the setup comparison on the left

4.1. General configuration with a fixed refractive index (Synthetic microphysical retrievals for non-spherical particles)

Table 4.10: Comparison of lidar setups for particle size No 3. A rate (%) counts the number of appearances of a setup as best within a specified pair. A pair of rates corresponds to the setup comparison on the left column and is given in the same order. Each triple of pairs within a specified ERQ (Unc, Dif, Var) corresponds to the rate of appearances in the R-parameters (top), the S-parameters (middle) and the total rate i.e. no distinction in R, S (bottom).

Setup comp./ERQ	Uncertainty	Difference	Variability
(1) $333 - 331$	$61\% - 39\%$	$49\% - 51\%$	$53\% - 47\%$
	$63\% - 37\%$	$61\% - 39\%$	$53\% - 47\%$
	$62\% - 38\%$	$54\% - 46\%$	$53\% - 47\%$
(2) $333 - 323$	$30\% - 70\%$	$46\% - 54\%$	$42\% - 58\%$
	$55\% - 45\%$	$41\% - 59\%$	$50\% - 50\%$
	$41\% - 59\%$	$43\% - 57\%$	$45\% - 55\%$
(3) $333 - 322$	$48\% - 52\%$	$47\% - 53\%$	$43\% - 57\%$
	$61\% - 39\%$	$37\% - 63\%$	$54\% - 46\%$
	$54\% - 46\%$	$43\% - 57\%$	$48\% - 52\%$
(4) $333 - 321^2$	$53\% - 47\%$	$53\% - 47\%$	$39\% - 61\%$
	$59\% - 41\%$	$55\% - 45\%$	$57\% - 43\%$
	$56\% - 44\%$	$54\% - 46\%$	$47\% - 53\%$
(5) $331 - 322$	$36\% - 64\%$	$47\% - 53\%$	$42\% - 58\%$
	$43\% - 57\%$	$33\% - 67\%$	$57\% - 43\%$
	$39\% - 61\%$	$41\% - 59\%$	$49\% - 51\%$
(6) $331 - 321^1$	$44\% - 56\%$	$54\% - 46\%$	$36\% - 64\%$
	$46\% - 54\%$	$44\% - 56\%$	$50\% - 50\%$
	$44\% - 55\%$	$50\% - 50\%$	$42\% - 58\%$
(7) $331 - 321^2$	$40\% - 60\%$	$59\% - 41\%$	$44\% - 56\%$
	$51\% - 49\%$	$39\% - 61\%$	$57\% - 43\%$
	$45\% - 55\%$	$50\% - 50\%$	$50\% - 50\%$
(8) $323 - 322$	$83\% - 17\%$	$61\% - 39\%$	$59\% - 41\%$
	$50\% - 50\%$	$47\% - 53\%$	$47\% - 53\%$
	$69\% - 31\%$	$55\% - 45\%$	$54\% - 46\%$
(9) $323 - 321^2$	$83\% - 17\%$	$56\% - 44\%$	$44\% - 56\%$
	$40\% - 60\%$	$68\% - 32\%$	$78\% - 22\%$
	$72\% - 28\%$	$63\% - 37\%$	$50\% - 50\%$
(10) $322 - 321^2$	$59\% - 41\%$	$65\% - 35\%$	$42\% - 58\%$
	$54\% - 46\%$	$58\% - 42\%$	$50\% - 50\%$
	$57\% - 43\%$	$62\% - 38\%$	$46\% - 54\%$
(11) $321^1 - 321^2$	$55\% - 45\%$	$42\% - 58\%$	$34\% - 66\%$
	$37\% - 63\%$	$50\% - 50\%$	$41\% - 59\%$
	$47\% - 53\%$	$45\% - 55\%$	$37\% - 63\%$

column, given in the same order. Each triple of pairs within a specified ERQ (Unc, Dif, Var) corresponds to the rate of appearances in the R-parameters (top), the S-parameters (middle) and the total rate, i.e. no distinction in R, S (bottom). The interpretation of the results is based mostly on the total rate of the competing setups, provided that it does not deviate greatly from the partial rates related to the R- and S- parameters.

Focusing on the comparisons No 8-11 we can see that we have the order of setups from most to least efficient is $323 > 322 > 321^2 > 321^1$. The statement $321^2 > 321^1$ suggests that depolarization at 532 nm is more useful than at 355 nm from the point of view of the inversion. This is good news since most Raman-lidars with a single depolarization channel use the setup 321^2. The contribution of the channel at 355 nm seems also to subvert the action of 322, which mainly overcomes it with an overall better behavior vs 321^2, see No 10, but it is perhaps the reason of its undermined performance in the pie charts in Fig. 4.10. On the other hand the additional depolarization at 1064 nm is an overall improvement, see No 8 and 9, which is reconfirmed by the setup comparison No 1, where we have $333 > 331$. This finding is in agreement with simulations carried out by [44] suggesting that the depolarization at 1064 nm

4.1. General configuration with a fixed refractive index (Synthetic microphysical retrievals for non-spherical particles)
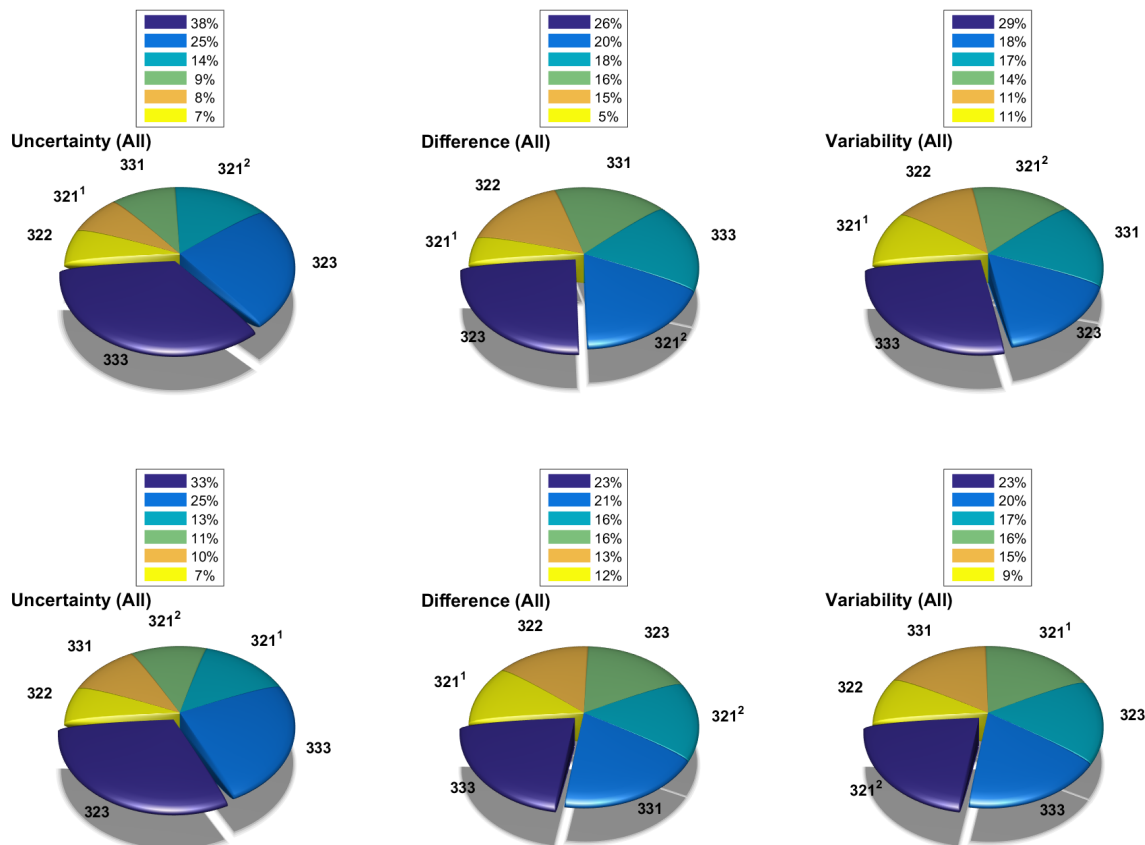
Figure 4.10: Comparison of lidar setups for the particle sizes No 2 (upper panel) and 3 (lower panel), through pie charts. Left to right: pie charts with respect to Unc, Dif, and Var for all parameters (R- and S-parameters). Each piece of a specified chart represents the rate of times that a setup appeared as the one with the lowest respective ERQ, for the specific group of parameters (R / S / T), for all refractive indices (i-v), shapes (a-c) and error levels (1%, 5%, 10%). The designated piece marks the highest percentage from which on the rest descend counter-clockwise.

offers an essential uncertainty reduction. In the case of size No 2 (not shown), 333 is much better in Unc and Var (77% and 58%) than 331, but worse in accuracy (38%) in R-parameters and all in all (R+S) they end up almost equivalent in Dif. Now, since $321^2 > 331$, see No 7, it seems that the additional extinction coefficient at 1064 nm does not provide a solid improvement. This is also supported by the comparison $333 - 323$ (No 2) in which 333 is clearly an inferior option. In the case of size No 2, although 323 is even more frequently more accurate (Dif: 64%) than 333, and the latter has a clear advantage in the uncertainties (Unc, Var): (66%, 56%). However, this actually enhances the argument that we cannot rely on an additional extinction (at 1064 nm), since the results lack the consistency of a general improvement. The notion, that coming up with the right combination of data points matters more than blindly adding more data points, is proved numerous times throughout the comparisons. In addition, from the comparison No 5 pertaining to setups having equal amount(7) of data-points, we obtain $322 > 331$ which suggests that the algorithm is more eager to go down the path of adding more depolarization- rather than extinction information. The comparisons No 6 and 7 lend even more credence to this argument, showing that even though $321^1, 321^2$ use one data point less than 331, they are still comparable or better than 331. Note, that for size No 2 they are more pronounced differences in favor of $321^1, 321^2$ and against 331.

Conclusively, we have now a solid basis in favor of 323 as more suitable and consistent setup for the microphysical retrieval problem. 333 provides in many cases an improvement but it does not seem to be a fulfilling answer to the coming lidar advancements. Finally, it remains an open question for future

investigations if the wavelength 355 nm acts in a restraining or a supportive way, i.e. whether or not the setup $3\beta + 2\alpha + 2d(532, 1064)$ has an overall advantage against 323.

4.2 Synthetic retrievals with unknown refractive index

4.2.1 Retrieval details in view of the fixed-kernel database

We proceed now to the second phase of simulations considering limited knowledge on the refractive index (RI). As explained earlier, the RI cannot be fully unknown because of the vast raise in non-linearity of the Fredholm integral equation and therefore one has to order a grid beforehand. In a measurement case, it is often possible to have at least a very rough sense of the atmospheric scenario under consideration, to an extent that this grid can be reasonably restricted and then refined to achieve a desired accuracy see e.g. [113, 131]. The refinement of the grid is a crucial step as shown in [131], which is unfortunately not available in our case and is a bottleneck in all current adaptations of aerosol microphysical retrieval using a fixed kernel database. In all experiments that follow, we take as a grid all (42) possible combinations of real- (RRI) and imaginary parts (IRI) of refractive index from Miescka's database, see Table 3.2.

The solution algorithm SA2 (Sec. 3.6) followed here is basically an advanced version of the used for simulations with fixed RI (SA1) reran over and over again for all possible RI in our grid. The final retrieval products, which now include the refractive index too, are again the result of the same minimization process based on least residuals. Obviously, running every single inversion 42 times increases considerably the computational time of massive simulations. For instance, for Pade-DP, just by running for a fixed shape-size distribution for all spline numbers (6-14) and degrees (2-5) used before we would need about 2.6 times more time for an inversion over the whole RI grid, leading to 27-35 minutes of run time. Pade-LC is extremely slower than all the other methods, due to its vast memory needs for running the iteration scheme multiple times (100 here) for every discretization matrix, which, in terms of the previous example, results in several hours (> 3) of run time. Again, this computational hindrance for Pade-LC is only a problem for the massive nature of our experiments in order to assure the statistical significance of our results, which is not usually the case for a measurement. However, preliminary numerical experiments with SA2 combined with Pade-LC and Pade-DP showed that the algorithm works better with the latter. For these reasons we are going to continue the simulations from now on exclusively with the Pade-DP.

In these simulations we calculate the complex refractive index (RRI+IRIi) and the single scattering albedo (SSA) at 355 nm (SSA355) and 532 nm (SSA532). We should stress that our endeavor to extract the refractive index is much more challenging than the retrievals with fixed RI. Simulations in pursuit of the RI have been proven over the years of the microphysical-retrieval history a handicap even in the simplified case of the Lorenz-Mie-model (spherical particles) with the epicenter of difficulty being the IRI. In addition to the usual ill-posedness caused by the RI, the main obstacle here is that there is actually poor resolution in the grid (because of the use of a fixed-kernel database), which means that if the minimization process fails to find the correct refractive index, e.g. $1.33 + 0.01i$, then the next guesses, here $1.33 + 0.005i$, $1.33 + 0.03i$, $1.4 + 0.005i$, $1.4 + 0.01i$, and $1.4 + 0.03i$, will not be reasonably vicinal. On the one hand, our hybrid algorithm is built in such a way to manage this very situation to some extent, since it tries to distinguish the best solutions and therefore if it "misses" the correct RI occasionally but is successful to identify these guesses and circles around them, then it should be able to converge on average to the initial refractive index. An effective way to illustrate this and represent graphically the solution space is by drawing the real- (y-axis) and imaginary parts (x-axis) of the RI separately against the solution error-levels found with forward calculations, so that the solution quality (least residuals) and the physical characteristics (RI) are shown simultaneously. Fig. 4.11 shows such an example. There we show 3 instances of a random dataset (out of 10) from a simulation of a sphere-spheroid mixed particle ensemble with the size distribution No 1 (Table 4.1) and 1% data error, where the input refractive index is $1.5 + 0.01i$. Each of these plots corresponds to one of the 36 solutions, specified in the title in terms of their spline point No and spline degree. The white circle marks the input RI and the black asterisk the one retrieved. The colorbars on the right distinguish the calculated solution error-levels. In these plots we see two successful attempts of the algorithm to find either the exact (middle plot) or the closest not-exact (left plot) refractive index and one less successful attempt (right plot). The latter is not among the 5 best solution picked by the algorithm. As a side-note, we observe that while the error levels are pretty close to each other for the three instances, the algorithm can still make a distinction and correctly avoid the faulty RI 30/36 times.

4.2. Synthetic retrievals with unknown refractive index (Synthetic microphysical retrievals for non-spherical particles)

It should be obvious though that this is a far greater struggle for the inversion than the fixed-RI retrievals, especially for the imaginary part of the refractive index, where the resolution gap is much larger than the one for the real part. For this reason, a retrieval with mean IRIs which belong to a "similar class" of absorption with the initial one, will be considered successful. A less successful but satisfying result in regard of these limitations is to accept the next *best* guess, e.g. an initial IRI = 0.01 with retrieved value 0.005 will be acceptable while 0.03 will not. In order to further support this, the respective retrieved SSA, as a parameter strongly dependent on RI, should be close to the initial one within 5% relative difference. A disagreement in the initial and retrieved RI will be fairly acceptable if the corresponding difference in SSA is also small. Fig. 4.12 illustrates the sensitivity of SSA in the RI with a plot where IRI $\in [0, 0.1]$. First we see the expected decreasing trend of SSA with respect to the IRI, and further we observe that (here) deviations in the IRI of order 0.001-0.002, bring generally small changes $(0.7 - 1.4\%)$ in SSA and thus they can be assumed negligible. On the other hand, larger deviations in the IRI alter the SSA immensely, e.g. see IRI equal to 0.01 and 0.03. This should not leave the reader with the impression that a good accuracy in IRI is unimportant, but rather that because of the limitations described, another priority is also to assure that the rest of the retrieved parameters (a-g) are affected the least possible even if the RI is not strictly accurate. We deal with this issue in the subsequent section 4.2.3. The calculations of the SSA in the previous example were done using Mieschka software tool with RRI = 1.33, aspect ratio $\eta = 1.3$, volume-equivalent radius $r = 2.2$ μm and wavelength $\lambda = 2\pi$ μm. It should be noted that this example was an attempt to show the response of SSA to a change in RI, but different sizes and shapes might change the SSA-sensitivity on the RI.

Unless the retrieval of the RI was flawless always, the rates Unc and Var for the IRI should be encountered with much higher tolerance, because of the large resolution gap. Consider, for example, the initial IRI = 0.001 and the not-worst-case scenario where the 5 best solutions consist of the values 0, 0.001, 0.001, 0.001, 0.005. This results in a Var of 60% and the little worse scenario where we replace 0 with 0.005 would raise Var to 120%. Moreover even if only one of the solutions for any initial IRI is systematically wrong (for all datasets) but directly vicinal in the database, then it is easy to see that Var will range from 8% to 20%. In this particular case, the median (m) instead of the mean value could be a more suitable measure, but it requires a redefinition of the ERQ. We will use the median as a supplementary tool in our explanations for the IRI as we go through the cases. For this, we need to consider a form of deviation for medians as an analog of the standard deviation used by the ERQ, which is done the following way. Assume s_i is an array of solutions for the $i-$th dataset with a median $k_i = m(s_i)$, then the *median deviation* $\mathscr{D}$ is found by

$$\mathscr{D} = \mathscr{D}(k_i) = m\left(|s_i - k_i \mathbb{1}|\right). \tag{4.2.1}$$

Simply put, $\mathscr{D}$ is the median absolute difference of the solutions from the computed median. Based
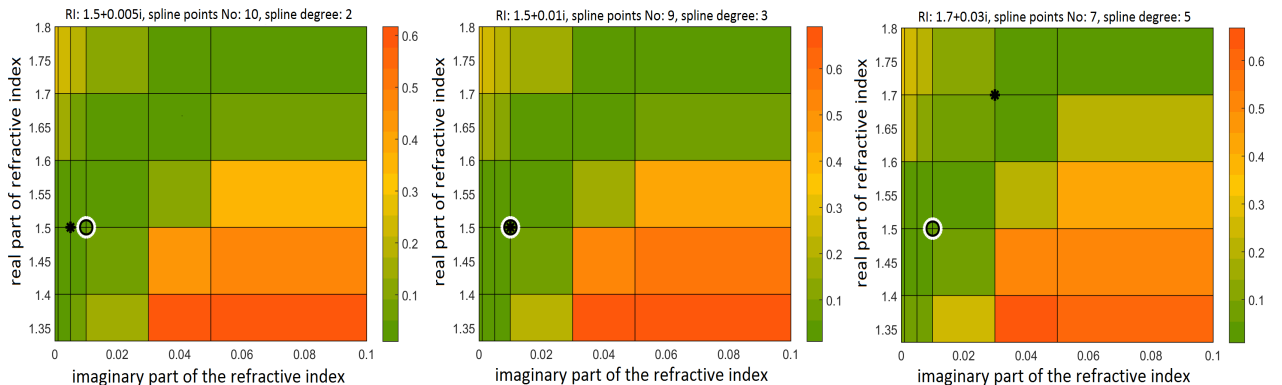
Figure 4.11: Illustration of the efficiency of the solution algorithm through several plots of solutions spaces built upon the RI-grid by the inversion. This simulation corresponds to a sphere-spheroid mixed particle ensemble, with the size distribution No 1, 1% data error and the input refractive index $1.5+0.01i$. Each of the three plots corresponds to one of the 36 solutions, specified in the title, for one (random) dataset (out of 10). The white circle marks the input RI and the black asterisk the one retrieved which is additionally given in the title. The colorbars on the right distinguish the solution error-levels.

on this we can define the variability of a single $(i-\text{th})$ dataset as the ratio $\text{var}_i^{(m)} = \mathscr{D}/k_i$, the *median variability* of all the datasets as $\text{Var}^{(m)} = m\left(\text{var}^{(m)}\right)$ and the *uncertainty* $\text{Unc}^{(m)} = \mathscr{D}(k)/m(k)$, where $k = [k_1, \ldots, k_n]$ (here, $n = 10$). Moreover, if $\mathscr{I}$ is the initial value, then the *median relative difference* is defined as $\text{Dif}^{(m)} = m\left(|s_i - \mathscr{I}\mathbb{1}|\right)/\mathscr{I}$.

4.2.2 Simulation configuration and retrieval results

The simulations are ran here using the same scheme as with RI-free ones, with the mere exception that the data are being regenerated 10 times (not 15) for a specified error level. The initial parameter configuration for these retrievals remains the same with respect to the shape-size distributions we used before (see 1-4 and a-c in Table 4.1), and we further extend the list of RI to: (i) $1.33 + 0.001i$, (ii) $1.4 + 0.005i$, (iii) $1.5 + 0.01i$, (iv) $1.6 + 0.001i$, (v) $1.7 + 0.05i$, (vi) 1.33, (vii) $1.33 + 0.01i$, (viii) $1.33 + 0.03i$, (ix) 1.4, (x) $1.4 + 0.001i$, (xi), $1.4 + 0.1i$, (xii), $1.6 + 0.005i$, (xiii) $1.6 + 0.03i$, and (xiv) $1.8 + 0.1i$, see the updates in Table 4.11. All the examined cases stem from combinations in this table. The resulting lidar ratios in $532\,\text{nm}$ reach up to $80\,\text{sr}$. We also keep the form (size, shape, RI, error level, parameter, ERQ) and its conventions in order to refer briefly to a case. The cases together with the retrieval results are found on Tables 4.12 and in App. C in Table C.21 and C.24, the given Var/ty and Unc/ty refer to the usual ERQ as defined in Sec. 4.1 through the mean and the usual standard deviation, and the Average refers to the mean computed value from all datasets. Especially for the IRI we include the median version of the ERQ defined through Eq. 4.2.1. For the RRI, we can safely consider that there is not much difference between the mean- and the median-related ERQ. Note that the reference to a case in these tables may correspond to a table continued in a subsequent page labeled by "Table ** continuation". Tables 4.12 and C.21 consist of retrieval results for size No 2 and 3 (the central sizes) respectively combined with all the RI used in the fixed-RI retrievals (i-v), all the basic geometries (a-c) and all the error levels (1%, 5%, 10%). Table C.24 focuses on comparisons of different cases with 1% error level with respect to either size (1-4) or shape (a-c) and also includes more cases under the label "Other cases" (last sub-table). Unless it is stated otherwise, "variability" (Var), "uncertainty" (Unc), and "uncertainties" (Unc, Var) will refer to the mean-related ERQ.

As a general remark, the real part of the refractive index is retrieved accurately with a few exceptions and further with very low uncertainties in the vast majority of cases. Indeed we have a tiny variability $(< 5\%)$ and a very small uncertainty $(< 10\%)$, remarkably for all error levels. There are mainly two exceptions attributed to prolate particles, the case $(3, c, v, 1\%)$ in Table C.21 with initial $\text{RI} = 1.7 + 0.05i$ poorly approximated by $1.33 + 0.005i$, which is a worst-case scenario, and the case $(1, c, xiii, 1\%)$ in Table C.24 with initial $\text{RI} = 1.6 + 0.03i$ retrieved as $1.412 + 0.0106i$ ($m = 1.4 + 0.01i$, $\text{Unc}^{(m)} = 0\%$), which is another rare case. The latter and especially the former case show very pronounced differences between the initial- and the retrieved SSA, e.g. at $355\,\text{nm}$ we have $0.8044 - 0.8870$, and the chasm $0.5820 - 0.8249$
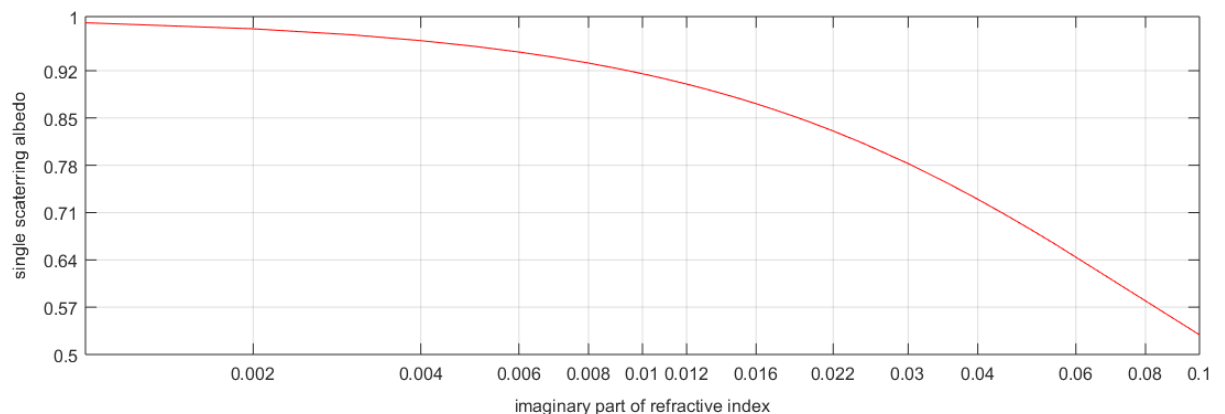
Figure 4.12: Single scattering albedo vs imaginary part of the refractive index with IRI $\in [0, 0.1]$ and RRI: 1.33. The calculations were done with Mieschka software tool using with RRI = 1.33 and aspect ratio $\eta = 1.3$, volume-equivalent radius $r = 2.2\,\mu\text{m}$ and wavelength $\lambda = 2\pi\,\mu\text{m}$.

respectively. This already predisposes us for large discrepancies in the rest of the parameter-retrievals as well, which indeed holds as we will see in the following section (4.2.3). By contrast, the imaginary part is much harder to retrieve and the associated uncertainties are in general much higher. However, as already explained, the high Unc- and Var- rates for the IRI are to be expected in some degree, unless all the best solutions are exactly spot on, which is the case for many of our results but not the rule. Moreover, the median variability $\text{Var}^{(m)}$ was found 0% in every single case (Tables 4.12, and C.21-C.24), except (3, c, ii, 1%) in Table C.21, which means that at very least 60% of the best solutions of every solution space is closer to the retrieved median value. The same is obviously true whenever $\text{Unc}^{(m)}$ is zero. This gives a good level of confidence for the retrieved solutions in case of a reasonable approximation by the criteria discussed before.

Focusing now on results with 1% data error, see Table C.24 and the corresponding parts of Tables 4.12 and C.21 (for 1%), we see quite reasonable approximations of the IRI. Especially noteworthy are the retrievals with high- (IRI: 0.01, 0.03) and extreme (IRI: 0.05, 0.1) absorption in which we get high accuracy, a variability mostly below 20% and a reasonable uncertainty mostly below 50%, where at the same time the $\text{Unc}^{(m)}$ is very often zero. Exceptions among the high-absorption cases with 1% (i.e. Var or Unc larger than 50%) are the cases (1-2, c, viii, 1%) in Table C.24 and (2-3, c, iii, 1%) in Tables 4.12 and C.21. The former cases (RI = $1.33 + 0.03i$) are actually accurate retrievals with very low disagreement among the solutions since they have zero $\text{Unc}^{(m)}$ and $\text{Var}^{(m)}$ and further the respective SSA are marginally distant from the initial values, all of which point to an algorithm convergence towards the initial RI. On the other hand, this is not true for the other cases (RI = $1.5 + 0.01i$) where we have a prediction of weak absorption with IRI = 0.00116 for size No 2 and IRI = 0.000580 for size No 3 ($m = 0.001$ for both sizes No 1 and 2) and as a result the retrieved SSA differ considerably from the initial ones. Now turning to lower-absorption cases, it appears that the largest discrepancies in IRI-accuracy are found in $1.33 + 0.001i$ and secondarily in $1.4 + 0.005i$, $1.4 + 0.001i$ and $1.4 + 0i$. This conforms with earlier findings in the fixed-RI simulations, where it was shown that $1.33 + 0.001i$ and $1.4 + 0.005i$ were related to lower accuracy levels for the R-, and the S-parameters see Sec. 4.1.4. What's interesting is that the retrieval quality especially of $1.4 + 0.001i$ and $1.4 + 0i$ seem to depend prominently on particle size, see Table C.24. Intriguingly, the larger sizes No 3 and 4 have very good approximations of the IRI, while the smaller sizes No 1, 2 do not. In order to test this hypothesis, we ran more examples for all available sizes. Especially in the non-absorbing-particle case with an RI = $1.4 + 0i$ the retrievals for sizes No 3 and 4 are almost flawless while sizes No 1 and 2 falsely predict IRI = 0.01 (median). Now raising a little higher the IRI with an RI = $1.4 + 0.001i$ we see a similar situation, only now for sizes No 1 and 2 we get more accurate RI but with higher uncertainties and also retrievals with size No 3 start to get noisy too. Involving higher absorption with RI = $1.4 + 0.005i$, see Table C.24, we see that retrievals for size No 1 get overall even better than before and for size No 2 slightly worse (see also the respective SSA values) and further that retrievals with size No 4, despite being the best among the other sizes, they became worse as compared to the case of RI = $1.4 + 0.001i$. Finally, we observe that for very absorbing particles with $1.33 + 0.03i$ the pattern starts to reverse again favoring the larger sizes. Therefore we see that particle size definitely affects the retrieval in a way, where very weak or very strong absorption levels combined with large particles have a better chance of a good RI-retrieval than with smaller ones. This agrees with our physical intuition, since distinctions in optical properties are indeed expected to be harder in smaller rather than in larger particle sizes.

Alongside we have to consider the rare cases of low accuracy at the RRI and IRI simultaneously, i.e. the cases shown earlier (3, c, v, 1%) in Table C.21 and (1, c, xiii, 1%) in Table C.24, and further the case (2, c, v, 1%) in Table 4.12, all of which we discuss individually later on (Sec. 4.2.3). For now, there are two points to acknowledge. The first is that fixing the RRI to the correct one and rerunning these cases, the IRI is precisely found with 100% certainty (not shown). This is indeed very hopeful, but it is not so helpful in a global sense, since most of the cases already have a satisfactory the RRI-prediction. It is interesting to observe though, that larger discrepancies from the initial RRI, may affect also the IRI, while the converse does not seem to strongly follow from our retrieval record. Second, let us see the effect of the common denominator of all previous problematic cases which appears to be the prolate shape. Looking closely at all the aforementioned prolate-particle cases (see also previous paragraphs) and examining the corresponding oblate- or sphere-spheroid-mixed-particle cases, i.e. the cases (2-3, a, b, iii, 1%), (3, a, b, v, 1%) in Tables 4.12 and C.21 and (1, a, b, xiii, 1%) in Table C.24, we observe that the cases with a, b are overall superior in accuracy and/or the uncertainties. This is also visible in the cases of extreme absorption (1, a-c, x, xi 1%) in Table C.24 with RI equal to $1.4 + 0.1i$ and $1.8 + 0.1i$, where we

otherwise have almost perfect retrievals for all shapes. In addition, going through the rest of the cases from Tables 4.12, C.21 and C.24, suggests that mixed-particle cases are mostly better retrieved than oblate- and prolate-particle cases, therefore there is an overall efficiency hierarchy following $c < a < b$ (least-to-most). The exceptional cases (3, a-c, ii, 1%) in Table C.21 with RI $= 1.4 + 0.005i$ following the efficiency-order $a < c < b$, and cases (2, 3, a-c, iv, 1%) in Tables 4.12 and C.21 with RI $= 1.6 + 0.001i$ following $a \approx b < c$ and $a \approx c < b$ for size No 2 and 3 respectively might suggest that the prolate-particle defect is more correlated with stronger absorption.

Higher data errors do impose additional difficulty in the retrievals. The results for the RRI are very satisfying for all error levels, and for the IRI can be tolerated up to 5% data error when RRI > 1.4. This is most easily observed by looking at the median-related ERQ in conjunction with the retrieved SSA. The accuracy of the IRI remains in general within the discussed standards although in some cases is greatly diminished. 60% of the cases with 5% data error (Tables 4.12 and C.21) have $\text{Unc}^{(m)} = \text{Var}^{(m)} = 0$, and 73% of the same cases have $\text{Unc}^{(m)}$ below or equal to 33.33%, which means that whenever the mean-related variability and/or uncertainty increase as compared to the respective cases with 1% data error, then it follows that mainly the good solutions remain good (and more numerous) and the bad ones become worse. Thus the efficiency trend of the algorithm is not drastically altered. The reliability of the IRI is questionable for cases with 10% data error, 47% of which have zero $\text{Unc}^{(m)}$ and $\text{Var}^{(m)}$. It seems, nevertheless, that the refractive index is essentially a greater problem to deal with than the error level since its smoothing effect is there even if we assure error-free data. This is perhaps the reason why we found that strongly absorbing cases are the least affected by the error level, which is at the same time a very relieving incidence. Of course this kind of comparison of the RI- vs the data-error effect is possible for the relatively small errors used here (1-10%), and it is not difficult to conceive that much larger (measurement) errors could have a devastating effect. The inefficiency of the algorithm in many of cases with $1.33 + 0.001i$ and $1.4 + 0.005i$ for all error levels still remains physically inexplicable.

The SSA has a very good retrievability following conservatively the quality of the RI-approximation. The SSA retrievals are very reasonable in accuracy in the vast majority of cases and with extremely low uncertainties. The SSA is by definition a percentage rate for the amount of absorption from the total attenuation of light. This allows for a good measure of the "effective" absorption in order to compare the effect of the RI in the retrievals. However, if the refractive index is the only thing one aims for, one has to know exactly how sensitive the SSA is with respect to the variation of RI (the way it was shown in Fig. 4.12), which has to do also with the involved shape-size distribution.

4.2.3 Influence of the variation of the refractive index

As we saw up to now, the retrieval of the refractive index faces many difficulties, with the imaginary part raising the highest concerns. It is important to know what is the impact of the retrieved RI in the prediction of the rest of the microphysical parameters we dealt in the previous sections. For this, we calculate the parameters, surface-area concentrations (a_t), volume concentration (v_t), effective radius (r_eff), the effective aspect ratio (a_eff), and the spherical volume concentration fraction ($svcf$) for all the cases from Tables 4.12 and C.21, i.e. (2, 3, a-c, i-iv, 1%, 5%, 10%). We will often refer to the aforementioned parameters as the "rest parameters" to distinguish them from the RI and SSA. The results are given concisely in Table 4.15, where we show the ranges for each of the ERQ (except the Dif for $svcf$ for reasons explained in Sec. 4.1) and every error level. Moreover a collection of the most characteristic and dubious cases encountered in Sec. 4.2.2 are shown in full in Table 4.16 in order to demonstrate the highlights of these retrievals. In what follows, we considered the rates $35 - 40\%$ to be the highest acceptable for the ERQ.

The cases (3, c, v, 1%), and (1, c, xiii, 1%) with the high discrepancies for both the RRI and IRI, discussed in the previous section (4.2.2), see Tables C.21 and C.24, are really troubling, see Table 4.16, F and H, both showing very low accuracy in the volume concentration (v_t) and surface-area concentration (a_t). These are isolated instances of algorithm failure, as one can see e.g. in the respective retrievals with 10% data error, which are reasonable. Furthermore, the similar case (2, c, v, 1%) in terms of faulty RRI and IRI (Table 4.12) manages to have a much better prediction of v_t ($\sim 40\%$), see Table 4.16, D. However, all the ERQ (Dif, Var, Unc) have considerably risen as compared to the extremely low ones of the same case with fixed-RI shown in Table C.3. Now, turning to cases with $1.33 + 0.001i$, $1.4 + 0.005i$ which often had a divergent IRI (see e.g. C.21), we see by contrast reasonable retrievals which do not reflect at all the high discrepancies in IRI, see Table 4.16 cases (2, b, i, 1%, 10%) (A), (2, a, ii, 1%,

4.2. Synthetic retrievals with unknown refractive index (Synthetic microphysical retrievals for non-spherical particles)

Table 4.11: Simulation setup for retrievals with unknown refractive index.

Distribution data generated with

log-normal distribution

No	1	2	3	4
median radius (r_{med})	0.05	0.25	0.5	0.8
mode width (σ)	2.3	1.6	1.2	1.3
radius range (µm)	[0.01, 1.2]	[0.01, 1.2]	[0.01, 2.2]	[0.01, 2.2]
number concentration (N_{t})	1	1	1	1

aspect ratio distribution

(a) oblate	(b) sphere-spheroid mixture	(c) prolate
$\begin{cases} 1/2, & \text{if } \eta = 0.77, \\ 1/2, & \text{if } \eta = 0.87, \end{cases}$	$\begin{cases} 1/3, & \text{if } \eta = 0.87, \\ 1/3, & \text{if } \eta = 1, \\ 1/3, & \text{if } \eta = 1.15, \end{cases}$	$\begin{cases} 1/2, & \text{if } \eta = 1.3, \\ 1/2, & \text{if } \eta = 1.5, \end{cases}$

Optical data generated with

refractive index	(i) 1.33+0.001i, (ii) 1.4+0.005i, (iii) 1.5+0.01i, (iv) 1.6+0.001i, (v) $1.7 + 0.05i$, (vi) 1.33, (vii) $1.33 + 0.01i$, (viii) $1.33 + 0.03i$, (ix) 1.4, (x) $1.4 + 0.001i$, (xi), $1.4 + 0.1i$, (xii), $1.6 + 0.005i$, (xiii) $1.6 + 0.03i$, (xiv) $1.8 + 0.1i$
number of spline points	$6, 7, 8, 9, 10, 11, 12, 13, 14$
spline degree	$2, 3, 4, 5$
relative error level ($\times 10$ repetitions)	$1\%, 5\%, 10\%$

10%) (B), (3, c, i, 1%, 10%) (E). Comparing the latter case (E) for 1% data error with the one with fixed RI in Table C.15 we see that v_{t} now increased by about 15% (12.97% vs 27.70%), r_{eff} increased by about 12% (3.34% vs 15.20%) while a_{t}, *svcf* and a_{eff} remain almost the same; for 10% data error the differences are less pronounced but the v_{t} is already too noisy (Dif: 45.89%) for the non-fixed-RI cases (Table 4.16, E). Thus, it seems that the RI-discrepancies, however large, are not granted failures for the retrieval of the rest parameters, meaning that there are more factors that decide for the outcome, e.g. the shape-size distribution. In support of this, we see that the cases (1-4, b, ix, 1%) with $1.4 + 0i$, which had a very large disagreement in IRI for the sizes No 1 and 2 ($m(\mathrm{IRI}) = 0.01$, see Table C.24), retrieve the rest microphysical parameters very well, see Table 4.16 (G). On the other hand, the almost flawless RI-retrievals for sizes No 3 and 4 (same case), appear to have reasonable but relatively less efficient retrievals for the rest parameters (higher ERQ).

As discussed, it is very difficult to quantify by single experiments the extent of the RI-effect upon small or large variations of its ERQ. Therefore we address this statistically by gathering all the results for the cases (2, 3, a-c, i-v, 1%, 5%, 10%), see the synoptic Table 4.15. This table distinguishes only the particle size (size No 2 upper table and size No 3 lower table) and contains the full range of the ERQ for every microphysical parameter for every shape (a-c) and every RI (i-v) and further the mean value of the range below each of the ERQ. First, we see that the ranges are greatly expanded as compared to the ones with fixed-RI, see Table 4.8. However, the mean value of the ranges (shown parenthesized) are admittedly much lower in most of the cases in Table 4.15. Second, we distinguish two levels of efficiency between the retrievals with size No 2 and 3. As demonstrated many times in this work, cases with size No 3 are the most difficult to retrieve in general, even from the larger-particle cases (size No 4, Table

4.2. Synthetic retrievals with unknown refractive index (Synthetic microphysical retrievals for non-spherical particles)

Table 4.12: Retrieval results of the refractive index and the single scattering albedo with Pade-DP for the cases (2, a-c, i-v, 1%, 5%, 10%), see Table 4.11. The "Average", "Var/ty" and "Unc/ty" relate to ERQ as defined in Sec. 4.1 through the mean and the usual standard deviation. Especially for the IRI we include the median version of the ERQ defined through Eq. 4.2.1 on the right of the mean-related ERQ and separated by a slash (/). The indications "1%", "5%" and "10%" on the left of a given part of the table refer to retrievals with the respective input data error.

oblate (2, a, i-v, 1%, 5%, 10%)

	Parameters	RRI	IRI (mean/median)	SSA355	SSA532
	Synthetic	1.330	0.001000	0.9890	0.9922
1%	Average	1.330	0.000160/0.000000	0.9982	0.9987
	Var/ty	0.00%	36.05%/0.00%	0.12%	0.08%
	Unc/ty	0.00%	202.42%/0.00%	0.37%	0.27%
5%	Average	1.400	0.015500/0.001000	0.9241	0.9361
	Var/ty	0.35%	60.69%/0.00%	1.40%	1.13%
	Unc/ty	11.29%	208.85%/100%	13.77%	11.92%
10%	Average	1.413	0.017020/0.005000	0.9128	0.9287
	Var/ty	0.28%	4.26%/0.00%	0.40%	0.37%
	Unc/ty	11.58%	193.35%/60%	14.51%	12.31%
	Synthetic	1.400	0.005000	0.9439	0.9625
1%	Average	1.386	0.002080/0.001000	0.9744	0.9833
	Var/ty	0.00%	33.58%/0.00%	1.02%	0.52%
	Unc/ty	2.13%	93.36%/50%	2.25%	1.57%
5%	Average	1.444	0.014200/0.000000	0.9114	0.9320
	Var/ty	2.90%	78.01%/0.00%	4.06%	3.03%
	Unc/ty	9.04%	139.92%/0.00%	12.06%	9.27%
10%	Average	1.482	0.020180/0.000000	0.8905	0.9120
	Var/ty	0.00%	59.53%/0.00%	1.06%	0.38%
	Unc/ty	11.52%	127.20%/0.00%	15.40%	12.14%
	Synthetic	1.500	0.010000	0.8839	0.9242
1%	Average	1.548	0.014800/0.010000	0.8627	0.9081
	Var/ty	1.93%	16.35%/0.00%	1.99%	2.61%
	Unc/ty	4.69%	49.01%/0.00%	4.45%	3.30%
5%	Average	1.604	0.022400/0.020000	0.8309	0.8847
	Var/ty	3.43%	22.65%/0.00%	2.98%	2.85%
	Unc/ty	6.46%	64.60%/50%	9.80%	6.96%
10%	Average	1.631	0.024300/0.030000	0.8307	0.8777
	Var/ty	2.53%	36.82%/0.00%	4.19%	2.44%
	Unc/ty	8.27%	59.79%/66.67%	9.78%	7.13%
	Synthetic	1.600	0.001000	0.9836	0.9902
1%	Average	1.608	0.004760/0.005000	0.9316	0.9578
	Var/ty	0.89%	22.12%/0.00%	1.11%	0.64%
	Unc/ty	0.87%	26.04%/0.00%	1.67%	0.84%
5%	Average	1.650	0.006380/0.005000	0.9231	0.9475
	Var/ty	1.40%	26.81%/0.00%	2.23%	2.03%
	Unc/ty	2.93%	39.86%/0.00%	2.26%	2.33%
10%	Average	1.686	0.005260/0.005000	0.9392	0.9626
	Var/ty	2.29%	47.27%/0.00%	2.35%	1.34%
	Unc/ty	4.00%	61.60%/90.00%	3.92%	2.30%
	Synthetic	1.700	0.050000	0.6354	0.7155
1%	Average	1.700	0.050000/0.050000	0.6439	0.7336
	Var/ty	0.00%	0.00%/0.00%	0.28%	1.95%
	Unc/ty	0.00%	0.00%/0.00%	0.53%	2.12%
5%	Average	1.702	0.049200/0.050000	0.6592	0.7268
	Var/ty	0.78%	3.89%/0.00%	1.22%	2.78%
	Unc/ty	0.87%	3.43%/0.00%	2.63%	4.70%
10%	Average	1.724	0.044700/0.050000	0.6978	0.7609
	Var/ty	2.75%	10.46%/0.00%	4.43%	3.17%
	Unc/ty	4.54%	17.77%/0.00%	4.21%	4.37%

4.11). As an overview of the results, we see that the vast majority of all the retrievals for the parameters a_t, v_t, and r_{eff} and a_{eff} have a Dif, Var and Unc below 25%, 22% and 11% respectively for size No 2 and

4.2. Synthetic retrievals with unknown refractive index (Synthetic microphysical retrievals for non-spherical particles)

Table 4.13: Table 4.12 continuation (1)
sphere-spheroid mixture (2, b, i-v, 1%, 5%, 10%)

	Parameters	RRI	IRI (mean/median)	SSA355	SSA532
	Synthetic	1.330	0.001000	0.9890	0.9921
1%	Average	1.347	0.003560/0.001000	0.9691	0.9771
	Var/ty	1.06%	80.62%/0.00%	2.63%	1.97%
	Unc/ty	2.09%	106.98%/50.00%	3.04%	2.25%
5%	Average	1.454	0.026340/0.0075	0.8648	0.8909
	Var/ty	2.00%	52.01%/0.00%	3.98%	3.20%
	Unc/ty	11.29%	121.55%/100.00%	14.44%	11.97%
10%	Average	1.465	0.027140/0.005500	0.8590	0.8848
	Var/ty	0.00%	13.69%/0.00%	0.40%	0.54%
	Unc/ty	11.65%	124.56%/136.36%	16.18%	13.57%
	Synthetic	1.400	0.005000	0.9437	0.9419
1%	Average	1.436	0.009360/0.005000	0.9302	0.9498
	Var/ty	2.08%	51.03%/0.00%	3.85%	2.81%
	Unc/ty	5.29%	126.82%/0.00%	6.40%	4.98%
5%	Average	1.496	0.022020/0.003000	0.8703	0.8985
	Var/ty	1.95%	60.69%/0.00%	2.56%	1.84%
	Unc/ty	10.30%	109.94%/83.33%	15.17%	11.76%
10%	Average	1.494	0.022480/0.015000	0.8710	0.8983
	Var/ty	0.82%	44.77%/0.00%	2.14%	1.37%
	Unc/ty	10.90%	109.83%/103.33%	15.65%	12.08%
	Synthetic	1.500	0.010000	0.8811	0.9234
1%	Average	1.576	0.017600/0.010000	0.8427	0.8919
	Var/ty	2.63%	22.43%/0.00%	2.52%	2.48%
	Unc/ty	5.14%	46.02%/0.00%	5.06%	3.94%
5%	Average	1.634	0.023600/0.030000	0.8213	0.8720
	Var/ty	4.15%	31.51%/0.00%	5.15%	3.93%
	Unc/ty	5.35%	47.07%/0.00%	8.44%	6.11%
10%	Average	1.647	0.023520/0.030000	0.8258	0.8759
	Var/ty	3.79%	27.48%/0.00%	3.95%	2.09%
	Unc/ty	5.99%	40.17%/0.00%	6.11%	5.06%
	Synthetic	1.600	0.001000	0.9838	0.9901
1%	Average	1.668	0.003700/0.005000	0.9384	0.9698
	Var/ty	0.27%	9.85%/0.00%	2.95%	1.49%
	Unc/ty	2.84%	52.05%/0.00%	3.61%	1.70%
5%	Average	1.680	0.003200/0.005000	0.9601	0.9722
	Var/ty	2.39%	59.81%/0.00%	2.13%	1.88%
	Unc/ty	3.81%	70.53%/0.00%	2.89%	2.37%
10%	Average	1.720	0.002460/0.005000	0.9736	0.9822
	Var/ty	1.99%	93.51%/0.00%	2.09%	1.06%
	Unc/ty	3.38%	106.08%/33.33%	2.55%	1.92%
	Synthetic	1.700	0.050000	0.6359	0.7154
1%	Average	1.700	0.050000/0.050000	0.6307	0.7099
	Var/ty	0.00%	0.00%/0.00%	0.59%	0.12%
	Unc/ty	0.00%	0.00%/0.00%	0.36%	0.25%
5%	Average	1.736	0.046000/0.050000	0.6733	0.7450
	Var/ty	2.30%	10.07%/0.00%	2.46%	1.65%
	Unc/ty	3.43%	12.96%/0.00%	3.64%	2.79%
10%	Average	1.736	0.042800/0.050000	0.6980	0.7644
	Var/ty	2.16%	12.03%/0.00%	3.63%	2.64%
	Unc/ty	4.34%	18.59%/0.00%	4.97%	3.82%

33%, 17% and 16% for size No 3. This means that the ERQ here increase roughly by 3-20% on average as compared to the fixed-RI retrievals, see Table 4.8. The variability of the chosen solutions is generally less affected on average than the uncertainty (Unc) which shows 6-7% increase in the transition to higher error levels for the parameters v_t and r_{eff}.

The most-distinctly affected parameter in accuracy is indeed the volume concentration, as one can immediately infer from the given ranges, especially for the size No 3. The effective radius has much narrower ranges and ends up with a better average retrieval behavior than v_t which is more prominent

4.2. Synthetic retrievals with unknown refractive index (Synthetic microphysical retrievals for non-spherical particles)

Table 4.14: Table 4.12 continuation (2)

prolate (2, c, i-v, 1%, 5%, 10%)

	Parameters	RRI	IRI (mean/median)	SSA355	SSA532
	Synthetic	1.330	0.001000	0.9890	0.9921
1%	Average	1.330	0.005700/0.005000	0.9359	0.9519
	Var/ty	0.00%	36.73%/0.00%	2.38%	1.80%
	Unc/ty	0.00%	38.52%/0.00%	2.75%	2.11%
5%	Average	1.373	0.014800/0.005000	0.9119	0.9297
	Var/ty	0.23%	30.90%/0.00%	0.92%	0.80%
	Unc/ty	8.48%	203.39%/90.00%	11.47%	10.61%
10%	Average	1.367	0.015100/0.007500	0.9054	0.9240
	Var/ty	0.00%	0.00%/0.00%	0.27%	0.07%
	Unc/ty	8.56%	199.54%/33.33%	12.66%	11.15%
	Synthetic	1.400	0.005000	0.9428	0.9626
1%	Average	1.336	0.000980/0.001000	0.9878	0.9914
	Var/ty	0.23%	108.05%/0.00%	1.16%	0.77%
	Unc/ty	1.33%	145.09%/0.00%	1.48%	1.04%
5%	Average	1.363	0.002960/0.001000	0.9676	0.9775
	Var/ty	0.60%	72.97%/0.00%	1.71%	1.17%
	Unc/ty	2.77%	142.83%/50.00%	4.35%	3.04%
10%	Average	1.418	0.012700/0.003	0.9186	0.9381
	Var/ty	0.77%	9.32%/0.00%	0.92%	0.80%
	Unc/ty	9.67%	177.16%/66.67%	12.88%	10.17%
	Synthetic	1.500	0.010000	0.8763	0.9239
1%	Average	1.400	0.001160/0.001000	0.9805	0.9877
	Var/ty	0.00%	48.98%/0.00%	0.71%	0.45%
	Unc/ty	0.00%	94.36%/0.00%	1.89%	1.23%
5%	Average	1.395	0.003740/0.005000	0.9400	0.9620
	Var/ty	0.66%	35.21%/0.00%	2.41%	1.59%
	Unc/ty	2.39%	45.66%/0.00%	2.61%	1.70%
10%	Average	1.401	0.005380/0.000500	0.9449	0.9615
	Var/ty	1.20%	54.86%/0.00%	2.82%	2.37%
	Unc/ty	5.83%	177.89%/0.00%	7.90%	5.83%
	Synthetic	1.600	0.001000	0.9837	0.9905
1%	Average	1.500	0.000120/0.000000	0.9976	0.9985
	Var/ty	0.00%	72.11%/0.00%	0.40%	0.25%
	Unc/ty	0.00%	140.55%/0.00%	0.34%	0.21%
5%	Average	1.500	0.000300/0.000000	0.9941	0.9965
	Var/ty	0.00%	136.68%/0.00%	0.72%	0.43%
	Unc/ty	0.00%	95.58%/0.00%	0.57%	0.34%
10%	Average	1.492	0.000720/0.000000	0.9888	0.9937
	Var/ty	0.89%	119.93%/0.00%	1.63%	0.91%
	Unc/ty	2.30%	155.05%/0.00%	1.68%	0.89%
	Synthetic	1.700	0.050000	0.6344	0.7145
1%	Average	1.560	0.036000/0.030000	0.6532	0.7342
	Var/ty	3.26%	12.65%/0.00%	0.67%	1.07%
	Unc/ty	4.23%	18.33%/0.00%	0.66%	0.75%
5%	Average	1.546	0.036400/0.030000	0.6843	0.7565
	Var/ty	1.50%	9.40%/0.00%	2.34%	2.60%
	Unc/ty	5.14%	34.05%/33.33%	9.52%	7.27%
10%	Average	1.559	0.035200/0.040000	0.7331	0.7955
	Var/ty	1.81%	16.49%/0.00%	4.28%	3.14%
	Unc/ty	8.59%	51.97%/25.00%	13.75%	10.67%

for size No 3. The surface-area concentration is overall the least affected parameter. The ERQ for a_{eff} still allow for a characterization of the effective geometry, especially for prolate and sphere-spheroid mixed particles. The parameter *svcf* has the widest uncertainty ranges (Var, Unc), and while most retrievals lie within 10% Var and 17% Unc, the accuracy levels (not shown) are often prohibitive for a meaningful shape-size ditribution reconstruction.

One reason behind an inaccurate RI-retrieval is the overestimation of the number of iterations. In our simulations both with known an unknown RI, we fixed the maximum number of iterations (MNI) to 100

4.2. Synthetic retrievals with unknown refractive index (Synthetic microphysical retrievals for non-spherical particles)

Table 4.15: Retrieval of the parameters a_t, v_t, r_{eff}, $svcf$ and a_{eff} with Pade-DP, corresponding to all the cases from Tables 4.12 and C.21, i.e. (2, 3, a-c, i-iv, 1%, 5%, 10%). The indications "1%", "5%" and "10%" on the left of a given part of the table refer to retrievals with the respective input data error. The parenthesized terms show the mean value of the respective ERQ within the range specified above it.

Cases: (2, a-c, i-iv, 1%, 5%, 10%)

	Parameters	a_t	v_t	r_{eff}	$svcf$	a_{eff}
1%	Difference	$0.62 - 16.70\%$ (9.16%)	$0.25 - 40.26\%$ (13.51%)	$3.01 - 25.28\%$ (13.37%)	$-$	$0.98 - 31.97\%$ (15.79%)
	Variability	$0.60 - 5.54\%$ (2.82%)	$0.36 - 13.00\%$ (4.00%)	$0.43 - 10.06\%$ (3.56%)	$1.36 - 56.47\%$ (11.40%)	$0.19 - 3.40\%$ (1.17%)
	Uncertainty	$0.54 - 12.15\%$ (4.04%)	$1.26 - 20.27\%$ (7.72%)	$1.24 - 10.35\%$ (5.74%)	$1.41 - 41.01\%$ (17.10%)	$0.16 - 4.65\%$ (2.27%)
5%	Difference	$1.96 - 23.71\%$ (11.60%)	$2.37 - 46.33\%$ (14.23%)	$2.60 - 23.76\%$ (15.46%)	$-$	$1.47 - 31.63\%$ (17.89%)
	Variability	$1.16 - 5.15\%$ (2.55%)	$1.09 - 12.20\%$ (6.02%)	$0.95 - 11.78\%$ (5.03%)	$2.31 - 9.67\%$ (5.78%)	$0.27 - 1.18\%$ (0.73%)
	Uncertainty	$2.53 - 11.65\%$ (6.00%)	$3.58 - 24.45\%$ (15.04%)	$4.77 - 23.86\%$ (14.16%)	$4.29 - 29.79\%$ (10.96%)	$0.51 - 3.48\%$ (1.56%)
10%	Difference	$4.11 - 26.35\%$ (13.74%)	$0.40 - 45.19\%$ (15.00%)	$3.40 - 24.63\%$ (16.61%)	$-$	$2.87 - 31.66\%$ (18.46%)
	Variability	$1.22 - 3.96\%$ (2.07%)	$0.58 - 13.43\%$ (5.38%)	$1.07 - 12.37\%$ (4.81%)	$2.78 - 9.96\%$ (5.49%)	$0.28 - 1.45\%$ (0.69%)
	Uncertainty	$3.04 - 14.65\%$ (7.65%)	$12.11 - 32.31\%$ (22.35%)	$9.08 - 31.78\%$ (21.34%)	$5.99 - 23.14\%$ (11.38%)	$0.72 - 2.95\%$ (1.70%)

Cases: (3, a-c, i-iv, 1%, 5%, 10%)

	Parameters	a_t	v_t	r_{eff}	$svcf$	a_{eff}
1%	Difference	$1.48 - 20.55\%$ (9.06%)	$10.40 - 195.64\%$ (38.36%)	$5.22 - 172.81\%$ (30.39%)	$-$	$1.52 - 29.21\%$ (14.23%)
	Variability	$1.03 - 6.88\%$ (3.26%)	$0.58 - 23.68\%$ (13.31%)	$1.32 - 22.00\%$ (11.50%)	$1.11 - 68.63\%$ (17.39%)	$0.18 - 5.51\%$ (2.49%)
	Uncertainty	$0.50 - 2.70\%$ (1.20%)	$0.93 - 6.09\%$ (3.34%)	$0.69 - 5.12\%$ (3.07%)	$2.89 - 21.53\%$ (9.55%)	$0.61 - 2.60\%$ (1.18%)
5%	Difference	$2.56 - 23.59\%$ (11.16%)	$9.54 - 48.24\%$ (33.48%)	$1.65 - 43.25\%$ (23.50%)	$-$	$1.44 - 29.24\%$ (15.33%)
	Variability	$1.43 - 6.64\%$ (3.23%)	$2.32 - 17.57\%$ (9.95%)	$1.65 - 15.91\%$ (8.41%)	$3.77 - 57.39\%$ (15.17%)	$0.44 - 4.10\%$ (2.06%)
	Uncertainty	$1.95 - 10.20\%$ (4.43%)	$4.00 - 27.55\%$ (10.66%)	$2.58 - 23.69\%$ (10.45%)	$7.29 - 73.32\%$ (26.31%)	$0.80 - 4.80\%$ (3.38%)
10%	Difference	$0.73 - 29.92\%$ (14.10%)	$8.11 - 61.60\%$ (33.24%)	$3.44 - 38.22\%$ (20.06%)	$-$	$1.98 - 34.50\%$ (17.34%)
	Variability	$1.04 - 7.25\%$ (3.32%)	$1.95 - 16.69\%$ (9.70%)	$2.04 - 15.27\%$ (8.11%)	$5.10 - 15.80\%$ (10.30%)	$0.52 - 3.06\%$ (1.60%)
	Uncertainty	$3.83 - 17.26\%$ (8.34%)	$9.88 - 52.07\%$ (19.39%)	$7.64 - 41.54\%$ (16.93%)	$12.05 - 54.79\%$ (28.43%)	$1.95 - 6.29\%$ (4.11%)

for the retrievals in order to automatize the retrievals and provide more general results. For retrievals where the RI is known, the MNI plays a small role in the inversion outcome. However, in the case where the RI is sought, the MNI can affect the retrieval in an essential manner. For the cases with the largest disagreements in RI, the number of runs required before the iteration stopped, was most of the times 100, and this is not resolved by raising the MNI. In other words, the given discrepancy (relative error level) is never met, and the iteration exhausts the MNI. Rerunning problematic cases e.g. (3, c, v, 1%), (2, c, v, 1%) with MNI set to only 10 or less, we achieved 100% accuracy in the IRI, and also improved cases with 10% error level. Hence, for severely ill-posed cases and/or very noisy data, a small MNI (< 20 iterations) might generally be a good idea. The specification of a suitable MNI is often possible by observing systematic behaviors with preliminary runs which are vital for physically meaningful solutions in the case of real-life data.

Summarizing our findings for the retrievals, we saw that all in all, while the retrieval of the refractive index is tricky for the IRI, it is indeed viable and a remarkable achievement accounting all the limitations brought about by a fixed-kernel database and the inversion process. Except for minor cases where the algorithm does not perform well, the retrieval can give an accurate prediction for the real part of the refractive index and at least a sensible account for the level of absorption related to the imaginary part. Discrepancies in the retrieval of the refractive index do not necessarily spoil equivalently the quality of a_t, v_t, r_{eff}, and a_{eff}. However, the generally larger ERQ in the case of an unknown RI, may distort

Table 4.16: Retrieval results of the parameters a_t, v_t, r_eff, *svcf* and a_eff with unknown refractive index with Pade-DP for a collection of challenging cases from Tables C.21-C.24. The letters A-I are used for a prompt case recognition.

A: $1.33+0.001i$, Cases: (2, b, i, 1%, 10%)

	Parameters	a_t	v_t	r_eff	*svcf*	a_eff
1%	Difference	16.70%	0.89%	15.19%	0.1673	6.09%
	Variability	3.45%	5.63%	3.76%	4.89%	0.68%
	Uncertainty	4.09%	8.46%	6.16%	8.14%	1.02%
10%	Difference	22.74%	6.40%	22.78%	0.1877	6.66%
	Variability	1.30%	0.68%	1.07%	3.66%	0.37%
	Uncertainty	9.54%	24.64%	28.66%	5.99%	0.76%

B: $1.4+0.005i$, Cases: (2, a, ii, 1%, 10%)

		a_t	v_t	r_eff	*svcf*	a_eff
1%	Difference	12.34%	3.95%	8.00%	0.1457	31.14%
	Variability	2.90%	2.15%	2.28%	2.84%	0.56%
	Uncertainty	12.15%	20.27%	9.21%	12.48%	1.86%
10%	Difference	17.25%	2.31%	12.31%	0.1236	31.66%
	Variability	1.22%	1.19%	1.18%	3.98%	0.40%
	Uncertainty	9.87%	28.66%	29.51%	8.00%	1.12%

C: $1.5+0.01i$, Cases: (2, a, iii, 1%, 10%)

		a_t	v_t	r_eff	*svcf*	a_eff
1%	Difference	2.30%	10.44%	12.59%	0.1296	31.30%
	Variability	1.84%	5.29%	5.24%	15.25%	1.67%
	Uncertainty	1.82%	11.05%	9.98%	28.29%	4.40%
10%	Difference	7.18%	15.93%	21.70%	0.1242	31.60%
	Variability	2.30%	9.33%	8.90%	5.97%	0.83%
	Uncertainty	3.04%	32.31%	31.78%	12.02%	1.78%

D: $1.7+0.05i$, Cases: (2, c, v, 1%, 10%)

		a_t	v_t	r_eff	*svcf*	a_eff
1%	Difference	11.39%	40.26%	25.07%	0.1626	12.78%
	Variability	5.54%	13.00%	10.06%	56.47%	3.40%
	Uncertainty	5.52%	13.62%	10.35%	41.01%	3.90%
10%	Difference	6.15%	17.08%	9.95%	0.2990	19.27%
	Variability	2.22%	5.17%	4.23%	7.59%	0.77%
	Uncertainty	5.42%	27.99%	26.02%	21.33%	2.77%

E: $1.33+0.001i$, Cases: (3, c, i, 1%, 10%)

		a_t	v_t	r_eff	*svcf*	a_eff
1%	Difference	10.50%	27.70%	15.20%	0.1373	13.81%
	Variability	4.90%	13.38%	9.26%	27.34%	5.51%
	Uncertainty	0.68%	4.35%	3.84%	20.33%	2.60%
10%	Difference	20.93%	45.89%	20.27%	0.2776	17.53%
	Variability	3.55%	9.45%	6.76%	12.45%	1.76%
	Uncertainty	3.83%	10.91%	8.05%	29.72%	3.07%

F: $1.7+0.05i$, Cases: (3, c, v, 1%, 10%)

		a_t	v_t	r_eff	*svcf*	a_eff
1%	Difference	8.40%	195.64%	172.81%	0.3617	21.90%
	Variability	1.23%	0.58%	1.59%	1.11%	0.18%
	Uncertainty	1.13%	0.93%	1.75%	4.47%	0.85%
10%	Difference	9.08%	15.04%	5.57%	0.2783	17.95%
	Variability	1.04%	1.95%	2.04%	5.10%	0.52%
	Uncertainty	5.81%	11.45%	11.11%	15.93%	2.04%

significantly the solution reconstruction. We note that even though we did not include the whole body of cases used in our analyses, all the rest fall very well within the ranges in Table 4.15. We should stress that the two different efficiency levels between size No 2 and No 3 should not be treated equally. As pointed out throughout this work, the retrievals with size No 3 pose indeed greater difficulties as compared to the other particle sizes and, as such, it seems that the behavior of the retrievals related to size No 2 is more frequently encountered vs size No 3.

Table 4.17: Table 4.16 continuation

G: $1.4 + 0i$, Cases: (1-4, b, ix, 1%)

	Parameters	a_t	v_t	r_{eff}	$svcf$	a_{eff}
size No 1	Difference	5.59%	20.29%	15.74%	0.2288	8.42%
	Variability	2.74%	2.89%	3.82%	3.83%	0.58%
	Uncertainty	4.01%	11.89%	8.64%	12.57%	1.53%
size No 2	Difference	1.61%	18.11%	19.66%	0.2276	8.93%
	Variability	2.23%	3.55%	2.93%	9.38%	1.26%
	Uncertainty	4.10%	11.60%	7.57%	26.49%	3.30%
size No 3	Difference	10.72%	37.67%	23.59%	0.0002	0.76%
	Variability	3.63%	25.14%	21.86%	7.79%	1.00%
	Uncertainty	1.16%	4.44%	3.54%	3.80%	0.78%
size No 4	Difference	5.94%	31.48%	35.29%	0.2675	6.17%
	Variability	1.93%	20.11%	21.40%	36.39%	4.53%
	Uncertainty	1.75%	21.41%	20.68%	37.83%	4.35%
H: $1.6 + 0.03i$, Cases: (1, a, c, xiii, 1%)						
oblate	Difference	9.45%	8.26%	15.85%	0.1693	29.41%
	Variability	1.33%	1.18%	2.22%	2.81%	0.37%
	Uncertainty	4.36%	4.63%	8.98%	7.47%	1.15%
prolate	Difference	18.80%	61.20%	35.31%	0.2763	18.65%
	Variability	4.21%	5.59%	3.91%	15.03%	1.81%
	Uncertainty	6.29%	7.23%	3.27%	9.51%	1.92%
I: $1.4 + 0.1i$, Cases: (1, a, c, xi, 1%)						
oblate	Difference	6.63%	4.89%	1.65%	0.1136	32.48%
	Variability	0.84%	0.43%	0.77%	4.92%	0.51%
	Uncertainty	3.35%	6.99%	5.75%	3.18%	0.32%
prolate	Difference	8.26%	5.70%	2.40%	0.2912	19.14%
	Variability	1.11%	0.53%	0.91%	5.06%	0.52%
	Uncertainty	3.31%	7.81%	6.21%	3.75%	0.37%

Chapter 5

Microphysical retrieval from measurement cases

Foreword

After thoroughly testing our methods and algorithms we will finally apply our approach to real-life lidar data. Here, we use the algorithm SA2 (Sec. 3.6) with the (2,1) Padé iterative regularization method to a collection of measurement cases captured by different lidar stations and extract the microphysical properties from lidar data. Every lidar system involved in the measurement cases here is capable of supporting the $3\beta + 2\alpha$ setup which consists of 3 backscatter coefficients at the wavelengths 355, 532 1064 nm and 2 extinction coefficients at 355 and 532 nm and additionally providing the cross-polarized signal at least at 532 nm. The optical data profiles retrieved by these systems become then the input for our inversions, after they are averaged to produce a dataset, which is done by specifying certain layers of interest. Throughout our retrievals the spheroid-particle approximation is considered, confined in the aspect-ratio range [0.67, 1.5] preset by the Mieschka fixed-kernel database.

We will either make assumption of data error and use the discrepancy principle as parameter choice rule (Pade-DP) or restrict the iteration to a specific number of iterations, based on preliminary numerical tests and experience with our software so far. Since there is no equivalent in the literature of a two-dimensional particle distribution, we introduce the *reduced volume size distribution $v_a(r)$*, defined as the volume shape-size distribution $v(r,a)$ integrated over the aspect-ratio domain, i.e.

$$v_a(r) = \int_{a_{\min}}^{a_{\max}} v(r,a)\,da, \tag{5.0.1}$$

where r is volume-equivalent particle radius and a is the aspect ratio. All parameter notations and units are found in Table 5.1. The function $v_a(r)$ is able to provide the collective trend of all contributing particle geometries in the particle distribution. However, we note that this limited (in terms of information as compared to $v(r,a)$) particle distribution is not directly comparable with the usual size distribution used in literature, but it can be used in order to have a general sense qualitatively.

Furthermore, in our analyses we use data derived by inversions of sun-photometer measurements provided by the Aerosol Robotic Network's (AERONET) database, [60]. The algorithm used by AERONET postulates that aerosols have both a spherical and a non-spherical component, where the former is modeled by an ensemble of polydisperse, homogeneous spheres, and the latter considers a mixture of polydisperse, randomly-oriented homogeneous spheroids. These advanced machines offer a series of inversion products including the effective radius, the volume concentration, the complex refractive index, the single scattering albedo and the aerosol optical depth, which can be available in two quality levels, namely 1.5 and 2.0, for cloud screened and quality assured data respectively. In our studies, level 2.0 data were used whenever they were available. Sun-photometers are passive remote sensing instruments with different operation principles from lidars by definition and using different inversion techniques based on the theory of optimal estimation, see [34, 36]. Although we will not expand on the latter, we will point out some incompatibilities with our approach, which are essential to recognize for our subsequent microphysical analyses. The first and most important difference is that AERONET retrievals relate to the

Table 5.1: Notation and units of aerosol parameters. The dash indicates dimensionless quantities.

Parameter	Notation	Units
Ångström exponent 532/355 $\alpha-$ / $\beta-$ related	$\text{AE}^{\alpha/\beta}$ 355/532, AE^{β} 532/1064	–
aspect ratio	a	–
aspect ratio width	a_{var}	–
backscatter coefficient (total) at 355, 532, 1064 nm	$\beta355, \beta532, \beta1064$	$\text{Mm}^{-1}\text{sr}^{-1}$
effective aspect ratio	a_{eff}	–
effective radius	r_{eff}	µm
extinction coefficient at 355, 532 nm	$\alpha355, \alpha532$	Mm^{-1}
lidar ratio at 355, 532 nm	LR355, LR532	sr^{-1}
number concentration	n_{t}	$\text{µm}^{-1}\text{cm}^{-3}$
particle depolarization ratio at 355, 532, 1064 nm	$\delta355, \delta532, \delta1064$	–
refractive index (real and imaginary part)	RRI+IRIi	–
single scattering albedo (SSA) at 355, 532 nm	SSA355, SSA532	–
spherical volume concentration fraction	$svcf$	–
surface-area concentration	a_{t}	$\text{µm}^2\text{cm}^{-3}$
volume concentration (total, AERONET)	u_{t}	$\text{µm}^3\text{µm}^{-2}$
volume concentration (total, lidar)	v_{t}	$\text{µm}^3\text{cm}^{-3}$
volume concentration size distribution (AERONET)	VCSD	$\text{µm}^3\text{µm}^{-2}$
volume concentration size distribution (reduced)	VCSD (reduced)	$\text{µm}^3\text{µm}^{-2}\text{km}^{-1}$
volume shape-size distribution	$v(r,a)$	$\text{µm}^3\text{µm}^{-1}\text{cm}^{-3}$
volume size distribution (reduced)	$v_a(r)$	$\text{µm}^3\text{µm}^{-1}\text{cm}^{-3}$
wavelength	λ	nm

whole atmospheric column while lidar data target specific layers and therefore the comparison cannot be quantitative. Moreover, the size distribution of the particle volume $u(r)$ retrieved by AERONET is defined as the derivative $du/d\ln r$ with the associated total volume concentration u_t, both given in $\text{µm}^3\text{µm}^{-2}$. From Eq. 3.1.5 following the LM-model, the volume size distribution (for lidars) is found by $v(r) = dv_{\text{t}}/dr$ and measured in $\text{µm}^3\text{µm}^{-1}\text{cm}^{-3} = \text{µm}^3\text{µm}^{-2}\text{m}^{-2}$. In order to make sense of these two different measures and have some kind of comparison we turn to the quantity $\tilde{v}(\ln r) = dv_{\text{t}}/d\ln r = rv(r)$, which indicates that the difference in units with $du/d\ln r$ lies within a multiple of the meter. Here we apply the same concept also for our generalized model just by replacing $v(r)$ with $v_a(r)$. In practice, we often multiply $\tilde{v}(\ln r)$ with the aerosol layer thickness (usually several kilometers), see [114, 131], which is the motivation behind the units given in Table 5.1 for the so-called (reduced) *volume concentration size distribution* (VCSD), following the terminology from [131]. We will use these functions as a lidar-analog for a common basis to discuss the retrieval efficiency. Obviously, a converted reduced size distribution to a VCSD is an even more involved quantity, but it should indicate to some extent the main features of a size distribution. AERONET's VCSD is retrieved in 22 logarithmically equidistant bins between 0.05 and 15 µm. For the shape-size distribution we use a 30×30 $(r \times a)$ grid points with the radius range either $[0.01, 1.2]$ (µm) or $[0.01, 2.2]$ (µm) and the aspect ratio range $[0.67, 1.5]$. For clarity we note that whenever we show here an one-dimensional size distribution or VCSD associated with the lidar, it is always implied that the shape-size distribution is first converted to a reduced size distribution.

Second, many of AERONET's inversion products are given as a function of wavelength at least at the spectral bands of 442, 675, 872, 1020 nm where the four almucantar scans take place, in which category fall also the parameters aerosol (extinction) optical depth, the refractive index (RI) and single scattering albedo (SSA). Especially for the RI and the SSA we will consider a spectral average of these values in order to compare with the respective parameters from our retrievals. The ranges of the real (RRI) and imaginary part (IRI) of the refractive refractive index, $1.33 \leq \text{RRI} \leq 1.6$ and $0.0005 \leq \text{IRI} \leq 0.5$ form the predefined grid necessary for AERONET's inversion.

Following AERONET's mode distinction in the inversion products we calculate in some cases in addition to the total effective radius (whole radius range), the one for the fine mode and coarse mode. This is done by looking for the minimum of the shape-size distribution between 0.5 and 1 µm and setting it as the higher and the lower integration boundary for the fine and coarse mode respectively.

5.1. Data from National Institute for Optoelectronics, Bucharest (Microphysical retrieval from measurement cases)

Table 5.2: Case studies used for the microphysical retrievals from data captured by INOE's lidar in Romania. The table shows the date and time interval for the measurements, the lidar ratio (LR532) and Ångström exponents (AE$^{\alpha/\beta}$ 532/355) and particle depolarization ratio δ532, as well as the layer used for the inversion here and also in [131].

Case No.	Date (dd.mm.yy.)	Time interval	Layer (km)	LR532 (sr)	AE$^{\alpha}$ 532/355	AE$^{\beta}$ 532/355	δ532 (%)
1	14.06.2012	$17:52 - 18:52$	$1.57 - 1.88$	35 ± 3	2.2 ± 0.1	1.7 ± 0.1	7 ± 3
2	24.06.2012	$19:26 - 20:26$	$1.39 - 1.57$	55 ± 5	1.7 ± 0.2	1.0 ± 0.2	7 ± 2
3	27.06.2012	$19:30 - 20:30$	$1.59 - 1.89$	41 ± 4	1.8 ± 0.1	0.9 ± 0.1	5 ± 2
4	09.07.2012	$19:01 - 20:01$	$1.57 - 2.31$	49 ± 4	1.4 ± 0.1	1.1 ± 0.1	7 ± 2
5	11.07.2012	$23:01 - 00:01$	$2.55 - 2.77$	42 ± 4	1.5 ± 0.1	2.0 ± 0.2	5 ± 2

5.1 Data from National Institute for Optoelectronics, Bucharest

As a first example for the interaction of our algorithm with real data we will consider cases with relatively low depolarization. Low particle depolarization ratio (PDR) is often considered a strong indication of particle sphericity, but it is only the converse proposition, i.e. that high PDR is a hint of particle non-sphericity, that can be used with confidence. This is because different particle distributions, can have a strong smoothing effect as to the point that it can result a miniscule PDR even for aspect ratios far from $a = 1$, as demonstrated in [112]. Therefore this example is of more general interest also from the point of view of non-spherical particles.

Here, we will investigate the 5 main cases (different days of measurements) presented in [131] which pertain to biomass burning aerosols mixed with urban aerosols of variable age and growth. Smoke particles are usually modelled as spheres, because of their relatively small size. In this publication, the lidar data were collected from a multi-wavelength depolarization Raman lidar, located in the National Institute for Optoelectronics (INOE) in Magurele, Romania (44.35° N, 26.03 E°). This lidar system is part of EARLINET [110] since November 2005 and uses a Nd-YAG laser emitting at 1064, 532 and 355 nm and a receiver collecting at 1064, 355, 607, 387 and 408 nm and additionally owns separate horizontal- and cross polarized channels at 532 nm. In other words, it is capable of providing the optical data setup $3\beta + 2\alpha$ plus depolarization profiling at 532 nm. The date and time interval for the measurements used here along with the optical properties, lidar ratio at 532 nm, Ångström exponent (AE$^{\alpha/\beta}$ 532/355) and particle depolarization ratio δ532 are given in Table 5.2. The layer used for the inversions in [131] and here are also found in this table. These altitude ranges, were selected by first identifying the aerosol layer by looking at the range-corrected signal in the given time intervals and further focusing on layer sections where the intensive parameters lidar ratio and Ångström exponent are almost constant. More details on this methodology, examples of the optical data profiles and the raw lidar signal, and the origin of the biomass burning aerosols detected by this lidar system can be found in the aforementioned paper.

The microphysical properties retrieved in [131] are based on a hybrid algorithm applied in truncated singular value decomposition (HTSVD) using the Lorenz-Mie model for the calculation of the scattering efficiencies. Here, we retrieved the parameters r_{eff}, RI, and SSA532 and compare with the HTSVD-retrieved ones and further with the inversion products of the collocated sun-photometer (INOE). The sun-photometer measurements, considered most relevant in [131], were the ones early in the morning after the respective lidar measurements and will be used here as well. In addition, we retrieved the parameters $n_{\text{t}}, a_{\text{t}}, a_{\text{eff}}, a_{\text{var}}$ and *svcf*. All results are found in Table 5.3. As we can see from Table 5.2, the extinction-related Ångström exponents range from $1.2 - 2.3$, suggesting quite small particles, i.e. a predominant fine mode, which is expected for this aerosol type. With this indication and some preliminary tests we established the upper radius bound $r_{\text{max}} = 1.2\,\mu\text{m}$ in our generalized (Fredholm) integral model. We set the refractive index grid to RRI × IRI = $[1.33, 1.4, 1.5, 1.6] \times [0, 0.001, 0.005, 0.01]$, the spline points to $6 - 14$, the spline degree to $2 - 5$, the maximum number of iterations to 30, and the amount of least residual solutions to 5. These settings were based on preliminary tests performed in [131] and on further tests with our software.

As we see in Table 5.3 the effective radii predicted by our algorithm (about $0.25\,\mu\text{m}$) are a little above the mean value between the HTSVD- and the AERONET-retrieved values, and they are normal values for fine particles. The refractive index was found $1.33(\pm0.0) + 0.004(\pm0.0055)i$ in case No. 1
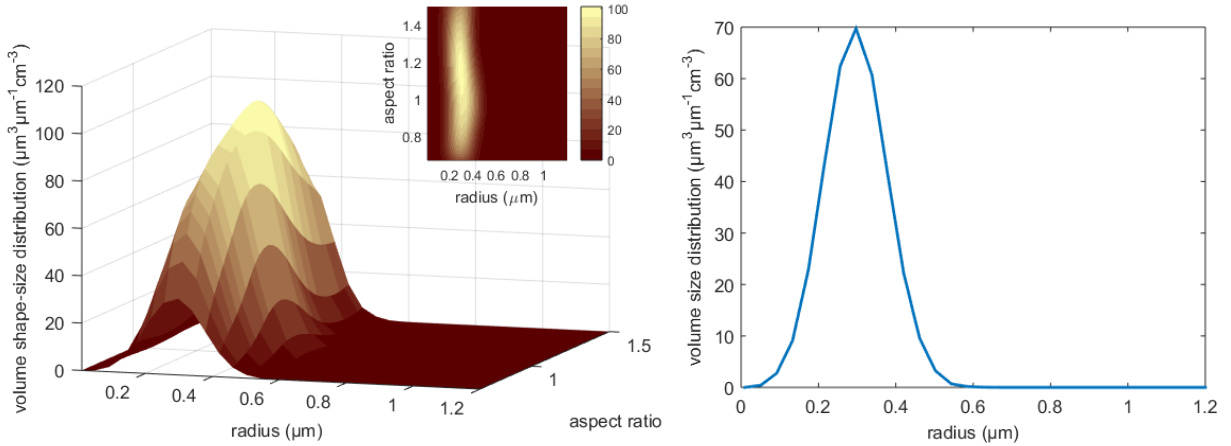
Figure 5.1: Left (main plot): the retrieved shape-size distribution shown in 3D and in the ar-plane (small plot on top). Right: the volume size distribution (reduced) for the case study No. 2 in Bucharest, see Table 5.2.

and $1.33(\pm 0.0) + 0.001(\pm 0.0)i$ in cases No. 2-5. The RRI is closer to the retrieved value of HTSVD (about 1.36) than the one of AERONET (about 1.44). By contrast, the IRI retrieved by Padé iteration is much larger indicating quite absorbing particles while the other approaches (especially AERONET) show very weakly absorbing particles in the IRI-range $0.0005 - 0.0024$. Nevertheless, a high level of absorption is indeed more physically explicable for smoke particles. The retrieved single scattering albedos follow these findings, i.e. the Padé-retrieved (0.931-0.971) are lower than the HTSVD- (0.983-0.995) and the AERONET-retrieved (0.991-0.995). It is noteworthy though that although there is a distinct disagreement in the IRI among these approaches, the SSA has rather conservative variation, reconfirming its dependence also in the particle distribution.

Now looking at the additional parameters we retrieved for these cases in the lower sub-table of Table 5.3 we have the following concentration ranges $n_{\rm t} : 191.30 - 611.29\,{\rm cm}^{-3}$, $a_{\rm t} : 115.62 - 397.18\,{\rm \mu m}^2{\rm cm}^{-3}$ and $v_{\rm t} : 9.30 - 33.19\,{\rm \mu m}^3{\rm cm}^{-3}$, all of which are retrieved with very low solution variability ($< 4\%$), see the standard deviations. The effective aspect ratio is about 1.10 with $a_{\rm var} = 0.048$, which lies within the close neighborhood of $a = 1$ (spheres) but suggest also other non-spherical contributions. This is also reflected in the spherical volume concentration fraction which is about 27% on average for all cases. In Fig. 5.1 we show one example (case No. 2) of the retrieved two-dimensional volume shape-size distribution (left) and the reduced volume size distribution (right), which is characteristic for all cases. Focusing on the shape-size distribution, we can see the spread along the aspect ratio axis, enabling the aforementioned non-sphericity, with a peak at about $a = 1.1$, $r = 0.3\,{\rm \mu m}$. The reduced size distribution gives a synoptic view of all the aspect ratio contributions, highlighting again the presence of a single particle (fine) mode. However, it is more likely that there is also a coarse mode, probably much smaller, which cannot be revealed perhaps because of the pronounced difference with the fine mode. This is an occasional numerical encounter, as explained in [131] which is resolved sometimes by extending the radius range up to $4\,{\rm \mu m}$. The only possibility here is rerunning the inversion with $r_{\rm max} = 2.2\,{\rm \mu m}$ which changes virtually nothing in the distribution data or the microphysical parameters. On the other hand, this feature could be an additional sign of stability in the optical data and our algorithm.

Finally, we note that we could possibly achieve better parameter approximations if we look each case individually rather than fixing identical projection-dimension ranges (spline features) for all cases. This was done primarily in order to demonstrate that for carefully chosen cases in terms of quality and good knowledge on aerosol type, wider dimension ranges (like the ones we used) can still provide acceptable solutions. Strongly non-spherical particles, mixed and/or aged aerosols, and/or too noisy data are always factors that require more delicate selection for the input parameters (splines, RIG, etc.).

5.2 Data from SALTRACE campaign, Barbados island country

5.2. Data from SALTRACE campaign, Barbados island country (Microphysical retrieval from measurement cases)

Table 5.3: Retrieved microphysical parameters for several case-studies of biomass burning aerosols captured by Romania's lidar station. For the lidar-based inversion, the given standard deviation represents the variability of the chosen (5) least-residual solutions and from the retrieved values, and for the sun-photometer-based inversion is based on the parameters retrieved from the consecutive measurements (AERONET) early in the morning (after the lidar measurements). Especially for the complex refractive index and the single scattering albedo retrieved by AERONET, spectral mean values in the four almucantar wavelengths are implied. The indications "HTSVD", "Padé" and "A" stand for inversion products with the method HTSVD in [131] and the Lorenz-Mie model, with Padé regularization with the generalized model and with AERONET's approach respectively. The HTSVD-retrievals shown here correspond to the ones with $r_{max} = 2\,\mu m$ in [131]. The parameter notation is given in Table 5.1.

HTSVD - Padé iteration - AERONET

Param. / Case No.	r_{eff}-HTSVD (μm)	r_{eff}-Padé (μm)	r_{eff}-A fine (μm)	RRI-HTSVD	RRI-Padé	RRI-A	IRI-HTSVD	IRI-Padé	IRI-A	SSA532-HTSVD	SSA532-Padé	SSA-A
1	0.275 ± 0.010	0.241 ± 0.003	0.177 ± 0.016	1.362 ± 0.039	1.33 ± 0.0	1.460 ± 0.039	0.0024 ± 3.4E-4	0.004 ± 0.0055	5E-4 ± 0.0	0.983 ± 1.3E-4	0.971 ± 0.040	0.994 ± 1.7E-4
2	0.324 ± 0.019	0.284 ± 0.002	0.184 ± 0.004	1.356 ± 0.005	1.33 ± 0.0	1.415 ± 0.039	6.7E-4 ± 1.5E-4	0.01 ± 0.0	5E-4 ± 0.0	0.995 ± 2E-5	0.937 ± 0.00075	0.995 ± 1.5E-4
3	0.301 ± 0.007	0.248 ± 0.002	0.152 ± 0.020	1.356 ± 0.005	1.33 ± 0.0	1.419 ± 0.026	9.5E-4 ± 1.2E-4	0.01 ± 0.0	5.8E-4 ± 1.8E-4	0.993 ± 0.0	0.930 ± 0.00081	0.993 ± 3.04E-3
4	0.325 ± 0.023	0.251 ± 0.003	0.148 ± 0.012	1.356 ± 0.004	1.33 ± 0.0	1.445 ± 0.032	0.00172 ± 3E-4	0.01 ± 0.0	8.3E-4 ± 5.5E-4	0.987 ± 1.6E-4	0.931 ± 0.00096	0.991 ± 4.57E-3
5	0.278 ± 0.008	0.251 ± 0.003	0.149 ± 0.003	1.352 ± 0.003	1.33 ± 0.0	1.439 ± 0.033	0.020 ± 1.8E-4	0.01 ± 0.0	7.5E-4 ± 3.0E-4	0.985 ± 1E-5	0.931 ± 0.00090	0.991 ± 3.47E-3

Padé iteration

Case No.	n_{t} (μm^{-1}cm^{-3})	a_{t} (μm^{2}cm^{-3})	v_{t} (μm^{3}cm^{-3})	$svcf$	a_{eff}	a_{var}
1.	191.30 ± 7.19	115.62 ± 1.47	9.30 ± 0.033	0.263 ± 0.018	1.102 ± 0.005	0.047 ± 0.002
2.	180.35 ± 5.44	145.98 ± 1.07	13.80 ± 0.043	0.290 ± 0.019	1.090 ± 0.011	0.048 ± 0.003
3.	233.95 ± 5.91	148.43 ± 0.80	12.26 ± 0.08	0.270 ± 0.017	1.096 ± 0.009	0.048 ± 0.002
4.	611.29 ± 22.84	397.18 ± 3.56	33.19 ± 0.27	0.265 ± 0.020	1.099 ± 0.009	0.049 ± 0.001
5.	279.57 ± 10.12	181.70 ± 1.70	15.20 ± 0.11	0.266 ± 0.002	1.099 ± 0.009	0.049 ± 0.002
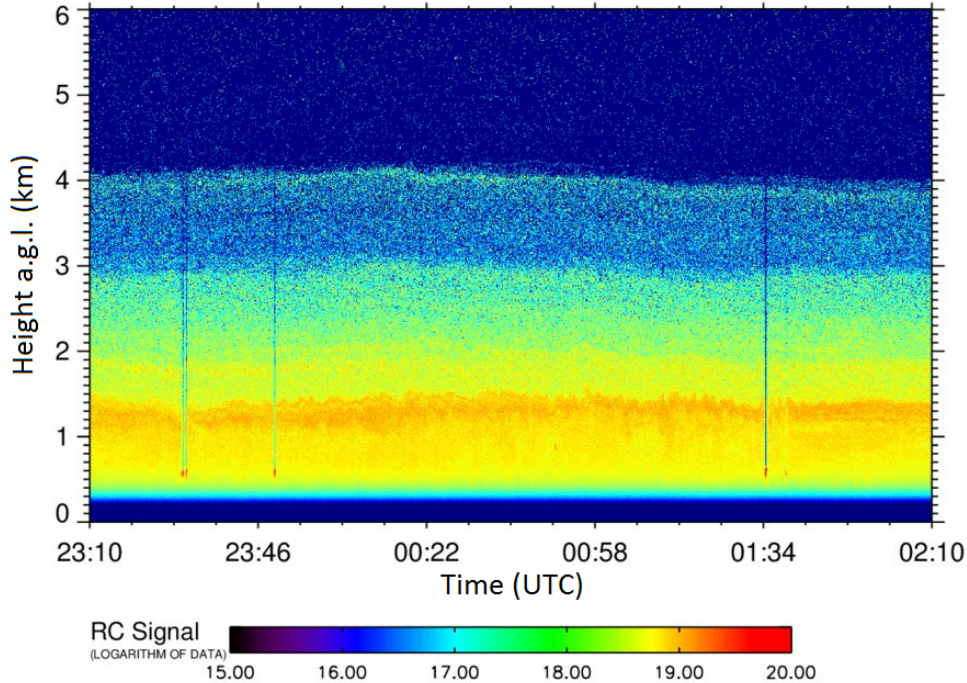
Figure 5.2: Time series of lidar range-corrected signal at 1064 nm collected by Barbados's lidar system BERTHA. An intense dust layer is detected in 0.3-4 km a.g.l.

We are going to investigate a case captured by one of the most advanced lidar systems to date, located at Barbados island east of the Caribbean sea, 13.15° N, 59.62° N. More specifically the measurements were carried out on 20 June 2014 between 23:10-02:10 UTC, by the lidar system of Leibniz Institute for Tropospheric Research (TROPOS) called *BERTHA*. This system is able to provide depolarization ratio profiles at 355, 532 and 1064 nm, see [51] in addition to the usual $3\beta + 2\alpha$ dataset. These measurements took place within the framework of the Saharan Aerosol Long-Range Transport and Aerosol-Cloud-Interaction Experiment (SALTRACE) (http://www.pa.op.dlr.de/saltrace/index.html) in 2013-2014, with the aim to characterize optical and microphysical properties of dust after transport across the Atlantic Ocean.

Let us have a look at the color plot of the range-corrected signal at 1064 nm for our case from 20 June 2014, see Fig. 5.2. We can distinguish a well defined intense aerosol layer between 0.5 and 4 km. Looking now at the optical profiles in Fig. 5.3, the linear particle depolarization ratio at all available wavelengths is well over 20% above 1.5 km and reaches up to 32% (δ532) at about 3.7 km, a clear indication of non-sphericity. The full overlap of this system is not reached before 1 km. Furthermore, the linear particle depolarization ratio at all available wavelengths in Fig. 5.3 has a steady raise in the region 0.5-1.5 km (not shown) from 8% to 20%. This is a clear signature of turbulence which differentiates the dust- (>1.5 km) from the mixing layer according to [49] as found in the similar experimental situation during SALTRACE campaign in summer 2013. This is why we are mostly interested in altitudes over 1.5 km. Focusing on the lidar ratio profiles at 355 and 532 nm in Fig. 5.3 in the altitude range 1.5-4 km we have values with small variation, about 50 ± 9 sr, typical of dust presence see e.g. [3, 49, 58]. Therefore the aerosol type seems to be reasonably confined, but looking at AE$^{\alpha}$ 532/1064 in Fig. 5.3, particle size is rather influenced significantly with height, mainly above the 3rd km where we see also contributions of smaller particles (larger AE). The values of AE$^{\alpha}$ 355/532 (0.027 ± 0.425) and AE$^{\beta}$ 532/1064 (0.486 ± 0.062) are also quite characteristic of Saharan dust particles, as it was found in the lidar-ratio-based climatology derived statistically from observations and put together by [103]. Moreover, the depolarization values and the lidar ratios at 355 and 532 nm fall within the ranges of aged Saharan dust found during SALTRACE campaign in 2013 in the dust layer (not the boundary or mixing layer), see [49].

5.2. Data from SALTRACE campaign, Barbados island country (Microphysical retrieval from measurement cases)
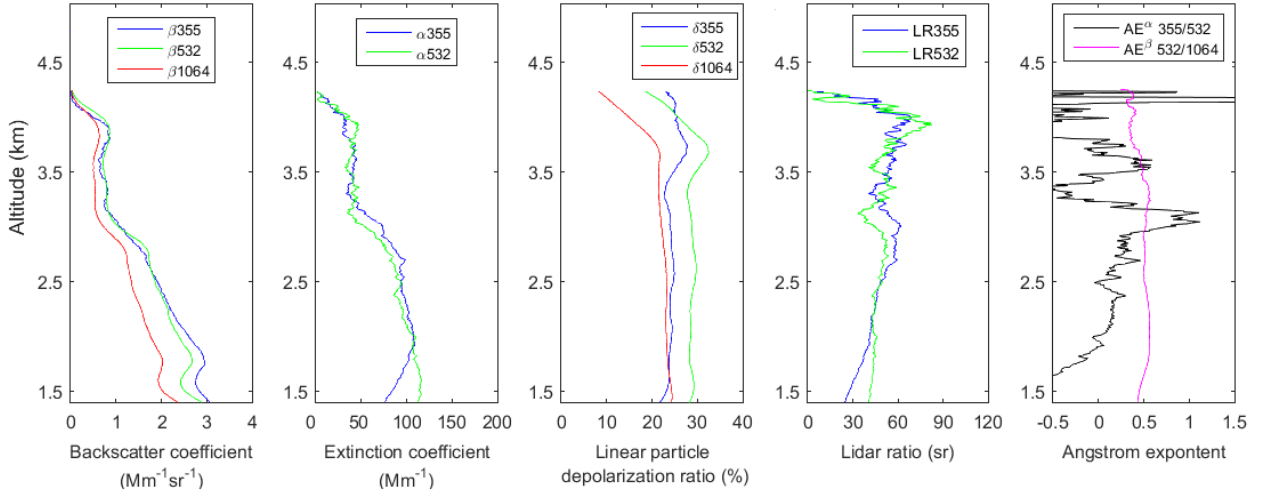
Figure 5.3: Optical properties retrieved by Barbados's lidar station. From left to right, the following profiles are shown: total backscatter coefficient at 355, 532 and 1064 nm, extinction coefficient at 355 and 532 nm, linear particle depolarization ratio at 355, 532 and 1064 nm, lidar ratio at 355 and 532 nm, the extinction- and backscatter-related Ångström exponents AE^{α} 355/532, AE^{β} 532/1064, see also the notation in Table 5.1.

In order to find out the probable origins of the particles examined here, we ran the NOAA HYSPLIT model ([32], http://ready.arl.noaa.gov/HYSPLIT.php), see Fig. 5.4. The produced backward trajectories suggest dusty air masses travelling above the African coastline (Western Sahara and Mauritania) and Mali, 8 days before arriving above Barbados. The intensity of this dust event is quite high with an aerosol optical depth (AOD) ranging between 0.36-0.52 found with direct sun measurements performed by the sun/sky radiometer in Barbados in Ragged Point (13.17° N, 59.43° W) 20 km far from the lidar site. Fig. 5.5 shows the daily evolution of the AOD in several wavelengths, and we see that during the last available measurement (18:44 UTC), about $4\frac{1}{2}$ hours before the lidar measurement, the AOD has reached its highest value (e.g. 0.5 for 500 nm).

A reasonable layer selection where both lidar ratio and the Ångström exponent are relatively constant, the aerosol properties are more representative of the total behavior and where the optical profiles (α and β) are still intense is the one in 2-2.75 km, see the average values and standard deviation of these properties tabularized in Table 5.4. However it is most interesting to investigate in addition, what is the microphysical parameter variability with respect to different altitudes as we move upwards in the atmospheric column, which will further give us feedback on the stability and layer sensitivity of our algorithm. For this purpose, we retrieve the parameters a_t, v_t, r_{eff} (total, fine, coarse), a_{eff}, a_{var}, $svcf$, RI, and SSA532 for the whole altitude range 1.5-4 km with a step of 250 m. For the inversion we used 100 iterations of Padé regularization, 9-14 spline points and spline degree within the range 2-5. Less spline points (e.g. 6) were cut off because the did not behave well with the strong tendency towards (radius-) bimodality, which was indicated as most probable by preliminary tests, e.g. by making unclear or eliminating the separation plane between the modes. The refractive index grid (RIG) was first defined in the broad form of RRI × IRI = $[1.4, 1.5, 1.6, 1.7, 1.8] \times [0, 0.001, 0.005, 0.01, 0.05]$ (RIG 1). The upper integration boundary of the Fredholm equation was set to the (maximum available) $r_{max} = 2.2\,\mu m$.

The results reveal a pattern which allows to categorize them in three altitude ranges, namely 1.5-2.75 km, 2.75-3.25 km and 3.25-4 km, only by observing the largest parameter variation, see Table 5.5. In this table, the variability (Var %) plays, as usual, the role of the variability of the 5 best solutions for a single dataset corresponding to a specific altitude range, and the mean variability when more than one datasets are involved. The uncertainty (Unc %) of the mean parameter value, found for every altitude range, is also given, and it is calculated the same way it was done throughout this thesis, with the sole qualitative difference that the input-datasets correspond now to different altitude ranges instead of random distributions of synthetic noise. Especially for the complex refractive index and the single

5.2. Data from SALTRACE campaign, Barbados island country (Microphysical retrieval from measurement cases)
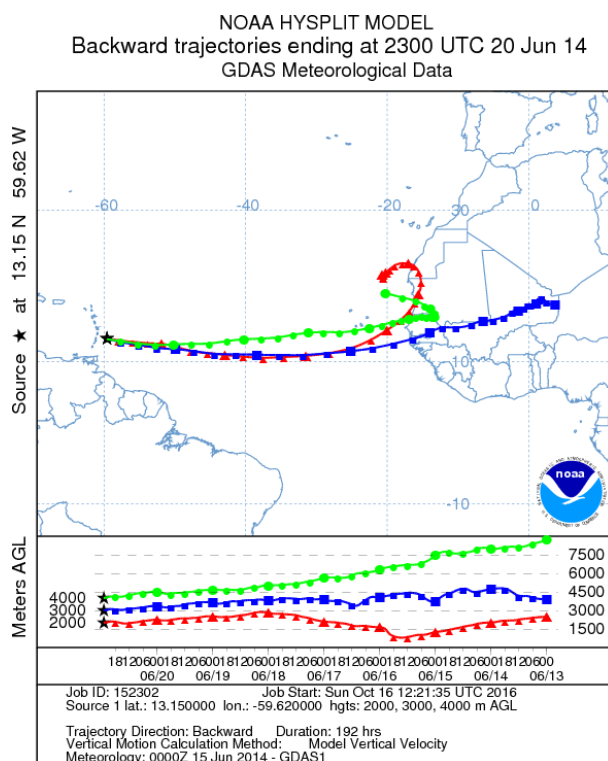
Figure 5.4: Air mass back-trajectories produced by HYSPLIT model for the case study captured by Barbados's lidar station.
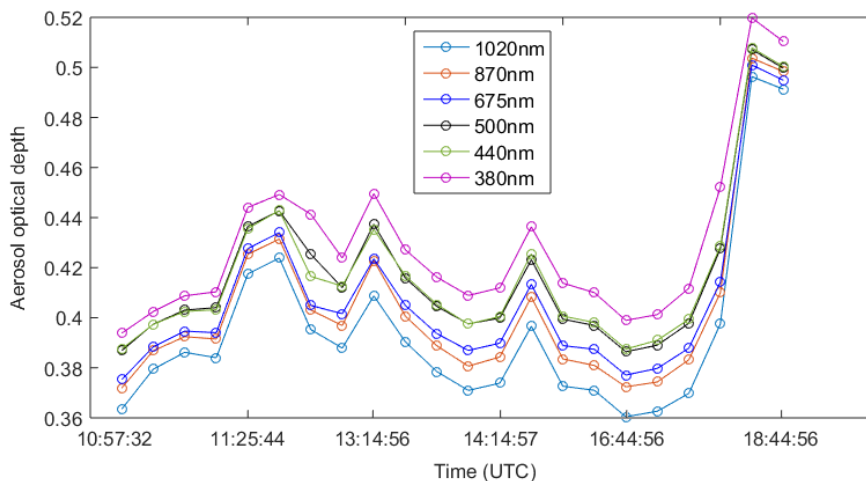
Figure 5.5: Daily evolution of the aerosol optical depth with spectral dependence derived by the sun-photometer in Ragged Point, 13.17° N, 59.43° W for the case study on 20.06.2014 in Barbados.

scattering albedo retrieved by AERONET, the given values represent spectral mean values in the four almucantar wavelengths. Hence, Var (%) corresponds to a mean spectral variability, and the given Unc (%) corresponds to the uncertainty of the mean retrieved parameters (spectrally) between the consecutive measurements.

We can see clearly from Table 5.5 that our algorithm demonstrates very good stability. There is virtually no difference in the microphysical retrieval between considering the whole range $2 - 2.75$ km and splitting the even larger range $1.5 - 2.75$ km to 5 smaller ranges of 250 m. The uncertainty of all

5.2. Data from SALTRACE campaign, Barbados island country (Microphysical retrieval from measurement cases)

Table 5.4: Optical and intensive properties derived by Barbados's lidar station, averaged in the dust layer in 2-2.75 km see Fig. 5.3.

Optical properties				
$\alpha 355$ (Mm^{-1})	$\beta 355^{\|/\perp}$ (Mm^{-1}sr^{-1})	$\alpha 532$ (Mm^{-1})	$\beta 532^{\|/\perp}$ (Mm^{-1}sr^{-1})	$\beta 1064^{\|/\perp}$ (Mm^{-1}sr^{-1})
98.50	1.69 / 0.41	92.51	1.56 / 0.45	1.17 / 0.27
Intensive properties				
$\delta 355/532/1064$ (%)	LR355 (sr)	LR532 (sr)	AE$^{\alpha}$ 355/532	AE$^{\beta}$ 532/1064
24±0.0 / 29±0.0 / 23±0.0	47.71 ± 5.2	46.34 ± 2.94	0.16 ± 0.09	0.48 ± 0.02

parameters is very low and thus we could consider any of these height ranges to arrive to the same result. We should note that this convenience could be largely the result of good quality data and the fact that we use the maximum number of depolarization data available at the present time. Our algorithm predicts large particles, as expected for an intense dust event, with a total effective radius of 0.71 µm ($1.5 - 2.75$ km) which is constituted by fully separated modes (as we will see later on), i.e. with r_{eff} fine 0.35 µm and r_{eff} coarse 1.45 µm. Now focusing on the altitude range $2.75 - 3.25$ km, we see that the total effective radius diminishes to 0.55 µm and also that the fine mode (0.21 µm) consists now of distinctly smaller particles. This is exactly as expected, from the higher values of the extinction-related Ångström exponent in these heights, we highlighted earlier, and it is a remarkable sensitivity feature of our algorithm. Moreover, going to even higher altitudes, i.e. $(3.25 - 4$ km), where AE$^{\alpha}$ 355/532 is close to the previous smaller values we saw in $1.5 - 2.75$ km (or even tinier), the effective radii (total, fine or coarse) are also "restored" or a little bit enhanced, following again the expected "resizing". Another notable characteristic is that the effective radius in $(3.25-4$ km) is still well-retrieved despite the dramatic attenuation of signal in these heights. The attenuation is already visible above 2.75 km, see Fig. 5.3, and in terms of the microphysical retrieval it is translated into a diminished surface-area- and total volume concentration see Table 5.5, as it was intuitively expected.

The effective shape behavior is attributed to prolate particle ensembles with $a_{\mathrm{eff}} = 1.10$ and $a_{\mathrm{eff}} = 0.046$. The sphericity rate 0.20% (Var: 17.18%) predicted by AERONET (lowest sub-table in Table 5.5) shows no involvement of spherical and (to some extent) fine particles. By comparison, the spherical volume concentration fraction (lidar) *svcf*, found 0.31 (Var: 3.79%, Unc: 1.33) in $1.5 - 2.75$ km, shows that there could be spherical-particle contributions. We note that AERONET's sphericity parameter refers to the percentage of the spherical- vs the non-spherical component (assumed by AERONET's forward model), and thus there is only a rough correspondence of this quantity with *svcf*. We get a more detailed visual of our retrieval by looking at the (mean) retrieved shape-size distribution for the altitude range $1.5 - 2.75$ km in Fig. 5.6, upper panel. There we see two very well separated modes, namely a narrower fine-to-medium-coarse mode and a much broader coarse mode, with volume concentration peaks about 58 and 48 µm^{3}cm^{-3} at about 0.43 and 1.45 µm respectively. There are contributions of all kinds of spheroidal particle geometries (also spherical), and for higher aspect-ratios ($a \geq 1.20$) the fine-coarse peak difference fades, so that both modes's maxima equalize at about 30 µm^{3}cm^{-3}. The lower panel of this figure shows also the reduced volume concentration size distribution (left, blue line) and the volume concentration size distribution retrieved by AERONET (right). The latter shows merely a very prominent coarse mode predicting very large particles. The complete absence of a fine mode is often a mathematical artifact when one of the expected modes is much more dominant than the other, and the smoothing process suppresses or eliminates the smaller one. Although the lidar-based (reduced) VCSD is not directly comparable quantitatively to the latter, as mentioned earlier, we can see that the volume concentration is of the same order in both figures by specifying the altitude. In this sense and by considering the thickness of the whole dust layer about 3.5 km, the estimated maximum lidar-retrieved concentration is about 0.14 µm^{3}µm^{-2} which is comparable with AERONET's maximum of about 0.24 µm^{3}µm^{-2}. Since the volume concentration is obviously not constant along the aerosol layer and also the sampled volume is different in the two cases, this calculation has no practical purpose other than the order comparison. This kind of comparison is also used and explained in detail in [131].

The refractive index is found $1.4 + 0.05i$ through all layers ($1.5 - 4$ km) and with 0% uncertainties (Var, Unc), and SSA532 = 0.684 (Var: 3.20%, Unc: 1.11%) which points to highly absorbing particles. Experimental findings have shown that such a high absorption can mainly be found near the sources

of dust events. For instance, a soil sample from Burkina Faso (rich in hematite and kaolinite) was found in [146] using also a spheroid-particle-based inversion scheme to have IRI = 0.0495 ± 0.0206 at 305 nm. Moreover, [73] found that the IRI increases a lot (up to 0.03) with decreasing particle size ($< 0.5\,\mu$m), again due to the predominant hematite / soot component in smaller particles. AERONET's retrieval suggests, on the contrary, a refractive index with RRI = 1.52 (Var: 1.02%, Unc: 1.54%) and IRI = 0.0017 (Var: 21.13%, Unc: 64.24%), and SSA = 0.963 (Var: 0.77%, Unc: 2.27%), i.e. weakly absorbing particles. However, this IRI is even lower than the usual values considered for Saharan dust particles, see e.g. [133]. The latter study also finds a dramatic increase in IRI (up to five times higher at 637 nm) when the dust concentration is lower so that a soot-type absorber prevails.

Rerunning the inversion for all the sub-layers in $1.50 - 2.75$ km with a narrower refractive index grid where IRI = $[0, 0.001, 0.005]$ (RIG 2), the retrieved values are RRI = 1.4 (Var, Unc: 0.0%) and IRI = 0.004 (Var: 55.90%, Unc: 0.0%) and SSA = 0.964 (Var: 2.75%, Unc: 1.14%). Looking at the recalculated parameters in Table 5.5, it is noteworthy that even with a retrieved IRI, which is an order of magnitude lower than the one previously retrieved, the differences are tolerable. The effective radius for the fine and the coarse mode remain almost intact, despite the essential degradation of the total r_{eff} to 0.32 μm, v_{t} is 22% higher and a_{t} is 32% lower. However the shape parameters *svcf* and a_{var} undergo a larger deviation from the previous values. The new values suggest that the spherical contribution is significantly decreased, which is now in better agreement with AERONET, and further the effective width in the aspect ratio domain is increased. These features make a qualitative difference indeed, leading to much different distributions. The new reduced VCSD (RIG 2) is also given in the lower left panel of Fig. 5.6 (red line) and shows an enhanced and broader fine-medium coarse mode and a narrower and smaller coarse mode. However, this pattern seems less likely for this kind of particles. Although, as it turns out both solutions (RIG 1, 2) may explain some part of the problem better than the other, we are inclined to accept the first solution (RIG 1) as more probable in a general sense to describe this case.

5.3 Data from ChArMEx campaign 2013, Granada

This is a case study from 16th, June, 2013 under the framework of the project *Chemistry-Aerosol Mediterranean Experiment* (ChArMEx) which took place from 11 June to 5 July 2013. This campaign's goal is to asses the current and future atmospheric state of the Mediterranean basin in chemical terms targeting gaseous reactive species and aerosol particles, and further to bridge the notion gap in the regional chemistry-climate system in Mediterranean in view of anthropogenic and climatic pressures. A detailed presentation of the motives and overview of this field work can be found in [96] and the site https://charmex.lsce.ipsl.fr/. We will investigate one of the several cases of mineral dust plumes observed in the period between 16 June and 3 July, over the western and central Mediterranean basins.

The measurements were performed by the Atmospheric Physics Group (GFAT), at the University of Granada, southeast of Spain using the lidar system MULHACEN, LR331-D400, located at 37.16°N, 3.61°W. This Raman multi-wavelength lidar is able to emit and detect the elastic signals at the wavelengths 355, 532 and 1064 nm, and the N_2 Raman-shifted signals at 387 and 607 nm, and thus it provides the $3\beta + 2\alpha$ setup. This is part of the EARLINET network and is fully described in [50]. A vital process to enhance the calibration accuracy of polarization lidars proposed by [42], known as the $\pm 45°$ *calibration method*, was applied in Granada's lidar system in 2010 so that it recently acquired an operational depolarization channel at 532 nm, see [22].

The sun-photometer data used here were taken from measurements of the GFAT with a Cimel deployed at Granada's station (680 m a.s.l.) a few hours later from the lidar measurements. The lidar range-corrected signal (RCS), see Fig. 5.7, was used to infer the aerosol layer between 2 and 3 km above sea level (a.s.l.), where there is an almost uniform particle spread in the atmospheric column above Granada, as shown in this color gradient plot. Fig. 5.8 depicts the profiles of the backscatter coefficients at 355, 532, and 1064 nm, the extinction coefficients at 355 and 532 nm, the lidar ratios at 355 and 532 nm and the Ångström exponent, see the notation in Table 5.1. The layer at $2.65 - 3.10$ km was selected for the inversion accounting for a small variation of the intensive properties LR355, LR532, AE^{α} 355/532, AE^{β} 355/532 and also for intense optical properties. From the point of view of depolarization, this layer choice might be seemingly uncharacteristic of the aerosols we investigate, because it gradually increases at this point. For one, the increase is less than 5% which is physically unimportant, since δ532 already exceeds 20%. Moreover, numerical experiments showed that the smoothing process suppresses these

Table 5.5: Retrieved microphysical parameters for the dust-case from 20.06.2014 captured by Barbados's lidar station. The variability (Var %) is calculated as it is defined in Sec. 4.1 from the chosen (5) least-residual solutions for the lidar-based inversion, and from the retrieved values in the consecutive measurements (AERONET) in the evening for the sun-photometer-based inversion. The uncertainty (Unc %) corresponds to the parameter uncertainty with respect to the different layer bins (250 m) within the specified altitude range in the associated sub-table. Especially for the complex refractive index and the single scattering albedo retrieved by AERONET, the given values represent spectral mean values in the four almucantar wavelengths, so that Var (%) is a mean spectral variability, and Unc (%) corresponds to the uncertainty of the mean retrieved parameters (spectrally) between the consecutive measurements. The parameter notation is given in Table 5.1.

Lidar-based inversion

RIG 1, RRI = 1.4 (Var, Unc: 0.0%), IRI = 0.05 (Var, Unc: 0.0%)

$2 - 2.75$ km   /   SSA532 = 0.685 (Var: 1.40%)

Parameter Unit	a_t $\mu m^2 cm^{-3}$	v_t $\mu m^3 cm^{-3}$	r_{eff} (total/fine/coarse) μm	$svcf$ —	a_{eff} —	a_{var} —
Average	160.68	36.44	0.68 / 0.29 / 1.45	0.31	1.10	0.046
Variability	3.71%	5.36%	4.62% / 3.09% / 1.54%	4.01%	0.38%	3.72%

$1.5 - 2.75$ km, step: 250 m   /   SSA532 = 0.684 (Var: 3.20%, Unc: 1.11%)

Average	163.07	38.63	0.71 / 0.35 / 1.45	0.31	1.10	0.046
Variability	2.88%	7.00%	5.54% / 4.67% / 1.68%	3.79%	0.53%	2.87%
Uncertainty	2.84%	6.75%	5.00% / 27.17% / 0.58%	1.33%	0.21%	1.55%

$2.75 - 3.25$ km, step: 250 m   /   SSA532 = 0.683 (Var: 1.90%, Unc: 1.78%)

Average	121.37	22.63	0.55 / 0.21 / 1.50	0.29	1.11	0.047
Variability	6.59%	7.75%	5.10% / 5.96% / 1.04%	3.71%	0.39%	2.66%
Uncertainty	21.68%	42.14%	21.52% / 13.67% / 3.07%	2.06%	0.16%	0.16%

$3.25 - 4$ km, step: 250 m   /   SSA532 = 0.677 (Var: 2.44%, Unc: 0.81%)

Average	65.24	16.28	0.753 / 0.398 / 1.46	0.32	1.10	0.046
Variability	2.65%	8.04%	6.71% / 7.26% / 1.36%	3.75%	0.54%	2.89%
Uncertainty	10.05%	3.22%	10.12% / 32.83% / 0.37%	3.89%	0.57%	2.42%

RIG 2, RRI = 1.4 (Var, Unc: 0.0%), IRI = 0.004 (Var: 55.90%, Unc: 0.0%)
SSA = 0.964 (Var: 2.75%, Unc: 1.14%)

$1.5 - 2.75$ km, step: 250 m

Average	199.42	26.44	0.32 / 0.40 / 1.63	0.19	1.18	0.084
Variability	2.88%	7.00%	5.33% / 4.08% / 4.60%	21.94%	4.55%	8.53%
Uncertainty	2.84%	6.75%	7.88% / 9.78% / 0.41%	28.38%	1.32%	7.10%

Sun-photometer-based inversion

Parameter Unit	u_t $\mu m^3 \mu m^{-2}$	r_{eff} (total/fine/coarse) μm	sphericity (%)	RRI —	IRI —	SSA —
Average	0.40	1.30 / 0.16 / 1.87	0.20	1.52	0.0017	0.963
Variability	6.21	7.25% / 6.35% / 7.27%	17.18%	1.02%	21.13%	0.77%
Uncertainty	—	—	—	1.54%	64.24%	2.27%

small differences in depolarization. At the same time the attenuated signal in a layer above or below the chosen one, affects the particle concentrations (as shown also in the Barbados case), and therefore the chosen layer seems to be a prudent choice.

The average values of the optical and intensive parameters used for the inversion are given in Table 5.6. Within the selected aerosol layer, the mean values of the lidar ratio at 532 nm 61.14±8.15, the extinction-related Ångström exponent 0.34 ± 0.19 and the particle depolarization ratio at 532 nm 25.87 ± 1.24, fall within the ranges for Saharan-dust particles from a lidar-ratio-based climatology shown in [103]. In fact, our case was attested in multiple ways (HYSPLIT backward trajectories, SIVIRI satellite products
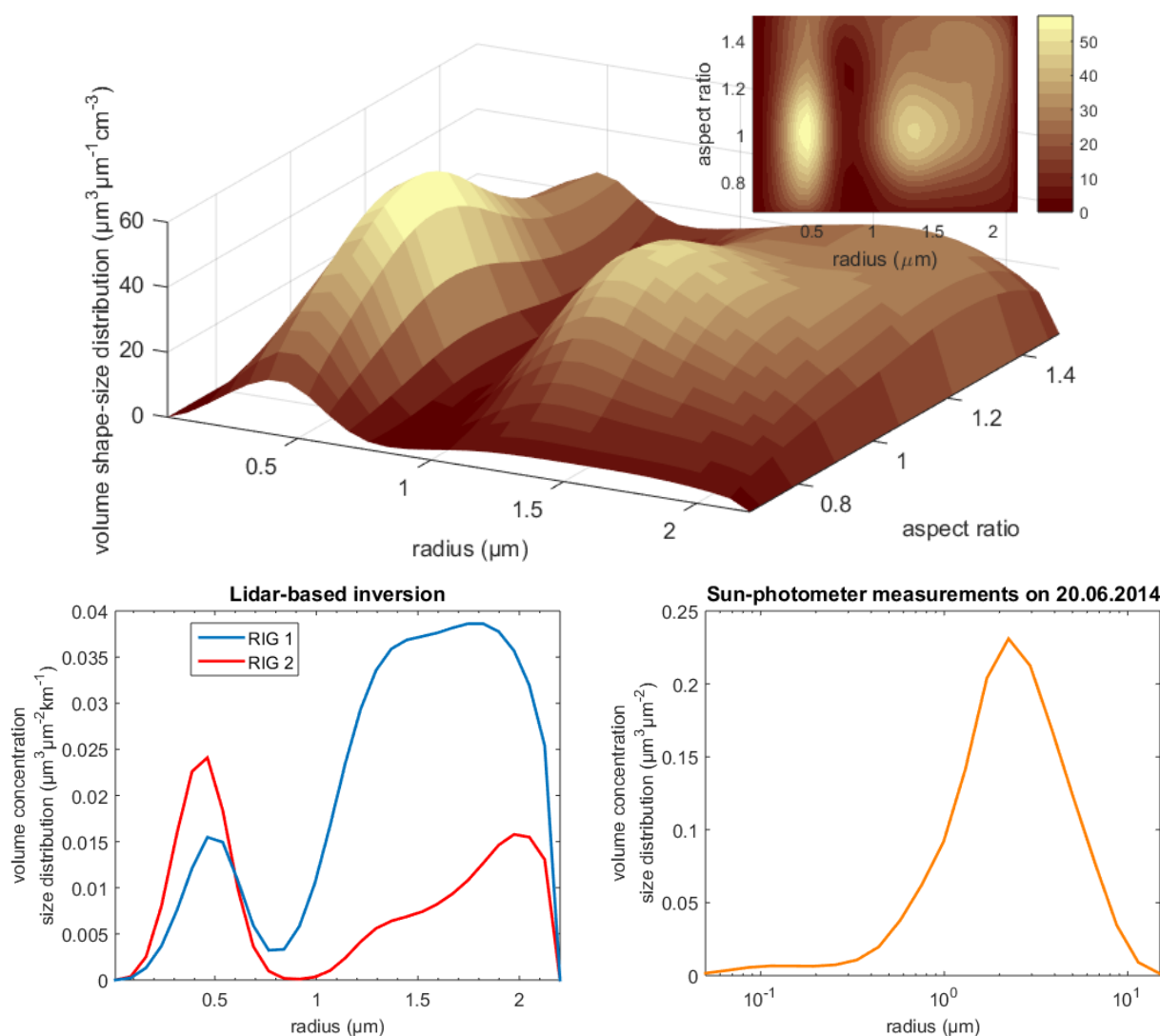
Figure 5.6: The retrieved shape-size distribution shown in 3D (upper panel, main plot) and in the *ar*-plane (small plot on top), the lidar-(reduced) VCSD for RIG 1 (lower panel, blue line), and RIG 2 (lower panel, red line), and AERONET's VCSD (lower panel, right) for the case study from 20.06.2014 in Barbados. The lidar-based distributions correspond to mean values for the altitude range $1.50 - 2.75$ km. The sun-photometer-based distribution corresponds to the mean retrieved distribution from consecutive measurements in the evening (AERONET).

and aircraft in situ measurements) during ChArMEx campaign to be only one case among many of a long-range transport of mineral dust mixed with urban/industrial pollution from Africa (in our case southwestern Algeria) travelling over the western Mediterranean basin, and it is documented in [31]. We give an example of a backward trajectory produced by the HYSPLIT model from 2 days before being detected by Granada's lidar in Fig. 5.9, where we clearly see the air masses originating from Algeria arriving in Granada at the altitudes 2.2 and 3 km. The sun-photometer measurements of direct solar irradiance, showed a small fluctuation of the aerosol optical depth at 500 nm from its daily average 0.21, also an indication of "dusty" conditions and large-particle predominance. In-situ aircraft measurements (French aircraft ATR-42, http://www.safire.fr) were performed in conjunction with the ground-based measurements. The flight temporally closest to our case was performed on June 16, 11:58-14:40 (UTC) with route Minorca-Granada, see [31]. The retrieval range of particle size of the mounted instruments reaches 20 μm, which is far beyond the observational potential of lidars and therefore a size comparison is not relevant here.
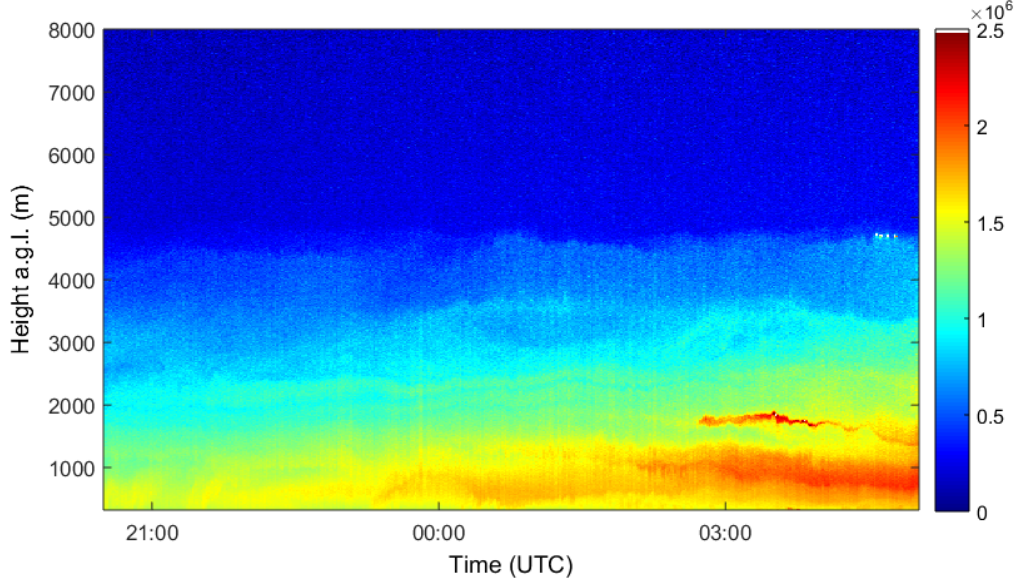
Figure 5.7: Time series of lidar range-corrected signal at $532\,\mathrm{nm}$ collected by Granada's lidar system MULHACEN, LR331-D400. A uniformly distributed dust layer is detected in $2 - 3\,\mathrm{km}$ above ground level (a.g.l). The ground level in this case is $680\,\mathrm{m}$ (elevation) above sea level. The colorbar is given in arbitrary units (a.u.).

Table 5.6: Optical data and intensive properties derived by Granada's lidar station, averaged in the dust layer $(2.65 - 3.10\,\mathrm{km})$, see also Fig. 5.8.

Optical data				
$\alpha 355$ (Mm^{-1})	$\beta 355$ $(\mathrm{Mm}^{-1}\mathrm{sr}^{-1})$	$\alpha 532$ (Mm^{-1})	$\beta 532^{\|/\perp}$ $(\mathrm{Mm}^{-1}\mathrm{sr}^{-1})$	$\beta 1064$ $(\mathrm{Mm}^{-1}\mathrm{sr}^{-1})$
115.60	1.56	100.88	1.33 / 0.34	1.62
Intensive properties				
$\delta 532$ (%)	LR355 (sr)	LR532 (sr)	AE^{α} 355/532	AE^{β} 355/532
25.87 ± 1.24	74.32 ± 1.88	61.14 ± 8.15	0.34 ± 0.19	-0.17 ± 0.11

The extinction-related Ångström exponent (AE^{α} 355/532) ranges generally in small values with a mean of 0.34 (see Table 5.6) in the chosen aerosol layer, which indicates quite large particles. This hint along with a few preliminary tests with our algorithm, led us to use the upper integration boundary of the Fredholm equation $r_{\max} = 2.2\,\mathrm{\mu m}$. The inversion took place within the predefined refractive index grid $\mathrm{RRI} \times \mathrm{IRI} = [1.4, 1.5, 1.6, 1.7, 1.8] \times [0, 0.001, 0.005]$. The confinement of the imaginary part of the refractive index to these values was also based on preliminary sensitivity tests for systematic algorithm behaviors. These tests also revealed a strong tendency of shape-bimodality, which led us to consider $6 - 8$ spline points and the spline degrees $2 - 3$, following the hint of a smaller projection dimension from Sec. 4.1.3. We assumed 5% and 10% data discrepancy leading to almost identical results, based on uncertainties given by the GFAT which were calculated through a standard procedure (Monte Carlo) used by EARLINET for the extinction- and backscatter coefficients, see [119].

All lidar-based inversion products are the mean values of the 5 best (least-residual) solutions, the standard deviation of which was used to compute the solution variability Var (%). For AERONET retrievals, Var (%) makes sense as a variability of the retrieved parameters from the concecutive evening measurements. The maximum number of iterations for Padé regularization was set to 30, in order to avoid overfit in case there are more than 10% actual errors in the data, even though preliminary runs with a maximum over 30 iterations did not show essential differences. We calculated the parameters RI, a_{t}, r_{eff} (total, fine, coarse), SSA532, $svcf$, a_{eff} and a_{var}. The results are found in Table 5.7, along with AERONET inversion products.

Figure 5.8: Optical properties retrieved by Granada's lidar station. From left to right, the following profiles are shown: total backscatter coefficient at 355, 532 and 1064 nm, extinction coefficient at 355 and 532 nm, particle depolarization ratio at 532 nm, lidar ratio at 355 and 532 nm, the extinction- and backscatter-related Ångström exponent 532/355 measured on 16.06.2013, between 22:00-22:30 UTC. The mean values used for the inversion are shown in Table 5.6.

The lidar-retrieved refractive index with RRI = 1.4 ($\pm 0.0\%$) and IRI = 0.0042 ($\pm 43\%$) is close enough to the experimental approximate value $1.52 + 0.003i$ observed for Saharan dust in the source region, see [133]. The retrieved RI-values are also not far (especially for the IRI) from the ones of AERONET, which predicts RRI = 1.57 (Var: 0.72%, Unc: 0.15%) and especially from the IRI = 0.0035 (Var: 47.75%, Unc: 0.86%). The lidar-based SSA at 532 nm ($0.961 \pm 1.77\%$) is a little higher than the computed spectral mean of AERONET's SSA in the almucantar wavelengths ($0.935 \pm 3.50\%$). On the other hand, our result agrees with the SSA estimated from chemical measurements (0.96) based on bulk aerosol samples collected during the aircraft flight on June 16, see [31] Table 5. The surface-area concentration was found 137.57 $\mu m^2 cm^{-3}$ ($\pm 5.31\%$) and the total effective radius 0.57 µm ($\pm 8.32\%$) , which is lower than AERONET's r_{eff} = 0.786 µm ($\pm 2.25\%$). The lidar-based coarse mode is also found lower and the fine mode higher than the AERONET-retrieved.

The parameter *svcf* was found 0.336 ($\pm$ 37.71%) indicating that there could be a considerable contribution of spherical particles to the volume concentration, and disagrees with AERONET's retrieved sphericity rate 0.0047 ($\pm 8.74\%$). Moreover, the effective aspect ratio ($1.19 \pm 7.67\%$) predicts a prolate particle-ensemble with a_{var} = 0.057 ($\pm 16.28\%$). The aforementioned shape observations based on the lidar are visualized through the two-dimensional shape-size distribution reconstruction in greater detail, see Fig. 5.10, where also its projection in the *ar*-plane is shown in a smaller plot above the main plot. This plot suggests that the expected coarse mode of the dust particles is merely a contribution of prolate particles. Smaller particles also appear quite dominantly in the spherical neighborhood ($a = 1$) and maybe there are oblate fine particles in lesser extent. The spherical contribution is perhaps a sign of presence of marine aerosols (sea salt) mixing with mineral dust during its transport in the marine boundary layer, see e.g. [74] where such mixtures where found for particles larger than 0.7 µm in the Caribbean aerosol (SALTRACE). It should be noted though that the sphericity of such particles depends on relative humidity, see [27, 70].

The right panel of Fig. 5.10 shows the volume concentration size distribution retrieved by AERONET. A comparison of the order of magnitude can be done, as in the case in Barbados, considering the thickness of the whole dust layer about 3 km. Then the estimated maximum lidar-retrieved concentration is about 0.06 $\mu m^3 \mu m^{-2}$ which is comparable with AERONET's maximum of about 0.082 $\mu m^3 \mu m^{-2}$. AERONET's size distribution shows a small fine mode and a very prominent coarse mode predicting very large particles. This conforms with measurements of the campaign where the effective diameter during the period 16.06-03.07 was found as high as $3.8 - 14.2$ µm, see [31]. Evidently, so large particles cannot even be observed
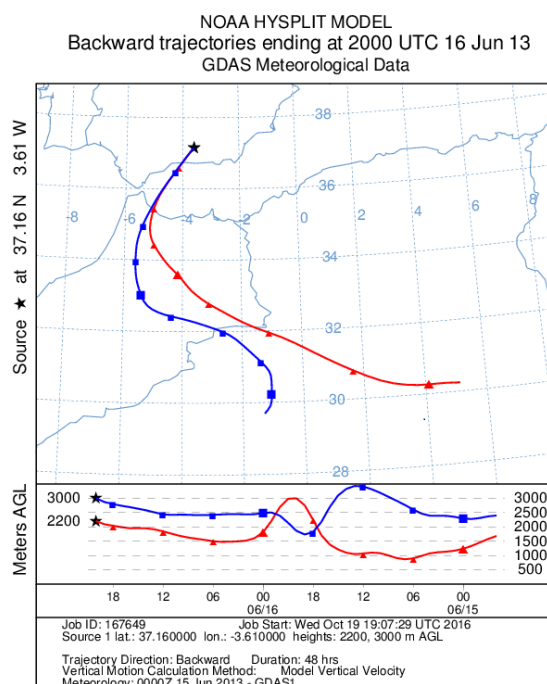
Figure 5.9: Air mass back-trajectories produced by HYSPLIT model for the case study captured by Granada's lidar station.

by lidar systems, and therefore our algorithm cannot have a complete picture of such coarse modes. Moreover, by converting the reduced size distribution to the lidar-analog for AERONET's $du/d\ln r$ (not shown) we observe that the reduced VCSD seems to have a forced steep ending towards its right end, which might also indicate the information gap. Nevertheless this lidar-based inversion is able to describe the physical phenomenon to a satisfying extent despite the algorithm-instrument limitations.

About the credibility of such a reconstruction as opposed to disregard of its multimodality as noise we have done a series of numerical theoretical experiments to verify that at least such distributions can be reconstructed, some of which were already shown in Sec. 4.1.3. We also designed a similar simulation tailored to this example (bimodal in shape without coarse mode) which reconfirmed this possibility. Furthermore, when multiple modes appear in simulations because of errors they are generally "messier" and they are often mixed, which is not the case here. In addition, the tests showed that the coarse mode can appear as a very mild artifact near the edge of the aspect ratio axis but not as prominent as in our case. Therefore we are confident enough to accept this result as a possible outcome both numerically and physically.

5.4 Data from Potenza's lidar station

The present case concerns another dust event from the record of the CNR-IMAA atmospheric observatory (CIAO), operated by the Institute of Methodologies for Environmental Analysis (Istituto di Metodologie per l'Analisi Ambientale - IMAA) of the National research council of Italy (Consiglio Nazionale delle Ricerche - CNR), also an EARLINET member since 2000. We are specifically interested in the multi-wavelength Raman Lidar *MUSA* (Multi-wavelength System for Aerosol), see [94], capable of retrieving the $3\beta + 2\alpha$ optical properties and additionally differentiating parallel and vertical depolarization signals at $532\,\text{nm}$ based on [42], and the CIMEL sun-photometer, both parts of CIAO located at Tito Scalo, Potenza, Italy ($40.60°$ N, $15.72°$ E, $760\,\text{m}$ a.s.l.). The aforementioned lidar system collected the optical data we are going to investigate on 04.09.2011 between 23:26-1:09 UTC.

The lidar range-corrected signal (RCS) in Fig. 5.11 shows an intense aerosol layer between 2 and $5\,\text{km}$ above sea level (a.s.l.). Altitudes below $2\,\text{km}$ where turbulence takes place (boundary layer) were not taken into account here. In Fig. 5.12 we show the back-trajectories created by HYSPLIT model

Table 5.7: Retrieved microphysical parameters for a dust-case captured by Granada's lidar station. The variability (Var %) is calculated as it is defined in Sec. 4.1 from the chosen (5) least-residual solutions for the lidar-based inversion, and from the retrieved values in the consecutive measurements (AERONET) in the evening for the sun-photometer-based inversion. Especially for the complex refractive index and the single scattering albedo retrieved by AERONET, the given values represent spectral mean values in the four almucantar wavelengths, so that Var (%) is a mean spectral variability, and Unc (%) corresponds to the uncertainty of the mean retrieved parameter (spectrally) between the consecutive measurements. The parameter notation is given in Table 5.1. The lidar-based SSA is calculated at 532 nm. The optical data used for the inversion are depicted in Fig. 5.8 and shown in Table 5.6.

Parameters	Average (Lidar)	Var (%)	Average (AERONET)	Var (%) / Unc (%)
a_t ($\mu m^3 \mu m^{-2}$)	137.57	5.31%	—	—
r_eff, fine (μm)	0.46	3.28%	0.125	1.70%
r_eff, coarse (μm)	1.51	7.89%	1.866	0.91%
r_eff, total (μm)	0.57	8.32%	0.786	2.25%
RRI	1.4	0.0%	1.57	0.72% / 0.15%
IRI	0.0042	43%	0.0035	47.75% / 0.86%
SSA	0.961	1.77%	0.935	3.50% / 0.05%
svcf	0.336	37.71%	—	—
sphericity	—	—	0.0047	8.74%
a_eff	1.19	7.67%	—	—
a_var	0.057	16.28%	—	—
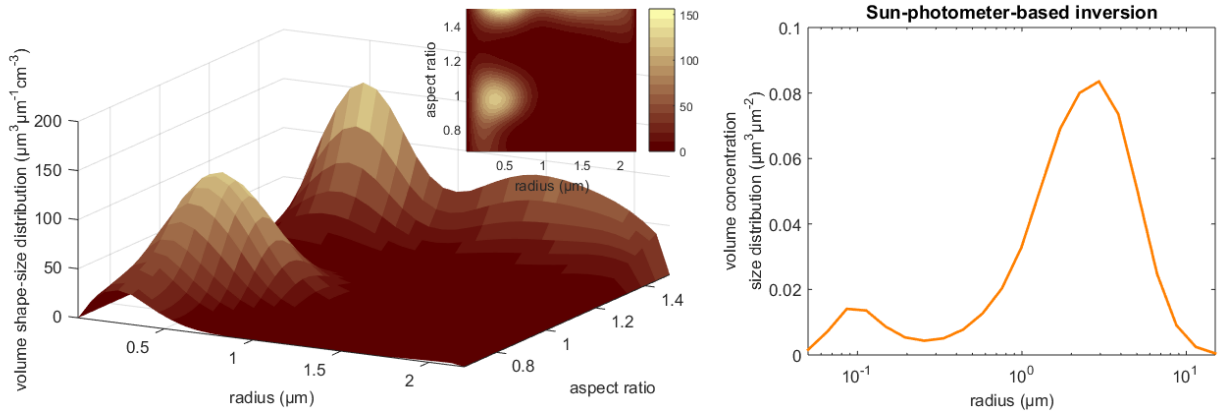
Figure 5.10: The retrieved shape-size distribution shown in 3D (left, main plot) and in the *ar*-plane (left, small plot on top), and AERONET's VCSD (right) for the case study from 16.06.2013 in Granada.

5 days before the air masses arrive above Potenza's lidar station. Here we observe clear contributions from African deserts and maybe from the industrialization of Morocco, which could result in a long range transport of dust particles mixed with pollution. At that time, the MODIS (Moderate Resolution Imaging Spectroradiometer) active fire product indicates areas around the lidar site and southwest of Italy where there could be fire events and thus there could be mixing of biomass burning aerosols with the polluted dust. However the significance of such contributions is unknown since the retrieved optical properties do not directly reflect this.

The optical profiles in Fig. 5.13 in $1.5 - 4.3$ km, show a very distinct aerosol layer with $\beta 532 = 1.5 \pm 0.3$ Mm^{-1}sr^{-1} and $\alpha 532 = 62.2 \pm 11.4$ Mm^{-1} and we further see the intensive properties LR355 $= 58.6 \pm 8.8$ sr, LR532 $= 43.4 \pm 5.5$ sr, AE$^\alpha = 0.45 \pm 0.16$, and $\delta 532 = 26.2 \pm 2.0$, which are typical values for dust particles. The relatively small variation of these properties is an ideal situation to test the stability of our algorithm by resolving the whole layer in smaller sub-layers and performing inversions to see variation of the microphysical parameters and the size distribution. For this, we divide the altitude range $2.45 - 3.95$ km with a step of 250 m and perform the microphysical retrieval of the properties $n_\mathrm{t}, a_\mathrm{t}, v_\mathrm{t}$, r_eff (total, fine, coarse), *svcf*, a_eff and a_var for the whole layer and all the sub-layers. The apparent choice
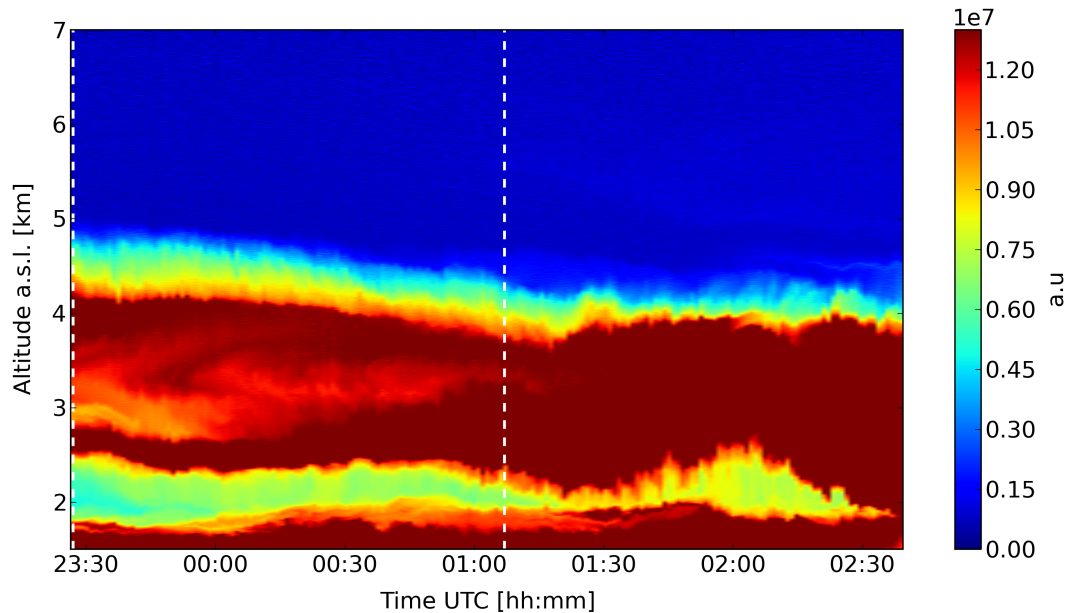
Figure 5.11: Time series of lidar range-corrected signal at 1064 nm collected by Potenza's lidar system MUSA. An intense aerosol layer is detected in 2 − 5 km a.s.l.
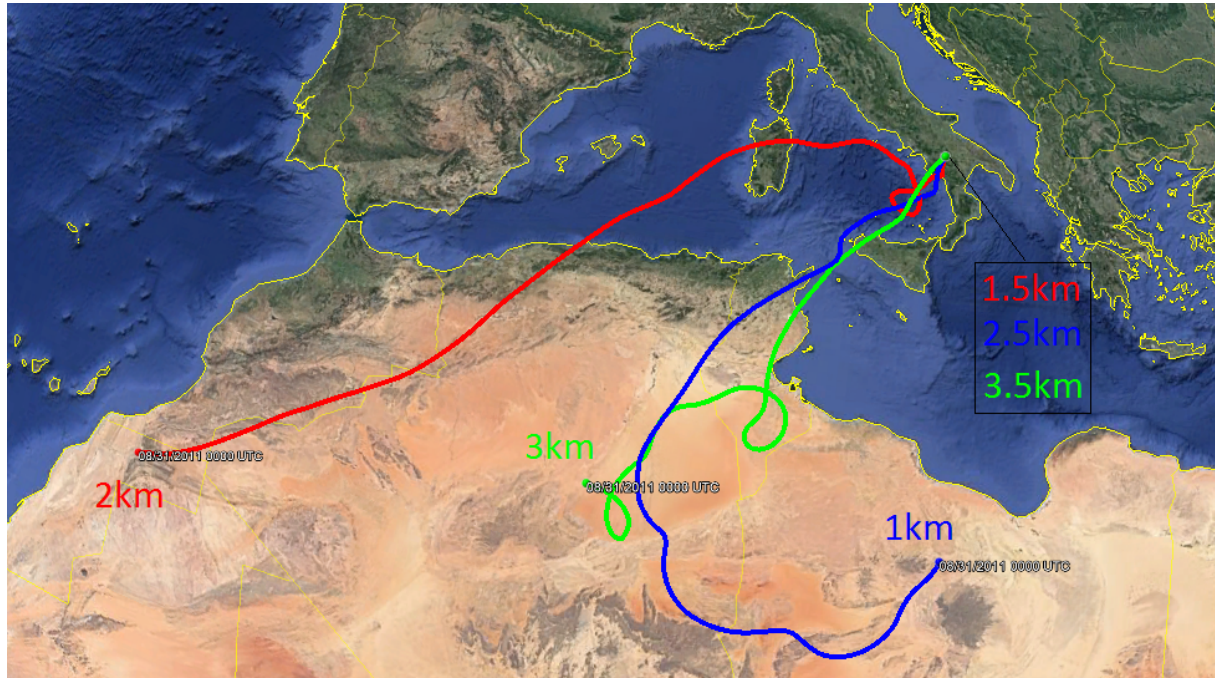
Figure 5.12: Air mass back-trajectories produced by HYSPLIT model for the case study captured by Potenza's lidar station. This plot was created by combining the HYSPLIT output trajectories with Google Earth tool. The colored distances mark the height of the air masses from the starting point (31.08.2011) to the finishing point (05.09.2011) a.g.l.

for the upper integration bound of the radius in the model equation was $r_{max} = 2.2\,\mu m$, but we also observed in preliminary tests that $r_{max} = 1.2\,\mu m$ restricts the distribution potential. With these tests we were also able to set the refractive index grid to $RRI \times IRI = [1.4, 1.5, 1.6, 1.7, 1.8] \times [0, 0.001, 0.005, 0.01]$, e.g. the option $IRI = 1.33$ was left out due to its vast mode suppression. Moreover, we used $6 - 14$ spline

points and $2 - 5$ degree splines, we set the maximum number of Padé iterations to 100, and the amount of least residual solutions to 5.

Table 5.8 shows the inversion results for the altitude range $2.45 - 3.95$ km with step 250 m and as a whole, and also for $2.45 - 2.7$ km separately, as the most intense layer with low variation of the lidar ratio and the Ångström exponent. In this table we also include AERONET inversion products from measurements of the sun-photometer early in the morning after the lidar measurements. As we can see there is a tiny difference in the retrieved values between $2.45 - 3.95$ km devided in smaller layers and as a whole which demonstrates stability. As compared to the Barbados's case in the regions where the variation of the intensive parameters is small (e.g. $1.5 - 2.75$ km, Table 5.5), here we have larger parameter uncertainties (Unc) as we reach higher altitudes, which are still very tolerable. Moreover, what is also different here is that the solution spaces have larger variability especially for the shape parameters $svcf$, a_{eff} and a_{var}. These features were expected since the inversion is less balanced here, i.e. with less depolarization data points than in the case of Barbados. However, it could also suggest that there are indeed particles with greater variation in shape.
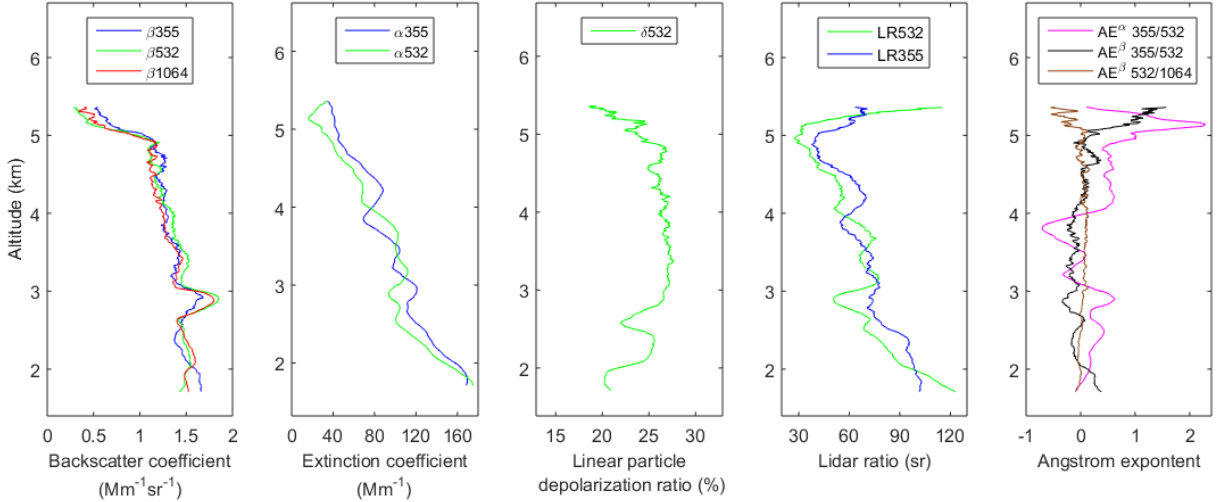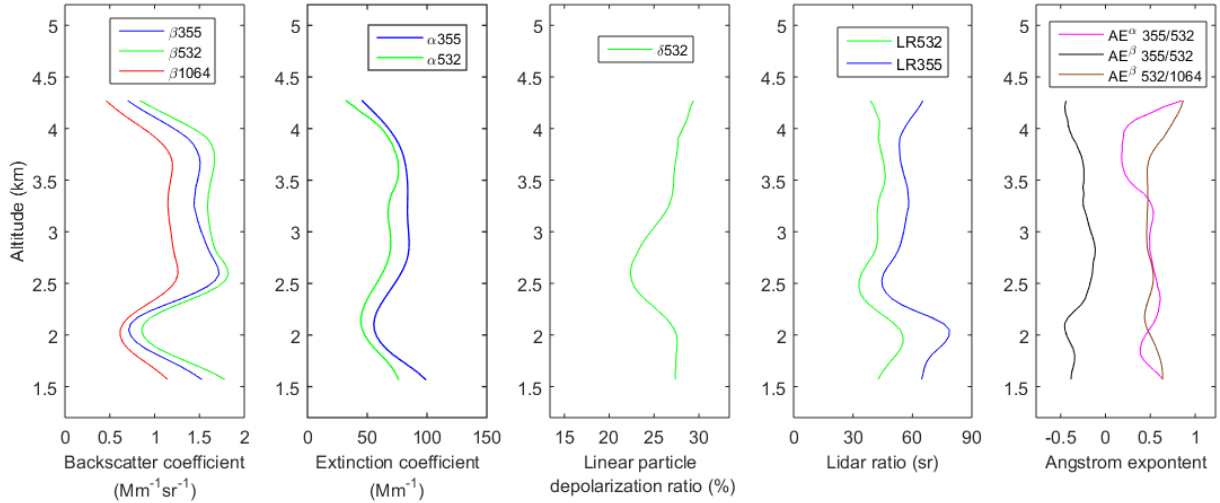

Figure 5.13: Optical properties retrieved by Potenza's lidar station. From left to right, the following profiles are shown: total backscatter coefficient at 532 nm, extinction coefficient at 355 and 532 nm, particle depolarization ratio at 532 nm, lidar ratio at 355 and 532 nm, the extinction- and backscatter-related Ångström exponents $AE^{\alpha/\beta}$ 355/532 and AE^{β} 532/1064 measured on 04.09.2011 between 23:26-1:09 UTC.

On the other hand, here we see very small variation of the volume concentration $v_t = 17.77 \, \mu m^3 cm^{-3}$ ($\pm 8.39\%$) between the successive sub-layers reflecting the relatively small variation of the signal intensity throughout the whole layer, which also shows stability. Although we have a total effective radius $r_{eff} = 0.39 \, \mu m$ ($\pm 4.93\%$) suggestive of medium-coarse particles, there is also a coarse mode of $1.70 \, \mu m$ ($\pm 1.23\%$) in $2.45 - 3.95$ km, see Table 5.8. AERONET also finds a coarse mode of $1.80 \, \mu m$ ($\pm 2.72\%$) and a very small fine mode of $0.12 \, \mu m$ ($\pm 5.59\%$), see lowest sub-table in Table 5.8. With our approach the contributions of the fine (medium-coarse) and coarse particles are attributed almost entirely to different shapes, namely to nearly spherical and prolate spheroidal particles respectively, as one can see through the mean retrieved shape-size distribution in Fig. 5.14 left panel. The finding of a quite enhanced fine mode, shown in this figure, backs the potential scenario of contributions by smoke particles. There is also a very small fine mode (much like AERONET's) of prolate particles with a peak at about $23 \, \mu m^3 \mu m^{-1} cm^{-3}$, but this could as well be an artifact. Performing a rough calculation as in the previous cases we can see that the volume concentration peak in AERONET's VCSD (not shown) of about $0.12 \, \mu m^3 \mu m^{-2}$ is consistent in the order of magnitude with the peak of the reduced VCSD of about $0.05 \, \mu m^3 \mu m^{-2}$, see Fig. 5.14 (right) $2.45 - 3.95$ km (average), considering a dust layer thickness of about 3 km. The temporal variability of the measurements and the difference in the sampled volume between the lidar and sun-photometer measurements might account for the difference in magnitude, but in the case of lidar this calculation has only qualitative value anyway.

Table 5.8: Retrieved microphysical parameters for the dust-case from 04.09.2011 captured by Potenza's lidar station. The variability (Var %) and uncertainty (Unc %) are calculated the same way as in Table 5.5. The parameter notation is given in Table 5.1.

Lidar-based inversion

2.45 − 2.70 km

RRI = 1.4 (Var: 0.0%), IRI = 0.008 (Var: 55.90%)
SSA532 = 0.943 (Var: 3.34%)

Parameter	n_t	a_t	v_t	r_{eff} (total/fine/coarse)	$svcf$	a_{eff}	a_{var}
Unit	$\mu m^{-1} cm^{-3}$	$\mu m^2 cm^{-3}$	$\mu m^3 cm^{-3}$	μm	−	−	−
Average	203.19	130.93	16.18	0.37 / 0.28 / 1.7224	0.30	1.11	0.063
Variability	9.52%	2.52%	12.14%	10.31% / 6.22% / 0.82%	15.74%	1.94	28.49

2.45 − 3.95 km, (whole)

RRI = 1.4 (Var: 0.0%), IRI = 0.008 (Var: 55.90%)
SSA532 = 0.934 (Var: 3.37%)

Average	198.57	137.85	17.77	0.39 / 0.30 / 1.68	0.31	1.07	0.074
Variability	12.07%	2.89%	12.36%	9.89% / 5.54% / 5.60%	17.35%	9.17%	47.70%

2.45 − 3.95 km, step: 250 m

RRI = 1.4 (Var, Unc: 0.0%), IRI = 0.008 (Var: 55.90%, Unc: 0.0%)
SSA532 = 0.944 (Var: 3.35%, Unc: 0.02%)

Average	198.00	138.05	17.81	0.39 / 0.30 / 1.70	0.31	1.11	0.063
Variability	7.30%	2.22%	10.60%	8.98% / 5.60% / 3.65%	12.47%	2.60%	27.02%
Uncertainty	8.94%	5.14%	8.39%	4.93% / 5.88% / 1.23%	4.50%	0.24%	0.41

Sun-photometer-based inversion

Parameter	u_t	r_{eff} (total/fine/coarse)	sphericity	RRI	IRI	SSA
Unit	$\mu m^3 \mu m^{-2}$	μm	(%)	−	−	−
Average	0.22	0.76 / 0.12 / 1.80	0.7331	1.53	0.0032	0.939
Variability	4.66%	6.96% / 5.59% / 2.72%	36.06%	0.76%	21.13%	2.17%
Uncertainty	−	−	−	1.41%	64.24%	1.11%
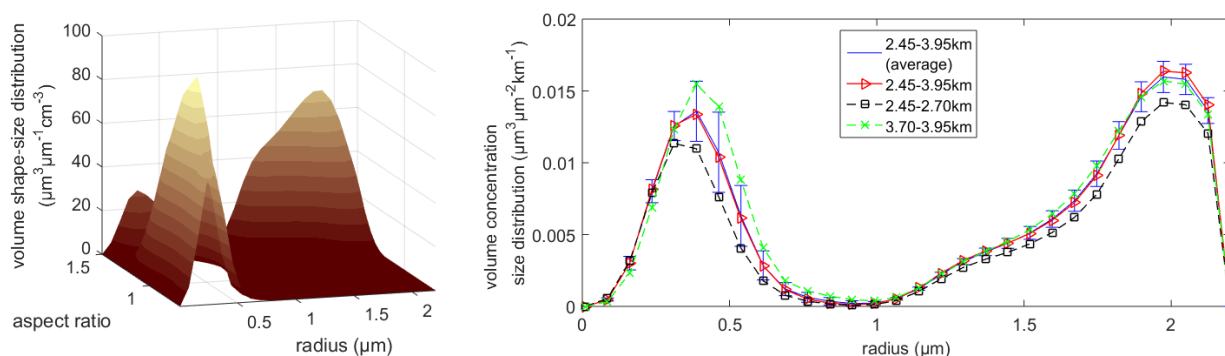
Figure 5.14: Left: mean retrieved shape-size distribution for the case study from 04.09.2011 in Potenza for the altitude range 2.45 − 3.95 km with step: 250 m. Right: (reduced) volume concentration size distribution for several layers. The mean VCSD corresponding to the mean shape-size distribution (left) is labeled as "2.45 − 3.95 km (average)", and the errorbars correspond to the standard deviation of the mean distribution computed for every sub-layer.

Looking closer in Fig. 5.14 (right), we observe that the (reduced) VCSD for the layer $2.45 - 3.95\,\mathrm{km}$ considered as a whole is almost coincident with the mean VCSD computed from all the sub-layers of $250\,\mathrm{m}$ with a distribution uncertainty $\mathrm{Unc} = 16.39\%$. The latter is found through the standard deviation of the mean distribution calculated for a every sub-layer from the 5 best solutions. We also show the resulting distributions for the inversion in the two major backscatter peaks in $2.45 - 2.70\,\mathrm{km}$ and $3.70 - 3.95\,\mathrm{km}$. Their distribution trends are very similar and the differences focus mainly on the peaks of the two modes where the largest variation among the sub-layers is found. However, their microphysical properties vary only a little as we can attest from Table 5.8 ($2.45 - 3.95\,\mathrm{km}$, step: $250\,\mathrm{m}$).

Summary, conclusions and future work

In this final part, we would like to summarize our findings, come up with some answers to our topic and elaborate further on several theoretical and practical issues which might extend and improve the present work.

In this work we addressed the problem of retrieving the microphysical properties of aerosol particles from multi-wavelength lidar data, which mathematically comes down to solving an inverse ill-posed problem. The theoretical requirement to approximate the latter with a well-posed problem, i.e. to have a unique stable solution, is the closure of the linear operator of the underlying model equation. The insightful approach of the theory is greatly attributed to the use of the singular value decomposition, as a means to decompose the operator in its building elements. The latter helped us define as a measure of the instability, namely the degree of ill-posedness, and introduce the regularization methods (RM) the very essence of which is to counteract the inherent instability of our problem. The amount of regularization imposed to an ill-posed problem is decisive to the usefulness of the inversion outcome, since too much of it can eliminate, along with the undesired noise, vital solution information as well, as the Riemann-Lebesgue Lemma illustrates. This brought us to the introduction of special techniques called parameter choice rules (PCR) to control the intensity of the regularization filter we force upon our solutions. A great effort was made here to include most of the RM and PCR widely used in literature for spherical particles and evaluate their performance with the non-spherical model in a first stage. These RM were, the truncated singular value decomposition (TSVD), Tikhonov's method (Tikh) and additionally Padé iteration (Pade), and the PCR, discrepancy principle (DP), L-curve method (LC) and generalized cross validation (GCV). The combinations RM-PCR used here were TSVD-DP, Tikh-LC, Pade-DP, Tikh-GCV, Tikh-DP and for the first time Pade-LC.

Exposing the general theory is very instructive in order to have a solid foundation and exploit our options in the best way but it is only one side of the coin. In order to have some insight in the real-life problem we are trying to solve it was necessary to explore it from the physical point of view. The input data to our inversion are the so-called optical properties retrieved by the radiation backscattered by the targeted atmospheric particles (aerosols) once they are struck by the emitted signal of a lidar system. Maxwell's equations of electromagnetism are the key to describe the scattering and absorption processes. Indeed, under certain assumptions (e.g. single scattering, isolated small finite scattering objects, etc.) we can get a full description of the physical scenery taking place through analyzing the interaction of matter with light, using time-harmonic fields and solving the famous wave equation. The missing link which connects these phenomena with lidar observations, i.e. the intensity of the backscattered signal, is the intrinsic quantity of light called polarization. It turns out that the full knowledge on this property consists only of four easily observable quantities, namely the Stokes parameters, every possible combination of which can be found in the so-called Poincaré sphere. Still, the relation between the incident field assumed to be known, the internal particle field, and the scattering field we are attempting to find out requires a enormous amount of thorough physical and mathematical ingenuity. The extended boundary condition method is perhaps the most favorable answer to this problem, which suggests that the formalization for the scattering field is extended also for the internal field. This way the scattering field can be calculated by the elements of the transition matrix (T-matrix) which finally depend exclusively on the incident field. The optical cross sections or the dimensionless optical efficiencies, associated with the kernel functions of the model equation, can further be translated to T-matrix language, which was the main goal for us here.

Directly after exposing the mathematical and physical toolbox we introduced the model equation, i.e. the Lorenz-Mie model (LMM), which simply states the intuitive proposition that the aerosol extinction and backscatter coefficients measured by lidars are equal to the associated optical cross efficiencies integrated by the rule of an aerosol size distribution over all radii. The LMM served many years the microphysical purpose as a reasonable choice for particles that can be assumed close to spherical, but for arbitrarily-shaped particles was proved insufficient to predict accurately the optical properties. Using a spheroid-particle approximation we have shown that theoretical calculations of the phase function, as a measure of the scattering proportion of the incident light in a specific direction, over polydisperse spheroid particle ensembles match the experimental ones in a higher level than surface-equivalent spherical ensembles. Motivated by this, we then follow a natural generalization of the LMM in two dimensions (GLMM) considering spheroidal optical efficiencies. The latter depend additionally on the aspect ratio, over whose domain the integration is extended. This brings a series of advancements and limitations which we would like to further discuss. The major issues here were (a) the computational demanding and highly unstable calculations of the optical efficiencies by T-matrix theory, and (b) the two-dimensional integrations required for the discretization which is also prohibitively costly for large-scale simulations. These problems were circumvented by employing a precalculated kernel database (Mieschka tool) and further by creating a discretized kernel database for a wide range of projection spaces. However, Miescka's database having precalculated optical efficiencies at the coarse refractive index grid of 6 real parts and 7 imaginary parts, and at only 7 aspect ratios, is for sure the greatest limitation of our approach.

Next, the new model promotes the traditional size distribution to a shape-size distribution (radius and aspect-ratio dependent), not following the usual assumption in literature where size and shape are independent, which may only occasionally be true. This offers a much wealthier particle distribution which in measurement cases allowed us to be able to discuss about potential properties of the observed particles like never before. Indeed it enabled the identification of contributions of different particle shapes and sizes within the same particle ensemble, and the exploration of the most dominant behaviors. Even if we accept that the discussion on those topics reflects only an "effective particle behavior" rather than what actually took place with the targeted particles, it still expands our physical notion and sets new grounds. For the sake of simplicity in our simulations we considered simple products of log-normal and aspect ratio distributions to model the shape-size distribution. It could be argued that this simple synthetic-data construction does not follow any realistic well established model. For one, there is not any standard model to our knowledge which fits our 2D particle distribution. Furthermore it was the only way to investigate explicitly a large diversity of particle shapes and sizes combining different particle sizes and different radius variances with basic shape distributions, i.e. oblate, prolate, and sphere-spheroid mixed ensembles. It is true, however, that at least for the aspect-ratio distribution, a more realistic model could be used based on a modification of the log-normal distribution to fit experimental data coming from very recent research results of [75]. Nevertheless the use of such an advanced model would only make sense in case the aspect ratio range was larger, and more importantly if there actually was a satisfying resolution for the aspect ratio in our disposal. It sure is a valid option for the future though, in view of a possible extension of the kernel database.

We should also point out that although for the sake of the microphysical-retrieval study we were occupied with the inversion of the GLMM, a careful study for the forward problem (with real data) is interesting for the future as well. In principle, the new forward model should work at least with the same efficiency as the 1D model, but since nowadays we have additional information coming from depolarization signals, one could see how this affects the reproduction of the latter thereby learning more about the efficiency of this model to represent physical reality.

The very first task in order to solve the model equation is the discretization (also a regularizing force) which requires some creativity as well. As we discussed the most appropriate method here is collocation, because the input data are given as single values, i.e. 5-8 points depending on the amount of lidar depolarization channels. However, there is no established collocation technique for a two-dimensional variable (shape-size distribution), where at the same time the input data still depend on a single variable, which is why we called this a quasi-2D generalization. Here, we adopt an approach of reducing the two dimensions to one augmented dimension with a bijective index reordering, where the "hidden" dimension is unfolded back with a simple inverse linear operator after the spline basis coefficients (solutions of the discretized problem) are found. Now, although this technique causes further unnecessary underdetermination of the linear system, it seems that there is actually no alternative to really use the full potential of the discretized matrix as a 3rd-order tensor. In fact, this is an open research problem in multilinear analysis

which can be solved under certain assumptions that are not met here. For instance, one of the latest published works on matrix-tensor relations [23], proves that only even-order tensors with a rectangular form can be inverted by a specific linear transformation described in that study. This article and also [30] are also enlightening about tensor decompositions, especially for multilinear SVD, which might be useful once we come up with other possible models that can accommodate such a tensor inversion.

Another tricky part of the discretization is the decision of the dimension to project our problem. The core of our hybrid algorithm is to identify the "best" projection spaces through the minimization of the residual error. The first round of our simulations was devoted to compare all the aforementioned regularization techniques (RM-PCR). This task is not an easy one at all, since the desired inversion outcome includes many microphysical parameters and a shape-size distribution, and one has to predefine what exactly one is interested in. Our preference here was an overall good behavior which made sense as we wanted them to be tested in a large sample of cases covering not only sufficient physical diversity but perhaps also in fictional cases (not necessarily observed experimentally) which might challenge the process mathematically. This is the second reason for the development of this type of algorithms used here as to allow such a comparison by keeping track of the variability of least residual solutions. This statistical approach offers a powerful first-stage evaluation of the methods missing from today's literature in such an extensive level. In this regard, we demonstrated a methodology to find out which method has a better balance of good accuracy (1-Dif%) and low uncertainties in terms of mean solution variability (Var %) of all solution spaces and randomness uncertainty (Unc %) associated with the imposed data errors.

The method fulfilling most of our criteria was found to be Pade-DP. Pade-LC fell short in the uncertainties as compared with most of the other methods, but was kept in our consideration, as it was found to be superior in the accuracy of the shape parameters and further because of its advantage of being a purely data-driven regularization method. In a detailed presentation of the microphysical parameter results with a fixed refractive index (RI) we found that Pade-DP retrieves the surface-area concentration a_t, the total volume concentration v_t and the effective radius r_{eff} (R-parameters - RP) exceptionally well, with more than 85% accuracy and the uncertainties (Var, Unc) are vastly below (5%, 15%) on average, for any shape, size, RI, and data-error level tested. Pade-LC is almost as good as Pade-DP in accuracy but owns a higher risk of isolated blow-up-incidences. Their largest disagreement is found on a_t where Pade-DP has on average less than 5% Dif and 6% Unc lower than Pade-LC, and Pade-LC appears to handle less effectively prolate particle ensembles (larger Var %). Moreover, Pade-DP also proved to be the best bet for the retrieval of number concentration, a parameter extremely vulnerable to noise which, as we discussed, can be manually corrected to provide very decent approximations.

Regarding the shape parameters (S-parameters - SP), spherical volume concentration fraction (*svcf*) and effective aspect ratio (a_{eff}), we have very good retrievals for prolate and sphere-spheroid mixed particle ensembles and less efficient retrievals for oblate ensembles, which is directly reflected in the reconstructions of the shape-size distribution we saw later on. A large collection of synthetic shape-size distributions are very well reconstructed with Padé iteration, taking into account the level of restriction we are dealing with for such a small aspect ratio resolution we have access to through the kernel database. Generally, among all the distribution features we can be most confident about the peak location which is another hint that the effective radius can be well reproduced. Especially good reconstruction performance is shown by Pade-LC which justifies the preliminary findings for its overall better accuracy in the shape parameters even if the differences (in SP) with Pade-DP are seemingly marginal. We went one step further to conceptualize, construct and quite successfully reconstruct limited cases of bimodal shape-size distributions, a quite impressive result, which intuitively applies to real-life atmospheric scenarios as shown later on. However, 10% data errors (the largest used) seems to be quite a strict barrier as large errors may have a destructive effect in the reconstructions.

Further statistical analysis showed that for larger particle sizes the accuracy of a_{eff} is enhanced for oblate ensembles by about 6% and marginally diminished for prolate ensembles by about 2%. The parameter *svcf* shows less predictive behavior with respect to increasing particle size, although it seems to be more accurate for smaller sizes. Moreover, it has the most alarming uncertainties (Unc), thereby doubling the rates (%) for larger sizes for oblate and sphere-spheroid-mixed particles, while *svcf*-retrievals with prolate particles mark by far the largest rates for all sizes; Var (%) also follows a similar pattern but with significantly lower rates. Particle size has the most direct effect in the degree of ill-posedness and thus the retrieval behavior. A higher susceptibility to noise was attested multiple times (shown also with SVD-analyses) to be correlated to larger particles. However statistically, most related to lower accuracy

and larger uncertainties (mostly Unc) on average are the particle shape and even more the RI; oddly, among the database values we used, most problematic were the ones with lower real part and not the ones with larger imaginary part. Finally, the data-error transition from lower to higher levels (1%-5%, 5%-10%) for the parameters a_t, v_t, r_{eff} and a_{eff} affects mainly, Dif (%) and Unc (%) by about 4% and 5% on average respectively.

A greater effort is required for synthetic microphysical retrievals where the refractive index is considered unknown. Despite the significant additional computational cost of this endeavor, the simulations were massive here too including 14 different RIs, combined with various particle sizes and the three basic particle ensembles. Our interest here was twofold, namely (1) the retrievability of the RI and the single scattering albedo (SSA) with our algorithm (SA2) and Pade-DP and (2) find out to what extent a divergent RI affects the rest of the parameters (RP, SP). Regarding (1), we saw that predefining an RI grid for the inversion with absolutely no hint about the true refractive index, i.e. using all the options from the database, the RI can be retrieved in a good level. Since there is practically poor RI-resolution in the database, a "good level" means to additionally accept the nearest RI-neighbors in Mieschka's database which at the same time lead to small variations of the SSA. It is shown that the major concern is the imaginary part of the RI (IRI) since the real part of the RI (RRI) is vastly retrieved with astounding accuracy and small uncertainties for all tested error levels. For cases with 1% data-error and high or extreme absorption (IRI $\in [0.01, 0.1]$), the IRI is retrieved with high accuracy, (median - m) $\text{Var}^{(m)} \lesssim 20\%$ and (median) $\text{Unc}^{(m)} \lesssim 50\%$, except for minor instances. Weak-absorption cases with small RRI seem to be more challenging for our algorithm, often severely overestimating the IRI. A collateral result is that the odds of a successful IRI-retrieval for very weak or very strong absorption levels are enhanced with large particles rather than with smaller ones. This essentially indicates that the echo of the optical properties of smaller sizes through the inversion process could be significantly diminished. Regarding the shape involvement, prolate particle ensembles are harder to retrieve and sphere-spheroid mixtures are the most safe. Higher data errors impose additional difficulty in the retrievals of the IRI, affecting both accuracy and the uncertainties, in many cases to an unreliable level. Regarding (2), a synopsis of our results revealed that the error-related quantities (Dif, Var, Unc - ERQ) increase roughly by 3-20% on average as compared to the corresponding fixed-RI retrievals for the parameters a_t, v_t, and r_{eff} and a_{eff}. The effect on the variability of the chosen solutions is generally minor on average showing stability in the solution spaces while the uncertainty (Unc) shows 6-7% increase in the transition to higher error levels for r_{eff}. This parameter is mostly influenced by the retrievals of v_t, which is the most distinctly affected parameter in accuracy (average Dif range 14-38%). Therefore the results for the rest of the parameters are tolerable even in view of severe IRI-discrepancies. Even more encouraging is that, as we saw, a wise selection (preliminary tests) of the maximum number of iterations for Padé iteration reversed inaccuracies in many of the highly divergent cases. Finally, the synthetic SSA retrievals at 355 and 532 nm follow in a much milder level the quality with which the refractive index is reproduced, and thus they are almost always very good.

A novel investigation of this work, was the comparison among different lidar setups in which we varied the amount of depolarization points (1d, 2d, 3d) and/or the extinction points (2α, 3α) at the wavelengths 355, 532, 1064 nm, using a similar methodology to the method comparison. Incidentally, the setup used throughout all our experiments, $3\beta + 2\alpha + 3d$ (323), was shown to be the best choice, accounting both for accuracy and stability. Several independent setup comparisons showed that the additional extinction coefficient at 1064 nm was not always beneficial, although it leads many times to reduced the uncertainties when it is combined with 3d. A rather intriguing outcome regarding depolarization data at 355 nm is that it is also theoretically dubious to which degree it is helpful for the retrieval, which suggests that the overall advantage of 323 might lie greatly within the depolarization data at 1064 nm.

Regarding the model equation there are some suggestions for future investigations. A possible shortcoming of the spherical model passed also in our generalization (GLMM) could be the mistreatment of the optical data information. By this is meant that although the optical properties are given in profiles, we only take into consideration their mean values in a specified layer. In other words we use single data points for the inversion, which might be restrictive from physical point of view. Instead, the model equation could be modified to exploit the whole layer information by using integrated extinction- and backscatter coefficients over the given altitude range. On the other hand, this might cause further undesired smoothing and therefore this approach requires a whole new investigation from scratch to assure the benefit of such a modification. Second, following the concept of the AERONET, we can take the generalized model one step further and assume that aerosol particles have separate spherical and

non-spherical (spheroidal) parts the proportion of which is decided by an additional unknown *asphericity* parameter. Some preliminary tests showed that this kind of advancement can lead occasionally to superior results in the microphysical parameter accuracy and/or the shape-size distribution reconstruction quality if we assume a convex combination of the involved aerosol parts. Despite the sincerest efforts of the author, a unified stable model of this kind could not be found mainly because of the lack of a simple (linear) way to derive the new parameter. However, this line of thought is encouraged for the future model developments. Finally it remains unknown if more complicated particle symmetries, could be the answer to occasional failure of the spheroidal approximation and this should also be one of the next steps under consideration in aerosol microphysics. Nevertheless this is still a long-term plan since the more involved nature of such particles would result in an even higher computational challenge for the optical efficiencies, for which the research stage is newly born but very promising, see [71, 102, 126].

The final attempt of this work was the application of our algorithm with Padé iteration using lidar data from measurement cases. Simulations, with all the limitations discussed by now, seem nearly ideal in the sight of real-data retrievals where additional uncertainties of which we have no control, e.g. measurement errors, multiple aerosol types etc., take over leading to a microphysical adventure. The intention here was to discuss the physical phenomena of the various cases through the retrieval from our algorithm and explore further the potential of our approach. At this point it is crucial to stress the lack of a well-established consensus on aerosol microphysics (even more when we include non-sphericity to the mix), primarily on modelling the optical properties and on the inversion methods. This problem in conjunction with the gap in physical knowledge give an extremely hard time in finding out how appropriate is an approach to follow. Currently the world's most used software to derive columnar aerosol microphysical properties is provided by the Aerosol Robotic Network (AERONET) of NASA, which despite its extensive usage, it is still an experimental tool operated massively in the absence of any other user-friendly alternatives. The purpose of using AERONET data here, was merely in order to have a widely used reference point and in an effort to understand deeper the differences and limitations of both approaches. The bigger point here is that the we need to be very cautious about any inversion results when it comes to real-life data.

Our first encounter with measurement data was with 5 cases of biomass burning aerosols mixed with urban pollution from the record of Bucharest's lidar (INOE), which uses the $3\beta + 2\alpha + 1d(532)$ setup, and the goal was to observe the response of the algorithm to data with low depolarization. As compared to a hybrid regularization method (HTSVD) and AERONET's retrieval, our approach (Pade-GLMM) delivered an equally reasonable retrieval mostly focused on the fine mode, which is the most dominant for this particle type. The most pronounced difference with HTSVD and AERONET was found in the refractive index, where we found stronger absorption, which is a consistent outcome for smoke particles. Furthermore we get a reasonable result for the fine mode through the shape-size distribution, and we were able to identify non-spherical contributions as well. However, the inversion process seems to wipe out any sign of coarse mode, which might be ascribed to the limited radius extent (fixed kernel database).

The next examined case was captured by one of the most advanced lidar systems located in Barbados islands and operated by the group of TROPOS in Leipzig. In addition to the usual lidar setup $3\beta + 2\alpha$, this lidar system is capable of emitting and collecting depolarization signal at 355, 532 and 1064 nm. The optical properties lidar ratio (LR), Ångström exponent (AE), and aerosol optical depth (AOD) showed characteristic values of an intense dust event, which was further indicated by the back-trajectories from HYSPLIT model pointing to Africa. The relatively small variation of the intensive properties gave us the opportunity in this case to test the stability of the algorithm and its sensitivity to changes in different layers. Performing retrievals to subsequent layers within the whole dust layer we got the very interesting proposition that the algorithm is able to sense the difference in particle size as expressed by the variation of AE. We also saw that as long as the optical properties (LR, AE) are relatively constant, the microphysical properties within a layer or smaller sub-layers have only small differences, which is very convenient provided that we have good quality data. Moreover, we found that lower signal intensity is associated with a decrease in the calculated concentrations but in principle it delivers similar effective radii. The shape-size distribution reveals two distinct modes both with spherical and non-spherical contributions. As seen from the point of view of the reduced volume concentration size distribution (VCSD), the coarse mode is prevailing as expected for dust-like particles. The retrieved IRI predicts a very high value (0.05), which seems that can happen under less usual circumstances we superficially explored. Finally we saw that in the extreme case where the IRI is an order of magnitude smaller, the change in microphysical properties is relatively conservative but with pronounced differences in the

reduced VCSD.

The next case was yet another dust case captured by Granada's lidar station with a $3\beta + 2\alpha + 1d(532)$ setup during the ChArMEx campaign in 2013. The optical properties and multiple indications from HYSPLIT and the literature showed clearly air masses originating from the African desert. Our retrievals for the RI, SSA, r_{eff} (total and coarse) and the order of magnitude of the total volume concentration in the dust layer are comparable to AERONET, while there are more essential differences in r_{eff} of the fine mode which is almost absent for AERONET. Here, the shape-size distribution attributes the contribution of coarser particles to prolate particles and the fine mode to both spherical and non-spherical ensembles. A clear downside for this particular case is the limited particle size extent of our approach but also of the lidar system itself in view of the extremely large particle sizes measured in situ during measurement-flights performed during the campaign.

The last case pertained to dust particles with potential contribution from biomass burning and was captured by the Raman lidar of the CNR-IMAA atmospheric observatory in Potenza, Italy which collected the optical data with the $3\beta + 2\alpha + 1d(532)$ setup. The relatively stable optical data gave also here the opportunity to test the performance of our algorithm in the same way as in the Barbados case. The results showed a stable response of our approach for the microphysical parameters but also for the retrieved (reduced) VCSD. There are, however, higher uncertainties as compared to the Barbados case, especially in the shape parameters. This might be due to the lack of more depolarization information which deeply relates to shape sensitivity, but can on the other hand point to different shape contributions as we further explored.

In this work we saw that there is a real benefit using lidar data in being able to produce height resolved information about the optical properties and thus perform investigations in greater detail. It is often the case, though, that part of the information is missing due to the lack of spectral or multi-angle scattering resolution (e.g. for the RI). Multispectral measurements, (e.g. sun photometer) are capable of a higher sensitivity in the polarization of light and can thus provide such complementary information. Furthermore orbital (spaceborne) remote sensing instruments have the advantage of covering large areas. Therefore it seems highly promising that the next step forward will occur in synergetic terms where we will be able to effectively combine observations from different instruments.

As frequently demonstrated, there is almost no aspect of the microphysical inversion that is not challenging either computationally or physically. Nonetheless, we saw a successful first attempt to address this problem for non-spherical particles through the prism of regularization in a statistically significant number of cases. Thus, we may conclude this work with optimism and the hope that it will stimulate further advancements in this field.

Acknowledgements

Appendices

Appendix A

Spherical wave functions

For a linear, isotropic (scalar permittivity) and homogeneous medium the electric field $\mathbf{E}$ is divergence-free so that from Eq. 2.4.1 we obtain the vector Helmholtz equation $\nabla^2 \mathbf{E}(\mathbf{r}) + k^2 \mathbf{E}(\mathbf{r}) = 0$. The latter is satisfied by the following two function sets (written compactly):

$$
\begin{matrix} \mathbf{M}_{mn}(kr, \theta, \phi) \\ \mathrm{Rg}\mathbf{M}_{mn}(kr, \theta, \phi) \end{matrix} = \left[\frac{(2n+1)(n-m)!}{4\pi n(n+1)(n+m)!} \right]^{1/2} \nabla \times \left(r \begin{matrix} \psi_{mn}(kr, \theta, \phi) \\ \mathrm{Rg}\psi_{mn}(kr, \theta, \phi) \end{matrix} \right) \tag{A.0.1}
$$

and

$$
\begin{matrix} \mathbf{N}_{mn}(kr, \theta, \phi) \\ \mathrm{Rg}\mathbf{N}_{mn}(kr, \theta, \phi) \end{matrix} = \frac{1}{k} \nabla \times \begin{matrix} \mathrm{M}_{mn}(kr, \theta, \phi) \\ \mathrm{Rg}\mathrm{M}_{mn}(kr, \theta, \phi) \end{matrix} \tag{A.0.2}
$$

where

$$
\begin{matrix} \psi_{mn}(kr, \theta, \phi) \\ \mathrm{Rg}\psi_{mn}(kr, \theta, \phi) \end{matrix} = \begin{matrix} h_n^{(1)}(kr) \\ j_n(kr) \end{matrix} (-1)^n \sqrt{\frac{(n+m)!}{(n-m)!}} d_{0m}^n(\theta) \mathrm{e}^{im\phi}. \tag{A.0.3}
$$

$j_n(kr)$ denotes the Bessel functions of the first kind and $h_n^{(1)}(kr)$ the Hankel functions of the first kind, both of which solve the scalar Helmholtz equation $(\nabla + k^2)\psi_{mn}(kr, \theta, \phi) = 0$ with separation of variables in spherical (or cylindrical) coordinates. $d_{0m}^n(\theta)$ denote the so-called Wigner d-functions defined by

$$
d_{bc}^s = \sqrt{(s+b)!(s-b)!(s+c)!(s-c)!} \sum_l (-1)^l \frac{(\cos \frac{1}{2}\theta)^{2s-2l+b-c}(\sin \frac{1}{2}\theta)^{2l-b+c}}{l!(s+b-l)!(s-b-l)!(c-b+l)!}, \tag{A.0.4}
$$

where b, c and s denote integers, $0 \leq \theta \leq \pi$ and the summation should exclude all l leading to negative factorials. The functions $\mathrm{Rg}\psi_{mn}$ are finite (regular) in the origin due to the relation

$$
\lim_{kr \to 0} j_n(kr) = \frac{(kr)^n}{(2n+1)!!}, \tag{A.0.5}
$$

unlike the functions ψ_{mn} since

$$
\lim_{kr \to 0} h_n^{(1)}(kr) = \frac{(kr)^n}{(2n+1)!!} - i(2n-1)!!(kr)^{-n-1} \quad \text{and} \quad \lim_{\substack{kr \to \infty \\ kr \gg n^2}} h_n^{(1)}(kr) = \frac{(-i)^{n+1}\mathrm{e}^{ikr}}{kr}. \tag{A.0.6}
$$

which indicates a behavior of outgoing scalar spherical waves at infinity and divergent at the origin. The same applies for the vector spherical wave functions $\mathrm{Rg}\mathbf{M}, \mathrm{Rg}\mathbf{M}$ as regular functions in the origin and $\mathbf{M}, \mathbf{N}$ as outgoing transverse vector spherical waves; this is known as the (Silver-Müller) radiation condition, see e.g. [124].

The expansion of a plane electromagnetic wave $\mathbf{E}(\mathbf{r}) = \mathbf{E}_0 \mathrm{e}^{ik\hat{\mathbf{r}}' \cdot \mathbf{r}}$, propagating in the direction of $\mathbf{r}'$, in vector spherical wave functions is

$$
\mathbf{E}(\mathbf{r}) = \sum_{n=1}^{\infty} \sum_{m=-n}^{n} \left[a_{mn} \mathrm{Rg}\mathbf{M}_{mn}(k_1 \mathbf{r}) + b_{mn} \mathrm{Rg}\mathbf{N}_{mn}(k_1 \mathbf{r}) \right], \tag{A.0.7}
$$

where the expansion coefficients are calculated by

$$a_{mn} = 4\pi(-1)^m i^n \gamma_n \mathbf{E}_0 \cdot \mathbf{C}_{mn}^*(\theta') e^{-im\phi'}, \tag{A.0.8}$$

$$b_{mn} = 4\pi(-1)^m i^{n-1} \gamma_n \mathbf{E}_0 \cdot \mathbf{B}_{mn}^*(\theta') e^{-im\phi'}, \tag{A.0.9}$$

$$\mathbf{B}_{mn}(\theta') = \hat{\theta} \frac{\mathrm{d}}{\mathrm{d}\theta} d_{0m}^n(\theta) + \hat{\phi} \frac{im}{\sin(\theta)} d_{0m}^n(\theta), \tag{A.0.10}$$

$$\mathbf{C}_{mn}(\theta') = \hat{\theta} \frac{im}{\sin(\theta)} d_{0m}^n(\theta) - \hat{\phi} \frac{\mathrm{d}}{\mathrm{d}\theta} d_{0m}^n(\theta), \tag{A.0.11}$$

$$\gamma_n = \left[\frac{2n+1}{4\pi n(n+1)} \right]^{1/2}. \tag{A.0.12}$$

The free space dyadic Green's function can be expanded in vector spherical wave functions as well

$$\overset{\leftrightarrow}{G}(\mathbf{r}, \mathbf{r}') = ik \sum_{n=1}^{\infty} \sum_{m=-n}^{n} (-1)^m \begin{cases} \mathbf{M}_{-mn}(kr, \theta, \phi) \otimes \mathrm{Rg}\mathbf{M}_{mn}(kr', \theta', \phi') \\ +\mathbf{N}_{-mn}(kr, \theta, \phi) \otimes \mathrm{Rg}\mathbf{N}_{mn}(kr', \theta', \phi') & r > r' \\ \mathrm{Rg}\mathbf{M}_{-mn}(kr, \theta, \phi) \otimes \mathbf{M}_{mn}(kr', \theta', \phi') \\ +\mathrm{Rg}\mathbf{N}_{-mn}(kr, \theta, \phi) \otimes \mathbf{N}_{mn}(kr', \theta', \phi') & r < r', \end{cases} \tag{A.0.13}$$

where $\mathbf{r} \neq \mathbf{r}'$, see [141]. Further relations and a more detailed presentation of the spherical wave functions see e.g. [100, 138].

Appendix B

Figures

B.1 Reconstructions of bimodal size distributions with Pade-DP and Pade-LC for spherical particles
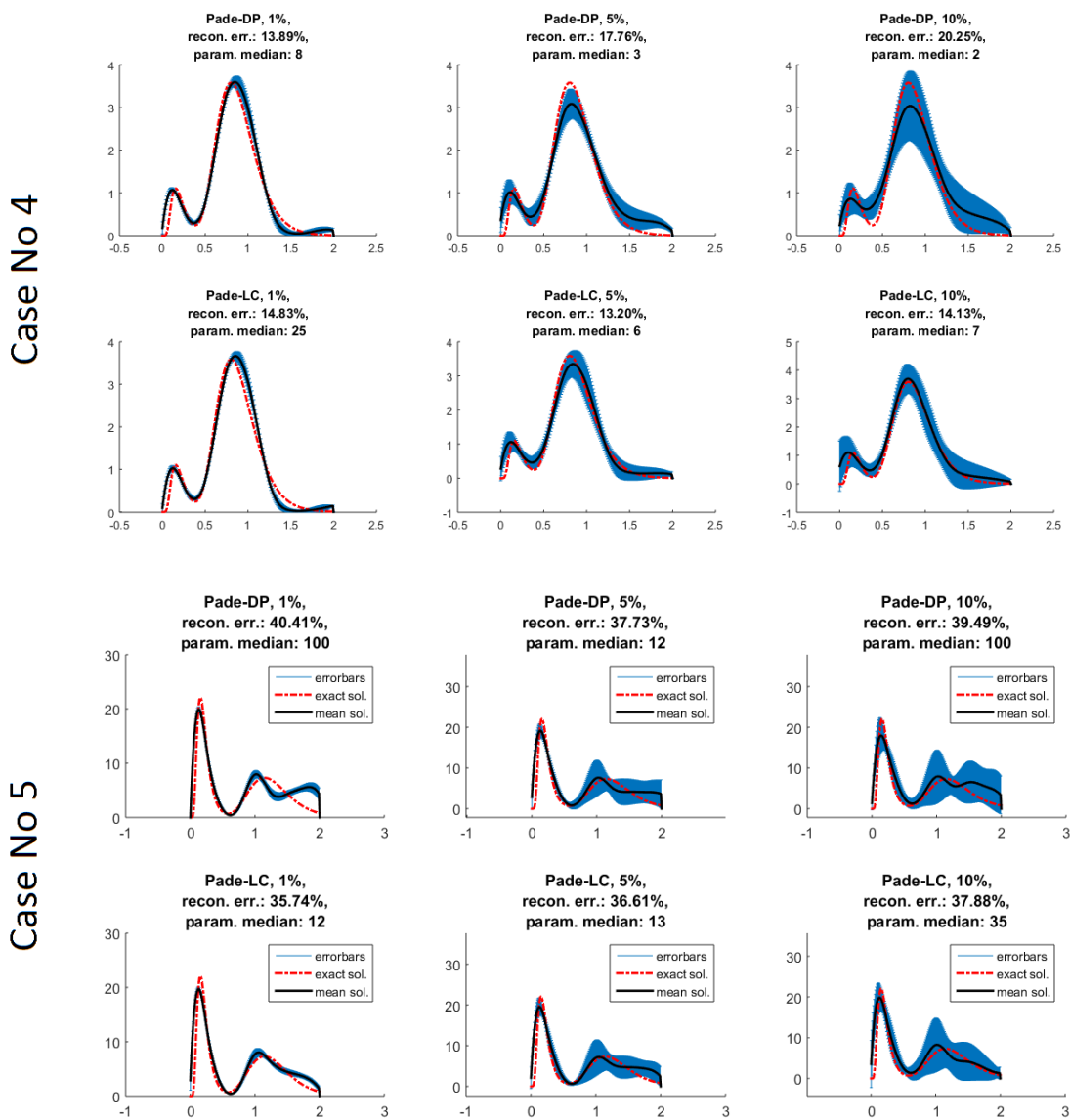
Figure B.1: Reconstructions of bimodal size distributions with Pade-DP and Pade-LC, corresponding to the cases 4 and 5 from Table 3.3. The plots follow the structure of Fig. 3.10.

B.2 Reconstructions of monomodal shape-size distributions with all methods
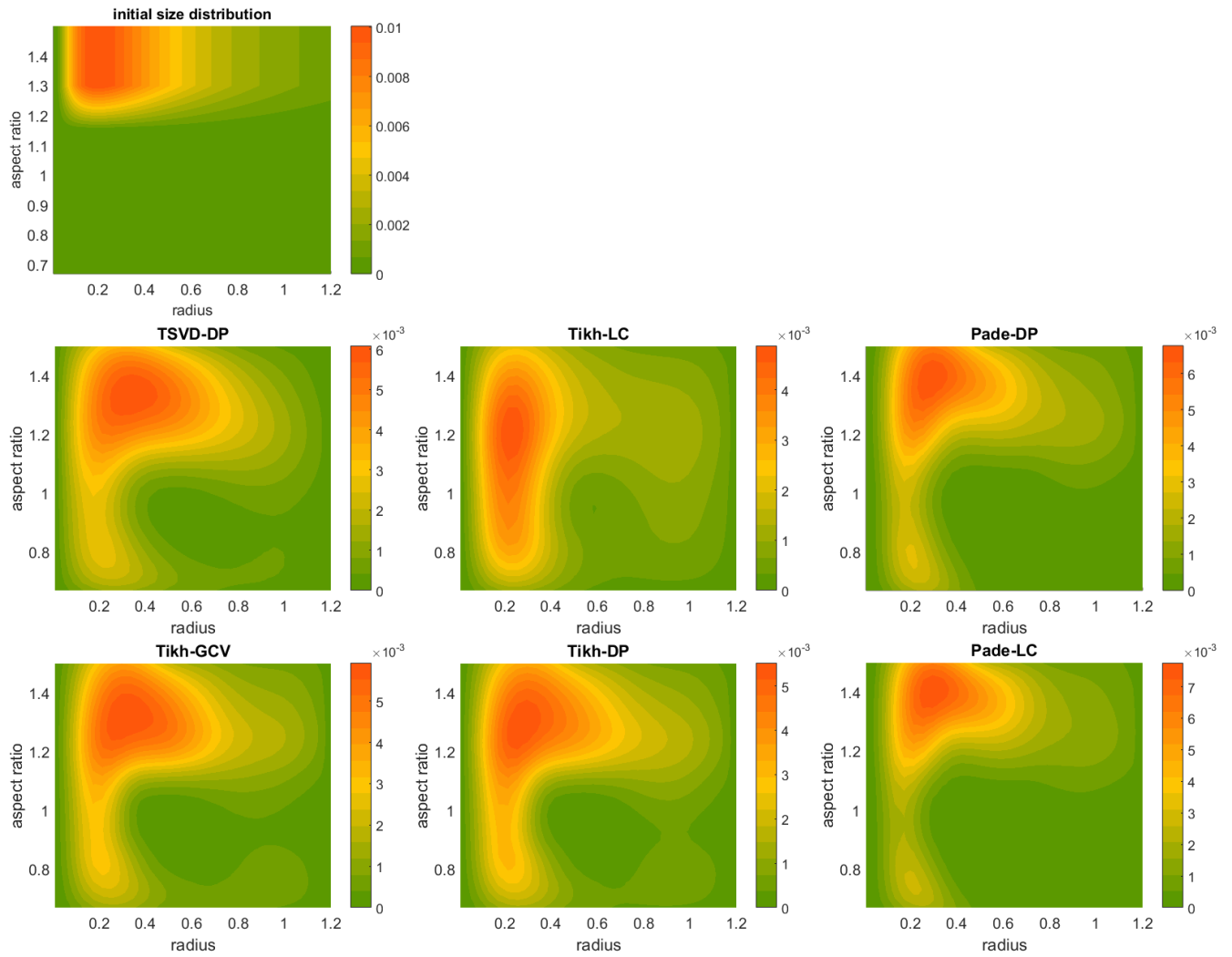
Figure B.2: Retrieved shape-size distributions from synthetic data produced with RI: 1.5 + 0.01i, 1% data error, the size distribution No 1 and prolate particle ensembles. The uppermost plot corresponds to the initial shape-size distribution.
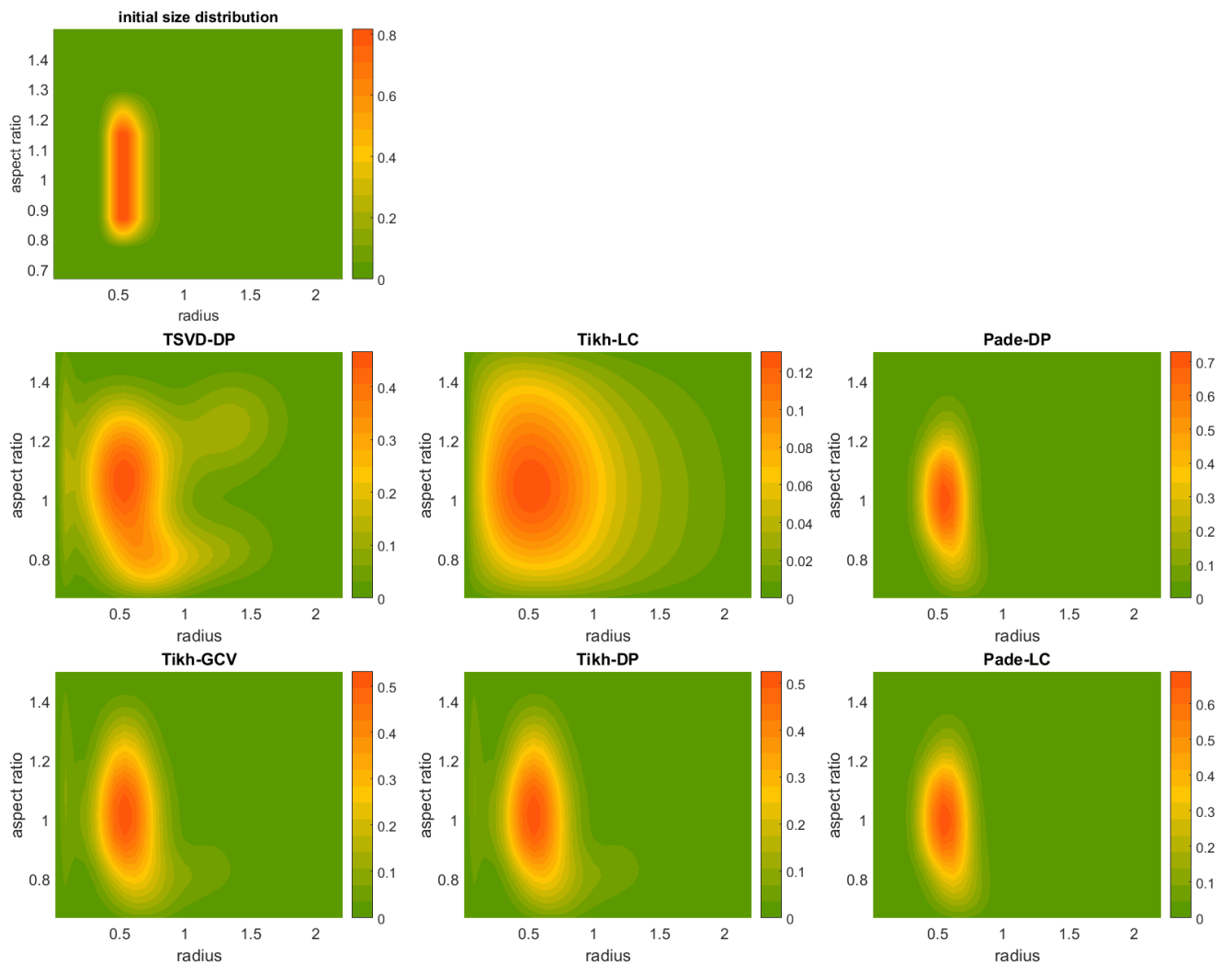
Figure B.3: Retrieved shape-size distributions from synthetic data produced with RI: 1.5 + 0.01i, 1% data error, the size distributions No 3 and sphere-spheroid particle ensembles. The uppermost plot corresponds to the initial shape-size distribution.

B.3 Reconstructions of monomodal shape-size distributions with Pade-DP, Pade-LC and Tikh-DP
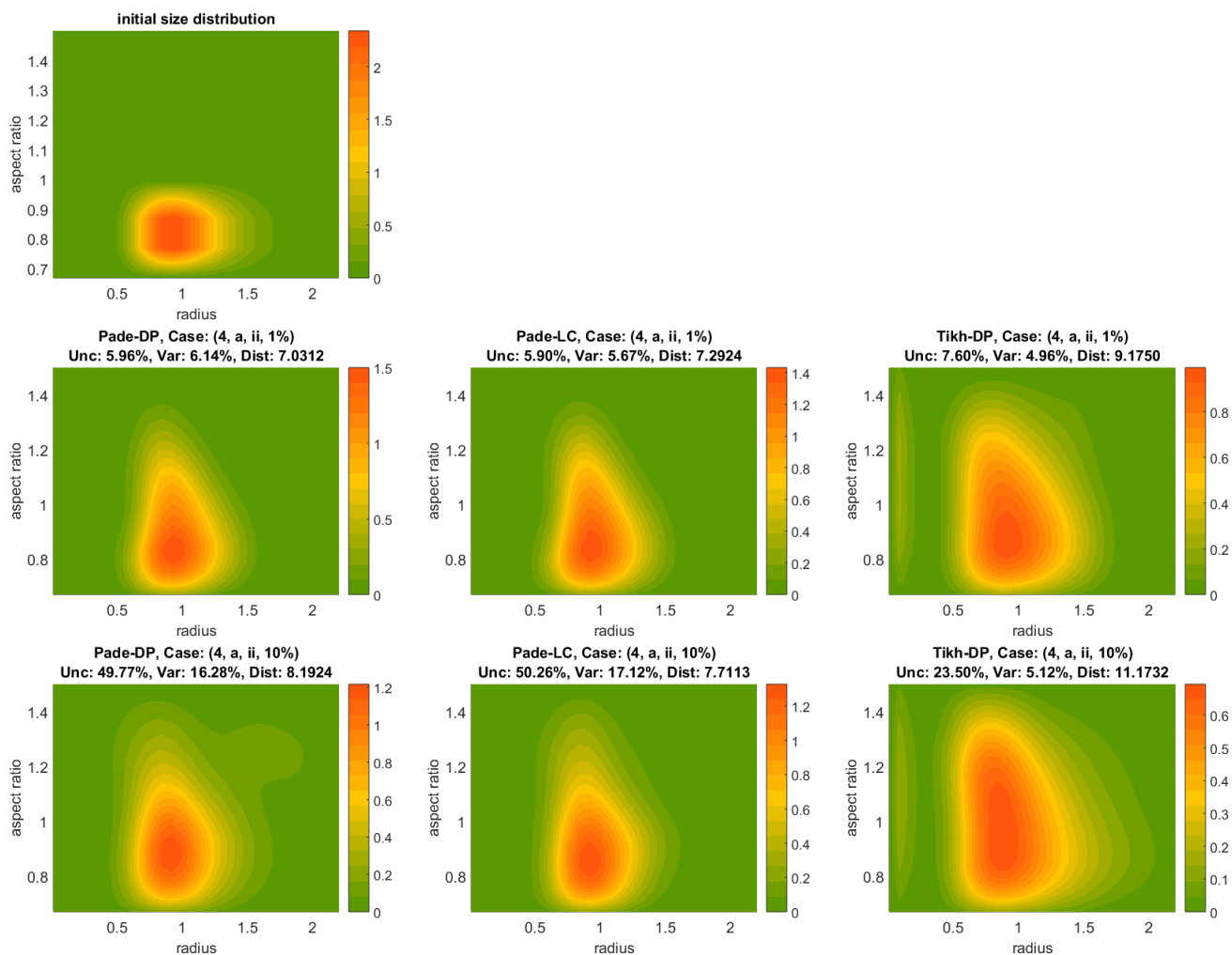
Figure B.4: Shape-size distribution reconstructions produced by Pade-DP, Pade-LC and Tikh-DP (left to right) for the case (4, a, ii) respectively for 1% and 10% error level. The uppermost plot corresponds to the initial shape-size distribution. The triple (Unc, Dist, Var) in the title of each plot refers to residual-error quantities of shape-size distribution described in Sec. 4.1.

B.4 Reconstructions of bimodal shape-size distributions with Pade-DP
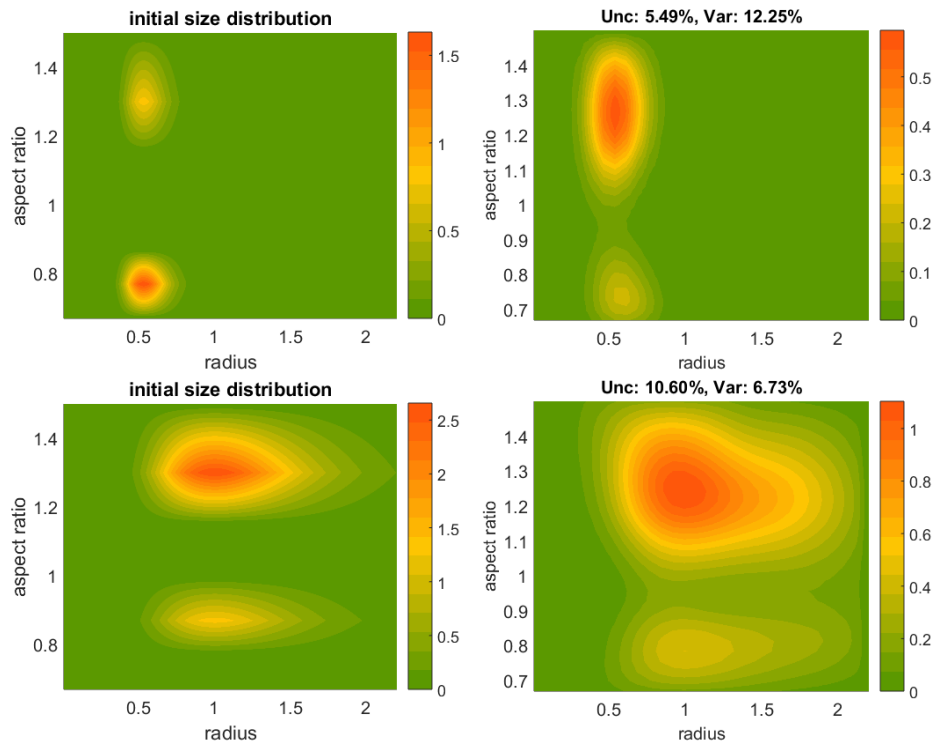
Figure B.5: Reconstructions of bimodal shape-size distributions with two distinct aspect-ratio modes. Right: reconstructions corresponding to the cases 5 (top) and 6 (bottom) from Table 4.7. Left: Initial shape-size distributions for the reconstructions on the right.

Appendix C

Tables

C.1 Synthetic retrievals with a fixed refractive index

Table C.1: Microphysical parameters retrieved with all methods for size distribution No 3, prolate particles, data error: 1% and RI: $1.5 + 0.01i$. The rightmost indication "error" corresponds to the mean relative residual error found with a forward calculation.

Parameters	n_t	a_t	v_t	r_eff	$svcf$	a_eff	a_var	error
Synthetic	0.1387	0.4624	0.0836	0.5426	0.000	1.3590	0.0072	4.70e-03
T S V D - D P								
Average	1.0989	0.7496	0.1501	0.5997	0.0870	1.2164	0.0383	0.0000
Var/ty	45.82%	12.01%	13.36%	2.22%	32.89%	0.68%	2.92%	18.00%
Unc/ty	22.67%	6.24%	7.52%	2.49%	20.02%	0.47%	1.34%	17.70%
T i k h - L C								
Average	0.8682	0.4534	0.0804	0.5321	0.2558	1.1112	0.0433	0.1155
Var/ty	16.22%	1.43%	0.39%	1.15%	7.15%	0.48%	2.39%	1.01%
Unc/ty	4.74%	0.54%	0.91%	0.87%	1.24%	0.08%	0.44%	3.43%
P a d e - D P								
Average	0.2476	0.4897	0.0882	0.5405	0.0203	1.3105	0.0141	0.0614
Var/ty	16.83%	1.45%	1.27%	0.53%	16.64%	0.27%	10.34%	23.63%
Unc/ty	7.10%	1.23%	1.33%	0.71%	12.90%	0.32%	9.06%	12.95%
T i k h - G C V								
Average	0.8730	0.6273	0.1147	0.5486	0.0470	1.22	0.0398	0.3715
Var/ty	16.53%	3.03%	3.01%	1.19%	28.32%	0.22%	1.82%	11.02%
Unc/ty	8.64%	2.35%	2.20%	1.03%	15.18%	0.20%	0.64%	8.88%
T i k h - D P								
Average	0.8260	0.6367	0.1184	0.5579	0.0459	1.2256	0.0395	0.3894
Var/ty	19.90%	2.91%	2.79%	1.44%	28.80%	0.26%	0.67%	10.32%
Unc/ty	12.17%	2.55%	2.76%	1.61%	14.79%	0.20%	1.01%	9.41%
P a d e - L C								
Average	0.2922	0.4929	0.0892	0.5427	0.0291	1.29	0.0192	0.0962
Var/ty	36.34%	1.89%	1.51%	0.72%	37.79%	1.68%	32.38%	22.18%
Unc/ty	8.38%	0.79%	0.81%	0.57%	31.07%	0.63%	9.77%	8.64%

Table C.2: Microphysical parameters retrieved with all methods for size distribution No 3, sphere-spheroid particle mixture, data error: 1% and RI: $1.5 + 0.01i$. The rightmost indication "error" corresponds to the mean relative residual error found with a forward calculation.

Parameters	n_t	a_t	v_t	r_{eff}	$svcf$	a_{eff}	a_{var}	error
Synthetic	0.1361	0.4537	0.0821	0.5426	0.4940	1.0238	0.0151	5.02e-03
T S V D - D P								
Average	10.5715	1.1472	0.1733	0.4517	0.3303	1.0413	0.0341	0.0002
Var/ty	28.43%	14.28%	19.71%	9.12%	10.13%	0.49%	6.63%	54.45%
Unc/ty	8.42%	6.54%	7.40%	1.39%	5.75%	0.73%	4.18%	207.40%
T i k h - L C								
Average	3.3729	0.4783	0.0738	0.4630	0.3373	1.0719	0.0383	0.2664
Var/ty	4.50%	1.24%	2.19%	1.09%	0.94%	0.13%	0.37%	0.24%
Unc/ty	1.08%	0.64%	0.85%	0.48%	0.09%	0.02%	0.09%	1.59%
P a d e - D P								
Average	2.2687	0.5384	0.0890	0.4969	0.4892	1.0004	0.0212	0.0712
Var/ty	46.28%	4.93%	1.18%	3.87%	3.43%	0.46%	4.07%	22.16%
Unc/ty	18.38%	1.47%	0.75%	1.75%	3.28%	0.69%	6.08%	6.88%
T i k h - G C V								
Average	6.2466	0.7639	0.1121	0.4408	0.4089	1.0180	0.0284	0.4079
Var/ty	17.98%	4.54%	2.20%	3.65%	0.83%	0.36%	1.29%	7.04%
Unc/ty	4.50%	1.81%	1.17%	1.43%	2.27%	0.33%	3.15%	5.69%
T i k h - D P								
Average	6.0223	0.7542	0.1111	0.4425	0.4106	1.0179	0.0283	0.3975
Var/ty	16.86%	4.07%	1.98%	3.53%	0.62%	0.32%	1.23%	6.45%
Unc/ty	4.68%	1.90%	1.60%	1.41%	2.31%	0.39%	3.42%	5.82%
P a d e - L C								
Average	2.5871	0.5524	0.0903	0.4913	0.4804	1.0005	0.0220	0.1114
Var/ty	38.19%	4.56%	1.20%	4.12%	4.33%	0.70%	6.06%	21.61%
Unc/ty	18.72%	2.14%	0.73%	2.09%	2.16%	0.51%	4.14%	7.08%

Table C.3: Retrieval results with Pade-DP for the combinations $(2) \times (a, b, c) \times (\mathrm{iii}, \mathrm{iv}, \mathrm{v})$ from Table 4.1.

oblate, $1.6 + 0.001i$

Parameters	a_t	v_t	r_eff	$svcf$	a_eff
Synthetic	0.1303	0.0185	0.4257	0.1802	0.8290
1% Difference	0.89%	6.00%	6.82%	0.2005	27.57%
Variability	0.94%	0.60%	0.91%	1.38%	0.73%
Uncertainty	0.84%	1.11%	1.11%	4.03%	1.00%
5% Difference	6.74%	2.19%	8.32%	0.1944	28.21%
Variability	1.30%	0.51%	1.07%	0.95%	0.18%
Uncertainty	2.52%	2.93%	3.41%	6.09%	1.05%
10% Difference	11.69%	0.64%	10.87%	0.1946	28.17%
Variability	1.59%	0.55%	1.29%	1.20%	0.19%
Uncertainty	4.69%	5.49%	6.85%	11.75%	2.05%

oblate, $1.5 + 0.01i$

	a_t	v_t	r_eff	$svcf$	a_eff
1% Difference	3.08%	2.30%	5.19%	0.1637	28.78%
Variability	1.36%	1.91%	2.53%	3.57%	2.07%
Uncertainty	1.38%	2.20%	2.73%	3.51%	1.90%
5% Difference	6.99%	1.91%	4.72%	0.1477	30.79%
Variability	0.78%	0.66%	0.99%	2.61%	1.10%
Uncertainty	2.48%	4.06%	4.05%	6.89%	1.27%
10% Difference	11.85%	3.43%	7.37%	0.1441	30.44%
Variability	1.16%	0.51%	1.00%	2.65%	0.20%
Uncertainty	4.59%	7.88%	8.60%	11.87%	1.81%

oblate, $1.7 + 0.05i$

	a_t	v_t	r_eff	$svcf$	a_eff
1% Difference	1.02%	3.24%	4.21%	0.1719	28.96%
Variability	0.53%	0.56%	0.54%	1.98%	0.32%
Uncertainty	0.57%	1.35%	1.17%	3.84%	1.06%
5% Difference	3.85%	5.51%	9.04%	0.1583	30.02%
Variability	1.10%	1.37%	1.04%	3.16%	0.40%
Uncertainty	1.72%	6.53%	5.80%	6.29%	0.97%
10% Difference	8.49%	5.11%	12.58%	0.1537	30.28%
Variability	1.23%	1.61%	1.20%	2.48%	0.31%
Uncertainty	3.28%	10.31%	9.34%	9.68%	1.43%

Table C.4: Table C.3 continuation (1)
sphere-spheroid mixture, $1.6 + 0.001i$

	Parameters	a_{t}	v_{t}	r_{eff}	$svcf$	a_{eff}
	Synthetic	0.1636	0.0232	0.4257	0.4938	1.0238
1%	Difference	6.09%	3.03%	2.85%	0.0279	0.04%
	Variability	1.34%	0.27%	1.31%	1.13%	0.18%
	Uncertainty	1.37%	0.75%	1.43%	3.20%	0.61%
5%	Difference	11.43%	9.67%	1.56%	0.0554	1.15%
	Variability	0.96%	0.91%	0.98%	1.69%	0.23%
	Uncertainty	2.58%	3.05%	2.82%	5.47%	1.11%
10%	Difference	17.56%	13.09%	3.59%	0.0619	1.52%
	Variability	1.06%	0.58%	1.05%	1.07%	0.14%
	Uncertainty	4.72%	4.83%	6.64%	9.28%	1.83%

sphere-spheroid mixture, $1.5 + 0.01i$

1%	Difference	13.33%	2.79%	9.14%	0.0671	0.08%
	Variability	3.95%	0.50%	3.45%	1.01%	0.20%
	Uncertainty	2.42%	0.89%	2.78%	5.05%	0.99%
5%	Difference	10.98%	9.52%	1.21%	0.1373	3.97%
	Variability	1.28%	0.57%	1.20%	2.02%	0.28%
	Uncertainty	3.40%	4.08%	4.96%	7.08%	1.26%
10%	Difference	15.84%	11.80%	3.28%	0.1473	4.38%
	Variability	1.62%	0.76%	1.59%	1.81%	0.25%
	Uncertainty	4.85%	7.61%	8.48%	10.66%	1.73%

sphere-spheroid mixture, $1.7 + 0.05i$

1%	Difference	10.25%	4.03%	5.56%	0.0606	1.19%
	Variability	1.99%	0.63%	1.46%	3.44%	0.51%
	Uncertainty	2.79%	1.19%	2.77%	4.79%	0.89%
5%	Difference	8.18%	0.15%	7.41%	0.1172	3.62%
	Variability	1.39%	1.57%	1.64%	4.53%	1.26%
	Uncertainty	3.39%	6.71%	5.84%	4.63%	1.28%
10%	Difference	10.93%	1.03%	10.85%	0.1366	4.57%
	Variability	1.56%	1.69%	1.78%	2.89%	0.60%
	Uncertainty	3.29%	11.12%	9.82%	8.00%	1.26%

Table C.5: Table C.3 continuation (2)

prolate, $1.6 + 0.001i$

	Parameters	a_t	v_t	r_eff	$svcf$	a_eff
	Synthetic	0.1668	0.0237	0.4257	0.0	1.3592
1%	Difference	2.88%	0.16%	2.64%	0.0099	2.41%
	Variability	1.20%	0.41%	0.93%	11.16%	0.18%
	Uncertainty	1.08%	1.57%	1.04%	14.25%	0.64%
5%	Difference	7.25%	3.61%	3.40%	0.0374	5.82%
	Variability	1.37%	0.79%	1.03%	14.10%	0.56%
	Uncertainty	2.79%	5.72%	4.72%	56.78%	2.93%
10%	Difference	15.35%	1.93%	11.55%	0.1109	10.44%
	Variability	3.39%	1.29%	3.02%	12.77%	0.60%
	Uncertainty	3.53%	13.51%	12.94%	61.48%	5.86%

prolate, $1.5 + 0.01i$

1%	Difference	2.66%	1.62%	1.00%	0.3862	6.52%
	Variability	0.96%	0.31%	0.77%	15.45%	0.11%
	Uncertainty	0.78%	1.31%	1.31%	14.89%	0.48%
5%	Difference	6.15%	0.15%	5.86%	1.9374	15.09%
	Variability	2.20%	1.29%	1.80%	11.06%	0.79%
	Uncertainty	2.82%	4.93%	5.42%	25.05%	2.69%
10%	Difference	10.04%	0.45%	9.40%	2.3073	16.75%
	Variability	1.88%	0.96%	1.70%	6.05%	0.50%
	Uncertainty	4.88%	8.26%	8.42%	15.10%	1.95%

prolate, $1.7 + 0.05i$

1%	Difference	1.13%	0.45%	1.56%	0.2629	5.41%
	Variability	0.95%	0.74%	0.52%	27.12%	0.48%
	Uncertainty	0.38%	1.81%	1.70%	40.22%	1.25%
5%	Difference	5.73%	1.34%	6.70%	1.4793	12.70%
	Variability	1.85%	2.51%	1.40%	29.14%	1.45%
	Uncertainty	1.80%	7.63%	7.31%	58.62%	5.90%
10%	Difference	10.41%	4.26%	13.23%	2.3381	17.02%
	Variability	2.28%	2.51%	2.20%	9.75%	0.73%
	Uncertainty	4.13%	11.55%	11.49%	21.24%	2.46%

Table C.6: Retrieval results with Pade-DP for the combinations $(3) \times (a, b, c) \times (\mathrm{i, iii, v})$ from Table 4.1.

oblate, $1.33 + 0.001i$

	Parameters	a_t	v_t	r_eff	$svcf$	a_eff
	Synthetic	0.3675	0.0653	0.5334	0.1802	0.8290
1%	Difference	4.38%	7.79%	3.26%	0.1697	31.49%
	Variability	2.62%	2.80%	0.42%	4.48%	1.42%
	Uncertainty	0.85%	1.45%	0.78%	7.50%	1.19%
5%	Difference	10.61%	21.26%	9.56%	0.1658	32.24%
	Variability	1.83%	2.57%	1.35%	7.86%	1.74%
	Uncertainty	2.24%	6.68%	5.22%	29.45%	3.90%
10%	Difference	19.51%	37.52%	14.92%	0.1356	34.20%
	Variability	2.97%	2.94%	2.01%	9.62%	1.47%
	Uncertainty	4.09%	11.38%	8.78%	37.72%	4.19%

oblate, $1.5 + 0.01i$

1%	Difference	10.76%	1.75%	10.97%	0.2350	22.73%
	Variability	6.29%	0.98%	6.32%	3.32%	0.81%
	Uncertainty	2.53%	1.57%	1.87%	4.25%	0.63%
5%	Difference	16.67%	3.48%	10.75%	0.2405	23.74%
	Variability	3.97%	1.57%	3.95%	3.38%	0.91%
	Uncertainty	7.92%	5.03%	8.11%	15.29%	2.76%
10%	Difference	20.11%	10.64%	6.72%	0.2310	25.08%
	Variability	2.90%	1.80%	2.65%	4.74%	0.95%
	Uncertainty	13.53%	9.65%	12.59%	24.28%	3.40%

oblate, $1.7 + 0.05i$

1%	Difference	6.17%	0.32%	5.46%	0.2296	26.59%
	Variability	3.51%	6.08%	6.20%	5.56%	0.77%
	Uncertainty	1.27%	2.19%	2.12%	3.04%	0.65%
5%	Difference	8.27%	1.24%	6.38%	0.2210	27.31%
	Variability	3.12%	3.43%	4.31%	8.32%	1.26%
	Uncertainty	4.65%	5.66%	5.40%	10.25%	1.72%
10%	Difference	6.70%	5.18%	11.06%	0.1912	28.36%
	Variability	2.19%	2.72%	2.43%	4.71%	0.66%
	Uncertainty	5.68%	10.33%	9.29%	10.62%	1.61%

Table C.7: Table C.6 continuation (1)
sphere-spheroid mixture, $1.33 + 0.001i$

	Parameters	a_t	v_t	r_{eff}	$svcf$	a_{eff}
	Synthetic	0.4524	0.0820	0.5438	0.4944	1.0224
1%	Difference	7.84%	8.77%	0.86%	0.0910	6.35%
	Variability	4.41%	4.52%	0.83%	5.03%	2.41%
	Uncertainty	0.73%	1.79%	1.62%	7.03%	1.37%
5%	Difference	13.67%	23.99%	8.94%	0.0970	6.98%
	Variability	3.22%	4.17%	1.91%	9.24%	2.81%
	Uncertainty	2.95%	8.70%	6.34%	24.24%	4.52%
10%	Difference	23.19%	39.84%	13.33%	0.1372	8.56%
	Variability	3.48%	3.44%	1.84%	12.56%	1.89%
	Uncertainty	4.75%	13.09%	10.23%	38.22%	4.65%

sphere-spheroid mixture, $1.5 + 0.01i$

1%	Difference	19.01%	8.55%	8.62%	0.0050	2.16%
	Variability	4.93%	1.18%	3.87%	3.43%	0.46%
	Uncertainty	1.47%	0.75%	1.75%	3.28%	0.69%
5%	Difference	25.85%	13.99%	8.80%	0.0060	1.30%
	Variability	4.46%	1.06%	4.11%	2.82%	0.79%
	Uncertainty	7.98%	4.18%	7.79%	14.16%	2.45%
10%	Difference	43.68%	26.26%	10.27%	0.0287	0.58%
	Variability	4.05%	1.55%	4.25%	4.17%	1.19%
	Uncertainty	15.88%	7.44%	14.56%	20.04%	4.20%

sphere-spheroid mixture, $1.7 + 0.05i$

1%	Difference	18.36%	8.02%	8.67%	0.0004	0.59%
	Variability	4.19%	2.86%	2.01%	6.47%	1.16%
	Uncertainty	1.49%	0.90%	1.20%	2.44%	0.55%
5%	Difference	20.86%	10.88%	8.08%	0.0179	0.53%
	Variability	3.10%	3.39%	2.58%	10.93%	2.32%
	Uncertainty	5.70%	4.66%	5.46%	8.15%	2.71%
10%	Difference	20.85%	9.94%	8.88%	0.0205	1.34%
	Variability	3.35%	3.67%	2.39%	10.59%	1.63%
	Uncertainty	10.89%	12.08%	8.23%	17.90%	2.48%

Table C.8: Table C.6 continuation (2)

prolate, $1.33 + 0.001i$

	Parameters	a_t	v_t	r_eff	$svcf$	a_eff
	Synthetic	0.4623	0.0840	0.5453	0.0	1.3525
1%	Difference	7.69%	10.24%	2.34%	0.1173	8.71%
	Variability	2.96%	3.41%	1.17%	27.71%	1.98%
	Uncertainty	1.11%	3.47%	2.66%	18.54%	1.52%
5%	Difference	13.57%	22.59%	7.82%	0.2084	12.44%
	Variability	2.72%	3.47%	1.32%	18.47%	1.98%
	Uncertainty	2.72%	8.48%	6.31%	42.93%	4.55%
10%	Difference	22.42%	38.52%	12.91%	0.2526	14.81%
	Variability	3.21%	3.38%	1.84%	13.94%	1.55%
	Uncertainty	4.14%	13.12%	10.09%	42.60%	5.14%

prolate, $1.5 + 0.01i$

1%	Difference	5.93%	4.99%	0.88%	0.01933	3.11%
	Variability	1.45%	1.27%	0.53%	16.64%	0.27%
	Uncertainty	1.23%	1.33%	0.71%	12.89%	0.32%
5%	Difference	7.64%	7.81%	0.16%	0.07087	6.99%
	Variability	1.42%	1.07%	0.93%	25.44%	1.37%
	Uncertainty	4.12%	5.26%	3.07%	84.41%	4.96%
10%	Difference	11.24%	13.47%	1.88%	0.1718	12.73%
	Variability	1.98%	1.55%	1.07%	17.15%	0.72%
	Uncertainty	7.21%	11.06%	6.55%	66.34%	8.21%

prolate, $1.7 + 0.05i$

1%	Difference	12.54%	30.96%	16.37%	0.9784	7.90%
	Variability	0.74%	4.41%	4.31%	18.95%	0.56%
	Uncertainty	1.37%	4.56%	4.67%	12.29%	0.81%
5%	Difference	10.30%	23.23%	11.54%	1.9546	13.59%
	Variability	1.18%	6.24%	5.73%	11.63%	0.51%
	Uncertainty	7.40%	13.67%	10.33%	43.23%	6.16%
10%	Difference	10.03%	10.99%	0.78%	2.4564	16.62%
	Variability	1.31%	3.81%	3.51%	9.72%	0.57%
	Uncertainty	8.70%	14.47%	10.32%	29.14%	4.81%

Table C.9: Retrieval results with Pade-DP for the combinations $(4) \times (a, b, c) \times (\mathrm{ii, iii, v})$ from Table 4.1.

oblate, $1.4 + 0.005i$

	Parameters	a_t	v_t	r_eff	$svcf$	a_eff
	Synthetic	0.9930	0.3141	0.9488	0.1802	0.8285
1%	Difference	11.88%	5.67%	5.47%	0.1686	11.89%
	Variability	3.27%	0.35%	3.21%	1.99%	0.59%
	Uncertainty	0.84%	0.91%	0.83%	4.26%	0.76%
5%	Difference	19.90%	8.26%	9.50%	0.1643	13.57%
	Variability	3.17%	0.43%	3.19%	2.87%	0.68%
	Uncertainty	4.06%	3.81%	5.31%	21.76%	3.03%
10%	Difference	31.25%	11.34%	14.85%	0.1774	18.89%
	Variability	3.43%	1.86%	3.20%	7.59%	1.64%
	Uncertainty	8.05%	9.57%	9.90%	24.47%	5.21%

oblate, $1.5 + 0.01i$

1%	Difference	3.57%	4.57%	7.86%	0.2079	23.92%
	Variability	0.69%	0.34%	0.60%	1.54%	0.59%
	Uncertainty	0.75%	1.21%	0.87%	5.66%	0.81%
5%	Difference	9.29%	2.79%	10.93%	0.1974	26.16%
	Variability	0.83%	0.88%	1.19%	3.32%	0.64%
	Uncertainty	5.36%	4.46%	4.33%	12.44%	1.57%
10%	Difference	18.06%	0.71%	14.48%	0.1820	27.32%
	Variability	2.14%	1.22%	2.31%	5.57%	1.21%
	Uncertainty	6.55%	8.30%	8.33%	22.61%	3.41%

oblate, $1.7 + 0.05i$

1%	Difference	1.62%	1.67%	0.04%	0.1850	28.27%
	Variability	0.29%	1.81%	1.57%	3.00%	0.47%
	Uncertainty	0.67%	1.78%	1.51%	4.10%	0.92%
5%	Difference	9.75%	10.07%	0.28%	0.1901	28.50%
	Variability	0.69%	2.03%	1.67%	3.81%	0.61%
	Uncertainty	2.67%	5.85%	4.98%	12.03%	2.59%
10%	Difference	10.81%	7.25%	16.66%	0.1419	31.50%
	Variability	2.30%	6.98%	5.65%	6.39%	0.92%
	Uncertainty	5.38%	14.36%	9.81%	14.34%	2.90%

Table C.10: Table C.9 continuation (1)
sphere-spheroid mixture, $1.4 + 0.005i$

	Parameters	a_t	v_t	r_eff	$svcf$	a_eff
	Synthetic	1.2462	0.3941	0.9488	0.4937	1.0240
1%	Difference	6.38%	0.04%	5.91%	0.0927	4.98%
	Variability	1.18%	0.49%	1.14%	2.38%	0.60%
	Uncertainty	2.15%	1.42%	2.63%	3.27%	1.01%
5%	Difference	20.96%	3.30%	14.14%	0.1338	2.53%
	Variability	2.36%	1.00%	1.94%	4.81%	1.16%
	Uncertainty	6.06%	4.00%	9.34%	13.83%	3.01%
10%	Difference	27.01%	6.24%	15.56%	0.1145	1.35%
	Variability	3.37%	1.87%	2.75%	4.96%	0.95%
	Uncertainty	9.69%	9.92%	14.08%	32.54%	3.92%

sphere-spheroid mixture, $1.5 + 0.01i$

1%	Difference	3.64%	7.07%	3.31%	0.0035	2.13%
	Variability	0.43%	0.78%	0.90%	1.22%	0.35%
	Uncertainty	0.67%	0.97%	0.88%	3.73%	0.48%
5%	Difference	12.36%	12.34%	0.10%	0.0506	0.72%
	Variability	1.01%	1.01%	1.68%	2.93%	0.57%
	Uncertainty	3.19%	3.36%	4.50%	16.90%	2.48%
10%	Difference	17.16%	10.22%	5.32%	0.0944	3.51%
	Variability	1.78%	1.16%	2.09%	5.04%	0.73%
	Uncertainty	10.94%	6.87%	7.12%	19.93%	2.31%

sphere-spheroid mixture, $1.7 + 0.05i$

1%	Difference	1.54%	4.82%	6.27%	0.0469	0.65%
	Variability	0.17%	1.09%	1.02%	1.59%	0.21%
	Uncertainty	0.84%	1.93%	1.96%	3.18%	0.74%
5%	Difference	10.56%	1.10%	8.53%	0.0684	2.01%
	Variability	0.56%	2.06%	2.16%	3.72%	0.52%
	Uncertainty	2.55%	4.71%	4.58%	11.14%	2.59%
10%	Difference	16.01%	2.26%	12.04%	0.1241	4.59%
	Variability	1.09%	2.89%	2.45%	4.20%	0.63%
	Uncertainty	5.82%	12.67%	8.99%	18.34%	3.51%

Table C.11: Table C.9 continuation (2)

prolate, $1.4 + 0.005i$

	Parameters	a_t	v_t	r_eff	$svcf$	a_eff
	Synthetic	1.2696	0.4014	0.9485	0.0	1.3598
1%	Difference	0.32%	0.65%	0.32%	0.0840	7.71%
	Variability	1.16%	0.17%	1.10%	6.87%	0.31%
	Uncertainty	1.33%	1.47%	1.29%	14.34%	1.00%
5%	Difference	0.69%	8.48%	9.11%	0.2274	16.90%
	Variability	1.15%	0.80%	1.38%	5.66%	0.36%
	Uncertainty	3.90%	8.50%	7.05%	23.18%	3.74%
10%	Difference	4.32%	16.36%	19.86%	0.2617	18.64%
	Variability	1.03%	1.44%	1.63%	4.32%	0.37%
	Uncertainty	5.25%	12.76%	10.86%	16.40%	2.46%

prolate, $1.5 + 0.01i$

1%	Difference	3.35%	10.51%	6.94%	0.0357	5.24%
	Variability	0.46%	0.42%	0.53%	25.08%	0.15%
	Uncertainty	1.03%	0.97%	1.16%	18.39%	0.44%
5%	Difference	7.11%	6.59%	0.49%	0.1306	10.17%
	Variability	1.25%	1.18%	1.18%	18.07%	1.04%
	Uncertainty	3.98%	6.99%	5.56%	61.10%	5.38%
10%	Difference	9.33%	3.10%	11.42%	0.2310	15.66%
	Variability	1.62%	2.01%	1.68%	10.80%	0.95%
	Uncertainty	7.49%	11.12%	7.72%	24.35%	3.72%

prolate, $1.7 + 0.05i$

1%	Difference	3.68%	17.65%	13.46%	0.1210	10.71%
	Variability	0.42%	1.44%	1.11%	7.17%	0.26%
	Uncertainty	0.84%	1.72%	1.17%	7.97%	0.61%
5%	Difference	10.31%	18.11%	7.00%	0.1610	12.23%
	Variability	1.33%	3.03%	2.67%	9.60%	0.61%
	Uncertainty	2.77%	8.43%	6.88%	37.34%	3.87%
10%	Difference	13.51%	2.16%	14.90%	0.2207	15.46%
	Variability	1.77%	5.42%	4.64%	12.17%	0.83%
	Uncertainty	7.49%	28.50%	21.70%	35.07%	5.34%

Table C.12: Retrieval results with Pade-LC for the combinations $(2) \times (a, b, c) \times (\mathrm{iii}, \mathrm{iv}, \mathrm{v})$ from Table 4.1.

oblate, $1.6 + 0.001i$

	Parameters	a_t	v_t	r_eff	$svcf$	a_eff
	Synthetic	0.1303	0.0185	0.4257	0.1802	0.8290
1%	Difference	0.08%	6.77%	6.67%	0.2289	25.88%
	Variability	1.41%	0.41%	1.31%	0.92%	0.22%
	Uncertainty	1.20%	2.02%	1.81%	5.65%	1.25%
5%	Difference	3.12%	2.33%	5.23%	0.2326	28.86%
	Variability	1.68%	0.55%	1.57%	1.34%	0.59%
	Uncertainty	3.95%	6.90%	6.19%	23.12%	4.96%
10%	Difference	13.98%	0.34%	10.19%	0.1957	30.34%
	Variability	1.78%	1.31%	1.53%	3.38%	0.89%
	Uncertainty	19.93%	9.23%	12.65%	29.31%	6.68%

oblate, $1.5 + 0.01i$

1%	Difference	2.15%	3.67%	5.66%	0.2192	26.67%
	Variability	1.31%	0.27%	1.14%	1.76%	0.75%
	Uncertainty	2.18%	1.59%	1.84%	8.12%	1.78%
5%	Difference	17.59%	0.28%	13.49%	0.2100	30.26%
	Variability	2.30%	0.44%	1.99%	1.86%	0.35%
	Uncertainty	12.66%	6.41%	13.28%	27.99%	4.77%
10%	Difference	36.05%	9.82%	15.40%	0.2240	30.71%
	Variability	5.44%	1.99%	4.14%	4.62%	1.14%
	Uncertainty	23.24%	8.78%	21.75%	34.25%	6.86%

oblate, $1.7 + 0.05i$

1%	Difference	0.75%	1.95%	2.68%	0.1769	27.33%
	Variability	0.67%	0.63%	0.48%	2.29%	0.65%
	Uncertainty	0.43%	1.90%	1.78%	6.56%	1.53%
5%	Difference	6.44%	1.87%	4.12%	0.1658	29.85%
	Variability	1.42%	1.14%	1.36%	4.18%	0.87%
	Uncertainty	5.12%	7.58%	8.44%	29.66%	5.86%
10%	Difference	12.44%	0.43%	9.34%	0.1285	33.10%
	Variability	2.53%	2.00%	2.20%	5.41%	1.59%
	Uncertainty	17.15%	13.22%	15.43%	28.55%	4.97%

Table C.13: Table C.12 continuation (1)
sphere-spheroid mixture, $1.6 + 0.001i$

	Parameters	a_t	v_t	r_{eff}	$svcf$	a_{eff}
	Synthetic	0.1636	0.0232	0.4257	0.4938	1.0238
1%	Difference	4.85%	2.03%	2.64%	0.0102	0.87%
	Variability	1.26%	0.25%	1.18%	0.61%	0.18%
	Uncertainty	2.19%	1.66%	2.42%	4.78%	1.27%
5%	Difference	11.64%	7.66%	3.21%	0.0141	1.55%
	Variability	1.63%	1.52%	2.29%	4.08%	1.28%
	Uncertainty	6.50%	6.01%	8.56%	17.01%	3.79%
10%	Difference	27.82%	16.72%	6.76%	0.0231	3.50%
	Variability	2.56%	1.59%	2.15%	3.37%	1.04%
	Uncertainty	16.74%	8.73%	15.85%	27.82%	6.45%

sphere-spheroid mixture, $1.5 + 0.01i$

1%	Difference	12.15%	2.95%	8.01%	0.0106	1.48%
	Variability	3.97%	0.49%	3.52%	1.00%	0.18%
	Uncertainty	3.56%	1.41%	3.16%	6.25%	1.20%
5%	Difference	30.04%	9.55%	13.72%	0.0301	2.40%
	Variability	3.32%	0.69%	2.84%	3.05%	0.60%
	Uncertainty	16.45%	4.86%	15.33%	20.02%	4.42%
10%	Difference	33.71%	10.58%	11.98%	0.0780	3.96%
	Variability	4.00%	1.19%	3.21%	4.88%	0.81%
	Uncertainty	31.69%	11.95%	23.10%	34.29%	6.87%

sphere-spheroid mixture, $1.7 + 0.05i$

1%	Difference	6.60%	3.49%	2.83%	0.0229	0.33%
	Variability	2.07%	0.59%	1.58%	2.56%	0.20%
	Uncertainty	2.95%	1.64%	2.58%	6.36%	1.29%
5%	Difference	14.55%	7.35%	5.63%	0.0493	2.01%
	Variability	1.89%	1.01%	1.72%	3.84%	0.82%
	Uncertainty	8.97%	6.19%	10.15%	21.35%	4.54%
10%	Difference	26.01%	12.27%	8.98%	0.0693	3.94%
	Variability	3.36%	2.54%	2.43%	6.57%	1.48%
	Uncertainty	15.22%	9.41%	17.09%	32.47%	6.78%

Table C.14: Table C.12 continuation (2)
prolate, $1.6 + 0.001i$

	Parameters	a_t	v_t	r_eff	$svcf$	a_eff
	Synthetic	0.1668	0.0237	0.4257	0.0010	1.3592
1%	Difference	5.20%	2.26%	2.77%	0.0069	3.09%
	Variability	1.86%	1.02%	1.04%	34.54%	0.70%
	Uncertainty	1.36%	1.29%	1.06%	27.24%	0.50%
5%	Difference	6.48%	3.53%	2.55%	0.0186	3.66%
	Variability	1.60%	0.94%	1.06%	16.08%	0.44%
	Uncertainty	6.09%	4.67%	5.34%	70.82%	2.01%
10%	Difference	14.34%	7.82%	5.40%	0.0717	6.43%
	Variability	3.02%	1.44%	2.46%	18.21%	0.95%
	Uncertainty	6.71%	10.79%	11.05%	72.83%	4.69%

prolate, $1.5 + 0.01i$

1%	Difference	2.72%	0.50%	2.15%	0.0166	4.22%
	Variability	1.22%	0.41%	0.95%	22.59%	0.36%
	Uncertainty	0.81%	1.46%	1.23%	40.26%	0.71%
5%	Difference	5.81%	2.63%	2.93%	0.0517	6.15%
	Variability	2.01%	0.59%	1.53%	19.61%	0.90%
	Uncertainty	5.12%	8.21%	7.08%	65.04%	2.83%
10%	Difference	15.04%	8.68%	4.98%	0.1001	8.38%
	Variability	2.82%	1.40%	2.73%	23.93%	1.14%
	Uncertainty	11.71%	14.65%	13.40%	63.65%	4.91%

prolate, $1.7 + 0.05i$

1%	Difference	2.46%	0.13%	2.27%	0.0253	5.77%
	Variability	1.16%	1.02%	0.75%	35.38%	0.97%
	Uncertainty	0.71%	1.74%	1.65%	38.36%	1.05%
5%	Difference	4.51%	1.77%	2.59%	0.0691	7.26%
	Variability	1.26%	1.06%	1.13%	20.28%	0.62%
	Uncertainty	1.77%	7.83%	7.83%	86.85%	4.47%
10%	Difference	9.73%	7.13%	2.36%	0.1258	9.85%
	Variability	1.59%	2.40%	1.94%	32.87%	1.45%
	Uncertainty	4.57%	12.71%	12.00%	71.68%	6.71%

Table C.15: Retrieval results by Pade-LC for the combinations $(3) \times (a, b, c) \times (i, iii, v)$ from Table 4.1.

oblate, $1.33 + 0.001i$

	Parameters	a_t	v_t	r_{eff}	$svcf$	a_{eff}
	Synthetic	0.3614	0.0654	0.5426	0.1802	0.8291
1%	Difference	7.42%	9.51%	1.93%	0.2031	31.46%
	Variability	2.35%	2.98%	0.91%	4.27%	0.79%
	Uncertainty	0.82%	1.17%	0.57%	6.54%	0.94%
5%	Difference	11.05%	19.44%	7.52%	0.1843	31.16%
	Variability	2.16%	1.96%	0.99%	7.19%	1.52%
	Uncertainty	2.28%	6.71%	5.35%	27.16%	4.08%
10%	Difference	19.36%	35.87%	13.73%	0.2029	31.56%
	Variability	3.16%	3.02%	1.93%	10.22%	1.65%
	Uncertainty	4.44%	11.83%	9.63%	38.60%	5.85%

oblate, $1.5 + 0.01i$

		a_t	v_t	r_{eff}	$svcf$	a_{eff}
1%	Difference	11.98%	2.11%	12.35%	0.2371	22.73%
	Variability	5.45%	0.85%	5.62%	2.93%	0.48%
	Uncertainty	2.05%	1.26%	1.60%	3.59%	0.54%
5%	Difference	18.09%	2.45%	12.75%	0.2506	23.85%
	Variability	4.08%	1.13%	4.46%	3.18%	0.69%
	Uncertainty	7.35%	5.42%	7.97%	17.07%	2.82%
10%	Difference	29.25%	11.32%	12.59%	0.2623	26.82%
	Variability	5.46%	1.83%	4.93%	4.32%	2.44%
	Uncertainty	12.10%	9.46%	13.88%	27.02%	6.06%

oblate, $1.7 + 0.05i$

		a_t	v_t	r_{eff}	$svcf$	a_{eff}
1%	Difference	5.64%	0.16%	5.50%	0.2089	27.36%
	Variability	3.77%	5.73%	3.93%	7.58%	1.11%
	Uncertainty	1.25%	1.95%	2.20%	3.88%	0.68%
5%	Difference	9.69%	1.97%	6.89%	0.2280	27.12%
	Variability	2.75%	4.48%	3.96%	9.03%	1.30%
	Uncertainty	3.92%	6.20%	7.56%	13.92%	2.59%
10%	Difference	16.24%	7.38%	7.41%	0.2286	28.13%
	Variability	3.66%	6.73%	4.44%	11.91%	1.76%
	Uncertainty	5.62%	10.62%	12.07%	20.94%	4.22%

Table C.16: Table C.15 continuation (1)
sphere-spheroid mixture, $1.33 + 0.001i$

	Parameters	a_t	v_t	r_eff	$svcf$	a_eff
	Synthetic	0.4537	0.0821	0.5426	0.4940	1.0238
1%	Difference	9.33%	12.27%	2.68%	0.1369	6.99%
	Variability	3.38%	3.89%	1.22%	12.88%	1.63%
	Uncertainty	1.15%	1.68%	1.01%	5.21%	0.78%
5%	Difference	12.99%	22.44%	8.30%	0.0932	5.90%
	Variability	3.14%	3.09%	1.30%	8.51%	1.86%
	Uncertainty	3.60%	7.44%	5.22%	24.54%	3.93%
10%	Difference	20.64%	39.44%	15.39%	0.0781	6.78%
	Variability	3.73%	3.75%	1.98%	11.37%	2.72%
	Uncertainty	4.67%	12.80%	9.86%	33.49%	5.68%

sphere-spheroid mixture, $1.5 + 0.01i$

1%	Difference	21.75%	10.02%	9.46%	0.0136	2.28%
	Variability	4.56%	1.20%	4.12%	4.33%	0.70%
	Uncertainty	2.14%	0.73%	2.09%	2.16%	0.51%
5%	Difference	26.99%	13.83%	9.66%	0.0001	1.57%
	Variability	5.25%	1.41%	4.70%	3.57%	0.83%
	Uncertainty	8.14%	3.82%	8.12%	13.42%	1.88%
10%	Difference	36.29%	22.54%	8.88%	0.0046	0.10%
	Variability	6.53%	1.88%	6.35%	4.99%	1.32%
	Uncertainty	10.93%	7.86%	11.80%	22.22%	3.56%

sphere-spheroid mixture, $1.7 + 0.05i$

1%	Difference	14.58%	6.01%	7.44%	0.0653	1.83%
	Variability	5.28%	4.71%	2.23%	9.72%	1.43%
	Uncertainty	3.14%	2.86%	1.25%	2.90%	0.36%
5%	Difference	16.64%	7.46%	7.72%	0.0456	1.49%
	Variability	5.53%	5.86%	2.54%	16.24%	2.24%
	Uncertainty	6.07%	5.39%	4.77%	6.25%	1.07%
10%	Difference	24.49%	13.36%	8.66%	0.0287	1.52%
	Variability	5.37%	6.23%	3.72%	14.38%	2.35%
	Uncertainty	7.15%	7.23%	7.99%	14.03%	2.78%

Table C.17: Table C.15 continuation (2)
prolate, $1.33 + 0.001i$

	Parameters	a_t	v_t	r_{eff}	$svcf$	a_{eff}
	Synthetic	0.4624	0.0836	0.5426	0.0010	1.3590
1%	Difference	9.29%	12.97%	3.34%	0.1718	12.15%
	Variability	3.42%	4.22%	1.51%	26.45%	3.43%
	Uncertainty	1.17%	2.25%	1.51%	11.57%	0.98%
5%	Difference	12.02%	21.43%	8.28%	0.2168	14.08%
	Variability	2.34%	2.95%	1.59%	23.65%	2.47%
	Uncertainty	3.17%	8.73%	6.34%	38.18%	3.70%
10%	Difference	19.34%	36.61%	14.26%	0.2701	15.59%
	Variability	2.82%	2.98%	2.25%	20.09%	2.40%
	Uncertainty	4.35%	12.40%	9.52%	52.25%	5.86%

prolate, $1.5 + 0.01i$

1%	Difference	6.60%	6.61%	0.02%	0.0282	5.11%
	Variability	1.89%	1.51%	0.72%	37.79%	1.68%
	Uncertainty	0.79%	0.81%	0.57%	31.07%	0.63%
5%	Difference	8.39%	8.50%	0.12%	0.0577	7.18%
	Variability	2.14%	1.12%	1.56%	43.69%	2.12%
	Uncertainty	3.26%	4.79%	3.29%	66.77%	2.57%
10%	Difference	15.85%	16.02%	0.29%	0.1054	9.72%
	Variability	3.05%	1.93%	2.51%	30.92%	2.40%
	Uncertainty	5.53%	8.98%	7.87%	66.17%	4.34%

prolate, $1.7 + 0.05i$

1%	Difference	10.31%	27.26%	15.22%	0.1658	12.81%
	Variability	2.33%	8.11%	6.16%	38.20%	4.10%
	Uncertainty	1.55%	4.76%	3.72%	13.40%	1.53%
5%	Difference	12.47%	29.72%	15.52%	0.1436	11.42%
	Variability	1.57%	6.46%	6.01%	27.55%	2.35%
	Uncertainty	5.14%	10.28%	11.39%	43.83%	4.08%
10%	Difference	16.16%	30.23%	12.31%	0.1647	11.87%
	Variability	1.77%	7.99%	7.04%	28.90%	2.09%
	Uncertainty	7.40%	18.05%	18.66%	57.22%	5.73%

Table C.18: Retrieval results with Pade-LC for the combinations $(4) \times (a, b, c) \times (\mathrm{ii}, \mathrm{iii}, \mathrm{v})$ from Table 4.1.

oblate, $1.4 + 0.005i$

	Parameters	a_t	v_t	r_eff	$svcf$	a_eff
	Synthetic	0.9930	0.3141	0.9488	0.1802	0.8285
1%	Difference	17.51%	6.48%	9.25%	0.1738	12.91%
	Variability	3.73%	0.48%	3.73%	2.60%	0.66%
	Uncertainty	1.94%	0.95%	2.08%	4.18%	0.61%
5%	Difference	21.98%	8.63%	10.68%	0.1694	14.01%
	Variability	3.91%	0.61%	3.74%	2.96%	0.66%
	Uncertainty	4.33%	3.75%	5.52%	20.59%	2.87%
10%	Difference	33.34%	12.45%	15.07%	0.1683	17.61%
	Variability	4.05%	2.22%	3.94%	7.87%	1.55%
	Uncertainty	8.43%	6.56%	10.16%	32.30%	5.38%

oblate, $1.5 + 0.01i$

1%	Difference	3.68%	4.24%	7.63%	0.2107	23.93%
	Variability	0.71%	0.67%	0.76%	1.16%	0.51%
	Uncertainty	0.83%	1.23%	0.82%	5.07%	0.80%
5%	Difference	9.72%	1.98%	10.60%	0.2141	25.06%
	Variability	1.44%	0.73%	1.49%	3.43%	0.58%
	Uncertainty	4.23%	5.55%	4.85%	21.34%	3.16%
10%	Difference	19.39%	0.97%	15.09%	0.2278	26.97%
	Variability	2.67%	1.63%	1.92%	8.12%	1.12%
	Uncertainty	7.50%	9.21%	10.26%	31.75%	4.69%

oblate, $1.7 + 0.05i$

1%	Difference	1.10%	1.86%	0.75%	0.1955	27.59%
	Variability	0.29%	1.55%	1.30%	2.10%	0.33%
	Uncertainty	0.81%	1.71%	1.72%	5.64%	1.00%
5%	Difference	6.94%	6.17%	0.75%	0.1891	28.21%
	Variability	0.82%	3.29%	2.93%	4.85%	0.81%
	Uncertainty	3.96%	9.85%	8.75%	7.75%	1.48%
10%	Difference	12.66%	0.55%	11.96%	0.1810	29.82%
	Variability	2.33%	6.59%	5.16%	6.64%	1.20%
	Uncertainty	4.18%	13.89%	11.51%	22.81%	3.70%

Table C.19: Table C.18 continuation (1)
sphere-spheroid mixture, $1.4 + 0.005i$

	Parameters	a_t	v_t	r_{eff}	$svcf$	a_{eff}
	Synthetic	1.2462	0.3941	0.9488	0.4937	1.0240
1%	Difference	8.28%	1.00%	6.63%	0.0800	5.46%
	Variability	2.20%	0.60%	2.10%	1.91%	0.31%
	Uncertainty	2.25%	1.06%	2.88%	4.04%	0.97%
5%	Difference	8.62%	0.51%	8.15%	0.1065	3.02%
	Variability	1.92%	0.40%	1.86%	2.37%	0.45%
	Uncertainty	6.88%	6.40%	7.04%	15.55%	4.45%
10%	Difference	26.66%	7.19%	14.44%	0.1177	1.47%
	Variability	3.12%	1.45%	3.39%	6.90%	0.93%
	Uncertainty	9.85%	7.41%	13.37%	35.48%	5.94%

sphere-spheroid mixture, $1.5 + 0.01i$

1%	Difference	3.67%	7.53%	3.72%	0.0053	2.08%
	Variability	0.31%	0.78%	0.75%	1.44%	0.26%
	Uncertainty	0.58%	0.84%	0.75%	3.64%	0.52%
5%	Difference	10.19%	10.61%	0.47%	0.0157	0.35%
	Variability	0.88%	0.92%	1.34%	2.33%	0.39%
	Uncertainty	3.90%	4.58%	5.04%	16.83%	2.55%
10%	Difference	19.11%	14.40%	3.72%	0.0457	1.97%
	Variability	2.20%	1.73%	2.20%	6.88%	0.96%
	Uncertainty	5.67%	8.20%	8.98%	26.59%	4.05%

sphere-spheroid mixture, $1.7 + 0.05i$

1%	Difference	1.88%	3.84%	5.61%	0.0461	0.59%
	Variability	0.47%	1.60%	1.37%	2.15%	0.27%
	Uncertainty	0.91%	0.99%	0.76%	2.69%	0.61%
5%	Difference	9.07%	0.44%	8.68%	0.0513	1.41%
	Variability	0.83%	2.10%	2.10%	3.42%	0.52%
	Uncertainty	3.07%	4.64%	4.65%	11.77%	2.63%
10%	Difference	16.75%	3.24%	11.63%	0.0836	3.13%
	Variability	1.45%	3.65%	3.52%	8.02%	1.31%
	Uncertainty	4.42%	10.71%	8.96%	19.25%	3.47%

Table C.20: Table C.18 continuation (2)

prolate, $1.4 + 0.005i$

Parameter	a_t	v_t	r_{eff}	$svcf$	a_{eff}
Synthetic	1.2696	0.4014	0.9485	0.0010	1.3598

		a_t	v_t	r_{eff}	$svcf$	a_{eff}
1%	Difference	0.24%	0.23%	0.02%	0.9262	8.28%
	Variability	1.24%	0.26%	1.10%	11.07%	0.49%
	Uncertainty	0.92%	1.30%	1.30%	11.14%	0.80%
5%	Difference	3.40%	2.17%	1.06%	1.3035	11.05%
	Variability	1.60%	0.51%	1.61%	14.70%	0.88%
	Uncertainty	3.32%	4.80%	6.07%	54.85%	3.87%
10%	Difference	10.31%	6.51%	3.09%	1.8293	13.99%
	Variability	2.44%	1.23%	2.27%	18.04%	0.94%
	Uncertainty	6.14%	8.24%	10.13%	61.08%	6.51%

prolate, $1.5 + 0.01i$

		a_t	v_t	r_{eff}	$svcf$	a_{eff}
1%	Difference	3.41%	10.34%	6.72%	0.4325	5.77%
	Variability	0.58%	0.49%	0.50%	19.43%	0.57%
	Uncertainty	1.15%	0.96%	1.29%	14.35%	0.42%
5%	Difference	6.99%	9.24%	2.12%	0.8600	7.58%
	Variability	1.67%	3.31%	2.31%	32.27%	2.10%
	Uncertainty	2.99%	6.89%	7.40%	70.74%	3.44%
10%	Difference	14.25%	10.03%	3.40%	1.1888	9.35%
	Variability	2.82%	5.28%	3.66%	38.68%	3.07%
	Uncertainty	9.42%	10.39%	10.02%	48.90%	3.55%

prolate, $1.7 + 0.05i$

		a_t	v_t	r_{eff}	$svcf$	a_{eff}
1%	Difference	3.90%	19.12%	14.64%	1.3705	11.43%
	Variability	0.36%	1.08%	0.87%	9.95%	0.55%
	Uncertainty	0.94%	1.63%	1.10%	9.43%	0.64%
5%	Difference	9.00%	19.15%	9.17%	1.5079	12.16%
	Variability	1.19%	3.57%	2.89%	17.20%	1.35%
	Uncertainty	3.12%	8.13%	6.28%	24.28%	2.56%
10%	Difference	13.47%	4.46%	8.42%	2.1847	15.59%
	Variability	3.85%	14.31%	12.32%	13.83%	1.57%
	Uncertainty	8.05%	20.78%	18.85%	19.03%	2.53%

C.2 Synthetic retrievals with unknown refractive index

Table C.21: Retrieval results of the refractive index and the single scattering albedo with Pade-DP for the cases (3, a-c, i-v, 1%, 5%, 10%), see Table 4.11. The "Average", "Var/ty" and "Unc/ty" relate to ERQ as defined in Sec. 4.1 through the mean and the usual standard deviation. Especially for the IRI we include the median version of the ERQ (see Eq. 4.2.1) on the right of the mean-related ERQ separated by a slash (/). The indications "1%", "5%" and "10%" on the left of a given part of the table refer to retrievals with the respective input data error.

oblate (3, a, i-v, 1%, 5%, 10%)

	Parameters	RRI	IRI (mean/median)	SSA355	SSA532
	Synthetic	1.330	0.001000	0.9843	0.9923
1%	Average	1.330	0.005960/0.005000	0.8974	0.9455
	Var/ty	0.00%	40.82%/0.00%	4.76%	2.70%
	Unc/ty	0.00%	20.25%/0.00%	2.37%	1.31%
5%	Average	1.330	0.006640/0.0075	0.8755	0.9356
	Var/ty	0.00%	48.67%/0.00%	6.61%	2.54%
	Unc/ty	0.00%	43.20%/33.33%	6.99%	2.92%
10%	Average	1.336	0.009120/0.010000	0.8602	0.9162
	Var/ty	0.84%	45.16%/0.00%	6.07%	3.64%
	Unc/ty	0.98%	57.53%/0.00%	6.43%	4.11%
	Synthetic	1.400	0.005000	0.9083	0.9572
1%	Average	1.348	0.000160/0.000000	0.9975	0.9980
	Var/ty	1.91%	178.89%/0.00%	0.56%	0.46%
	Unc/ty	0.50%	52.70%/0.00%	0.22%	0.11%
5%	Average	1.341	0.000400/0.000000	0.9852	0.9951
	Var/ty	1.26%	141.03%/0.00%	2.66%	0.66%
	Unc/ty	1.08%	23.57%/0.00%	1.74%	0.12%
10%	Average	1.338	0.000800/0.001000	0.9810	0.9909
	Var/ty	1.03%	130.49%/0.00%	2.41%	1.18%
	Unc/ty	0.88%	74.54%/0.00%	1.41%	0.69%
	Synthetic	1.500	0.010000	0.8373	0.8908
1%	Average	1.506	0.005300/0.005000	0.9179	0.9493
	Var/ty	0.88%	11.18%/0.00%	1.00%	0.44%
	Unc/ty	0.64%	9.11%/0.00%	0.69%	0.32%
5%	Average	1.532	0.005820/0.003000	0.9302	0.9535
	Var/ty	2.14%	73.24%/0.00%	4.49%	2.94%
	Unc/ty	3.60%	96.73%/66.67%	4.92%	3.40%
10%	Average	1.517	0.007380/0.003000	0.9264	0.9483
	Var/ty	2.18%	40.95%/0.00%	2.41%	1.75%
	Unc/ty	9.13%	139.83%/100.00%	8.77%	6.40%
	Synthetic	1.600	0.001000	0.9772	0.9837
1%	Average	1.648	0.000500/0.001000	0.9907	0.9935
	Var/ty	3.89%	114.11%/0.00%	1.03%	0.72%
	Unc/ty	0.85%	21.08%/0.00%	0.22%	0.15%
5%	Average	1.672	0.001620/0.000500	0.9754	0.9824
	Var/ty	2.81%	112.17%/0.00%	2.12%	1.46%
	Unc/ty	2.77%	102.21%/100.00%	2.55%	1.78%
10%	Average	1.704	0.001200/0.001000	0.9849	0.9868
	Var/ty	2.32%	111.38%/0.00%	1.56%	0.83%
	Unc/ty	3.53%	134.94%/50.00%	2.90%	1.78%
	Synthetic	1.700	0.050000	0.5761	0.6021
1%	Average	1.664	0.041600/0.050000	0.6234	0.6533
	Var/ty	3.67%	25.58%/0.00%	5.27%	5.32%
	Unc/ty	1.24%	7.09%/0.00%	1.68%	1.35%
5%	Average	1.692	0.046400/0.050000	0.6135	0.6482
	Var/ty	2.71%	13.27%/0.00%	3.61%	3.57%
	Unc/ty	1.78%	8.57%/0.00%	2.63%	2.04%
10%	Average	1.690	0.040800/0.050000	0.6511	0.6952
	Var/ty	2.70%	14.62%/0.00%	2.77%	2.59%
	Unc/ty	4.51%	18.52%/0.00%	3.81%	3.53%

Table C.22: Table C.21 continuation (1)

sphere-spheroid mixture (3, b, i-v, 1%, 5%, 10%)

	Parameters	RRI	IRI (mean/median)	SSA355	SSA532
	Synthetic	1.330	0.001000	0.9839	0.9923
1%	Average	1.330	0.007580/0.010000	0.8713	0.9307
	Var/ty	0.00%	42.85%/0.00%	6.24%	3.36%
	Unc/ty	0.00%	11.96%/0.00%	1.80%	0.83%
5%	Average	1.331	0.007720/0.010000	0.8681	0.9284
	Var/ty	0.23%	42.38%/0.00%	6.14%	3.26%
	Unc/ty	0.33%	18.65%/0.00%	2.36%	1.24%
10%	Average	1.330	0.007140/0.010000	0.8730	0.9275
	Var/ty	0.00%	47.48%/0.00%	4.66%	2.56%
	Unc/ty	0.00%	44.05%/0.00%	6.10%	3.33%
	Synthetic	1.400	0.005000	0.9067	0.9570
1%	Average	1.358	0.001180/0.001000	0.9697	0.9815
	Var/ty	2.82%	92.41%/0.00%	2.72%	2.62%
	Unc/ty	0.00%	37.86%/0.00%	1.40%	2.36%
5%	Average	1.350	0.000800/0.001000	0.9780	0.9909
	Var/ty	2.11%	123.50%/0.00%	2.61%	1.09%
	Unc/ty	1.00%	60.09%/0.00%	1.26%	0.51%
10%	Average	1.343	0.000740/0.001000	0.9806	0.9911
	Var/ty	1.31%	137.20%/0.00%	2.46%	1.35%
	Unc/ty	1.15%	69.84%/50.00%	1.71%	0.78%
	Synthetic	1.500	0.010000	0.8253	0.8873
1%	Average	1.552	0.007600/0.007500	0.8984	0.9327
	Var/ty	3.34%	34.61%/0.00%	1.98%	1.48%
	Unc/ty	1.24%	12.71%/33.33%	0.81%	0.58%
5%	Average	1.560	0.007620/0.007500	0.9086	0.9345
	Var/ty	1.96%	42.80%/0.00%	4.07%	2.06%
	Unc/ty	2.90%	41.42%/33.33%	2.92%	2.22%
10%	Average	1.582	0.009500/0.010000	0.8904	0.9253
	Var/ty	1.38%	50.68%/0.00%	4.27%	2.24%
	Unc/ty	3.55%	71.35%/0.00%	6.97%	4.89%
	Synthetic	1.600	0.001000	0.9778	0.9834
1%	Average	1.650	0.000240/0.000000	0.9954	0.9969
	Var/ty	3.26%	206.27%/0.00%	0.91%	0.61%
	Unc/ty	0.86%	35.14%/0.00%	0.16%	0.11%
5%	Average	1.708	0.000800/0.001000	0.9854	0.9900
	Var/ty	2.57%	108.85%/0.00%	1.53%	1.05%
	Unc/ty	1.26%	114.87%/0.00%	1.58%	1.10%
10%	Average	1.714	0.001160/0.000500	0.9807	0.9870
	Var/ty	2.31%	87.43%/0.00%	1.39%	0.91%
	Unc/ty	1.83%	135.47%/100.00%	2.56%	1.76%
	Synthetic	1.700	0.050000	0.5825	0.6021
1%	Average	1.636	0.037200/0.030000	0.6267	0.6588
	Var/ty	3.22%	28.32%/0.00%	4.81%	4.64%
	Unc/ty	0.52%	4.53%/0.00%	1.04%	0.80%
5%	Average	1.630	0.034400/0.030000	0.6379	0.6708
	Var/ty	3.40%	21.80%/0.00%	3.16%	2.96%
	Unc/ty	1.19%	8.58%/0.00%	3.06%	2.33%
10%	Average	1.662	0.037600/0.030000	0.6467	0.6805
	Var/ty	3.49%	17.11%/0.00%	4.01%	2.51%
	Unc/ty	3.33%	17.69%/0.00%	4.65%	3.45%

Table C.23: Table C.21 continuation (2)

prolate (3, c, i-v, 1%, 5%, 10%)

	Parameters	RRI	IRI (mean/median)	SSA355	SSA532
	Synthetic	1.330	0.001000	0.9843	0.9923
1%	Average	1.330	0.007400/0.010000	0.8779	0.9311
	Var/ty	0.00%	54.96%/0.00%	7.80%	4.18%
	Unc/ty	0.00%	8.55%/0.00%	1.62%	0.73%
5%	Average	1.331	0.008360/0.010000	0.8604	0.9185
	Var/ty	0.23%	29.99%/0.00%	4.62%	2.68%
	Unc/ty	0.33%	15.45%/0.00%	2.35%	1.30%
10%	Average	1.336	0.006740/0.007500	0.9018	0.9375
	Var/ty	0.93%	58.66%/0.00%	7.02%	3.38%
	Unc/ty	0.54%	35.69%/33.33%	5.01%	2.93%
	Synthetic	1.400	0.005000	0.9087	0.9636
1%	Average	1.350	0.001780/0.001000	0.9679	0.9948
	Var/ty	2.53%	130.74%/100.00%	3.94%	4.23%
	Unc/ty	0.54%	27.75%/0.00%	0.76%	3.98%
5%	Average	1.347	0.000980/0.001000	0.9803	0.9895
	Var/ty	1.59%	123.58%/0.00%	2.51%	1.29%
	Unc/ty	1.28%	45.58%/0.00%	0.81%	0.38%
10%	Average	1.359	0.001160/0.001000	0.9759	0.9869
	Var/ty	1.59%	132.18%/0.00%	2.90%	1.54%
	Unc/ty	1.64%	78.30%/0.00%	1.94%	1.03%
	Synthetic	1.500	0.010000	0.8260	0.8906
1%	Average	1.400	0.000580/0.001000	0.9841	0.9915
	Var/ty	0.00%	96.88%/0.00%	1.86%	0.95%
	Unc/ty	0.00%	19.57%/0.00%	0.87%	0.17%
5%	Average	1.400	0.000420/0.000000	0.9888	0.9931
	Var/ty	0.00%	117.75%/0.00%	1.12%	0.68%
	Unc/ty	0.00%	65.25%/0.00%	0.73%	0.45%
10%	Average	1.439	0.002480/0.00	0.9625	0.9727
	Var/ty	2.84%	105.26%/0.00%	3.34%	2.62%
	Unc/ty	4.18%	160.04%/100.00%	4.41%	3.23%
	Synthetic	1.600	0.001000	0.9770	0.9839
1%	Average	1.550	0.000500/0.001000	0.9890	0.9924
	Var/ty	3.47%	118.21%/0.00%	1.20%	0.82%
	Unc/ty	0.91%	28.28%/0.00%	0.32%	0.22%
5%	Average	1.550	0.000240/0.000000	0.9946	0.9962
	Var/ty	1.57%	100.62%/0.00%	0.62%	0.43%
	Unc/ty	2.30%	129.10%/0.00%	0.68%	0.48%
10%	Average	1.542	0.000100/0.000000	0.9977	0.9984
	Var/ty	0.00%	53.85%/0.00%	0.34%	0.23%
	Unc/ty	3.08%	194.37%/0.00%	0.41%	0.30%
	Synthetic	1.700	0.050000	0.5820	0.5984
1%	Average	1.330	0.005000/0.005000	0.8249	0.8638
	Var/ty	0.00%	0.00%/0.00%	0.10%	0.17%
	Unc/ty	0.00%	0.00%/0.00%	0.23%	0.22%
5%	Average	1.543	0.033100/0.030000	0.6764	0.7164
	Var/ty	1.62%	15.04%/0.00%	2.69%	2.65%
	Unc/ty	8.01%	44.69%/33.33%	11.30%	9.84%
10%	Average	1.583	0.034580/0.040000	0.7229	0.7524
	Var/ty	0.00%	5.59%/0.00%	0.47%	1.16%
	Unc/ty	8.93%	55.10%/25.00%	17.48%	15.52%

Table C.24: Retrieval results of the refractive index and the single scattering albedo by Pade-DP for the cases (1-4, b, ix, 1%), (1-4, c, x, 1%), (1-4, c, ii, 1%), (1-4, c, viii, 1%), (1, a-c, xiii, 1%), (1, a-c, xi, 1%), (1, a-c, xiv, 1%), (4, a, xii, 1%), (2, c, vii, 1%) see Table 4.11. The "Average", "Var/ty" and "Unc/ty" relate to the ERQ as defined in Sec. 4.1 through the mean and the usual standard deviation. Especially for the IRI we include the median version of the ERQ (see Eq. 4.2.1) on the right of the mean-related ERQ separated by a slash (/). The indications "size No 1-4" and further "oblate", "sphere-spheroid mix" and "prolate" on the left of a given part of the table refer to retrievals with the respective size and shape.

	Parameters	RRI	IRI (mean/median)	SSA355	SSA532
		Cases: (1-4, b, ix, 1%)			
	Synthetic	1.400	0.000000	1.0000	1.0000
size No 1	Average	1.480	0.008000/0.010000	0.9425	0.9526
	Var/ty	0.62%	27.95%/0.00%	0.91%	0.55%
	Unc/ty	2.55%	47.14%/0.00%	2.89%	2.35%
	Synthetic	1.400	0.000000	1.0000	1.0000
size No 2	Average	1.480	0.008060/0.010000	0.9304	0.9519
	Var/ty	0.76%	43.14%/0.00%	2.20%	0.69%
	Unc/ty	2.38%	42.53%/0.00%	3.24%	2.12%
	Synthetic	1.400	0.000000	1.0000	1.0000
size No 3	Average	1.368	0.000000/0.000000	1.0000	1.0000
	Var/ty	0.00%	0.00%/0.00%	0.00%	0.00%
	Unc/ty	0.00%	0.00%/0.00%	0.00%	0.00%
	Synthetic	1.400	0.000000	1.0000	1.0000
size No 4	Average	1.470	0.000000/0.000000	1.0000	1.0000
	Var/ty	0.00%	0.00%/0.00%	0.00%	0.00%
	Unc/ty	0.00%	0.00%/0.00%	0.00%	0.00%
		Cases: (1-4, c, x, 1%)			
	Synthetic	1.400	0.001000	0.9905	0.9921
size No 1	Average	1.348	0.003600/0.005000	0.9567	0.9626
	Var/ty	0.52%	20.74%/0.00%	0.72%	0.60%
	Unc/ty	2.14%	51.85%/0.00%	2.58%	2.23%
	Synthetic	1.400	0.001000	0.9879	0.9922
size No 2	Average	1.350	0.001640/0.0005	0.9789	0.9858
	Var/ty	0.56%	100.40%/0.00%	1.10%	0.71%
	Unc/ty	2.14%	118.21%/100.00%	2.36%	1.59%
	Synthetic	1.400	0.001000	0.9800	0.9911
size No 3	Average	1.373	0.000580/0.000000	0.9875	0.9939
	Var/ty	2.74%	95.85%/0.00%	1.23%	0.60%
	Unc/ty	0.32%	10.90%/0.00%	0.17%	0.09%
	Synthetic	1.400	0.001000	0.9665	0.9773
size No 4	Average	1.400	0.001000/0.001000	0.9688	0.9797
	Var/ty	0.00%	0.00%/0.00%	0.02%	0.31%
	Unc/ty	0.00%	0.00%/0.00%	0.04%	0.43%
		Cases: (1-4, c, ii, 1%)			
	Synthetic	1.400	0.005000	0.9553	0.9620
size No 1	Average	1.334	0.003680/0.003000	0.9562	0.9613
	Var/ty	0.52%	57.99%/0.00%	1.94%	1.72%
	Unc/ty	0.71%	93.48%/66.67%	4.41%	3.93%
	Synthetic	1.400	0.005000	0.9428	0.9626
size No 2	Average	1.336	0.000980/0.001000	0.9878	0.9914
	Var/ty	0.23%	108.05%/0.00%	1.16%	0.77%
	Unc/ty	1.33%	145.09%/0.00%	1.48%	1.04%
	Synthetic	1.400	0.005000	0.9087	0.9636
size No 3	Average	1.350	0.001780/0.001000	0.9679	0.9948
	Var/ty	2.53%	130.74%/100.00%	3.94%	4.23%
	Unc/ty	0.54%	27.75%/0.00%	0.76%	3.98%
	Synthetic	1.400	0.005000	0.8619	0.8989
size No 4	Average	1.394	0.004680/0.005000	0.8767	0.9117
	Var/ty	0.23%	9.94%/0.00%	0.56%	1.34%
	Unc/ty	1.27%	21.62%/0.00%	2.57%	2.29%

Table C.25: Table C.24 continuation (1)

Cases: (1-4, c, viii, 1%)

	Parameters	RRI	IRI (mean/median)	SSA355	SSA532
	Synthetic	1.330	0.030000	0.7891	0.7979
size No 1	Average	1.347	0.037000/0.030000	0.7746	0.7820
	Var/ty	0.00%	0.00%/0.00%	0.11%	0.45%
	Unc/ty	3.99%	59.83%/0.00%	6.67%	7.00%
	Synthetic	1.330	0.030000	0.7751	0.8202
size No 2	Average	1.347	0.037000/0.030000	0.7481	0.7875
	Var/ty	0.00%	0.00%/0.00	0.12%	0.17%
	Unc/ty	3.99%	59.83%/0.00%	7.21%	7.29%
	Synthetic	1.330	0.030000	0.7061	0.8178
size No 3	Average	1.330	0.030000/0.030000	0.6634	0.7774
	Var/ty	0.00%	0.00%/0.00	1.72%	1.00%
	Unc/ty	0.00%	0.00%/0.00%	0.86%	0.59%
	Synthetic	1.330	0.030000	0.5886	0.6676
size No 4	Average	1.333	0.030800/0.030000	0.6273	0.6963
	Var/ty	0.28%	2.88%/0.00	1.81%	1.29%
	Unc/ty	0.66%	8.21%/0.00%	1.72%	1.61%

Cases: (1, a-c, xiii, 1%)

	Parameters	RRI	IRI (mean/median)	SSA355	SSA532
	Synthetic	1.600	0.030000	0.8029	0.8305
oblate	Average	1.672	0.044400/0.050000	0.7591	0.7928
	Var/ty	0.60%	4.83%/0.00%	1.61%	0.77%
	Unc/ty	2.53%	19.09%/0.00%	3.58%	3.29%
	Synthetic	1.600	0.030000	0.8017	0.8294
sphere-spheroid mix	Average	1.780	0.050000/0.050000	0.7448	0.7837
	Var/ty	0.00%	0.00%/0.00%	0.27%	0.06%
	Unc/ty	2.37%	0.00%/0.00%	1.11%	1.13%
prolate	Synthetic	1.600	0.030000	0.8044	0.8319
	Average	1.412	0.010600/0.010000	0.8870	0.9085
	Var/ty	1.36%	13.58%/0.00%	1.09%	1.04%
	Unc/ty	1.91%	30.55%/0.00%	2.56%	2.16%

Cases: (1, a-c, xi, 1%)

	Synthetic	1.400	0.100000	0.5971	0.5967
oblate	Average	1.386	0.095000/0.100000	0.5998	0.6053
	Var/ty	0.00%	0.00%/0.00%	0.14%	0.35%
	Unc/ty	2.13%	16.64%/0.00%	5.51%	6.28%
	Synthetic	1.400	0.100000	0.5965	0.5965
sphere-spheroid mix	Average	1.386	0.095000/0.100000	0.5991	0.6045
	Var/ty	0.00%	0.00%/0.00%	0.18%	0.20%
	Unc/ty	2.13%	16.64%/0.00%	5.54%	6.37%
prolate	Synthetic	1.400	0.100000	0.5971	0.5967
	Average	1.379	0.090000/0.100000	0.6094	0.6142
	Var/ty	0.00%	0.00%/0.00%	0.20%	0.63%
	Unc/ty	2.45%	23.42%/0.00%	7.25%	7.81%

Cases: (1, a-c, xiv, 1%)

	Synthetic	1.800	0.100000	0.6292	0.6631
oblate	Average	1.800	0.100000/0.100000	0.6245	0.6600
	Var/ty	0.00%	0.00%/0.00%	0.27%	0.27%
	Unc/ty	0.00%	0.00%/0.00%	0.63%	0.73%
	Synthetic	1.800	0.100000	0.6285	0.6628
sphere-spheroid mix	Average	1.800	0.100000/0.100000	0.6223	0.6582
	Var/ty	0.00%	0.00%/0.00%	0.35%	0.21%
	Unc/ty	0.00%	0.00%/0.00%	0.57%	0.66%
prolate	Synthetic	1.800	0.100000	0.6290	0.6625
	Average	1.734	0.088600/0.100000	0.6367	0.6663
	Var/ty	0.77%	3.64%/0.00%	1.86%	3.10%
	Unc/ty	7.19%	23.48%/0.00%	2.31%	3.28%

Table C.26: Table C.24 continuation (2)

Other cases

Case: (4, a, xii, 1%)

Parameters	RRI	IRI (mean/median)	SSA355	SSA532
Synthetic	1.600	0.005000	0.8525	0.8894
Average	1.600	0.005000/0.005000	0.8680	0.9045
Var/ty	0.00%	0.00%/0.00%	0.04%	0.70%
Unc/ty	0.00%	0.00%/0.00%	0.26%	0.71%

Case: (2, c, vii, 1%)

Synthetic	1.330	0.010000	0.9043	0.9276
Average	1.330	0.010000/0.010000	0.9040	0.9270
Var/ty	0.00%	0.00%/0.00%	0.03%	0.21%
Unc/ty	0.00%	0.00%/0.00%	0.23%	0.32%

Appendix D

The software tool SphInX

D.1 Understanding & running SphInX

D.1.1 Installing SphInX

Unzip SphInX.zip into *C:*. The extracted SphInX folder should consist of four folders: *Work*, *DB*, *temp* and *SphInX_source* and the pdf file *SphInX user's guide*. Copy *SphInX_source* to Matlab folder.
Run *compile* in Matlab's command line. The software is ready to use.

D.1.2 About SphInX and its main interfaces

SphInX (Spheroidal Inversion eXperiments) was created by Stefanos Samaras as an auxiliary tool for his Ph.D. work, conducted in the University of Potsdam in the framework of the European Union's Seventh Framework Programme for research, technological development and demonstration under grant agreement No 289923 - "ITaRS" (Initial Training for atmospheric Remote Sensing) during 2013-2015. This software provides a fully automated process to carry out microphysical retrievals from synthetic and real lidar data inputs and further to completely evaluate statistically the inversion outcomes. SphInX software was created to handle non-spherical particles using a generalized Mie model and considering a spheroid-particle particle approximation. The sphere-particle approach was much later added in the software for completeness and is now fully functional (version ≥ 10.5). It is created almost entirely in Matlab script language, version R2013a. Some files were initially created in Octave and C language but reimplemented and compiled in Matlab. The software package consists of 3 (main) graphical user interfaces (gui), serving different purposes:

1. The **SphInX Configurator**, where all calculation parameters for the inversion are set. E.g. size distribution characteristics (for simulation mode), loading a netcdf/text file with the optical parameters (for measurement cases), lidar setup, mathematical parameter settings (methods, splines, interval partitions), etc.

2. The **SphInX Main**, where the inversion takes place. This gui is responsible for the resulting microphysical parameters, including quick looks on size distribution. Here one can perform simultaneous runs and observe promptly *"if everything works well"*, so that one can either cancel the procedure and go back to SphInX Configurator and change the settings, or save the work and proceed to microphysical parameter analysis using *SphInX MPP*.

3. The **SphInX MPP**, where all microphysical parameters are stored in tables with error analysis, regarding accuracy, variability and randomness uncertainty. The user can either load the results, right after *SphInX main* finishes the inversion, or load previously saved work. While there is no

inversion-related calculation here, this gui is very suitable in performing error analysis, distribution comparisons and possibly search for solution patterns.

The guis 1, 2, 3 open by executing in Matlab command line *SphInX_configurator, SphInX_main* and *SphInX_mpp* respectively. While the *"normal"* running sequence is 1-2-3, all the guis can perform autonomously as well (2 and 3, however, need appropriate file loading).

This software is a unique tool for lidar-based aerosol microphysics for the following multitude of reasons.

- It is a fully automated software with a graphical user interface using both Mie- and T-matrix code, i.e. handling both spherical and non-spherical particles.

- It has a user-friendly interface and can be used both for theoretical (mathematical) and practical (physical) research answering to various levels of expertise and sophistication.

- It makes use of discretization databases minimizing essentially the time factor for massive retrievals either for simulations or multiple measurement cases. The databases are expandable and such an expansion can be used thereafter on demand.

- It has a unique presentation of the inversion products in moving sequences, thereby allowing for identification of possible systematic algorithm behaviors and a better understanding of the physical scenery.

- It makes use of the most widely used regularization methods in contemporary literature. The most recent software versions allow for an expansion also in terms of other user-made methods (alpha version).

- It is the only software providing a methodology to characterize regularization methods in terms of accuracy and stability and a full set of uncertainties vital for any practical purpose.

D.1.3 Theory & practice

SphInX is mainly based on a 2-Dimensional generalization on the Mie model, firstly presented in [129], for all available lidar setups except '3b + 2a'. The discretization of the integral equation is done with spline collocation. For the spherical case ('3b + 2a') we can achieve a stable discretization for the Fredholm integral equation in relatively little time using the well understood Mie kernel functions. On the other hand, the underline (and dominating) theory for the calculation non-spherical kernel function, called *T-matrix* theory, has overwhelming computational cost even if we reduce the non-sphericity to *"simple"* spheroids.

Indeed, a spheroid-particle approximation is accompanied with such a complexity regarding the convergence the infinite sums involved that a real-time inversion is technologically not in our reach yet. This is the reason SphInX operates with precalculated look-up tables instead of real-time calculations. This involves a discretized-kernel (optical effieciencies) database for several projection spaces, which was built using interpolation and collocation on kernel values produced by the software tool Mieschka [124]. This discretized-database is used for all lidar setups except for *3b + 2a* (spheres). Discretization in projection spaces missing from the database can also be achieved expanding the database (real calculations), see following sections for the limits of the look-up tables.

Finally, more advanced generalizations are proposed and implemented in this software treating the particle as a sphere-spheroid mixture through an additional non-sphericity parameter (asphericity), initially presented in [130]. The use of these models being part of ongoing research is not covered by this guide.

D.2   SphInX configurator

D.2.1   Modes

Before setting any parameter for the inversion one has to choose between two possible modes which are a click away in *"Mode"* tab:
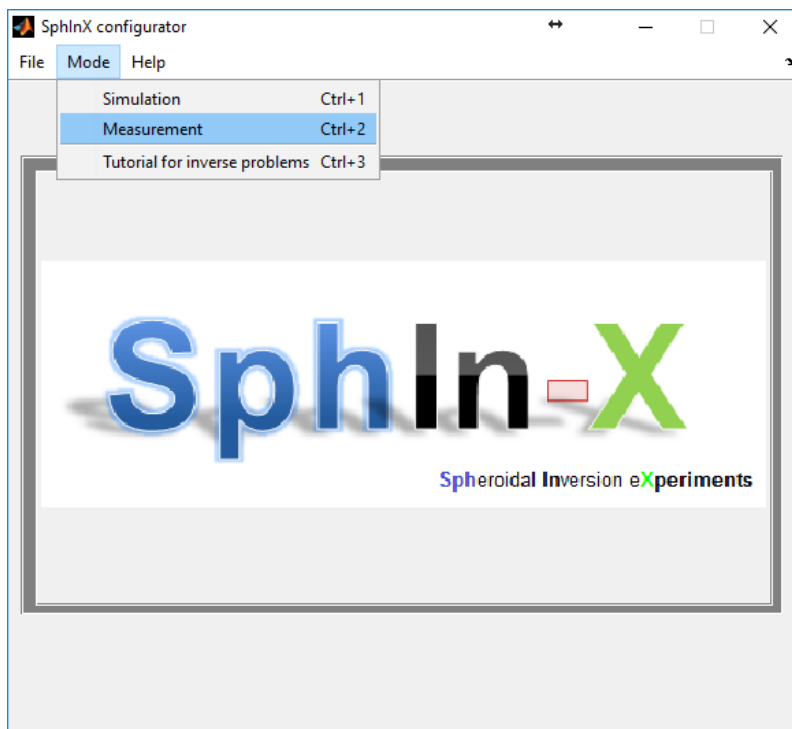
1. Simulation, and

2. Measurement.

There is one more option, named *Tutorial for inverse problems,* which is a separate software tool (*Tute*) developed for educational purposes, as a companion for introductory lectures in inverse ill-posed problems, based on [57]. For more information about Tute software, please contact Stefanos Samaras (samaras@math.uni-potsdam.de).

The scenery in modes (i), (ii) is almost the same with the following tabs:
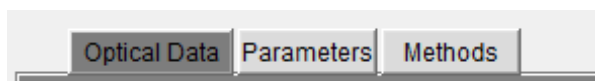
1. **Optical Data**, where the optical parameters (extinction- and backscatter coefficients) are loaded.

2. **Parameters**, where all the calculations settings take place, and

3. **Methods**, where a specific regularization technique with a parameter choice rule is to be chosen.

D.2.2   Optical Data tab.

The only difference in options between simulation- and measurement modes lies within this very tab. At first one needs to enter the lidar setup from the popup menu *Setup*; the default being *3b + 2a + 3d*. All the available are:
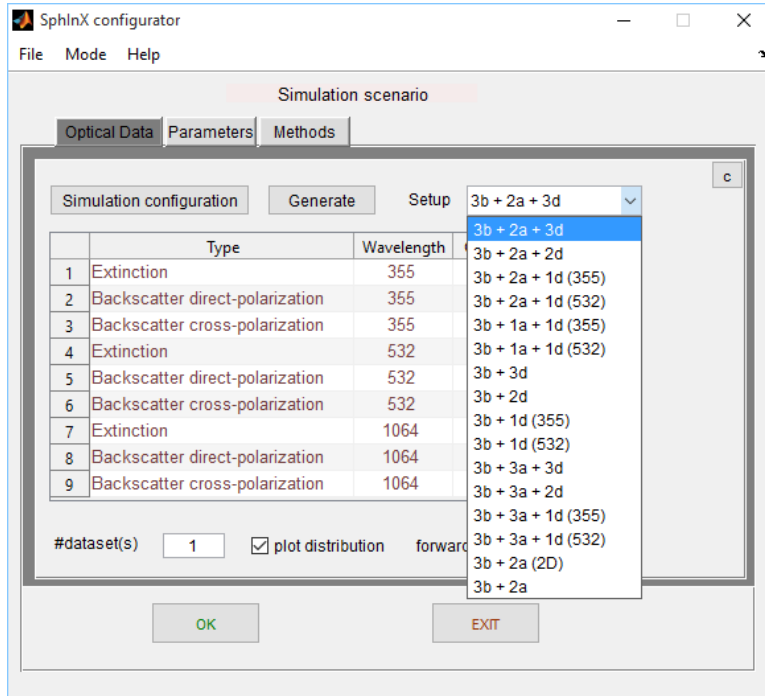
3b + 2a + 3d, 3b + 2a + 2d, 3b + 2a + 1d (355), 3b + 2a + 1d (532), 3b + 1a + 1d (355), 3b + 1a + 1d (532), 3b + 3d, 3b + 2d, 3b + 1d (355), 3b + 1d (532), 3b + 3a + 3d, 3b + 3a + 2d, 3b + 3a + 1d (355), 3b + 3a + 1d (532), 3b + 2a (2D), 3b + 2a,

where b denotes the backscatter coefficient, a the extinction coefficient and d the depolarization. Whenever the wavelength is not specified, the depolarization is meant in the wavelength order 532, 355, 1064 nm. E.g. "3d" contains depolarization in all three wavelengths, while "2d" corresponds to 532 and 355 nm. Finally the *3b + 2a (2D)* (with capital D) is the case of spherical particles but from the point of view of the 2-Dimensional generalization of the Mie-model used in the present software. Moreover the setup *3b + 2a (2D)* makes use of he kernel database of the MIESCHKA software, while "3b + 2a" runs Mie-model in real time. In addition, note that whenever a given setup misses the depolarization in one of the wavelengths, e.g. *3b +2a +2d* misses the depolarization in 1064 nm, the direct (horizontal) polarization plays (should play) the role of the total optical property. For instance, in a measurement case with the setup *3b +2a +2d*, one should fill in the field *Backscatter direct-polarization* at 1064 nm with value of the *total* backscatter in 1064 nm and leave the *Backscatter cross-polarization* blank. For a simulation scenario, this process is handled automatically by the software.
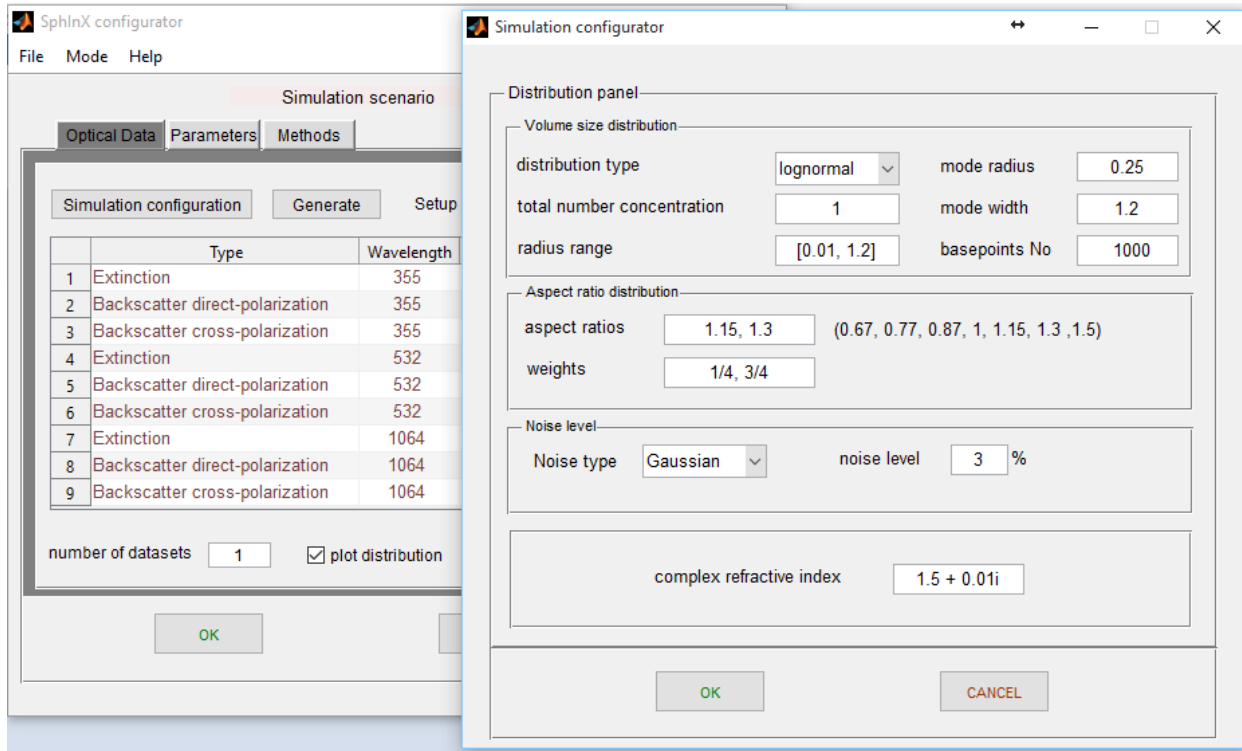
Simulation scenario

Generate optical data
For a simulation scenario one has to set complimentary a set of values, one wants to experiment with. These values pop up in the separate window *Simulation configurator* once one presses *Simulation configuration*.

In the general case the settings refer to a 2-dimensional distribution which is constructed by multiplication of two separate parts.

1. The radius-related part, where one can choose between log-normal, gamma and normal distributions with the corresponding settings for each of them, e.g. *total number concentration*, *median radius*, *mode width*, and specify the *radius range* and *basepoints No* in case of the lidar setup '3b + 2a' (spheres). For every other setup the *radius range* can either be [0.01, 1.2] (default) or [0.01, 2.2] and the *basepoints No* is fixed to the default value 1000. Any other value in both fields is ignored and goes back to the default values.

2. The aspect-ratio related part, where one can set a distribution in terms of a probability function according to the desired spheroid-particle ensemble (oblate, prolate, sphere-spheroid), e.g. the default values describe a prolate particle ensemble with aspect ratios 1.15, 1.3 with probability of occurrence 1/4 and 3/4 respectively. Note that the kernel functions in the database are only known exactly in the following aspect ratios 0.67, 0.77, 0.87, 1, 1.15, 1.3, and 1.5.

Moreover, the noise levels for the optical parameter set, being under construction, are specified in terms of the relative residual error $\|Ax - b\|_2/\|b\|_2$ (%), where A is the discretization matrix, b is the optical dataset and x is the solution vector (distribution coefficients). One can further choose between *Gaussian* and *Poisson* error type. The *true refractive index* has to be set also in this window.

Once everything is set we press *OK* and then the *generate* button to produce datasets, the number of which is specified by the edit box on the left hand side below the table. By the time SphInX finishes the calculation of the optical dataset(s), it shows by default the synthetic size distribution corresponding to the simulation settings. This can be deactivated by unchecking the check-box *plot distribution* below the optical data table.
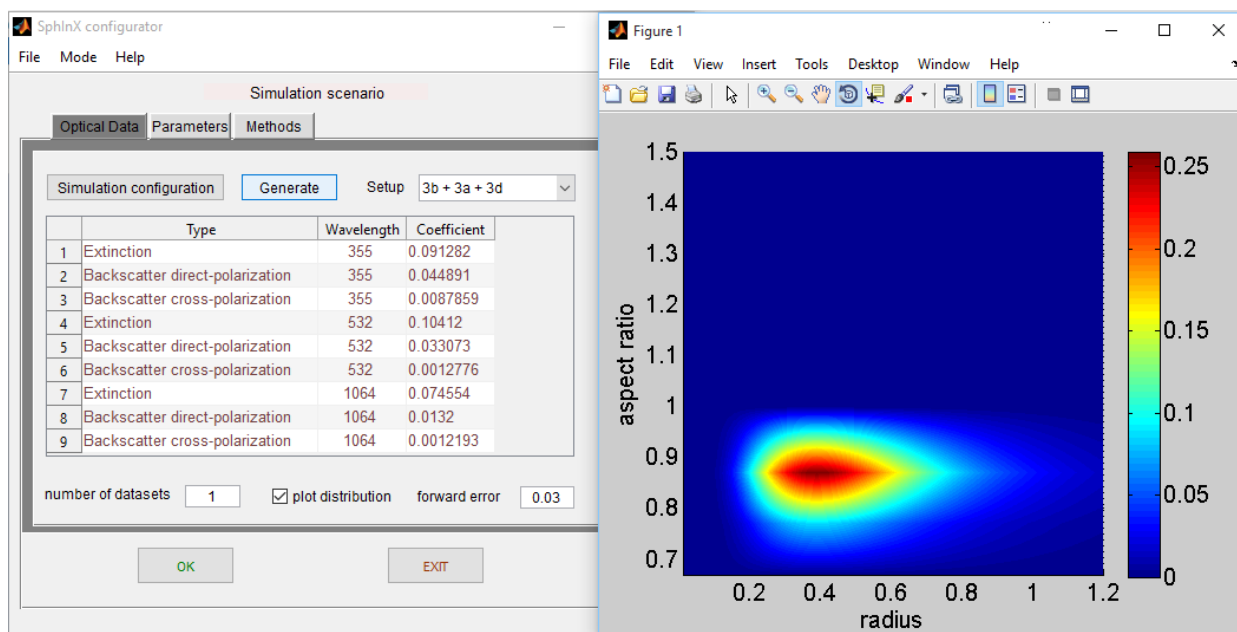
Keeping older settings

By pressing *OK* the software saves one's settings for the next time this window reopens and *CANCEL* keeps the previous setting while *X* erases them and *Simulation configurator* returns to the default ones. This gui's state information is stored in *C:\SphInX\temp*, as *sim_state.mat*.

Measurement case

Choosing to perform an inversion with real-life data comes with two options. Either one manually writes the entries in the table or one loads them from a netcdf (recommended) or an ascii file. Note that in any case in the measurement mode the lidar setup needs to be specified by the user (*Setup* popup menu) either before or after the entries are loaded in the table.

Optical profiles gui

Optical Data < Load netcdf / ascii file option opens a window-gui *Optical Profiles*, where the optical profiles can be manipulated once they are chosen by clicking *Open profiles* button. This tool can also be used independently by calling it from Matlab command line with *optical_profiles_gui.* Once the files are chosen they are plotted in the specified *Altitude range* and the *mean/median* value is automatically calculated. One can plot not only every the optical profile but also several other intensive and extensive properties (e.g. lidar ratio, Ångström exponent) using the list box *Plot profiles*. The list box notation "||" and "L" in the specification of backscatter (*bsca*) is an abbreviation for parallel and vertical polarization respectively; whenever none of these two symbols are provided, the total value is meant. The profiles are plotted in real time when the *Altitude range* is changed. The average profiles values are saved and displayed in the optical data table in the configurator gui by pressing *OK* (*Cancel* or *X* provide no change).
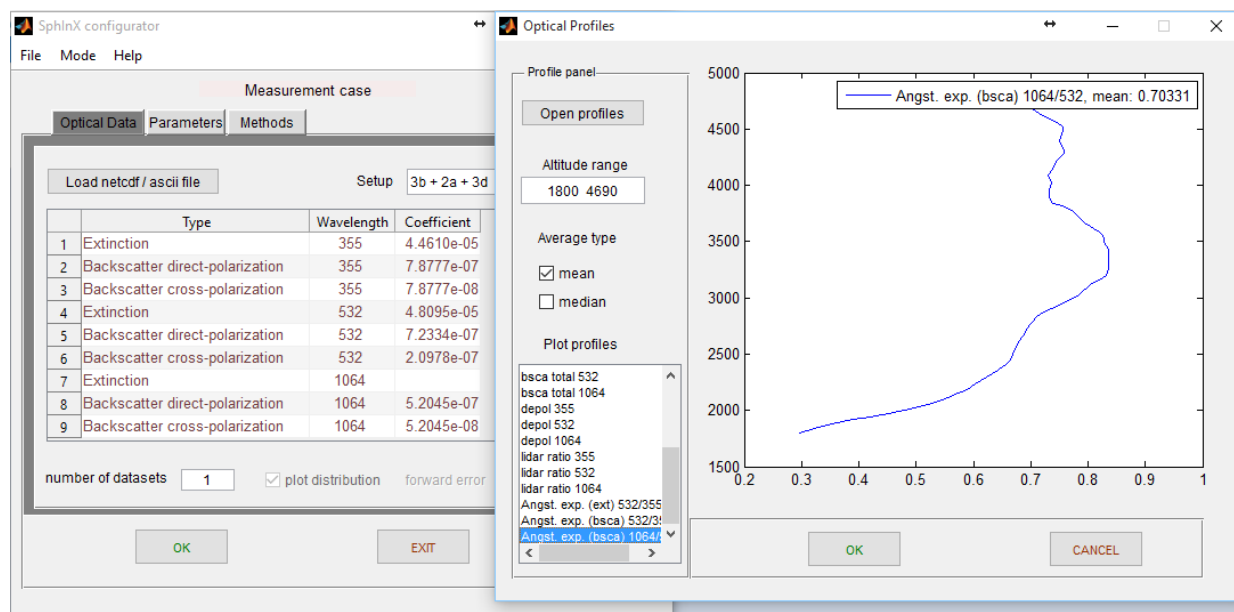
Regarding the file type two options are available: *netcdf* and *ascii.*

1. In the case of netcdf files, all the files needed for the inversion (e.g. .e355, .e532 and .b1064) must be loaded simultaneously. Single files can also be loaded for profile inspection but they overwrite any previously loaded profile.

2. Loading optical data from an ascii file comes with two basic rules that the files should take on:

   (a) all profiles should be given as columns in a single file,

   (b) above the columns there should be equal amount of identifiers (labels) of the columns, which should at least contain the following *non-case-sensitive* string characters: *"alt", "ext", "alpha", "bsca", "beta", "depol"* **and**, *"355", "532", "1064". "alt"* stands for the altitude range, *"ext"* and *"alpha"* refer to extinction coefficients, *"bsca"* and *"beta"* refer to backscatter coefficients and *"depol"* refers to depolarization. The order of the columns can be arbitrarily chosen. Here is a sample file structure:

```
alt            ext355        bsca355       ext532        bsca532       bsca1064      dep532
1.2020000e+03  1.6709000e-04 3.5020000e-06 9.4705000e-05 1.7894000e-06 8.9413000e-07 1.0000000e-01
1.2620000e+03  1.4393000e-04 3.6206000e-06 1.0408000e-04 1.8621000e-06 9.1262000e-07 1.0000000e-01
1.3220000e+03  1.3060000e-04 3.6446000e-06 8.9932000e-05 1.9351000e-06 9.4688000e-07 1.0000000e-01
1.3820000e+03  1.3986000e-04 3.7762000e-06 8.5098000e-05 2.0473000e-06 9.6950000e-07 1.0000000e-01
1.4420000e+03  1.2246000e-04 4.0041000e-06 8.6827000e-05 2.1637000e-06 1.0267000e-06 1.0000000e-01
1.5020000e+03  1.2874000e-04 4.0105000e-06 7.5035000e-05 2.1228000e-06 1.0710000e-06 1.0000000e-01
1.5620000e+03  1.1546000e-04 3.6338000e-06 7.0883000e-05 1.9032000e-06 1.0053000e-06 1.0000000e-01
1.6220000e+03  1.0434000e-04 3.2345000e-06 7.3703000e-05 1.6723000e-06 8.6189000e-07 1.0000000e-01
1.6820000e+03  9.5662000e-05 2.8848000e-06 6.5058000e-05 1.4405000e-06 7.3412000e-07 1.0000000e-01
1.7420000e+03  9.3636000e-05 2.7897000e-06 5.6014000e-05 1.3364000e-06 6.4962000e-07 1.0000000e-01
1.8020000e+03  1.0161000e-04 2.6582000e-06 5.0750000e-05 1.2277000e-06 5.8139000e-07 1.0000000e-01
1.8620000e+03  1.0657000e-04 2.5531000e-06 4.6173000e-05 1.0898000e-06 5.2206000e-07 1.0000000e-01
1.9220000e+03  9.8961000e-05 2.4929000e-06 5.2524000e-05 9.8843000e-07 4.5944000e-07 1.0000000e-01
1.9820000e+03  8.5036000e-05 2.4119000e-06 4.3354000e-05 9.3066000e-07 4.2290000e-07 1.0000000e-01
2.0420000e+03  7.6673000e-05 2.2002000e-06 3.9785000e-05 8.9643000e-07 4.0438000e-07 1.0000000e-01
2.1020000e+03  5.8816000e-05 2.0922000e-06 4.3596000e-05 8.3960000e-07 3.7920000e-07 1.0000000e-01
2.1620000e+03  7.3956000e-05 1.9864000e-06 3.8592000e-05 8.5958000e-07 3.6368000e-07 1.0000000e-01
2.2220000e+03  6.8475000e-05 2.1284000e-06 3.7351000e-05 9.4124000e-07 3.7574000e-07 1.0000000e-01
2.2820000e+03  7.5999000e-05 2.4693000e-06 4.4275000e-05 1.0857000e-06 4.1915000e-07 1.0000000e-01
2.3420000e+03  8.8345000e-05 2.5971000e-06 4.3842000e-05 1.1881000e-06 4.7826000e-07 1.0000000e-01
2.4020000e+03  9.0353000e-05 2.4212000e-06 4.7604000e-05 1.1339000e-06 5.0607000e-07 1.0000000e-01
2.4620000e+03  9.4728000e-05 2.3353000e-06 4.9875000e-05 1.0041000e-06 4.7243000e-07 1.0000000e-01
2.5220000e+03  9.2414000e-05 2.3313000e-06 5.1376000e-05 1.0979000e-06 4.2196000e-07 1.0000000e-01
2.5820000e+03  9.0590000e-05 2.5568000e-06 4.0645000e-05 1.1454000e-06 4.7406000e-07 1.0000000e-01
2.6420000e+03  8.4135000e-05 2.2517000e-06 3.4755000e-05 9.3246000e-07 4.4046000e-07 1.0000000e-01
```

The units for altitude must be given in km and all the rest in SI units.

D.2.3 Parameters
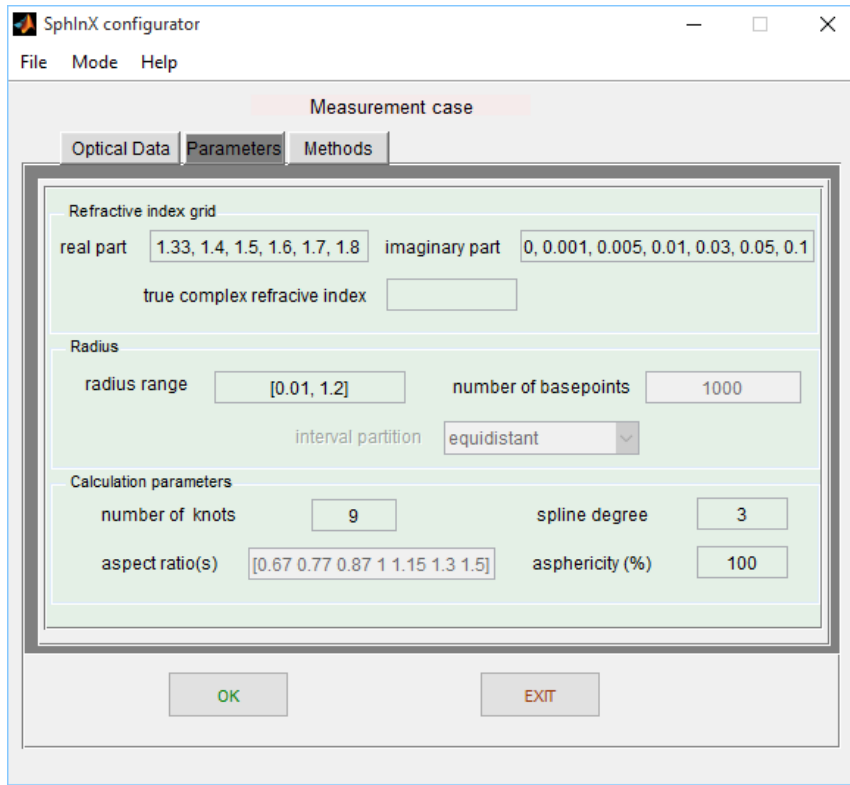
This tab contains all the parameters needed mainly for the discretization and the regularization. These involve:

1. The *Refractive index* (RI) *grid*, which should be given in separate real and imaginary parts. Note that MIESCHKA kernel database allows only for the following values:

Real part of RI: 1.33, 1.4, 1.5, 1.6, 1.7 and 1.8 and the Imaginary part of RI: 0, 0.001, 0.005, 0.01, 0.03, 0.05 and 0.1, which are also the default values.

For the spherical case, the user is free to choose a finer RI grid specifying the *steps*, in which case the fields *real part* and *imaginary part* should admit a range, e.g. [1.33, 1.8], [0, 0.1]. If the *steps* edit-boxes remain empty the software considers only the values used in the fields *real part* and *imaginary part.* If *steps* edit-box is filled and any of the fields *real part* and *imaginary part* have more than two values (not a range), then the software chooses automatically the minimum and maximum parts of the refractive index as the range.

Furthermore, note that the field *true refractive index*, does not have to be filled when in *Simulation* mode, as it is automatically updated once *generate* button is triggered.

The *Radius* panel. The *radius range should* given in µm. The field *number of basepoints* and the popup-menu *interval partition* are available to the user only in the spherical case (lidar setup '3b + 2a'). In this case, there are four choices for the node grid:

1. equidistant,

2. Chebyshef [-1,0],

3. Chebyshef [-1,1], and

4. Chebyshef [0,1].

The options 2,3, and 4 refer to a non-equidistant partition with Chebyshef polynomial roots as the nodes in the designated range.

Note that the *radius range* and the *number of basepoints* do not need to be filled for *Simulation* mode since they are automatically updated by the *generate* button; at the same time there should be an agreement between these fields and ones in *simulation configurator.*

1. The *Calculation parameters* panel. The discretized kernel database (spheroids) has the following ranges: number of knots: 3 up to 20 and spline degree: 2 up to 6. Here, the *number of knots* (s), the *spline degree* (d) and the spline number (n) fulfil the relation $n=s+d-1$.

If the software reads a value beyond the extent of the precalculated database (e.g. *s=21*) it performs the discretization of the new projected space on site and saves the work also for future calls. In the spherical case the whole regularization is performed in real time and there is no software limitation for these parameters.
*** There are two more options in this panel:

1. The predefined aspect ratio values for which the discretization is performed, is only included for possible future use. At this point it is out of reach for two reasons. First, the kernel database is not available beyond the aforementioned values and second, even if it was, one needs to recreate the discretized kernel database from scratch for any new aspect ratio value.

2. *aphericity* percentage option. This is an experimental feature refering to a preferred separation of spherical and non-spherical part of the size distribution or the optical data. As part of ongoing research, this feature exceeds the scope of the present guide.

D.2.4 Methods

The user can choose from the popup-menu among the following regularization methods combined with a parameter choice rule:

1. Truncated Singular Value Decomposition & Discrepancy Principle (TSVD-DP),

2. Tikhonov method& L-Curve method (Tikh-LC),

3. Padé iteration & Discrepancy principle (Pade-DP),

4. Tikhonov method & Generalized Cross Validation (Tikh-GCV),

5. Tikhonov method & Discrepancy Principle (Tikh-DP),

6. Padé iteration & L-Curve method (Pade-LC),
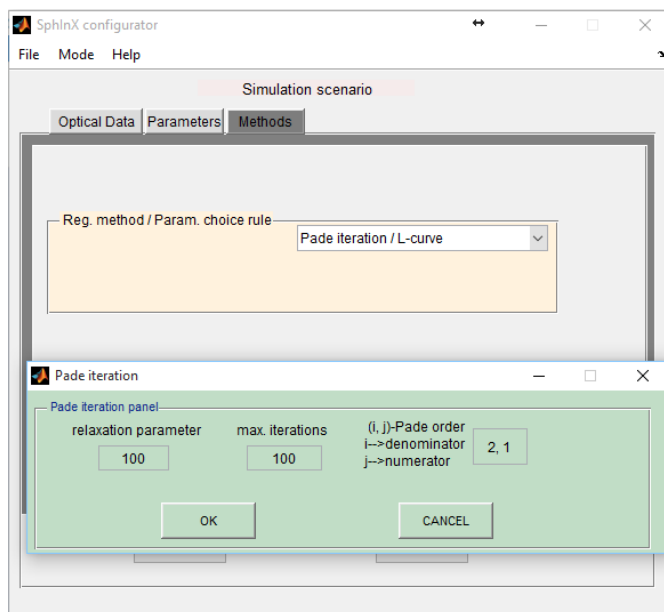
and fill in the fields associated with each one accordingly. Especially for methods 3. and 6. another window gui (*Pade iteration*) pops up with more options about Padé iteration; previous settings are saved the same way as in *Simulation configurator.*

D.2.5 Proceed to the inversion

SphInX configurator admits all the configuration settings given in all three tabs (*Optical Data, Parameters, and Methods*) with *OK* button which automatically opens regularization gui *SphInX main* to perform the inversion.

The configuration data can be saved as a *.mat* file with *File < Save data* (after the *OK* button is hit) which opens a modal dialogue box asking the user for a name for the file. As we will see later on, there is a more complete option for this action in *SphInX main*, see the corresponding section for detailed description. Therefore the latter option is only useful when one intends to save the configuration for later use. Such configuration files (identified as *config_data* files) and also later on the files associated with the solution grid (identified as *sol_grid* files) and the final regularization products (identified as *reg_data* files) can be loaded in SphInX configurator.

D.3 SphInX main

D.3.1 Split inversion & checkpoints

By "full inversion" is meant here the final retrieval outcome (microphysical parameters) using the least residual reconstructed size distributions.

One of the efficiencies of *SphInX main* is the ability to separate the inversion in two stages:

1. Calculation of the solution, which is really the coefficients of the approximation of the solution from the spline collocation.

2. Calculation of the size distribution and the microphysical parameters.
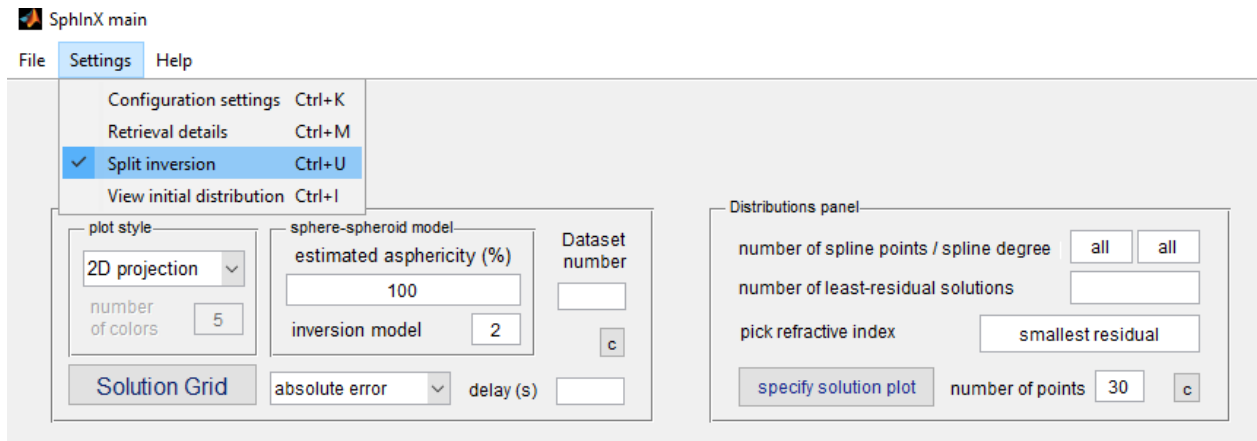
By default the inversion is not split, but rather the software performs (1) and then (2). On demand the inversion can be stopped, saved and used another time from the point it was left using *File < Split inversion.* This feature is possible only for multiple error-runs.

Generally, the inversion process (triggered by the *Solution Grid* button) can be stopped at any time. Keep in mind that this action might take some time for huge runs (many different numbers of spline points and spline degrees).

Plot settings
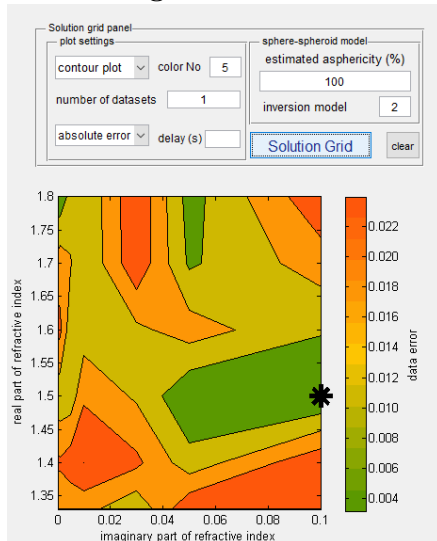
This panel allows the user to choose plot style either as a *2D projection* or a *contour plot* of the refractive index grid with respect to either the *absolute error* or the *relative error*.

Delay
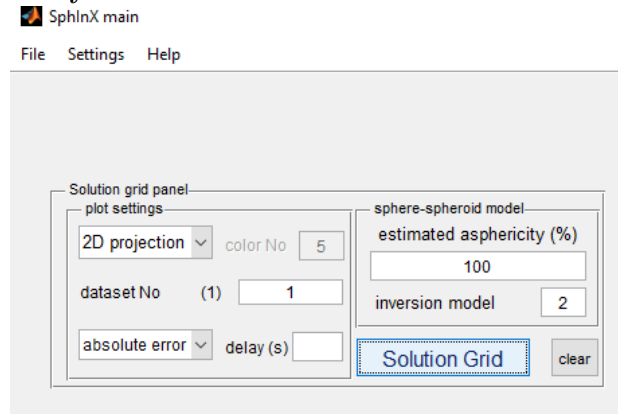
This feature controls how fast will be the change between figures of the solution grid and/or the size distributions and the table-data. Since *SphInX main* specializes in investigating closely the solution space and seeking patterns and the visual data change might occasionally be too rapid for inspection, *Delay* option given in seconds can offer a pause between subsequent datasets.

D.3.2 Save data
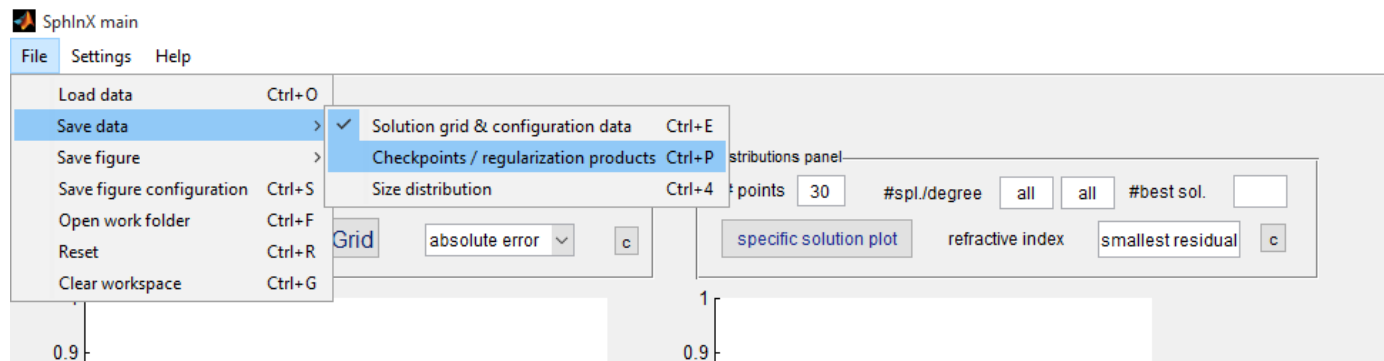
Saving data in *SphInX main* has two aspects:

The option File < save data < Solution grid & configuration data
This option has a double use.

(i) If there exists a checkmark, once the *Solution Grid* button is pressed, the configuration settings (from SphInX configurator) along with the produced solution space are automatically saved and stored after each error-run (different datasets) in a folder within the *Work* folder. The inverted data include only the solution grid (not the final regularization products), i.e. all the spline coefficients (numbers related to the spline basis) for the whole refractive index grid, all the numbers of spline points and spline degrees and all error-runs (in case of a simulation). The automatically generated folder contains a *.mat* file with the solution grid data and an ascii file of the same name with the configuration used to produce the latter. The folder and the files in it are named after some minimum quickly-recognizable details.

For the *Simulation* mode

Folder name:

'method'_'median_radius'_'mode_width'_'radius'_'error level'_'lidar

setup'_'leftmost aspect ratio value', e.g. TSVD-DP_0.5_1.2_rad.1.2_3%_3b + 2a_1.15.

For the *Measurement* mode

Folder name:

method'_'radius'_'lidar setup'_'asphericity', e.g. Pade-LC_rad.1.2_3b + 2a_asph.100.

For both modes the *.mat* and ascii files appear with same name according to the scheme:

date: DD-MM-YY-HH-MM-SS'_sol_grid_'method_datasetNo'',

e.g. 07-Feb-2015-15-41-32_sol.grid_TSVD-DP_2 (the number 2 means that there are at least two datasets). For instance, for 3 error-runs, the generated folder should have 3 *.mat* + 3 ascii files. As long as there is no folder named *exactly* like this, a new folder is created, otherwise the saved files are appended to the existent folder.

(ii) The user can always save the configuration data before or after the inversion for later use.

This action opens a modal dialog box and the user is asked to give a name for the configuration files (*.mat* and ascii) that will be saved. Apart from the fact that there are no solutions involved here, the difference with (i) is that the configuration files concern the run as a whole, as it was ordered by SphInX configurator while in (ii) the run is separated in partial runs for individual use if desired.

The option File < save data < Checkpoints / regularization products
This option has a double use.

(i) If an inversion for multiple datasets is initiated and stopped by the user pressing the same button (*Solution Grid*), *SphInX main* creates automatically a checkpoint. If the window remains open, the inversion will continue from where it was left by pressing *Solution Grid*. If not, one can still save the work before closing *SphInX main* with *File < save data < Checkpoints / regularization products* and run the rest when reopened. Moreover if a run has already been made, by pressing *Solution grid* again, the button's name turns to *"inverted"* and the software display again the solution grid plot(s) without recalculating. Nevertheless, if desired, one can reproduce the run by clearing the workspace with *File < Clear workspace.* The different dataset-runs do not have to be done in a row (default), but rather specified by the user through the *dataset No* edit-box, e.g. for 5 datasets one can run only 1, 4 and 5. The checkpoint-logic still applies here for the rest datasets of the incomplete run (2 and 3 in the previous example). In addition, if an incomplete run is loaded, the software informs the user about the datasets which are not inverted yet in the edit-box *dataset No*.

(ii) It opens a modal dialog box (similar to previous option) and saves the size distributions and the final regularization products, i.e. the microphysical parameters. This option is perhaps the most important in SphInX because it saves everything that the inversion produced. In addition, it includes the configuration and the solution grid.

Save gui figures
File < Save figure has three options:

1. Save solution grid figures with *File < Save figure < Solution grid*,

2. Save (size) distribution figures with *F*ile < Save figure < Size distribution and

3. Save a snapshot of the window with *File < Save figure < Window figure.*

The options (i) and (ii), once activated, they save *all* instances of the solution grid and the size distribution that are currently being plotted as *.png* figures. The user is asked to give a name for the folder where the figure is to be saved and the with the following name format:
'refractive index'_'asphericity'_'error'_'splinepoint_No'_'spline_degree',
e.g. 1.5+0.01i_100_0.080782_9_2.

The plot is saved with a title with similar name for a quick identification.

Note that these options (i, ii) are complementary, meaning that once a folder is chosen for one of them, any figure in *SphInX main* will be saved in the same folder if not respecified. E.g. if one ordered distribution figures in a folder named *"Folder 1"* then any plot of the solution grid will also be saved in *Folder 1* without further notice (unless one chooses too).

***This feature is deactivated either by resetting *SphInX main* or by using *File < clear workspace* (both of which erase the solution grid and regularization products).

The option (iii) saves a snapshot of the current workspace window as a *.png* figure to the user-specified folder.

D.3.3 The microphysical retrieval

Specify retrieval data

If the user does *not* change the default setting of *not* splitting the inversion, the software proceeds in calculating (and ploting) the size distributions and the microphysical parameters of the least residual solutions for each dataset and each spline setup which are shown one by one as a movie. Retrieval data that refer to a random solution (not least residual) are not automatically calculated, but can be shown on demand too, see the following section (*specify solution plot* button) for more details. The retrieved microphysical parameters, either for least-residual- or random solutions, are shown in the parameter table under the column *Retrieved*, once the associated size distribution is plotted. In addition, if running a simulation scenario, the column *Synthetic* is updated too, corresponding to the microphysical parameters calculated using the initial distribution for comparison.

Perform a preliminary analysis

After *at least* a split inversion has been fulfilled one can perform a first data analysis by pressing *specify solution plot* button. This can be done in two ways:

1. *Smallest residual* solutions. If the edit-box *pick refractive index* is filled with *smallest residual* or *sr* then one can see single solutions or several solutions in a motion updating the microphysical parameter table accordingly. The specification of the displayed solutions is done *either* through the boxes

   - *number of spline points / spline degree*, where the user specifies a range of the associated field, e.g. 9:14, 2:5, or

   - through the box *number of least residual solutions*, where the associated number of "best" solutions are plotted for each datasets.

2. Random solutions. In this case the user has to specify for which refractive index, the software should calculate the microphysical parameters and plot the size distribution. This can be done in two ways:

   - as an entry in the *pick refractive index* edit-box, inserted manually by the user or

   - by leaving empty the edit-box *pick refractive index* and selecting (with the mouse) the desired refractive index directly from the solution-grid plot. User's selection will appear in the edit-box *pick refractive index*.

In case the given refractive index is not part of the solution grid (specified by the user in SphInX configurator) the software returns the solution for the closest existing one.

The initial distribution can be shown at any time in the size-distribution axis with *Settings < View initial distribution*. In case the axis is already occupied by a retrieved size distribution, the axis is held for comparison.

A thorough analysis including errors can be done using the *SphInX MPP* gui which is activated by *Show details* button.

D.3.4 Save size distributions

The size distributions can be saved in an ascii file with *File < Save data < Size distribution.* Once activated the distribution data continue to be saved and appended to same ascii file until it is deactivated the same way. A modal dialogue box asks the user for a folder name, which will be placed in *Work* folder and in which the size distribution is going to be saved in an automatically generated folder *size distributions* with the following name format:
'date'_'size_dist'_'method', e.g. *23-Feb-2015-12-20-15_size_dist._TSVD-DP.*
The distribution data, which are to be saved, are ordered in the same way we specify the solutions and they are finally saved once we hit *specify solution plot.*
The ascii files contain:

1. information as to which size distribution is picked for saving with a header including *refractive index, spline points No, spline degree, dataset No,* and *error, e.g.*

% size distribution ||refractive index: 1.5+0.1i ||spline points No.: 9 ||spline degree: 3 ||dataset No.: 1 ||error: 0.0031733

1. (a) two column vectors next to each other, for the spherical case, the first being the radius range *r* and the second being the size distribution *v(r).*

(b) two column vectors and a matrix next to each other, for the non-spherical case, corresponding to the radius range *r*, the aspect ratio range *a* and the size distribution *v(r,a)* respectively.
New distribution data are appended to the same file below older ones, unless the user chooses a different folder name.

D.4 SphInX MPP

SphInX MPP 22-Sep-2015-00-15-59_reg_data_tgcv_bimodalR_1.5+0.005i_1%.mat

File Settings Help

Solution Controller

dataset No (15) 1:15   spline points No / spline degree (9) [all] [all] (4)

refractive index [smallest residual]   loaded file index [1]

best solution No [6]   error type [relative error ▾] less / equal [0.1]

method [Tikh-GCV ▾]   lidar setup: [3b + 2a + 3d ▾] mode: Simulation

initial size distribution   retrieved size distribution

distribution uncertainty (%) [3.6165]   mean difference (%) [69.1213]

[c] [Retrieve parameters]

	number concentration	surface-area concentration	volume concentration	oblate vol. concentration	spherical vol. concentration	prolate vol. concentration	effective radius	effective aspect ratio	aspect ratio width	refractive index	single scattering albedo 355 / 532	non-sphericity (%)	error	#spl. / degr
Synthetic values	134.3139	14.9043	2.8883	0.012562	0.55779	0.43189	0.58137	1.0832	0.008721	1.5+0.005i	0.9158 0.92965	100	0.12915	
Average values	175.2544	16.0102	3.0459	0.22218	0.41809	0.35981	0.57088	1.0448	0.030799	1.5+0.005i	0.91332 0.9283	100	0.034718	10 / 3
Deviation	9.3931	0.27866	0.052262	0.0077553	0.015533	0.022082	0.0091948	0.0089853	0.0017011	0	0.0018011 0.00049323	0	0.012015	
Variability (%)	4.1305	1.2158	0.51556	1.0277	1.0804	1.3369	1.0923	0.2314	2.6477	0	0.21242 0.031938	0	7.4323	
Difference (%)	30.4812	7.4198	5.4542	1668.6655	25.045	16.6901	1.8053	3.5501	253.1618	0	0.0027168 0.0014451	0		
Uncertainty (%)	5.3597	1.7405	1.7158	3.4905	3.7153	6.1372	1.6106	0.86002	5.5232	0	0.19721 0.053133	0	34.6075	

	number concentration	surface-area concentration	volume concentration	oblate vol. conc. frac.	spherical vol. conc. frac.	prolate vol. conc. frac	effective radius	effective aspect ratio	aspect ratio width	refractive index	single scattering albedo 355 / 532	non-asphericity (%)	error	#spl. / degree
Retrieved values (1)	164.6927	15.7621	3.0387	0.21353	0.40706	0.37925	0.57846	1.0538	0.032378	1.5+0.005i	0.91053 0.9	100	0.031758	10 / 4
Retrieved values (2)	171.7293	15.7984	2.9983	0.23125	0.42807	0.34037	0.56936	1.0348	0.028871	1.5+0.005i	0.91424 0.9	100	0.025074	13 / 3
Retrieved values (3)	174.4799	15.9906	3.0769	0.2133	0.40559	0.38089	0.57727	1.0535	0.032241	1.5+0.005i	0.91326 0.9	100	0.038221	9 / 3
Retrieved values (4)	183.1613	16.3919	3.1014	0.22347	0.42885	0.34769	0.56773	1.039	0.029559	1.5+0.005i	0.91415 0.9	100	0.056623	10 / 3
Retrieved values (5)	187.6652	16.4954	3.0905	0.22429	0.40269	0.37278	0.56209	1.0491	0.032604	1.5+0.005i	0.91403 0.9	100	0.040359	13 / 2
Retrieved values (6)	178.7671	16.0542	3.0377	0.2264	0.43135	0.34235	0.56774	1.0382	0.029538	1.5+0.005i	0.91442 0.9	100	0.041459	11 / 3
Retrieved values (7)	177.2143	15.9615	3.0182	0.23137	0.42175	0.34703	0.56729	1.0392	0.030748	1.5+0.005i	0.91392 0.9	100	0.018459	13 / 2
Retrieved values (8)	184.1011	16.3763	3.0939	0.22254	0.42529	0.35456	0.5669	1.0453	0.030328	1.5+0.005i	0.91379 0.9	100	0.053667	10 / 3

D.4.1 General overview

SphInX MPP is a gui responsible for a detailed presentation and a statistical analysis of the solutions. This guigroups solutions and calculates averages to test the credibility of the results, but does not make

any microphysical calculations. This gui operates with a single button *Retrieve parameters* once the user-specified fields (*Solution Controller panel*) and preferences are set. There are two ways to load data in *SphInX MPP*:

1. open *SphInX MPP* with the button *Show details* right after completing an inversion with *SphInX main* (or after loading data to *SphInX main*), or

2. directly load regularization data to *SphInX MPP* with *File < Load results*

Solution Controller is a panel similar to the one in *SphInX main* (containing *specify solution plot*) but wealthier in possibilities; the user controls which results to be shown, both regarding the size distribution and the microphysical parameters. The user specifies the exact dataset (*dataset No*), the discretization space (*spline points No / spline degree*) and the *refractive index* for the size distribution (right graph) and the microphysical parameters (tables below) to be shown. The *refractive index* edit-box should in principle contain the retrieved refractive index from the minimization procedure, i.e. the entry should be either *smallest residual* or sr, or the correspondig least-residual complex numeric value. If random (non-least-residual) solutions were calculted in using *SphInX main* gui then user can use the corresponding refractive indices too.

Once *Retrieve parameters* is pressedthe requested microphysical parameters appear in detail in the lower table and the size distribution are plotted in the right axis. In case of a simulation the initial microphysical parameters (upper table) and the initial size distribution (left) are shown for comparison. The minimum error-related quantity is the relative difference between the retrieved and the initial values, represents a measure of accuracy and goes by the name *Difference (%)* in the upper table.

If more than one entry is given in *dataset No and / or spline points No / spline degree SphInX MPP* responds with averages discussed in following sections. Averages appears in two flavors using *Settings < Average type* either as the *mean* or the *median* value.
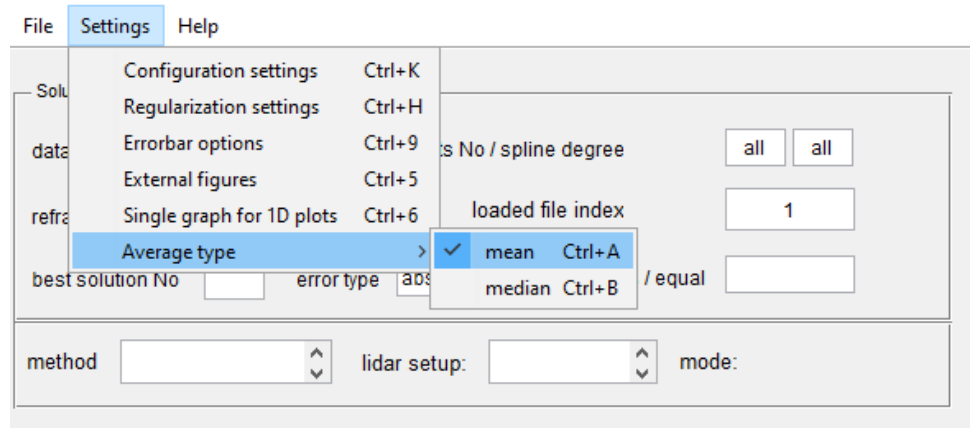
In case of the *mean* the *Deviation* parameter appearing in the upper table is the usual standard deviation, while in the case of the median, *Deviation* is the median absolute deviation of the values from the median value. Generally, the upper table contains the statistics, while the lower table includes details about the solution involved.

D.4.2   Single dataset & multiple discretization spaces

This section concerns the case where we have a single dataset and multiple entries in either of the *spline points No / spline degree* edit-boxes. If so, the lower table shows all the ordered solutions, e.g. if we have 5 entries for the spline points number and 3 for the spline degree, 20 solutions should be shown in total. The upper table shows additionally the average value and the deviation of the parameters from the lower table. Moreover the *Variability (%)* of the solutions is shown as the quotient of the deviation to the average value. In the case of a simulation scenario *Difference (%)* is the relative difference between the average and the initial values. The retrieved size distribution shown corresponds to the average (*mean* or *median*) value of the size distributions involved.

D.4.3 Multiple datasets

For simulation scenarios, this section makes sense for the use of different datasets produced by random error generator (e.g. gaussian) with the same error level. For a measurement case, the datasets could be different in any possible way physically (e.g. different time, place, altitude of measurements etc.) but they all have to correspond to the same lidar setup. This section further refers to the case of multiple datasets with or without multiple entries in *spline points No / spline degree* edit-boxes; the user specifies the indices of the desired datasets, e.g. 3, 5, 10. A hit in the button *Retrieve parameters* calculates the average values and the associated *Deviation*, *Variability (%)* and *Difference (%) for each dataset* and the subsequently finds the averages among these values to calculate the *Uncertainty (%)* among the different datasets. Since the epicenter here is the averages between the datesets, the lower table contains as many sets of microphysical values (table rows) as the amount of datasets (in our example 3) i.e. the average values for each dataset, while the displayed *Average values, Deviation, Variability (%)* and *Difference (%)* refer to the average of the latter values among all the involved datasets. Finally, the additional parameter *Uncertainty (%)* is found by taking the quotient of the deviation to the average value (similar to *Variability (%)* but applied to the average values from each dataset).

The values *Variability (%), Difference (%) and Uncertainty (%)*, are summarized by default (it can be deactivated) in a graph popping up right after the calculations in a separate window, where the x-axis contains the microphysical parameter names and the y-axis contains their values. There are also errorbars in this graph depicting the *Uncertainty (%)*. This option will be explored further in the following section in the case of multiple files where it becomes a necessity.

D.4.4 Multiple files

This section excausts the operation range of *SphInX MPP* and makes full exploitation of its capability. Note that this section makes sense only for simulation scenarios with multiple datasets.

Loading files

SphInX MPP allows the user to load multiple files for a comparison between different methods or error levels. All the files have to be loaded at once using *File < Load results*. *SphInX MPP* detects and shows in the info-panel below the panel *Solution Controller* which are the methods involved and reveals the sequence in which the files are loaded (file index) so that one can restrict only to some of them if desired using the edit-box *loaded file index*. For instance, loading 6 files (which currently the maximum amount of different methods), if the method edit-box reveals the following method sequence *TSVD-DP, Tikh-GCV, Tikh-DP, Pade-DP, Tikh-LC, Pade-LC*, then by entering *2, 6* in the edit box *loaded file index*, we pick only 2 of the files and specifically those with *Tikh-GCV* and *Pade-LC*. We can get back to choosing all files (default) or any other sequence of indices without reloading the files. The edit-box *loaded file index* is set to *1* in case we load only one file.

Giving only single entries in the edit-box *loaded file index* has the same use as discussed in the previous sections with multiple discretization spaces and / or multiple datasets, only now we specify the method too through the file index.

Solution Controller has a similar but wealthier functionality than than *Distributions panel* in *SphInX main* regarding the ways to handles "best" (least-residual) solutions. The desired number of "best" solutions is entered through the field *best solution No*. If the latter is non-empty, then the corresponding amount of solutions are shown in the lower table with ascending-error order from top to bottom with respect to the error-type specified by the popupmenu *error type*. The user can also order a maximum error tolerance above which the solutions are inadmissible, by editting the field *less / equal* again with respect to the *error type*. All previous options are also available in the case of multiple files and / or multiple datasets and / or multiple projection spaces (spline points number and spline degree). In case the amount of best solutions specified is larger than the one of the solutions existing (given or not an error tolerance) the software returns the maximum number of solutions fulfilling the setting if it is more than zero, otherwise one should keep loosen up the error constraint.

D.4.5 Errorbar settings

Multiple entries in the edit-box *loaded file index combined* with multiple dataset entries results in a graph in a separate window, where the x-axis contains the microphysical parameter names and the

y-axis contains their values and where each dashed line represents a different method (explained by a legend). Each point in this graph has also an errobar representing *Uncertainty (%)*. The values *Variability (%), Difference (%) and Uncertainty (%)* (abbrev. *VDU %*) are shown from top to bottom after being calculated for each file. The methods and the error levels which make it to the graph near these values are the one with the lowest (%) values. E.g. t let us focus on the values above the parameter *vt* in the figure below:

Pade-DP, 0.68%
Pade-DP, 5.24%
Tikh-LC, 0.79%,

This means that among the 3 methods in the legend of this graph, Pade-DP has the smallest *Variability* with *0.68%,* the smallest *Difference* with *5.24 %* and Tikh-LC has the smallest *Uncertainty with 0.79%* regarding the parameter vt (prolate volume concentration fraction). Furthermore, the title of this graph informs the user which is the best method regarding accuracy (*1-Difference*) and overall (VDU %) counting the freqeuncy of appearance of every method for all displayed parameters.
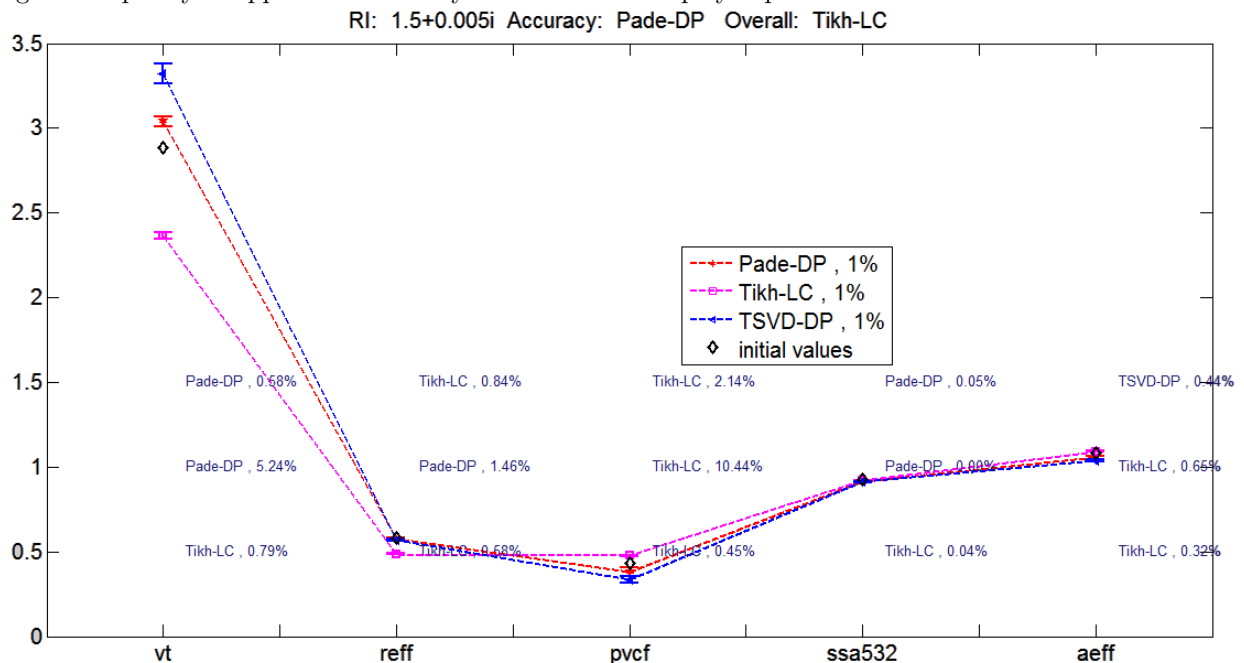
There are a few settings regarding the parameters displayed and the appearance of the graph which are available under *File < Errorbar*. This action opens *Errorbar display* gui with the following options:
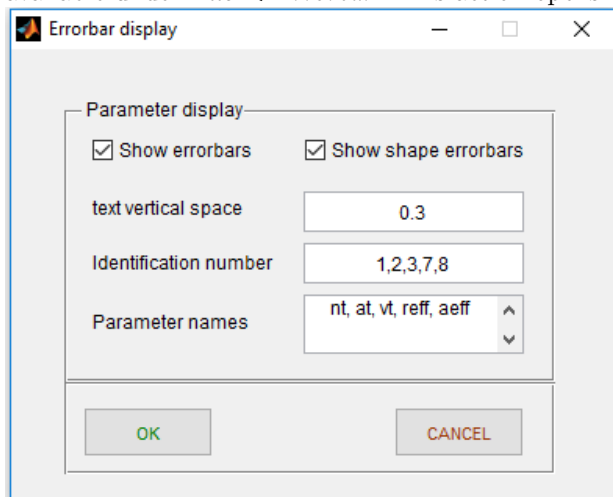
1. Show errorbars. The graph described before is shown *only* if this check-box is checked (default). If unchecked, the option *Show shape errorbars* turns to unchecked too.

2. Show shape errorbars. Although any of the parameters from the table, number concentration (nt), surface-area concetration (at), volume concentration (vt), oblate volume concentration fraction (ovcf), spherical volume concentration fraction (svcf), prolate volume concentration fraction (pvcf), effective radius (reff), effective aspect ratio (aeff), aspect ratio width (avar), refractive index (ri), single scaterring albedo 355 / 532 (ssa) and non-sphericity can be displayed one can check this box in order to create a separate graph for the shape-related parameters ovcf, svcf, pvcf, aeff and avar. This option does not apply obviulsy for the spherical setup '3b + 2a'.

3. Identification number (idNo). This refers to the position of the parameter in the lower table. E.g. the idNo of the volume concentration is 3 since it is the 3rd parameter. The following conventions has to be taken into account.

   - For the setup '3b + 2a' the shape-related columns ovcf, svcf, pvcf, aeff and avar are ignored. E.g. reff has in this case idNo 4, while in every other setup is 7.
   - ri counts for two entries with indices 10, 11, for the real part and imaginary part respectively. For the setup '3b + 2a' the idNo is 5 and 6.
   - ssa counts for two entries with indices 12, 13, for 355 nm and 532 nm respectively. For the setup '3b + 2a' the idNo is 7 and 8.

4. Parameter names. These are user-specified names of the parameters displayed in the graph.

The button *OK* saves the settings for a reopenning of the gui, *CANCEL* has no effect, while *X* returns the *default settings.* This gui's state information is stored in *C:\SphInX\temp*, as *param_sel_state.mat.*

D.4.6 Save size distributions

The size distributions can be saved in an ascii file with *File < Save size distribution.* This option has the same use as *File < Save data < Size distribution* in *SphInX main*, see the corresponding passage for details.

The essential difference is that now not only the distributions specified by the *Solution Controller* settings are saved but also the corresponding average size distribution in case of multiple projection spaces. The position of the latter in the ascii file is below the last of the distributions being averaged. Moreover in the case of multiple datasets, the average distribution of different dataset is placed (in the same ascii file) below the average distribution of the last dataset involved. The header above each size distribution data contains now all the information (discussed in the case of *SphInX main*) but also additional one regarding the dataset No and the regularization method used (since in *SphInX MPP* the user can load multiple files with different methods). The following example exposes the structure of the file in case 2 datasets with splinepoints No = [9, 10] and spline degree = [2, 3] with TSVD-DP method (the distribution data follow the same column-conventions as is *SphInX main* and are missing from this example for brevity):

% size distribution ||refractive index: 1.33+0.03i ||spline points No.: 9 ||spline degree: 2 ||dataset No.: 1 ||error: 2.4825e-16 ||method: TSVD / Discrep. principle
[distr. data]
% size distribution ||refractive index: 1.6+0.03i ||spline points No.: 9 ||spline degree: 3 ||dataset No.: 1 ||error: 2.0955e-16 ||method: TSVD / Discrep. principle
[distr. data]
% size distribution ||refractive index: 1.33+0.01i ||spline points No.: 10 ||spline degree: 2 ||dataset No.: 1 ||error: 2.0955e-16 ||method: TSVD / Discrep. principle
[distr. data]
% size distribution ||refractive index: 1.4+0.001i ||spline points No.: 10 ||spline degree: 3 ||dataset No.: 1 ||error: 1.6653e-16 ||method: TSVD / Discrep. principle
[distr. data]

% average distribution (same dataset) ||mean refractive index: 1.415+0.01775i ||dataset No.: 1 ||error: 2.0847e-16 ||method: TSVD / Discrep. principle
[average distr. data]
% size distribution ||refractive index: 1.8+0.005i ||spline points No.: 9 ||spline degree: 2 ||dataset No.: 2 ||error: 2.2377e-16 ||method: TSVD / Discrep. principle
[distr. data]
% size distribution ||refractive index: 1.5+0.01i ||spline points No.: 9 ||spline degree: 3 ||dataset No.: 2 ||error: 1.4947e-16 ||method: TSVD / Discrep. principle
[distr. data]
% size distribution ||refractive index: 1.4+0.03i ||spline points No.: 10 ||spline degree: 2 ||dataset No.: 2 ||error: 2.2377e-16 ||method: TSVD / Discrep. principle
[distr. data]
% size distribution ||refractive index: 1.7+0.03i ||spline points No.: 10 ||spline degree: 3 ||dataset No.: 2 ||error: 2.8441e-16 ||method: TSVD / Discrep. principle
[distr. data]
% average distribution (same dataset) ||mean refractive index: 1.6+0.01875i ||dataset No.: 2 ||error: 2.2036e-16 ||method: TSVD / Discrep. principle
[average distr. data]
% average distribution (different datasets) ||mean refractive index: 1.5075+0.01825i ||Up to dataset No.: 2 ||error: 2.1441e-16
[average distr. data]

For as long as *File < Save size distribution* stays checked the size distributions keep getting saved once the *Retrieve parameters* button is pressed and appended to the same txt file.

D.4.7 Latex tool

The results of both tables can be converted to latex to be used further in a document. This is achieved the follwing way.

1. Activate the option under *File < Texify* (checkmark should be on)

2. Display the data you desire (i.e. set *Solution Controller* panel as you please and hit *Retrieve parameters button*)

For as long as the *Texify* option stays activated (checked) the latex-tables are saved in ascii files in *Work* folder with the following conventions:

1. Every hit of the *Retrieve parameters* button saves 2 files *for each file* involved, one for each table. The lower table has a vertical alignment in latex, meaning that the rows of the table become columns in the latex file, while the upper table keeps its horizontal alignment.

2. The files are named after '*date*'-'method'-'identifier', where *identifier* is *latex_table_all* for the file with the lower table and *latex_table_ave* for the file with the upper table,

e.g. *11-Mar-2015-01-24-25_Tikh-LC_latex_table_ave.*

D.4.8 Additional figure options

The option *Settings < External Figures* opens external matlab figures instead of occupying the axes of *SphInX MPP*. Note that choosing this option results in the plots of *all* the size distributions for every single parameter (file index, dataset, spline points number, spline degree) and *all* the associated average distributions; generally it is advised to use this option for single dataset- and spline entries, since with multiple-entries it is easy to lose track of which graph correspond to which set of parameters. Multiple entries in combination with this option are proposed in order to get the average size distributions, which is always the last graph appearing.
In case of the setup *3b + 2a*, it is possible to merge the graph of the initial and the retrieved size distribution to a single plot with *File < Single graph for 1D plots*. The latter can be combined with the external-figure option too.

D.5 Miscellaneous actions

- The working folder (*Work*) can be accessed promptly by any of the main guis from *File < Open work folder*.

- Almost every action has a shortcut key, which is shown near the corresponding option e.g. choosing *Simulation* mode is achieved with *ctrl-1*. Especially in *SphInX main*, the inversion process can be interrupted (after being triggered by the button *Solution Grid*, or *specific solution plot*) by the shortcut *ctrl-P* which stands for *File < save data < Regularization products*. This is useful e.g. when one performs multiple runs and wants to save the work already been ran without stopping it. Moreover there are more "invisible" shortcuts which take place with keyboard buttons:

    (i) *SphInX configurator:* "o", "p" and "m", for the *Optical Data*, the *Parameters* and the *Methods* tab respectively, "d" to edit the *number of datasets* field, "F5" + "space" for the *OK* button,

    (ii) *SphInX main:* "F5" + "space" for the *Solution Grid* button, "F9" + "space" for the *specific solution plot* button, "o" to edit the field *dataset No*, "s" or "d" to edit the fields number *of spline degree*, and "b" to edit the field *number of least residual solutions*,

    (iii) *SphInX MPP:* "F5" for the *Retrieve parameters* button, "o" to edit the field *dataset No*, "s" or "d" to edit the fields number *of spline points No / spline degree,* and "b" to edit the field *best solution No*.

    (iv) *Simulation configurator*: "F5" + "space" for the *OK* button,

    (v) *Optical Profiles*: "F5" + "space" for the *OK* button, "o" to trigger *Open profiles button,* "a" to edit the field *Altitude range,*

    (vi) *Errobar gui*: "F5" + "space" for the *OK* button, "o" to trigger *Open profiles button*.

    (vii) *Pade iteration*: "F5" + "space" for the *OK* button.

- The option *File < Clear workspace* clear the regularization products but keeps the configuration settings.

- Resetting *SphInX configurator* exits both *SphInX main* and *SphInX MPP*; this will clear the workspace entirely. Resetting *SphInX main / SphInX MPP*, the user is able to choose through a modal dialogue box if SphInX configurator stays open (if it was) or resets too. If *SphInX configurator* stays open the regularization products are cleared but the configuration settings remain and passed to *SphInX main / SphInX MPP*. Resetting *SphInX configurator* close all guis and figures and clears the workspace entirely.

- When *OK* is pressed in SphInX configurator while there was a previous run in *SphInX main* the results of this run are cleared (lost). This is done on purpose so that the data structures involved in a new calculation do not include a previous calculation when we save them. *SphInX main* is well suit for multiple experiments in the search for a final configuration, e.g. in order to run a bigger experiment. Nevertheless, by when going back and forth between the two guis and/or stopping the inversion and/or interchangeably use the button *Solution Grid* and *specific solution plot* one has to be cautious when saving the work. A good practice is to use often *File < Clear workspace* and to reset *SphInX main* before running an experiment, the results of which one intends to finally save.

- SphInX configurator and *SphInX main* can be saved as a Matlab *.fig* file with *File < Save figure configuration* which can retrieved by opening a saved *.fig* file (e.g. command line open(nameOfFigFile.fig)), the previous state of the gui *visually* (and only visually, workspace structure is cleared), but it is generally ill-advised to work with such files.

- The previous states of the guis *Simulation configurator, Pade iteration and Errorbar settings* are save under *C:\SphInX\temp* as discussed in the relevant sections. Each new gui-state overwrites the previous. If one wishes to save more than one state, it can be done manually by renaming the associated *.mat* file, e.g. for the case of *Simulation configurator,* before hitting *OK* (which saves the gui state every time)change the default file name *sim_state* of the previous configuration to sim_state_old. Change the latter back to *sim_state* in order to load the older settings.

References

[1] Bureau: La Météorologie 3. (292), 1946.

[2] L. Alados-Arboledas, D. Müller, J. L. Guerrero-Rascado, F. Navas-Guzmán, D. Pérez-Ramírez, and F. J. Olmo. Optical and microphysical properties of fresh biomass burning aerosol retrieved by Raman lidar, and star-and sun-photometry. *Geophysical Research Letters*, 38(1), 2011.

[3] A. Ansmann, J. Bösenberg, A. Chaikovsky, A. Comerón, S. Eckhardt, R. Eixmann, V. Freuden-thaler, P. Ginoux, L. Komguem, H. Linné, M. A. L. Márquez, V. Matthias, I. Mattis, V. Mitev, D. Müller, S. Music, S. Nickovic, J. Pelon, L. Sauvage, P. Sobolewsky, M. K. Srivastava, A. Stohl, O. Torres, G. Vaughan, U. Wandinger, and M. Wiegner. Long-range transport of saharan dust to northern europe: The 11–16 october 2001 outbreak observed with EARLINET. *Journal of Geophysical Research: Atmospheres*, 108(D24), 2003. 4783.

[4] A. Ansmann, A. Petzold, K. Kandler, I. Tegen, M. Wendisch, D. Müller, B. Weinzierl, T. Müller, and J. Heintzenberg. Saharan mineral dust experiments SAMUM-1 and SAMUM-2: what have we learned? *Tellus B*, 63(4):403–429, 2011.

[5] A. Ansmann, M. Riebesell, and C. Weitkamp. Measurement of atmospheric aerosol extinction profiles with a Raman lidar. *Optics Letters*, 15(13):746–748, July 1990.

[6] R. Bahreini, J. L. Jimenez, J. Wang, R. C. Flagan, J. H. Seinfeld, J. T. Jayne, and D. R. Worsnop. Aircraft-based aerosol size and composition measurements during ace-asia using an aerodyne aerosol mass spectrometer. *Journal of Geophysical Research: Atmospheres*, 108(D23).

[7] C. T. H. Baker. *The Numerical Treatment of Integral Equations*. Clarendon Press, Oxford, 1977.

[8] A. Bakushinskiĭ. Remarks on choosing a regularization parameter using the quasi-optimality and ratio criterion. *USSR Computational Mathematics and Mathematical Physics*, 24(4):181 – 182, 1984.

[9] P. Barber and S. Hill. *Light Scattering by Particles: Computational Methods*. Advanced series in applied physics. World Scientific, 1990.

[10] J. Baumeister. *Stable Solution of Inverse Problems*. Advanced Lectures in Mathematics. Vieweg Teubner Verlag, 1987.

[11] J. Baumeister and A. Leitão. *Topics in inverse Problems*. Publicações Matemáticas do IMPA., Rio de Janeiro, 25 Colóquio Brasiliero de Matématica, 2005.

[12] S. M. A. Becker. Regularization of statistical inverse problems and the Bakushinskiĭ veto. *Inverse Problems*, 27(11):115010, Nov. 2011.

[13] E. Beltrami. Sulle funzioni bilineari. *Giornale di matematiche*, 11:98–106, 1873.

[14] C. Böckmann. Hybrid regularization method for the ill-posed inversion of multiwavelength lidar data in the retrieval of aerosol size distributions. *Applied Optics*, 40(9):1329–1342, 2001.

[15] C. Böckmann. Runge-kutta type methods for ill-posed problems and the retrieval of aerosol size distributions. *Proceedings in Applied Mathematics and Mechanics*, 1(1):486–487, 2002.

References

[16] C. Böckmann and A. Kirsche. Iterative regularization method for lidar remote sensing. *Computer Physics Communications*, 174(8):607–615, 2006.

[17] C. Böckmann, I. Mironova, D. Müller, L. Schneidenbach, and R. Nessler. Microphysical aerosol parameters from multiwavelength lidar. *Journal of the Optical Society of America A*, 22(3):518–528, 2005.

[18] C. Böckmann and L. Osterloh. Runge-kutta type regularization method for inversion of spheroidal particle distribution from limited optical data. *Inverse Problems in Science and Engineering*, 22(1):150–165, 2014.

[19] C. F. Bohren and B. M. Herman. Asymptotic scattering efficiency of a large sphere. *Journal of the Optical Society of America*, 69(11):1615–1616, Nov 1979.

[20] C. F. Bohren and D. R. Huffman. *Absorption and scattering of light by small particles.* New York: Wiley, 1983.

[21] J. Bossler, J. Jensen, R. McMaster, and C. Rizos. *Manual of Geospatial Science and Technology.* Manual of Geospatial Science and Technology. Taylor & Francis, 2001.

[22] J. A. Bravo-Aranda, N.-G. Francisco, G.-R. J. Luis, D. Pérez-Ramírez, M. J. Granados-Muñoz, and A.-A. Lucas. Analysis of lidar depolarization calibration procedure and application to the atmospheric aerosol characterization. *International Journal of Remote Sensing*, 34(9-10):3543–3560, 2013.

[23] M. Brazell, N. Li, C. Navasca, and C. Tamon. Solving multilinear systems via tensor inversion. *SIAM Journal on Matrix Analysis and Applications*, 34(2):542–570, 2013.

[24] J. C. Butcher. Coefficients for the study of runge-kutta integration processes. *Journal of the Australian Mathematical Society*, 3:185–201, 5 1963.

[25] J. C. Butcher. *The Numerical Analysis of Ordinary Differential Equations: Runge-Kutta and General Linear Methods.* Wiley-Interscience, New York, NY, USA, 1987.

[26] J. C. Butcher. *Numerical Methods for Ordinary Differential Equations.* John Wiley & Sons, 2008.

[27] K. Chamaillard, S. Jennings, C. Kleefeld, D. Ceburnis, and Y. Yoon. Light backscattering and scattering by nonspherical sea-salt aerosols. *Journal of Quantitative Spectroscopy and Radiative Transfer*, 79−80:577 – 597, 2003. Electromagnetic and Light Scattering by Non-Spherical Particles.

[28] K. Chen. *Matrix Preconditioning Techniques and Applications.* Cambridge University Press, 2005. Cambridge Books Online.

[29] C. De Boor. *A practical guide to splines.* Springer, New York, 2001.

[30] V. de Silva and L.-H. Lim. Tensor rank and the ill-posedness of the best low-rank approximation problem. *SIAM Journal on Matrix Analysis and Applications*, 30(3):1084–1127, Sept. 2008.

[31] C. Denjean, F. Cassola, A. Mazzino, S. Triquet, S. Chevaillier, N. Grand, T. Bourrianne, G. Momboisse, K. Sellegri, A. Schwarzenbock, E. Freney, M. Mallet, and P. Formenti. Size distribution and optical properties of mineral dust aerosols transported in the western mediterranean. *Atmospheric Chemistry and Physics*, 16(2):1081–1104, 2016.

[32] R. R. Draxler and G. D. Rolph. *HYSPLIT (HYbrid Single-Particle Lagrangian Integrated Trajectory) model access via NOAA ARL READY website (http://www. arl. noaa. gov/ready/hysplit4. html). NOAA Air Resources Laboratory, Silver Spring.* Md, 2014.

[33] O. Dubovik, B. Holben, T. F. Eck, A. Smirnov, Y. J. Kaufman, M. D. King, D. Tanré, and I. Slutsker. Variability of absorption and optical properties of key aerosol types observed in worldwide locations. *Journal of the Atmospheric Sciences*, 59(3):590–608, 2002.

[34] O. Dubovik and M. D. King. A flexible inversion algorithm for retrieval of aerosol optical properties from sun and sky radiance measurements. *Journal of Geophysical Research: Atmospheres*, 105(D16):20673–20696, 2000.

[35] O. Dubovik, A. Sinyuk, T. Lapyonok, B. N. Holben, M. Mishchenko, P. Yang, T. F. Eck, H. Volten, O. Muñoz, B. Veihelmann, W. J. van der Zande, J.-F. Leon, M. Sorokin, and I. Slutsker. Application of spheroid models to account for aerosol particle nonsphericity in remote sensing of desert dust. *Journal of Geophysical Research: Atmospheres*, 111(D11), 2006.

[36] O. Dubovik, A. Smirnov, B. N. Holben, M. D. King, Y. J. Kaufman, T. F. Eck, and I. Slutsker. Accuracy assessments of aerosol optical properties retrieved from aerosol robotic network (aeronet) sun and sky radiance measurements. *Journal of Geophysical Research: Atmospheres*, 105(D8):9791–9806, 2000.

[37] H. Engl, M. Hanke, and A. Neubauer. *Regularization of Inverse Problems.* Mathematics and Its Applications. Springer Netherlands, 2000.

[38] I. Fenyö and H. Stolle. *Theorie und Praxis der linearen Integralgleichungen.* Number v. 4 in Lehrbücher und Monographien aus dem Gebiete der exakten Wissenschaften: Mathematische Reihe. Birkhäuser, Basel, 1984.

[39] F. G. Fernald. Analysis of atmospheric lidar observations: some comments. *Appied Optics*, 23(5):652–653, 1984.

[40] G. Fiocco and L. O. Smullin. Detection of scattering layers in the upper atmosphere (60-140 km) by optical radar. *Nature*, 199(4736):1275–1276, 1963.

[41] P. Forster, V. Ramaswamy, P. Artaxo, T. Berntsen, R. Betts, D. Fahey, J. Haywood, J. Lean, D. Lowe, G. Myhre, J. Nganga, R. Prinn, G. Raga, M. Schulz, and R. V. Dorland. *Changes in Atmospheric Constituents and in Radiative Forcing. In: Climate Change 2007: The Physical Science Basis. Contribution of Working Group I to the Fourth Assessment Report of the Intergovernmental Panel on Climate Change.* Cambridge University Press, Cambridge, United Kingdom and New York, NY, USA, 2007.

[42] V. Freudenthaler, M. Esselborn, M. Wiegner, B. Heese, M. Tesche, A. Ansmann, D. Múller, D. Althausen, M. Wirth, A. Fix, G. Ehret, P. Knippertz, C. Toledano, J. Gasteiger, M. Garhammer, and M. Seefeldner. Depolarization ratio profiling at several wavelengths in pure saharan dust during samum 2006. *Tellus B*, 61(1):165–179, 2009.

[43] B. G. Galerkin. Expansions in stability problems for elastic rods and plates. *Vestnik inzkenorov 19*, pages 897–908, 1915. (In Russian).

[44] J. Gasteiger and V. Freudenthaler. Benefit of depolarization ratio at $\lambda = 1064$ nm for the retrieval of the aerosol microphysics from lidar measurements. *Atmospheric Measurement Techniques*, 7(11):3773–3781, 2014.

[45] D. Goldstein. *Polarized Light, Revised and Expanded.* Optical engineering. Taylor & Francis, 2003.

[46] G. Golub and W. Kahan. Calculating the singular values and pseudo-inverse of a matrix. *Journal of the Society for Industrial and Applied Mathematics Series B Numerical Analysis*, 2(2):205–224, 1965.

[47] G. H. Golub, M. Heath, and G. Wahba. Generalized cross-validation as a method for choosing a good ridge parameter. *Technometrics*, 21(2):215–223, 1979.

[48] D. J. Griffiths. *Introduction to Electrodynamics (3rd Edition).* Benjamin Cummings, 1998.

[49] S. Groß, V. Freudenthaler, K. Schepanski, C. Toledano, A. Schäfler, A. Ansmann, and B. Weinzierl. Optical properties of long-range transported saharan dust over barbados as measured by dual-wavelength depolarization Raman lidar measurements. *Atmospheric Chemistry and Physics*, 15(19):11067–11080, 2015.

[50] J. Guerrero-Rascado, B. Ruiz, and L. Alados-Arboledas. Multi-spectral lidar characterization of the vertical structure of saharan dust aerosol over southern spain. *Atmospheric Environment*, 42(11):2668–2681, 2008.

[51] M. Haarig, D. Althausen, A. Ansmann, A. Klepel, H. Baars, R. Engelmann, S. Groß, and V. Freudenthaler. Measurement of the linear depolarization ratio of aged dust at three wavelengths (355, 532 and 1064 nm) simultaneously over barbados. *EPJ Web of Conferences*, 119:18009, 2016.

[52] J. Hadamard. *Lectures on the Cauchy Problem in Linear Partial Differential Equations*. Yale University Press, New Haven, 1923.

[53] P. Hansen. Computation of the singular value expansion. *Computing*, 40(3):185–199, 1988.

[54] P. C. Hansen. The truncated SVD as a method for regularization. *BIT Numerical Mathematics*, 27(4):534–553.

[55] P. C. Hansen. Analysis of discrete ill-posed problems by means of the l-curve. *SIAM Review*, 34(4):561–580, 1992.

[56] P. C. Hansen. The l-curve and its use in the numerical treatment of inverse problems. In *in Computational Inverse Problems in Electrocardiology, ed. P. Johnston, Advances in Computational Bioengineering*, pages 119–142. WIT Press, 2000.

[57] P. C. Hansen. *Discrete inverse problems: Insight and Algorithms*, volume 7. SIAM, 2010.

[58] B. Heese, D. Althausen, T. Dinter, M. Esselborn, T. Müller, M. Tesche, and M. Wiegner. Vertically resolved dust optical properties during samum: Tinfou compared to Ouarzazate. *Tellus B*, 61(1):195–205, 2009.

[59] P. Hobbs. *Aerosol-Cloud-Climate Interactions*. International Geophysics. Elsevier Science, 1993.

[60] B. N. Holben, T. F. Eck, I. Slutsker, D. Tanre, J. P. Buis, A. Setzer, E. Vermote, J. A. Reagan, Y. J. Kaufman, T. Nakajima, F. Lavenu, I. Jankowiak, and A. Smirnov. AERONET—A federated instrument network and data archive for aerosol characterization. *Remote Sensing of Environment*, 66(1):1–16, 1998.

[61] K. Huang, G. Zhuang, J. Li, Q. Wang, Y. Sun, Y. Lin, and J. S. Fu. Mixing of asian dust with pollution aerosol and the transformation of aerosol components during the dust storm over china in spring 2007. *Journal of Geophysical Research: Atmospheres*, 115(D7), 2010. D00K13.

[62] IPCC. *Climate Change 2007: The Physical Science Basis. Contribution of Working Group I to the Fourth Assessment Report of the Intergovernmental Panel on Climate Change*. Cambridge University Press, Cambridge, United Kingdom and New York, NY, USA, 2007.

[63] IPCC. *Annex I: Atlas of Global and Regional Climate Projections*, book section AI, pages 1311–1394. Cambridge University Press, Cambridge, United Kingdom and New York, NY, USA, 2013.

[64] IPCC. *Climate Change 2013: The Physical Science Basis. Contribution of Working Group I to the Fifth Assessment Report of the Intergovernmental Panel on Climate Change*. Cambridge University Press, Cambridge, United Kingdom and New York, NY, USA, 2013.

[65] IPCC. *Summary for Policymakers*, book section SPM, pages 1–30. Cambridge University Press, Cambridge, United Kingdom and New York, NY, USA, 2013.

[66] J. Jackson. *Classical electrodynamics*. Wiley, 1975.

[67] D. Jaggard, C. Hill, R. Shorthill, D. Stuart, M. Glantz, F. Rosswog, B. Taggart, and S. Hammond. Plumes and visibility measurements and model components-supplement light scattering from particles of regular and irregular shape. *Atmospheric Environment (1967)*, 15(12):2511 – 2519, 1981.

References

[68] J. T. Jayne, D. C. Leard, X. Zhang, P. Davidovits, K. A. Smith, C. E. Kolb, and D. R. Worsnop. Development of an aerosol mass spectrometer for size and composition analysis of submicron particles. *Aerosol Science & Technology*, 33(1-2):49–70, 2000.

[69] E. A. Johnson, R. C. Meyer, R. E. Hopkins, and W. H. Mock. The measurement of light scattered by the upper atmosphere from a search-light beam. *Journal of the Optical Society of America*, 29(12):512–517, Dec 1939.

[70] R. Kahn, P. Banerjee, D. McDonald, and D. J. Diner. Sensitivity of multiangle imaging to aerosol optical depth and to pure-particle size distribution and composition over ocean. *Journal of Geophysical Research: Atmospheres*, 103(D24):32195–32213, 1998.

[71] M. Kahnert, T. Nousiainen, M. A. Thomas, and J. Tyynelä. Light scattering by particles with small-scale surface roughness: Comparison of four classes of model geometries. *Journal of Quantitative Spectroscopy and Radiative Transfer*, 113(18):2356 – 2367, 2012. Electromagnetic and Light Scattering by non-spherical particles {XIII}.

[72] J. Kallrath. Rational function techniques and Padé approximants, in: Hagel, j. (ed.), nonlinear perturbation methods with emphasis to celestial mechanics. pages 97–107, 1995.

[73] K. Kandler, N. Benker, U. Bundke, E. Cuevas, M. Ebert, P. Knippertz, S. Rodríguez, L. Schütz, and S. Weinbruch. Chemical composition and complex refractive index of Saharan mineral dust at Izaña, Tenerife (Spain) derived by electron microscopy. *Atmospheric Environment*, 41(37):8058 – 8074, 2007.

[74] K. Kandler, M. Hartmann, M. Ebert, S. Weinbruch, B. Weinzierl, A. Walser, D. Sauer, and K. Wadinga Fomba. Long-range-transported Saharan dust in the Caribbean - an electron microscopy perspective of aerosol composition and modification. In *EGU General Assembly Conference Abstracts*, volume 17 of *EGU General Assembly Conference Abstracts*, page 6150, Apr. 2015.

[75] K. Kandler, L. Schütz, C. Deutscher, M. Ebert, H. Hofmann, S. Jäckel, R. Jaenicke, P. Knippertz, K. Lieke, A. Massling, A. Petzold, A. Schladitz, B. Weinzierl, A. Wiedenscholer, S. Zorn, and S. Weinbruch. Size distribution, mass concentration, chemical and mineralogical composition and derived optical parameters of the boundary layer aerosol at Tinfou, Morocco, during SAMUM 2006. *Tellus B*, 61(1):32–50, 2009.

[76] Y. J. Kaufman, D. Tanré, and O. Boucher. A satellite view of aerosols in the climate system. *Nature*, 419(6903):215–223, 2002.

[77] L. Kiefert, G. H. McTainsh, and W. G. Nickling. *The Impact of Desert Dust Across the Mediterranean*, chapter Sedimentological Characteristics of Saharan and Australian Dusts, pages 183–190. Springer Netherlands, Dordrecht, 1996.

[78] C. S. Kim and C. Yeh. Scattering of an obliquely incident wave by a multilayered elliptical lossy dielectric cylinder. *Radio Science*, 26(5):1165–1176, 1991.

[79] M. Kirby and L. Sirovich. Application of the Karhunen-Loève procedure for the characterization of human faces. *IEEE Transactions on Pattern Analysis and Machine Intelligence*, 12(1):103–108, Jan 1990.

[80] A. Kirsche. *Regularisierungsverfahren. Entwicklung, Konvergenzuntersuchung und optimale Anpassung für die Fernerkundung.* Ph.D. thesis, University of Potsdam, 2007.

[81] A. Kirsche and C. Böckmann. Rational approximations for ill-conditioned equation systems. *Applied Mathematics and Computation*, 171(1):385 – 397, 2005.

[82] A. Kirsche and C. Böckmann. Padé iteration method for regularization. *Applied Mathematics and Computation*, 180(2):648 – 663, 2006.

[83] J. D. Klett. Stable analytical inversion solution for processing lidar returns. *Applied Optics*, 20(2):211–220, Jan 1981.

[84] P. Koepke, J. Gasteiger, and M. Hess. Technical note: Optical properties of desert aerosol with non-spherical mineral particles: data incorporated to opac. *Atmospheric Chemistry and Physics*, 15(10):5947–5956, 2015.

[85] P. Koepke and M. Hess. Scattering functions of tropospheric aerosols: the effects of nonspherical particles. *Applied Optics*, 27(12):2422–2430, Jun 1988.

[86] A. Kolgotin and D. Müller. Theory of inversion with two-dimensional regularization: profiles of microphysical particle properties derived from multiwavelength lidar measurements. *Applied Optics*, 47(25):4472–4490, 2008.

[87] M. A. Krasnoselskii, G. Vainikko, P. Zabreko, and Y. Rutitskii. *Approximate solution of operator equations*. Wolters-Noordhoff, Groningen, 1972.

[88] R. Kress. *Linear Integral Equations*. Applied Mathematical Sciences. Springer New York, 1999.

[89] J. D. Lambert. *Numerical methods for ordinary differential systems: the initial value problem*. Wiley, 1991.

[90] L. Landweber. An Iteration Formula for Fredholm Integral Equations of the First Kind. *American Journal of Mathematics*, 73:615–624, 1951.

[91] C. L. Lawson and R. J. Hanson. *Solving least squares problems*, volume 161. SIAM, 1974.

[92] J. Lian, D. Yao, and B. He. A new method for implementation of regularization in cortical potential imaging. In *Engineering in Medicine and Biology Society, 1998. Proceedings of the 20th Annual International Conference of the IEEE*, volume 4, pages 2155–2158 vol.4, Oct 1998.

[93] U. Lohmann and J. Feichter. Global indirect aerosol effects: a review. *Atmospheric Chemistry and Physics*, 5(3):715–737, 2005.

[94] F. Madonna, A. Amodeo, A. Boselli, C. Cornacchia, V. Cuomo, G. D'Amico, A. Giunta, L. Mona, and G. Pappalardo. Ciao: the cnr-imaa advanced observatory for atmospheric research. *Atmospheric Measurement Techniques*, 4(6):1191–1208, 2011.

[95] T. H. Maiman. Stimulated optical radiation in ruby. *Nature*, 187(4736):493–494, Aug. 1960.

[96] M. Mallet, F. Dulac, P. Formenti, P. Nabat, J. Sciare, G. Roberts, J. Pelon, G. Ancellet, D. Tanré, F. Parol, C. Denjean, G. Brogniez, A. di Sarra, L. Alados-Arboledas, J. Arndt, F. Auriol, L. Blarel, T. Bourrianne, P. Chazette, S. Chevaillier, M. Claeys, B. D'Anna, Y. Derimian, K. Desboeufs, T. Di Iorio, J.-F. Doussin, P. Durand, A. Féron, E. Freney, C. Gaimoz, P. Goloub, J. L. Gómez-Amo, M. J. Granados-Muñoz, N. Grand, E. Hamonou, I. Jankowiak, M. Jeannot, J.-F. Léon, M. Maillé, S. Mailler, D. Meloni, L. Menut, G. Momboisse, J. Nicolas, T. Podvin, V. Pont, G. Rea, J.-B. Renard, L. Roblou, K. Schepanski, A. Schwarzenboeck, K. Sellegri, M. Sicard, F. Solmon, S. Somot, B. Torres, J. Totems, S. Triquet, N. Verdier, C. Verwaerde, F. Waquet, J. Wenger, and P. Zapf. Overview of the chemistry-aerosol mediterranean experiment/aerosol direct radiative forcing on the Mediterranean climate (ChArMEx/ADRIMED) summer 2013 campaign. *Atmospheric Chemistry and Physics*, 16(2):455–504, 2016.

[97] G. Mie. Beiträge zur optik trüber medien, speziell kolloidaler metallösungen. *Annalen der Physik*, 330(3):377–445, 1908.

[98] M. Mishchenko, L. Travis, and A. Lacis. *Scattering, Absorption, and Emission of Light by Small Particles*. Cambridge University Press, 2002.

[99] M. I. Mishchenko, L. D. Travis, R. A. Kahn, and R. A. West. Modeling phase functions for dustlike tropospheric aerosols using a shape mixture of randomly oriented polydisperse spheroids. *Journal of Geophysical Research: Atmospheres*, 102(D14):16831–16847, 1997.

[100] M. I. Mishchenko, L. D. Travis, and D. W. Mackowski. T-matrix computations of light scattering by nonspherical particles: A review. *Journal of Quantitative Spectroscopy and Radiative Transfer*, 55(5):535 – 575, 1996.

[101] P. Morse and H. Feshbach. *Methods of theoretical physics.* Number v. 2 in International series in pure and applied physics. McGraw-Hill, 1953.

[102] A. Mugnai and W. J. Wiscombe. Scattering from nonspherical chebyshev particles. 3: Variability in angular scattering patterns. *Applied Optics*, 28(15):3061–3073, Aug 1989.

[103] D. Müller, A. Ansmann, I. Mattis, M. Tesche, U. Wandinger, D. Althausen, and G. Pisani. Aerosol-type-dependent lidar ratios observed with Raman lidar. *Journal of Geophysical Research: Atmospheres*, 112(D16), 2007. D16202.

[104] D. Müller, I. Mattis, A. Ansmann, U. Wandinger, C. Ritter, and D. Kaiser. Multiwavelength Raman lidar observations of particle growth during long-range transport of forest-fire smoke in the free troposphere. *Geophysical Research Letters*, 34(5), 2007.

[105] D. Müller, F. Wagner, D. Althausen, U. Wandinger, and A. Ansmann. Physical properties of the indian aerosol plume derived from six-wavelength lidar observations on 25 march 1999 of the indian ocean experiment. *Geophysical Research Letters*, 27(9):1403–1406, 2000.

[106] D. Müller, F. Wagner, U. Wandinger, A. Ansmann, M. Wendisch, D. Althausen, and W. von Hoyningen-Huene. Microphysical particle parameters from extinction and backscatter lidar data by inversion with regularization: experiment. *Applied Optics*, 39(12):1879–1892, 2000.

[107] D. Müller, U. Wandinger, and A. Ansmann. Microphysical particle parameters from extinction and backscatter lidar data by inversion with regularization: simulation. *Applied Optics*, 38(12):2358–2368, 1999.

[108] D. Müller, U. Wandinger, and A. Ansmann. Microphysical particle parameters from extinction and backscatter lidar data by inversion with regularization: theory. *Applied Optics*, 38(12):2346–2357, 1999.

[109] T. Nakajima, M. Tanaka, M. Yamano, M. Shiobara, K. Arao, and Y. Nakanishi. Aerosol optical characteristics in the yellow sand events observed in may, 1982 in nagasaki-Part II Models. *Journal of Meteorological Society of Japan*, 67(2):279–291, 1989.

[110] D. Nicolae, A. Nemuc, D. Müller, C. Talianu, J. Vasilescu, L. Belegante, and A. Kolgotin. Characterization of fresh and aged biomass burning events using multiwavelength Raman lidar and mass spectrometry. *Journal of Geophysical Research: Atmospheres*, 118(7):2956–2965, 2013.

[111] T. Nousiainen. Optical modeling of mineral dust particles: A review. *Journal of Quantitative Spectroscopy and Radiative Transfer*, 110(14-16):1261 – 1279, 2009. {XI} Conference on Electromagnetic and Light Scattering by Non-Spherical Particles: 2008.

[112] L. Osterloh. *Retrieving Aerosol Microphysical Properties from Multiwavelength Lidar Data.* Ph.D. thesis, Potsdam University, 2011.

[113] L. Osterloh, C. Böckmann, R. E. Mamouri, and A. Papayannis. An adaptive base point algorithm for the retrieval of aerosol microphysical properties. *Open Atmospheric Science Journal*, 5:61–73, 2011.

[114] L. Osterloh, C. Böckmann, D. Nicolae, and A. Nemuc. Corrigendum to Regularized inversion of microphysical atmospheric particle parameters: Theory and application [J. Comput. Phys. 237 (2013) 79–94] . *Journal of Computational Physics*, 237:696, 2014.

[115] L. Osterloh, C. Pérez, D. Böhme, J. M. Baldasano, C. Böckmann, L. Schneidenbach, and D. Vicente. Parallel software for retrieval of aerosol distribution from lidar data in the framework of EARLINET-ASOS. *Computer Physics Communications*, 180(11):2095–2102, 2009.

[116] H. Padé. Sur la représentation approchée d'une fonction par des fractions rationnelles. *Annales scientifiques de l'École Normale Supérieure*, 9:3–93, 1892.

[117] A. Papayannis, R. E. Mamouri, A. Nenes, G. Tsaknakis, V. Amiridis, G. Georgoussis, G. Avdikos, C. Böckmann, L. Osterloh, K. Eleftheriadis, D. Böhme, and A. Stohl. Optical, microphysical and chemical properties of tropospheric aerosols retrieved by a 6-wavelength Raman lidar system during a biomass burning event over Athens, Greece, Proceeding of the 24th international laser radar conference. 381-384, Boulder, Colorado, USA, 23-27 June, 2008.

[118] G. Pappalardo, A. Amodeo, A. Apituley, A. Comeron, V. Freudenthaler, H. Linné, A. Ansmann, J. Bösenberg, G. D'Amico, I. Mattis, L. Mona, U. Wandinger, V. Amiridis, L. Alados-Arboledas, D. Nicolae, and M. Wiegner. EARLINET: towards an advanced sustainable european aerosol lidar network. *Atmospheric Measurement Techniques*, 7(8):2389–2409, 2014.

[119] G. Pappalardo, A. Amodeo, M. Pandolfi, U. Wandinger, A. Ansmann, J. Bösenberg, V. Matthias, V. Amiridis, F. D. Tomasi, M. Frioud, M. Iarlori, L. Komguem, A. Papayannis, F. Rocadenbosch, and X. Wang. Aerosol lidar intercomparison in the framework of the EARLINET project. 3. Raman lidar algorithm for aerosol extinction, backscatter, and lidar ratio. *Appl. Opt.*, 43(28):5370–5385, Oct 2004.

[120] E. M. Patterson, D. A. Gillette, and B. H. Stockton. Complex index of refraction between 300 and 700 nm for saharan aerosols. *Journal of Geophysical Research*, 82(21):3153–3160, 1977.

[121] P. Pornsawad, C. Böckmann, C. Ritter, and M. Rafler. Ill-posed retrieval of aerosol extinction coefficient profiles from Raman lidar data by regularization. *Applied Optics*, 47(10):1649–1661, Apr 2008.

[122] M. Rezghi and S. M. Hosseini. A new variant of l-curve for tikhonov regularization. *Journal of Computational and Applied Mathematics*, 231(2):914 – 924, 2009.

[123] A. Rieder. *Keine Probleme mit Inversen Problemen - Eine Einführung in ihre stabile Lösung.* Vieweg-Teubner Verlag, 2003.

[124] T. Rother. *Electromagnetic Wave Scattering on Nonspherical Particles.* Springer, New York, 2009.

[125] T. Rother and M. Kahnert. *Electromagnetic Wave Scattering on Nonspherical Particles.* Springer, New York, 2014.

[126] T. Rother, K. Schmidt, J. Wauer, V. Shcherbakov, and J.-F. Gayet. Light scattering on chebyshev particles of higher order. *Appl. Opt.*, 45(23):6030–6037, Aug 2006.

[127] W. Rudin. *Functional analysis.* McGraw-Hill series in higher mathematics. McGraw-Hill, 1973.

[128] S. Samaras. *Algorithm development for the retrieval of the aerosol microphysical properties using inverse scattering mathematical techniques.* Master's thesis, National Technical University of Athens, November 2011. (in Greek).

[129] S. Samaras and C. Böckmann. Aerosol microphysical retrieval from lidar data based on a two-dimensional spheroid-particle model. ACTRiS II workshop, Leipzig, 22-26.11.2015.

[130] S. Samaras, C. Böckmann, and D. Nicolae. Combined sphere-spheroid particle model for the retrieval of the microphysical aerosol parameters via regularized inversion of lidar data, Proceeding of the 27th international laser radar conference. New York, USA, 5-10 July 2015, 2015.

[131] S. Samaras, D. Nicolae, C. Böckmann, J. Vasilescu, I. Binietoglou, L. Labzovskii, F. Toanca, and A. Papayannis. Using Raman-lidar-based regularized microphysical retrievals and aerosol mass spectrometer measurements for the characterization of biomass burning aerosols. *Journal of Computational Physics*, 299:156 – 174, 2015.

[132] S. A. Schelkunoff. Some equivalence theorems of electromagnetics and their application to radiation problems. *The Bell System Technical Journal*, 15(1):92–112, Jan 1936.

[133] A. Schladitz, T. Müller, N. Kaaden, A. Massling, K. Kandler, M. Ebert, S. Weinbruch, C. Deutscher, and A. Wiedensohler. In situ measurements of optical properties at Tinfou (Morocco) during the Saharan Mineral Dust Experiment SAMUM 2006. *Tellus B*, 61(1):64–78, 2009.

[134] D. Showalter. Representation and computation of the pseudoinverse. *Proceedings of the American Mathematical Society*, 18(4):584–586, 1967.

[135] D. M. Showalter and A. Ben-Israel. Representation and computation of the generalized inverse of a bounded linear operator between hilbert spaces. *Atti Della Accademia Nazionale Dei Lincei Rendiconti-Classe Di Scienze Fisiche-Matematiche Naturali*, 48:184–194, 1970.

[136] A. Sinyuk, O. Dubovik, B. Holben, T. F. Eck, F.-M. Breon, J. Martonchik, R. Kahn, D. J. Diner, E. F. Vermote, J.-C. Roger, T. Lapyonok, and I. Slutsker. Simultaneous retrieval of aerosol and surface properties from a combination of AERONET and satellite data. *Remote Sensing of Environment*, 107(1-2):90 – 108, 2007. Multi-angle Imaging SpectroRadiometer (MISR) Special Issue.

[137] M. Stone. Cross-validatory choice and assessment of statistical predictions. *Journal of the Royal Statistical Society. Series B (Methodological)*, 36(2):111–147, 1974.

[138] G. Szego. *Orthogonal Polynomials*. New York, 1959.

[139] A. N. Tikhonov and V. Y. Arsenin. Solution of ill-posed problems. *Winston, Washington DC*, 1977.

[140] L. N. Trefethen and D. Bau III. *Numerical Linear Algebra*. SIAM, 1997.

[141] L. Tsang, J. Kong, and R. Shin. *Theory of microwave remote sensing*. Wiley series in remote sensing. Wiley, 1985.

[142] H. C. Van de Hulst. *Light scattering by small particles*. John Wiley & Sons, New York, 1957.

[143] I. Veselovskii, O. Dubovik, A. Kolgotin, T. Lapyonok, P. Di Girolamo, D. Summa, D. N. Whiteman, M. Mishchenko, and D. Tanré. Application of randomly oriented spheroids for retrieval of dust particle parameters from multiwavelength lidar measurements. *Journal of Geophysical Research: Atmospheres*, 115(D21), 2010.

[144] I. Veselovskii, P. Goloub, T. Podvin, V. Bovchaliuk, Y. Derimian, P. Augustin, M. Fourmentin, D. Tanre, M. Korenskiy, D. N. Whiteman, A. Diallo, T. Ndiaye, A. Kolgotin, and O. Dubovik. Retrieval of optical and physical properties of african dust from multiwavelength Raman lidar measurements during the shadow campaign in senegal. *Atmospheric Chemistry and Physics*, 16(11):7013–7028, 2016.

[145] I. Veselovskii, A. Kolgotin, V. Griaznov, D. Müller, K. Franke, and D. N. Whiteman. Inversion of multiwavelength Raman lidar data for retrieval of bimodal aerosol size distribution. *Applied Optics*, 43(5):1180–1195, 2004.

[146] R. Wagner, T. Ajtai, K. Kandler, K. Lieke, C. Linke, T. Müller, M. Schnaiter, and M. Vragel. Complex refractive indices of saharan dust samples at visible and near uv wavelengths: a laboratory study. *Atmospheric Chemistry and Physics*, 12(5):2491–2512, 2012.

[147] G. Wahba. *Spline Models for Observational Data*. Society for Industrial and Applied Mathematics, 1990.

[148] U. Wandinger and A. Ansmann. Experimental determination of the lidar overlap profile with Raman lidar. *Applied Optics*, 41(3):511–514, Jan 2002.

[149] U. Wandinger, A. Hiebsch, I. Mattis, G. Pappalardo, L. Mona, and F. Madonna. Aerosols and clouds: Longterm database from spaceborne lidar measurements. *Technical report*, 2010. ESTEC Contract 21487/08/NL/HE, Final Report.

[150] U. Wandinger, D. Müller, C. Böckmann, D. Althausen, V. Matthias, J. Bösenberg, V. Weiß, M. Fiebig, M. Wendisch, A. Stohl, et al. Optical and microphysical characterization of biomass-burning and industrial-pollution aerosols from-multiwavelength lidar and aircraft measurements. *Journal of Geophysical Research: Atmospheres (1984–2012)*, 107(D21):LAC–7, 2002.

[151] T. T. Warner. *Desert Meteorology*. Cambridge University Press, 2004. Cambridge Books Online.

[152] P. C. Waterman. Matrix formulation of electromagnetic scattering. *Proceedings of the IEEE*, 53(8):805–812, 1965.

[153] C. Weitkamp. *Lidar: Range-Resolved Optical Remote Sensing of the Atmosphere*. Springer Series in Optical Sciences. Springer, 2005.

[154] W. J. Wiscombe and A. Mugnai. Scattering from nonspherical chebyshev particles: A compendium of calculations. *NASA Reference Publications 1157*, 1986.

[155] A. Yariv and P. Yeh. *Photonics: Optical Electronics in Modern Communications*. The Oxford series in electrical and computer engineering. Oxford University Press, 2007.

[156] V. Zuev. *Laser beams in the atmosphere*. Consultants Bureau, 1982.

Eigenständigkeitserklärung

Hiermit erkläre ich, dass ich die vorliegende Arbeit selbständig und nur unter Verwendung der angegebenen Literatur und Hilfsmittel angefertigt habe.

Potsdam, am 12 Dezember 2016